Study of near surface defects using positrons and Development of a pulsed positron beam system

by

VARGHESE ANTO CHIRAYATH
(Enrollment No: PHYS02200704014)

Indira Gandhi Center for Atomic Research, Kalpakkam

A thesis submitted to the
Board of Studies in Physical Sciences
In partial fulfillment of requirements
For the degree of

DOCTOR OF PHILOSOPHY

of

HOMI BHABHA NATIONAL INSTITUTE

FEBRUARY, 2013

Homi Bhabha National Institute

Recommendations of the Viva Voce Board

As members of the Viva Voce Board, we certify that we have read the dissertation prepared by **Varghese Anto Chirayath** entitled **"Study of near surface defects using positrons and Development of a pulsed positron beam system"** and recommend that it may be accepted as fulfilling the dissertation requirement for the Degree of Doctor of Philosophy.

_____Date:
Chairman – C. S. Sundar

_____Date:
Convener/Guide – G. Amarendra

_____Date:
Member – K.G.M. Nair

_____Date:
Member – A.K.Arora

Final approval and acceptance of this dissertation is contingent upon the candidate's submission of the final copies of the dissertation to HBNI.

Date:
Place:

CERTIFICATE

I hereby certify that I have read this dissertation prepared under my direction and recommend that it may be accepted as fulfilling the dissertation requirement.

Date:

Place: **(G. Amarendra)**

Thesis Supervisor

STATEMENT BY AUTHOR

This dissertation has been submitted in partial fulfillment of requirements for an advanced degree at Homi Bhabha National Institute (HBNI) and is deposited in the library to be made available to borrowers under rules of the HBNI.

Brief quotations from this dissertation are allowable without special permission, provided that accurate acknowledgement of source is made. Requests for permission for extended quotation from or reproduction of this manuscript in whole or in part may be granted by the Competent Authority of HBNI when in his or her judgment the proposed use of the material is in the interests of scholarship. In all other instances, however, permission must be obtained from the author.

(Varghese Anto Chirayath)
Ph.D Candidate

DECLARATION

I, hereby declare that the investigation presented in the thesis has been carried out by me. The work is original and has not been submitted earlier as a whole or in part for a degree / diploma at this or any other Institution / University.

(Varghese Anto Chirayath)

Ph.D Candidate

This thesis is dedicated to

Abishikth

ACKNOWLEDGEMENTS

It would be foolish for someone to claim that the work done over a period of five and half years is a standalone enterprise (unless one is doing a PhD on meditation by meditation). In IGCAR, Kalpakkam where the intellectual density is high, it is impossible to move in the above said timescales without an inelastic knowledge scattering resulting in a change of one's career trajectory. The work also benefits from the emotional and intellectual growth attained during the period prior to the doctoral work. Hence the number of people to be remembered and acknowledged far exceeds the page limit set by the university. The order in which people appear has no bearing on their relative importance and if someone important is missing it is the drawback of the random wiring of neurons inside this brain.

I am deeply indebted to my guide and mentor Dr. G. Amarendra for taking me as a student under him for this thesis project. Through intellectual and emotional support he has helped me to embrace the project and the ensuing PhD life with vigor and an open mind. His method in human interaction is a guide for any person to see how humanity and kindness can lead to success and most importantly happiness. I also express my deep sense of gratitude for the infinite amount of freedom in work which has helped in my growth as an individual and independent researcher.

I am also thankful to the Doctoral committee members Dr. C. S. Sundar, Dr. K. G. M. Nair and Dr. A. K. Arora for providing me with valuable guidance, tips and necessary experimental support during the research work. On a personal note, I extend my special gratitude to Dr. C. S. Sundar and Dr. A. Bharathi for their personal interest in my scientific and career growth. I am also thankful to Shri. M. C. Valsakumar for his interest in the pulsed positron project and for his stimulating classes.

I thank Dr. P. R. Vasudeva Rao, Director IGCAR and former directors Shri S. C. Chetal and Dr. Baldev Raj for allowing me to work in IGCAR with all the material comforts. I thank Dr. M. Sai Baba for his continuous support and for the help to have my family with me during this period.

I was extremely lucky to be in the company of kind hearted and helpful people in Metal Physics Section whose efforts are instrumental in bringing out the thesis in this form. I am in awe of two highly intelligent and magnanimous people, Dr. R. Rajaraman and Dr. G. Venogopal Rao who have helped to sharpen my thinking and experimental

skills. They have stood shoulder to shoulder to bear the weight of the project and many failures. I am also indebted to Dr. S. Abhaya and Ms. J Parimala for the initial training in positron spectroscopy and for carrying out numerous works on my behalf. I thankfully remember Ms. M. Premila, Dr. R. Govindraj, Dr. J. Jayapandian and Dr. T. N. Sairam for their support.

I have enjoyed the friendship, company, collaboration and stimulating discussion with Dr. R. N. Viswanath, Mr. C. David, Dr. Sujoy Chakravarty and Mr. V Raghunathan. I have enjoyed the company of Dr. Shamima Hussain, Dr. G. Bhalerao and Dr. Neeraj Shukla during this period. I am also thankful to Dr. J. Arunkumar, Mr. P. Magudapathy, Dr. M. Kamaruddin, Dr. Prabhakar, Mr. Balamurugan, Dr. Gomathy Natarajan, Dr. Rajagoapalan and Dr. K. K. Mishra for their help and support at various stages of my research work. I have had the luck to interact with Ms. Annalakshmi, Mr. Gururaj, Mr. Satyanarayan and Mr. Rajeev Ranjan who have helped in clarifying many doubts. I am thankful to the staff of liquid Nitrogen plant for their tireless efforts which keep our instruments running. I am also thankful for the stimulating corridor discussions with Mr. P Manojkumar and to Dr. Ajikumar for the innumerable borrowed consumables.

I have some great friends with whom I have had lot of quality time in the lab and at tea shops discussing, gossiping and in some occasions fighting. The people who define these five years for me are Mr. S. Hari Babu, Mr. R. Renjith, Mr. L. Herojith Singh, Mr. Shilpam Sharma, Mr. Ashok Bahuguna, Mr. Y. Sorb, Mr. Trinadh Raja, Mr. Girish Padhy, Mr. K. Panda and Dr. Prasanna Kumar Sahoo. I am also thankful to all my PhD batch mates as well as seniors and juniors for their well wishes.

I acknowledge Dr. G. Ambika, Dr. C. Sunil Sunny and Cpt. Viji Varghese for being my role models and mentors. I am also thankful to all my teachers who have given the knowledge I have and who has shaped my character.

I am thankful for all near and dear family members for their love and support during all these years. I am especially thankful to my parents for their continued support and love.

I am who I am because of two people near me. They are an intrinsic part of my physical and mental being and all my pain and effort belong to them.

Contents

Chapter 1
Introduction

1.1 Defects

Among the various factors which affect the properties of materials, the most prominent ones are the defects in them. These defects can have thermal origin or can be the result of growth, processing or radiation. The concept of defect has grown to include simple point defects like vacancies to complex extended defects like dislocations or precipitates. There are also possibilities for different/same type of defects to interact and give rise to new stable structures or phenomenon. These can have useful properties as in the case of N-V (nitrogen-vacancy) centres in diamond [1] or be detrimental as in the case of transient enhanced diffusion (TED) of boron in silicon [2]. Defects can be introduced into the system in a controlled manner to tune the properties of the material. The entire semiconductor industry runs by including various defects or dopants into Silicon [3]. Titania nanostructures show an increase in field emission properties by controlled introduction of oxygen vacancies as well as by nitrogen incorporation into lattice structure [4]. It can also be created during in service condition as in the case of radiation damage of structural materials used in nuclear reactors [5]. In either case it is important to understand the dynamics of the defects introduced in the system to extend its in-service life or to derive maximum effective property out of it. For example, a control on void swelling of fuel clad material can increase the performance of the nuclear reactor expressed in terms of burnup [6]. The swelling can be avoided by pinning the segregation of vacancies by increasing the surface sinks for it. This is achieved by nano-precipitates in the material which are stable at the operating temperature [7]. Similarly,

controlling oxygen vacancies in Hafnium oxide integrated MOSFET (Metal Oxide Semiconductor Field Effect Transistor) devices helps in overcoming the threshold voltage instability and electron mobility degradation. This has been achieved in recent times by nitridation [8].

Incorporation of impurities in silicon at a specific depth for planar device fabrication in VLSI (Very Large Scale Integration) is achieved in the industry by ion implantation [9]. Even for controlled low dose, low current implantation, enough Frenkel pairs are produced which can affect the device properties by acting as traps for charge carriers. However this drawback can be overcome by optimizing defect annealing program through model ion-implantation and by subsequent studies on defects, material property changes and various annealing strategies. Similar strategy is also used in radiation damage studies where equivalent damage expressed in dpa (displacement per atom) are reproduced using ion implantation and subsequent defects are identified by various techniques like transmission electron microscopy (TEM) [10]. Their dynamic evolution during radiation or post irradiation thermal treatments also gives valuable information on effective operation principles or help in screening of newly developed materials. For example understanding of irradiation induced defect evolution in nuclear grade graphite was obtained from noble ion/electron implantation in crystalline graphite [11]. However, doubts are often raised on the equivalence of neutron damage and ion damage in a material. In scenarios where the primary motive is to produce controlled amount of defects, ion implantation provides the best possible option to study their as implanted properties, equilibrium structures and their thermodynamic evolution and complex interaction.

1.2 Ion-implantation

Ion implantation allows for the modification of near surface and sub surface region by incorporation of foreign species into material. Energy is lost by the impinging impurity atom by interacting with the electrons of the solid (electron energy loss) or by scattering from the lattice site (nuclear energy loss). The rate of loss of energy with depth or stopping power of a material can be expressed as $\left(\frac{dE}{dx}\right)$ where *dE* energy is lost over a distance *dx* by the ion which as mentioned above can be approximately written as

$$\left(\frac{dE}{dx}\right) = \left(\frac{dE}{dx}\right)_e + \left(\frac{dE}{dx}\right)_n \quad (1)$$

Here $\left(\frac{dE}{dx}\right)_e$ is the energy loss through electron interaction and $\left(\frac{dE}{dx}\right)_n$ is the energy loss through nuclear interaction. The rate of loss of energy via electron interaction or nuclear interaction is determined by the electronic (ε_e) and nuclear (ε_n) stopping cross sections and hence, the total stopping power is also equal to $N(\varepsilon_e+\varepsilon_n)$, where N is the density of scattering centres. It is usually through the ion-nucleus interaction that the atoms of the host matrix are removed from their site resulting in Frenkel pair formation. Electron energy loss does not contribute in damage production unless electron excitation results in bond breaking or bond structure changes. Nuclear energy loss dominates in the lower energy range (a few keV), whereas electron energy loss dominates at high ion energies (~100's keV) as shown in an example figure, Fig. 1 where the stopping cross-section is plotted against energy for Ge^+ implantation into Si [12]. Nuclear interaction also results in change of trajectory resulting in straggling in the final range of the ion. The interaction of the ion with host matrix is statistical in nature and the final position of the ion will also be statistical with a Gaussian like distribution. As the maximum damage happens just before the ion come to rest, the profile of the vacancies produced should also be statistical with the profile maximum appearing before the peak of ion distribution.

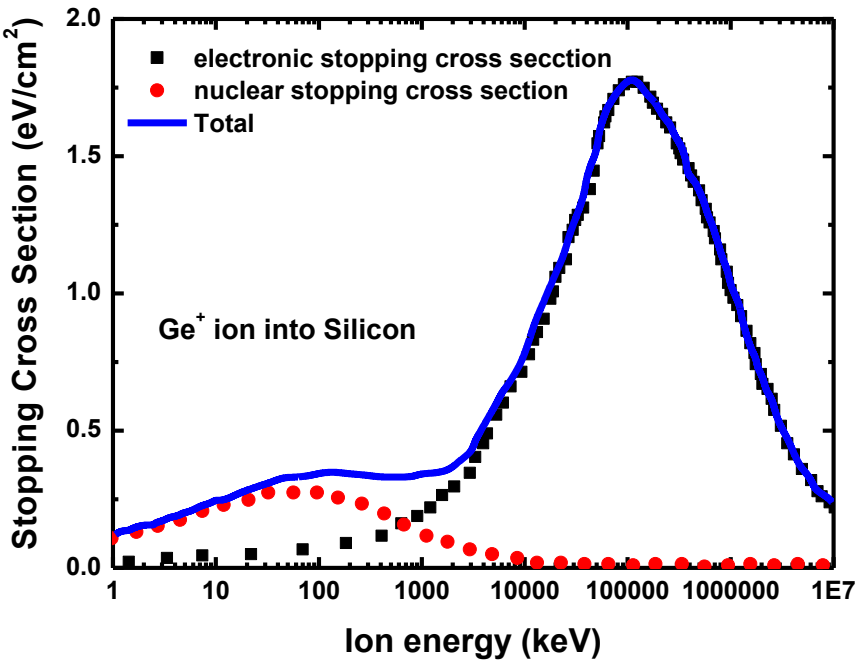

Fig.1: Stopping Cross section of Ge^{+} ion in Silicon plotted for different energies. The energy region where the nuclear and electronic cross section dominates is shown separately [12].

The final output of implantation depends on various parameters like the mass of the ion, its energy, the fluence or dose and the flux. The mass of the ion is determined by the species chosen for implantation which in turn depends on the final application. For example to produce damage similar to neutrons, it would be wise to use self-ions i.e. both host material and ions are same. There can be maximum mass transfer by considering the simple energy transfer process in hard ball collision and can simulate the primary knock on atom (pka) of sufficient energy created by the neutron as shown in Fig. 2. The figure also shows the cascade phenomenon produced by secondary knock on atoms having enough energy to produce well separated Frenkel pairs i.e. energy >> the displacement energy (E_d). Energy of the projectile is decided by the depth at which the ion or the damage is required, say for near surface modification low energy implantation has to be used.

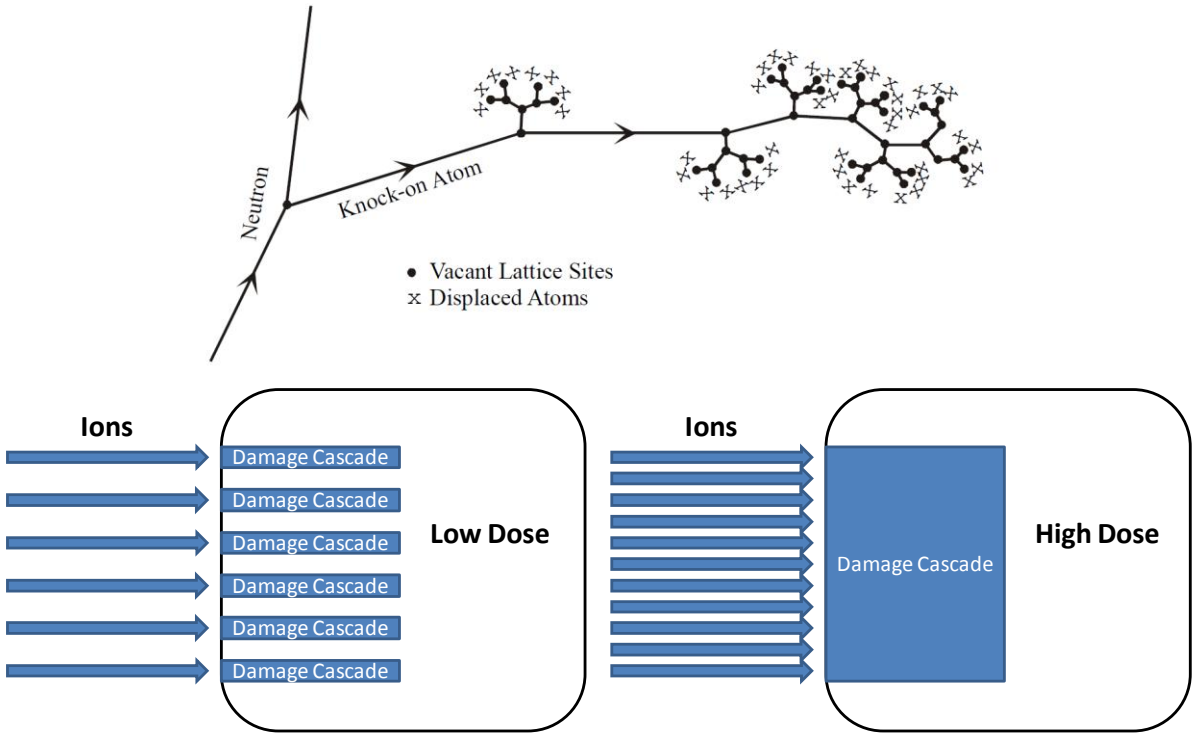

Fig.2: Formation of the primary knock on atom and the subsequent displacement cascade. The separation between vacancy and interstitial defects are also highlighted. The evolution of cascade with dose is also shown. For lower dose, the cascades are separated forming clusters of disordered region whereas in high dose sample the cascades overlap to form amorphous regions.

If sputtering instead of implantation is required, usually low energy and high mass species are used. Another important parameter is the total dose and beam current both of which decides the damage produced. For changing electrical or optical property the total dose will be such that the introduced impurity will be in the ppm (parts per million) range and hence a dose of 10^{12} - 10^{14} ions/cm^2 would do. For large structural change like amorphization or compound formation large dose of the order of 10^{16} - 10^{18} ions/cm^2 will be required [13]. At higher doses there will be an overlap of cascade resulting in the formation of higher order defects which proceeds to amorphous structure formation as shown schematically in Fig. 2. Beam current decides the number of ions impinging per second and thus decide whether enough time is available for structure relaxation before the next collision. High beam currents can also cause heating of the sample due to the energy deposited by bombarding ions. This may lead to uncontrolled structure changes

and will not help in cases where the as-implanted structure is under study or where diffusion of implanted species is not envisaged during implantation itself. Thus, the beam current is kept low in the range of micro or nano-ampere [13]. Other parameters like angle of the incident beam with the target is decided based on whether one has a crystalline sample which is susceptible to channeling. Thus, various parameters have to be taken into account for getting necessary property modification by implantation.

1.2.1 Ion-implantation in Silicon

Different ion implantation parameters are used to tailor the dopant profile in silicon. Energies from 5keV – 1 MeV and doses from 10^{11} – 10^{15} ions/cm^2 are used to introduce dopants like B, P, As etc into the system [14]. Ion implantation has numerous advantages like high purity, high reproducibility of as-implanted dopant profile, effective control of dopant concentration and possibility to have selective doping at various depths. Low energy implantations are used for shallow junction formation brought by the continuous scaling down of the devices. For shallow implants, the as-implanted dopant profile and the as-implanted damage profile and their mutual interaction during further thermal treatment for defect annealing are important optimizable parameters. The latter is very important due to the enhanced diffusivity of the impurity in the presence of defects, which inhibits the ability to have shallow junctions with broadened dopant profiles [15]. High energy and high dose implantations are explored to dope the substrate and for doped well or tub structures for MOS transistor fabrication. It has also been used for the fabrication of buried dielectric layer either by oxygen implantation or by Smart-cut technique which is a combination of combination of wafer bonding and ion-implantation. Metal impurities in active region of Silicon are highly detrimental to device properties since they reduce charge carrier life time and they increase leakage current.

This problem is attacked by providing gettering centres for impurity metal atoms. Intrinsic gettering scheme involves the production of oxide precipitates, which provide nucleation site for metal precipitate formation [14]. With scaling down of devices, the amount of acceptable metal concentration is also coming down which causes a serious limit to the intrinsic gettering process. Hence extrinsic gettering centres are produced by introducing defects by ion-implantation where the defects/nano-cavities produced by the process, trap the metal atoms eventually forming metal nanoclusters [14].

Apart from the electrically active dopants and oxygen atom other species which do not form electrically active structures in Silicon are introduced to tailor the properties like mechanical strength, gettering efficiency or for controlling the oxide layer formation in SIMOX process. The species which inadvertently gets into the system during Silicon crystal growth is Nitrogen. However, it was found to have positive effect on many quality parameters and now it is introduced in controlled fashion. To cite one example, the presence of nitrogen at the oxide-silicon interface inhibits oxide growth and this property has been utilised by implanting the nitrogen at the required interfacial depth [16]. Its introduction was also shown to increase oxide precipitation in silicon thereby increasing the efficiency of the intrinsic gettering process [17, 18]. The property enhancement of Silicon by nitrogen incorporation has been assigned to its interaction with vacancies in the system, though the physical process or the temperature activation of such interactions are still not clear [19]. This is an open area where ion-implantation can be effectively used to introduce controlled amount of defects and nitrogen in Silicon.

1.2.1 Ion-implantation in Graphite

Ion implantation studies in graphite in early part were driven by the need to understand the defect evolution and stored energy release in reactors employing nuclear

grade graphite. In order to identify defect structures responsible for the Wigner energy release, thermal conductivity changes and contraction along the basal plane, controlled implantation of graphite with noble ions were employed as a tool [20] and techniques like Raman spectroscopy and TEM were employed. Studies were also done on neutron irradiated graphite samples and the results were often explained based on set of ideas generated from the investigation of defects produced by both neutron and ion/electron implantations [21, 22]. The primary problems investigated were expansion along the c-axis and basal plane contraction which were proposed to be due to the interlayer interstitial clusters and collapsing vacancy line as shown in Fig. 3 [23]. However the understanding is still not complete with observed dimensional changes much higher than that is possible with these atomistic mechanisms.

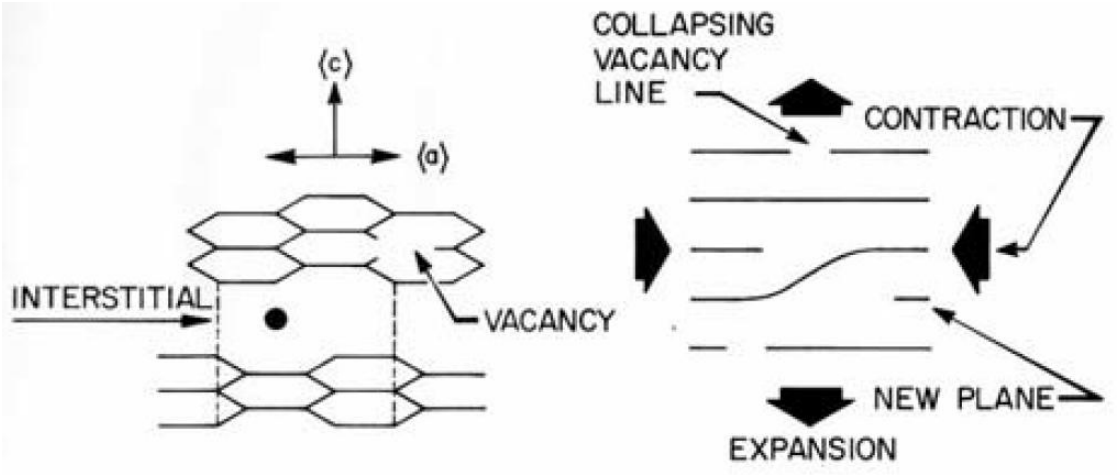

Fig.3: Proposed mechanism for dimensional change in irradiated graphite. The formation of interlayer interstitial clusters causes c-axis expansion whereas collapsing vacancy into line defect causes basal plane contraction [23].

With the phasing out of graphite from nuclear industry, other motivations kept ion implantation in graphite running. The discovery of carbon nanostructures and their subsequent modifications by electron/ion-irradiations has triggered new set of

investigations on defects in graphite which was helped by improved atomic level resolution in TEM. Some of the exotic defect structures proposed like the metastable intimate I(interstitial) – V(vacancy) pair [24] was discovered in double walled carbon nanotube (CNT) [25] which thus helped in taking the understanding of graphite defect dynamics forward. Ion-irradiation was successfully used as a methodology for the structural modification like welding two CNT's by the incorporation of defects, for the straightening of CNT wires to tailor the aspect ratio (to improve the field emission properties), for site specific functionalization and even for making nanotube based electronic devices by using FIB (focussed ion beam) to make quantum dot on nanotubes [26]. This knowledge of beam based nanostructure modification has now been extended to structural and physical property modification of graphene. It was shown recently that irradiation with swift heavy ions causes a change in work function of the exfoliated graphene sheets and results in a transformation from n-type to p-type graphene [27].

A more recent surge in the investigations on ion implantation induced defects in bulk graphite was due to the discovery of magnetic ordering among ion implantation induced vacancy defects created in highly oriented pyrolytic graphite resulting in a ferromagnetic behaviour [28]. As graphite tiles are proposed material for the plasma facing wall of fusion reactor and its use as structural materials in high temperature gas cooled next generation rectors like Gas-Turbine Modular Helium Reactor and Pebble Bed Modular Reactor [29], more detailed studies on radiation induced damage [30] and hydrogen retention in graphite [31] are emerging.

Hence there is a need to relook at some of the proposed defect dynamics by using controlled generation of defects using ion implantation and employing defect specific techniques. Self ion implantation would avoid the complexities due to impurity matrix interaction and such studies are reported scarcely in literature.

1.3 Defect Characterization

After the introduction of defects by ion implantation, a number of techniques can be used to investigate them and their evolution during further processing. Techniques like TEM, STM and AFM can be used to directly image the atomistic defects. However, the volume fraction probed, probe-material interaction, difficulty in interpreting the images of point defects like monovacancy or single interstitials and material preparation makes them difficult to use when the defect concentration is very low. Techniques like Ion channelling can be used in crystalline samples in the channelling direction for identifying the position of disordered region after implantation and are more likely to show the position of displaced lattice atoms or interstitials. Ion beam based techniques like Rutherford backscattering and Nuclear reaction analysis give similar information. Tracking a property change associated with the introduction of defects or tracking the property of defects themselves are other ways to explore them. Techniques which belong to this category are resistivity measurements, IR or Raman spectroscopy, DLTS, EPR etc. However, in these cases there is no defect specificity and hence it is difficult to identify the structures associated with them.

One technique which can overcome many of these drawbacks is positron annihilation spectroscopy. Here, the probe is positron which is specifically sensitive to atom sized open volume defects namely vacancies. Its random diffusion in the material to be probed before its annihilation and large affinity for vacancies makes it behave like a self seeking probe, which thus gives a good representation of the volume distribution of vacancy like defects [32]. It can be used with any material and does not require detailed sample preparation. It is limited by the lower and upper bound of defect concentration over which it has sensitivity and also by specificity to open volumes. Some of these aspects are discussed below.

1.3.1 Positron Annihilation Spectroscopy

A positron which enters the solid undergoes thermalisation process whereby it loses its energy to the matrix by scattering at ion sites, by electronic excitations and finally via phonon excitation [32]. The thermalisation process happens within ~ tens of pico seconds and can be ignored in the measurement process. In the thermalised state, the positron does a random walk through the ionic Bloch potential. In the absence of any defects, the positron wave function itself shows a Bloch like behaviour which is maximized around the interstitial position. In the presence of open volume defects, the positron gets trapped in the attractive potential of the vacancy. This attractive potential is a result of the absence of the repulsive ion core and thus, the positron gets preferentially trapped at the vacancy trap site as shown in Fig. 4 [32].

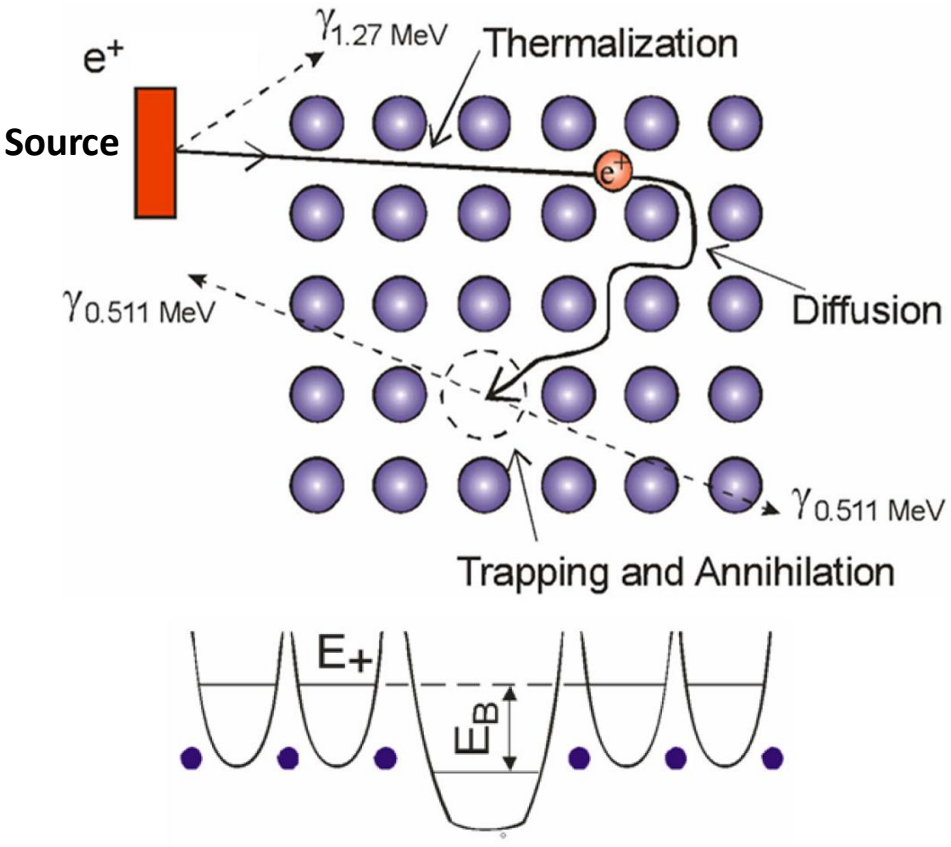

Fig.4: Schematic shows various processes which positron undergoes inside solid before annihilation. The potential trap at a vacancy site is also shown schematically.

The positron annihilation characteristics depend on the local electron density and the local electron momentum. The measureable parameters in positron annihilation experiments are its lifetime as well as the Doppler broadening and angular correlation of two annihilation gamma rays. These measurements can be combined with a mono energetic positron beam to get depth resolved information instead of the bulk averaged results. The positron lifetime is inversely dependent on the local electron density whereas the other two are momentum techniques. As angular correlation is not employed in the thesis, it will not be discussed further.

Positron Lifetime Spectroscopy

The annihilation rate of positrons (λ) which is inverse of the lifetime (τ) of positron inside the solid is directly proportional to the overlap of the positron ($n_+(\boldsymbol{r})$) and electron ($n_-(\boldsymbol{r})$) densities and is given as [32]

$$\lambda = \frac{1}{\tau} = \pi r_0^2 c \int n_+(\boldsymbol{r}) n_-(\boldsymbol{r}) \gamma d\boldsymbol{r} \qquad (2)$$

where γ is the enhancement in electron density around positron due to Coulomb attraction, r_0 is the classical electron radius and c is the speed of light. When a vacancy is created by the removal of ion core, the net reduction in the local electron density is reflected as an increase in the lifetime of positron trapped at the site. The intensity of such a lifetime component gives the concentration of such trap sites. The experimental lifetime spectrum can be understood in terms of simple rate equations, provided trapping of non-thermalised positrons is negligible and that the non interacting defects are homogeneously distributed in the sample. Under these conditions the time dependent positron diffusion equation for a sample with only one defect type can be written as [32]

$$\frac{dn_f(t)}{dt} = -\lambda_f n_f(t) - \kappa_1 n_f(t) \qquad (3.1)$$

$$\frac{dn_d(t)}{dt} = -\lambda_d n_d(t) + \kappa_1 n_f(t) \quad (3.2)$$

The solution to the coupled differential equation is the decay spectrum which is expressed as

$$D(t) = I_1 e^{-t/\tau_1} + I_2 e^{-t/\tau_d} \quad (4).$$

Here n_f is the fraction of positrons annihilating from the Bloch like delocalised state, $\lambda_f = 1/\tau_f$ is the annihilation rate in defect free state, κ_1 is the trapping rate of the defect d and $\lambda_d = 1/\tau_d$ is the annihilation rate at the defect site which has n_d fractions of positrons annihilating from it. τ_d is the positron lifetime pertaining to defect d. I_1 and I_2 are the intensities of these two annihilation sites such that $I_1 + I_2 = 1$. $\tau_1 = 1/(\lambda_f + \kappa_1)$ is the reduced bulk lifetime in the presence of the defect site d. The actual lifetime spectrum is the absolute value of the time derivative of the expression (4). Through the lifetime measurement, one tries to identify these lifetime components and thus get an idea of the defect species and their concentration in the sample.

The experiment is carried out by placing a ^{22}Na source encapsulated 1μm thick Nickel foil in between two identical samples in the sandwich geometry. The source has a half life of ~ 2.6 years. In order to generate the exponential decay spectrum composed of multiple slopes (if multiple trap sites are present), the time difference between the birth of positrons (tagged by the 1280 keV gamma emission produced by Ne de-excitation) and death of positrons (tagged by 511 keV from $e^- e^+$ annihilation) is measured for each event. The generated spectrum is fit to multiple exponential slopes which are convoluted with the Gaussian resolution functions of the spectrometer. The experimental set-up for this is a fast-fast positron lifetime unit represented by the block diagram shown in Fig. 5. A BaF_2 scintillator – XP2020Q Photomultiplier tube (PMT) combination is used as the gamma detectors. The gamma-photon scintillation happens mainly via a fast de-

excitation process with the emission of 220 nm photon [33]. The photon-electron conversion and voltage pulse amplifications happens inside the PMT through a set of photocathodes and dynodes. The resulting voltage pulse is discriminated as corresponding to 1280 or 511 keV using two constant fraction differential discriminators (CFDD). The time of arrival for each pulse is also generated via constant fraction algorithm [33] using the same units. One of the output pulses (called SCA pulse) from both the CFDD are sent to a fast coincidence unit which generates a true pulse for events happening within a time interval of 50 ns. The second output pulse (called Timing pulse) from the CFDD and the true pulse from coincidence unit are processed in the Time to amplitude converter (TAC) to generate voltage pulses with amplitudes proportional to the time difference between the two gamma rays. The TAC voltage pulses are collected and analysed using a PC based MCA (multi channel analyser unit) and the decay spectrum is generated. The obtained decay spectrum is fit to multiple exponential decay schemes using LT9 [34] program which takes care of Gaussian resolution functions and subtracts the self-annihilation events from the source found using measurement done on a standard sample, usually Iron or Silicon. An example of the lifetime spectrum fit is shown in Fig. 6, where the experimental spectrum has been shown to be fit to two components apart from the source component. The top plot shows the residue of the fit. A time resolution of ~250 ps is enough for resolving lifetimes of ~ 100 ps.

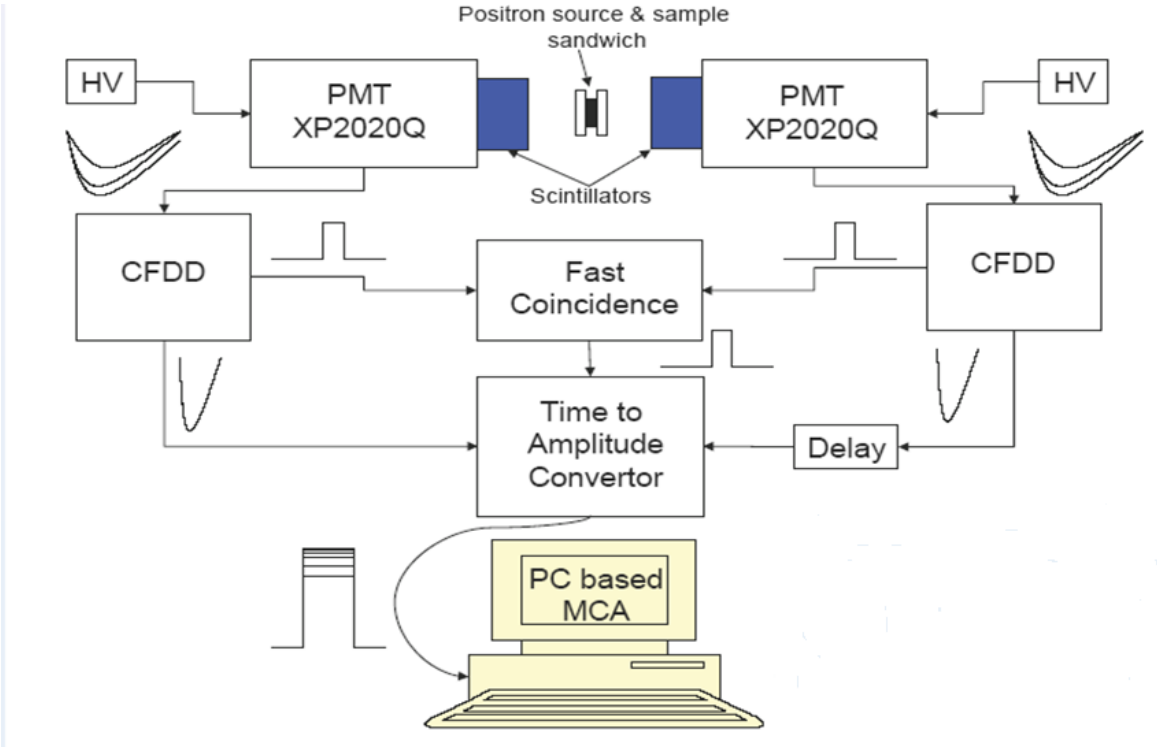

Fig.5: Block Diagram of the fast-fast positron lifetime spectrometer employed in the laboratory. The scintillators are BaF_2.

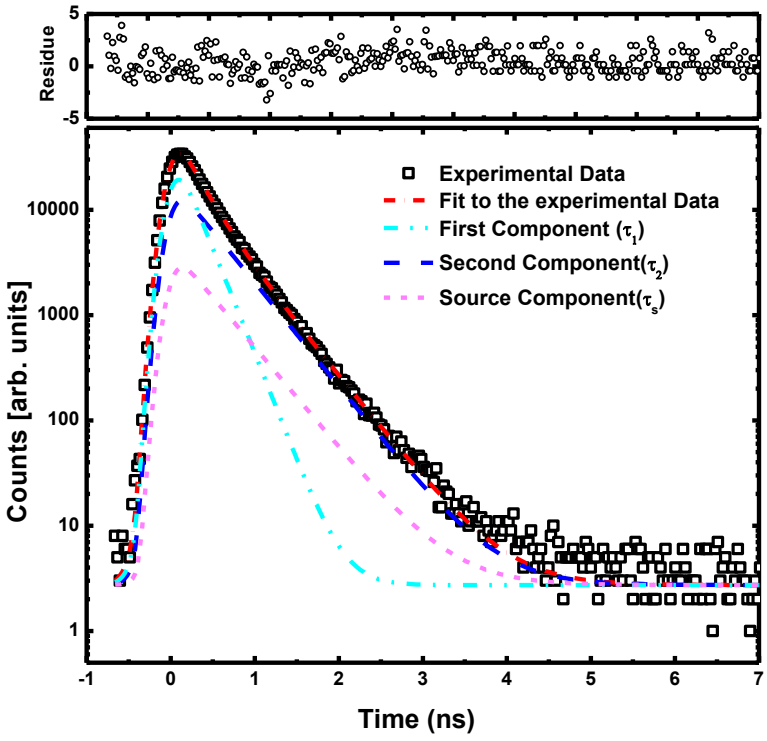

Fig.6: An example lifetime spectrum which shows the fit after subtracting the lifetime from the source. Two components have been resolved. The left side Gaussian like behaviour comes from the spectrometer resolution function with time resolution ~ 250 ps.

Doppler Broadening Spectroscopy

The momentum of the annihilating electron-positron pair in the direction parallel to motion of the resulting gamma causes Doppler broadening which can be measured using high resolution High purity Germanium (HPGe) detectors. The shift in the peak energy can be approximately given as [32]

$$\Delta E = \frac{p_L c}{2} \tag{5}$$

where p_L is the momentum parallel to the direction of annihilation gamma and c is the speed of light. As Doppler broadening happens in an isotropic manner, a uniform broadening around 511 keV would be seen. The total amount of broadening of the gamma ray including the detector resolution would be of the order of 2 keV or higher and thus a detector with an energy resolution of 1.5 keV or better can be effectively used to measure this broadening. The amount of broadening is parameterized by two factors called S or Shape parameter and W or Wing parameter which are defined as

$$S = \frac{\int_{E_0-E_S}^{E_0+E_S} N(D)}{\int N(D)} = \frac{A_S}{A} \tag{6.1}$$

$$W = \frac{\int_{E_0-E_{W2}}^{E_0-E_{W1}} N(D) + \int_{E_0+E_{W1}}^{E_0+E_{W2}} N(D)}{\int N(D)} = \frac{A_W}{A} \tag{6.2}$$

where E_0, E_s, E_{W1} and E_{W2} represent 511 keV, shift in peak region typically 1keV, lower shift in wing region typically 2.5 keV and larger shift in wing region typically 5 keV respectively. *N(D)* represents the Doppler broadened spectrum and thus the denominator in each expression represents total counts in the spectrum, whereas the numerator represents counts in respective regions i.e. either peak or wing. The definition is such that S-parameter represents annihilation with low momentum electrons, hence, less shift and W-parameter represents annihilation with high momentum electrons, therefore more shift. The definition thus includes a dependence on defect structure and concentration as

well as a dependence on chemical nature as the momentum distribution of electrons among various energy levels is element dependent. This is represented in Fig. 7 which shows a representative 511 keV background corrected gamma peak measured using an HPGe detector of resolution 1.45 keV for Silicon single crystal (Si(100)), polycrystalline Au (quenched from 1123 K) and a defected Au sample. The x-axis here is plotted in terms of shift from 511 keV. The presence of open volume region reduces the probability of annihilation with core-electrons and hence, for the same number of annihilation events (i.e. for area normalised peak), the wing region shrinks whereas the peak region swells. This will be represented as an increase in S-parameter and a decrease in W-parameter. For Silicon and Au sample, the curve represents that positrons are less likely to annihilate with core electrons in Si when compared to that in Au. From the definitions, it is also clear that the measured parameters (S/W) are qualitative. The area over which S and W parameters are defined may differ from laboratory to laboratory and from sample to sample. Similarly differences can be there in the detector resolution and stability which will reflect in the effectiveness in defining the broadening. S and W reflect chemical, type and concentration of defects together and there are no theoretical profiles defined for the Gaussian like curve to represent each of these separately. For example, let S_b, S_1 and S_2 represent S-parameter representing defect free annihilations and two defect types in a solid with concentrations f_1 and f_2. Then the net S-parameter measured in the experiment would be

$$S = f_b S_b + f_1 S_1 + f_2 S_2 \qquad (7)$$

where f_b is the fraction annihilating from the defect free bulk. Any change in these six parameters would cause a change in S and hence, it is not possible to single out the changes just by S-parameter measurements. Hence it is impossible to get quantitative information from the broadening measurements alone. However the experiment is very

fast compared to positron lifetime and hence, in well controlled experiment relative changes with respect to a reference sample would give qualitative information on defect

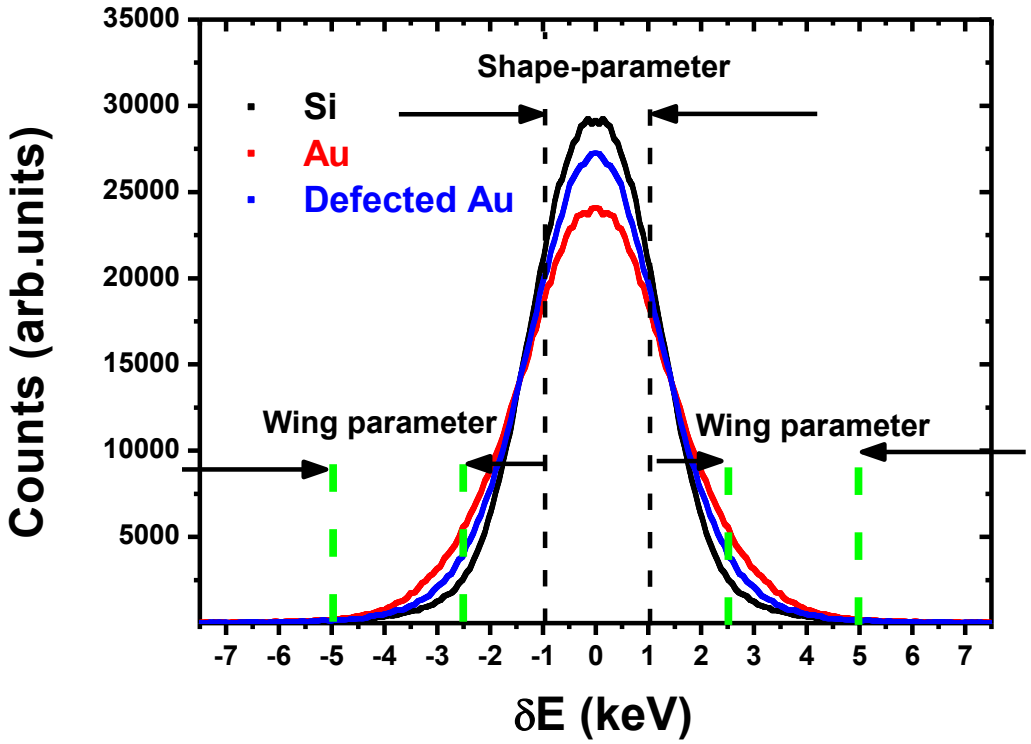

Fig.7: An example of 511 keV background corrected gamma peaks measured using an HpGe detector of resolution 1.45 keV for Silicon single crystal (Si(100)), polycrystalline Au (quenched from 850C) and a defected Au sample. The x-axis here is plotted in terms of shift from 511 keV.

evolution. If there are only two trapping sites present, one bulk and another defect then, the parameter defined as [35]

$$R = \left|\frac{S-S_b}{W-W_b}\right| \qquad (8)$$

is independent of change in defect concentration and hence can be used to identify change in nature of defect type during processing say for example thermal evolution. Here *S,W* are parameters measured for a sample whose defect free S and W parameters are S_b and W_b. The *R* parameter is nothing but a slope of a S-W plot and hence a change in slope of the line joining *(S,W)* to (S_b, W_b) will signal a change in defect type if the condition of only two trapping site is maintained. The S-W plot is called a correlation

plot and is regularly employed in beam based Doppler measurements. The experimental setup is simple with a high energy resolution HPGe detector usually with a 30% efficiency attached to a spectroscopic amplifier and a data acquisition system

Slow Positron Beam - Doppler Broadening Spectroscopy

The information from the above two techniques is averaged over a depth of few hundred micrometers. This depth is defined by the end point energy of the β^+ spectrum and for ^{22}Na this is about 540 keV. Hence it is not possible to investigate defects in the depth selective manner. If it is possible to control the energy of the positrons implanted into the solid, then depth resolved defect sensitive S-parameter can be derived. The discovery of the negative work function for positrons shown by certain metals [36] made this possible. A thermalised positron reaching the surface of a negative work function material would be emitted from the surface with an energy equal to the work function and this process is called moderation. If these slow positrons can be velocity filtered from the fast unmoderated positrons, then further control of the positron implantation energy is possible. This is achieved widely by using a W(Tungsten) (100) single crystals of thickness < 1μm [37] or W – polycrystalline mesh or by solid rare gas moderators [38]. The important factor which differentiates among them are their moderation efficiencies defined as the ratio of the number of monoenergetic positrons emitted from the moderator surface to the fast positrons reaching the moderator. The rare gas moderators have very high efficiency and narrow energy distribution. However they are very difficult to maintain. The W moderators are relatively low on efficieny of the order of 10^{-5} (i.e. 1 in 10^5 positrons get moderated) but are easy to maintain and prepare. Fig. 8 shows the β^+ spectrum before and after moderation. W moderated positrons are coming with energy around 2.8 eV.

This process of velocity control is achieved in a high vacuum or ultra high vacuum system where the positrons fall on to a thin moderator such that many positrons thermalise just near the surface of the W, from where they are emitted with work function energy (~2.8 eV for W(110)). These positrons are extracted electrostatically into the transport

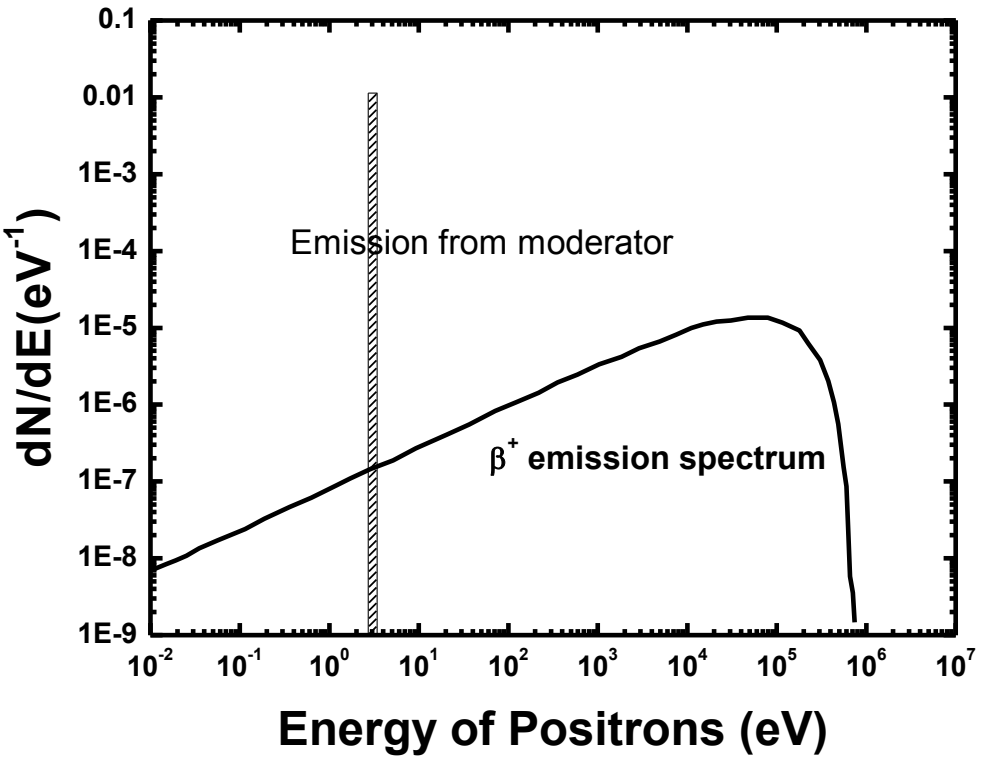

Fig.8: Positron emission spectrum before and after moderation. The β^+ decay spectrum reduces to a narrow curve centered at 2.8 eV after moderation in W moderator ([32]).

region which also contains the velocity filter. The filter can be a magnetic bend or an electric field – magnetic field transverse combination (E x B) which allows only positrons of specific energy to cross the filter [39]. The filtered positrons are accelerated to the required energy to implant them to different depths inside the target material. This process is schematically represented in Fig. 9. As the correlation between the the start gamma (1280 keV) and stop gamma (511 keV) is lost during the moderation and subsequent transport, positron lifetime measurement is not possible under these

conditions. Hence, a doppler broadening spectroscopy is commonly attached to a beam based positron system.

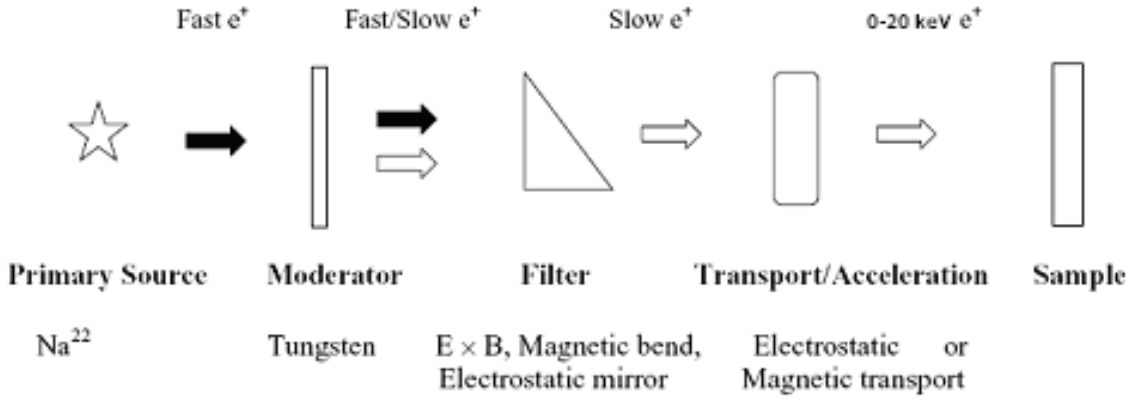

Fig. 9: Schematic representation of a slow positron beam set-up using a radioactive source.

Unlike bulk Doppler broadening measurements, the data analysis here is not straight forward even when the output of the experiment is S/W-parameter as a function of implanted positron energy. The S-parameter obtained at various positron energies is not a direct representation of the specific depth but rather is a combination of various S-parameters governed by the positron implantation profile, and the positron diffusion post thermalisation. The positron implantation profile is generally represented by a Makhovian profile [40] given by the form

$$P(z;E) = \frac{mz^{m-1}}{(z_0(E))^m} \exp\left[-\left(\frac{z}{z_0(E)}\right)^m\right] \quad (9)$$

where z is the depth from the sample surface, $m = 2.0$ for Si and z_0 depends on the positron energy E through relations

$$z_0 = \frac{\tilde{z}}{\Gamma\left(\frac{1}{m}+1\right)} \quad (10)$$

$$\tilde{z} = \frac{A}{\rho} E^n \quad (11)$$

where Γ is the gamma function and $\tilde{z}$ is the mean implantation depth, ρ is the density of the sample in g/cc. For most of the metals and semiconductors n=1.6 and A= 3.6 μgcm^{-2}keV^{-n} is sufficient. The profile calculated for representative energies in Silicon is given in Fig. 10. The post implantation diffusion of positrons can be approximated by a steady state one dimensional diffusion equation [32] given as

$$D_+ \frac{\partial^2 n}{\partial z^2} - \frac{D_+ e}{kT} \frac{\partial}{\partial z}(\varepsilon(z) n(z)) - \frac{n(z)}{\tau_1} + n_0(z) = 0 \qquad (12)$$

where $n(z)$ is the positron probability density, D_+ is the positron diffusion coefficient, T is the temperature, ε(z) is the electric field, e the positron charge and $n_0(z)$ is the positron stopping rate at depth z which is dependent on the implantation profile given in equation (9). τ_1 is the reduced bulk lifetime in the presence of defect d with trapping rate $\kappa_1 = \mu C_d(z)$ where μ is the trapping coefficient and $C_d(z)$ is the concentration of defect d at depth z.

Hence the experimentally observed S-parameter at a positron energy E can be approximately written as

$$S = f_b S_b + f_s S_s + f_j S_j \qquad (13)$$

where suffixes b,s and j represents the bulk layer, the surface layer and defected layers. f and S denote the fraction annihilating at each layer and the respective S parameter. Here layer is referred with respect to the depth from the surface. Bulk represents much deep in the solid where the chance of positron diffusing back to surface layer is almost negligible. The data analysis involves solving the diffusion equation taking the implantation profile into account and fitting to the experimentally obtained S vs E curve. This should give f and S values corresponding to each layer. This is achieved using the package VEPFIT [41]. S-W correlation plot drawn with energy as a running parameter

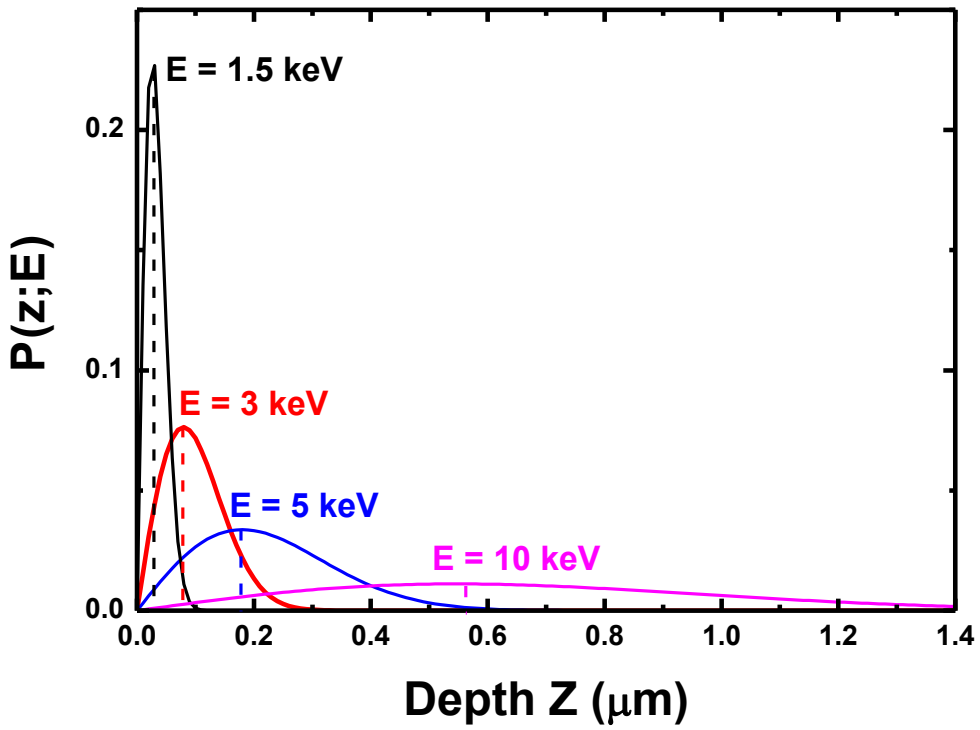

Fig.10: Makhovian profile for positron implantation at various energies in Si. For higher energies the profile is so broad that information comes from surface up to a few μm. The dotted line shows the mean implantation depth for different energies.

also gives important information as discussed above during say, thermal evolution [42]. Here, the change in slope is looked at qualitatively to distinguish different positron trapping defects.

Slow Positron Beam – Lifetime Spectroscopy

As lifetime cannot be derived in a slow positron beam due to the absence of the 1280 keV gamma ray, lifetime measurements is possible only if a time tag can be attached to each positron which then acts like the start pulse. The application of beam based lifetime has solved many a problems like identifying the defect structure in disordered and in amorphized silicon [43], defect structure in self-ion implanted graphite [44] or identifying the surface structure of thin film PbSe nanocrystals [45]. It has also been used effectively in understanding the pore structure variation in nanoporous thin

polymer films [46]. It could also be extremely powerful in ion-implantation based defect evolution studies. However, the beam based positron lifetime system has not been utilized effectively in such areas due to the complexities involved in setting it up. Only a handful of laboratories worldwide have such pulsed positron beam system.

Thus through the use of the experimental techniques mentioned above, qualitative or quantitative information on the open volume defect evolution can be derived in bulk as well as in near or sub surface regions of the materials.

1.4 Motivations and Plan of thesis

Ion implantation for processing and modelling has been taken up in two problems in this thesis. One is the incorporation of Nitrogen in Silicon using ion implantation and the interaction of these impurities with irradiation induced vacancies. There is a lack of clear understanding about the thermally activated interaction of Nitrogen with vacancy. Positron beam based spectroscopy could play a vital role in filling this gap. The second problem is where self ion implantation induced defect structure is investigated in highly oriented pyrolytic graphite. Self ion implantation is used to avoid complexity due to vacancy impurity interaction and to produce effect similar to a pka created by a 1 MeV neutron. The pursuit of these two problems shows the importance of having a beam based lifetime system and the thesis goes to the second part where a design of pulsed positron beam is made and its development has started. The organization of the thesis is as follows

The second chapter gives an introduction to the present knowledge about the interaction of Nitrogen with vacancies in Silicon and points towards a motivation for the problem. The details of experiments used are discussed and the results are presented with discussion and conclusion. The key findings of this work are the identification of deeper

defects in high dose sample and the identification of nitrogen-vacancy complexes after annealing up to 873K.

The third chapter gives an overview of the current understanding about the vacancy and interstitial structure and their thermal evolution and activation energies in Graphite. A motivation for the problem is presented followed by the details of experimental tools used. The results are discussed in detail which shows the dose dependence of the defect annealing. Fast and slow recovery process pertaining to interstitial vacancy recombination and vacancy migration has been identified in the present study. An experimental proof for an open volume defect which is stable up to 673 K has been provided.

An interlude is provided to give a motivation for the migration from the above two ion implantation problems to the development of a pulsed positron beam.

Chapter four discusses in detail the design of the pulsed positron beam starting from some of the beams existing worldwide. Different components and parts involved in the design and development are enumerated.

Chapter five highlights the achievement in the development of the pulsed positron beam, where the extraction of slow positron beam has been attained.

The sixth chapter gives conclusions and future outlook and the work to be taken up in each of the three problems dealt in the present thesis with a scope for future developments on the lifetime beam.

References:

1. Milburn G J 2010 *"Quantum Measurement and Control of Single Spins in Diamond" Science* **330** 1188.
2. Chelyadinskii A R and Komarov F F 2003 *"Defect-impurity engineering in implanted Silicon" Physics – Uspekhi* **46** 789.

3. http://www.intel.com/content/www/us/en/silicon-innovations/silicon-technologies-general.html
4. Antony R P, Mathews T, Panda K, Sundaravel B, Dash S and Tyagi A K 2012 *"Enhanced Field Emission Properties of Electrochemically Synthesized Self-Aligned Nitrogen-Doped TiO2 Nanotube Array Thin Films*" *J. Phys. Chem. C* **116** 16740.
5. Raj B and Vijayalakshmi M 2010 *"Ferritic steels for sodium-cooled fast reactors: Design principles and challenges" JOM* **62** 75.
6. Osman A, Thak San Byun, Toloczko M and maloy S A 2013 "*Mechanical Performance of Ferritic Martensitic Steels for High Dose Applications in Advanced Nuclear Reactors" Metallurgical and Materials Transactions A* **44** 70.
7. Murty K L and Charit I 2008 *"Structural materials for Gen-IV nuclear reactors: Challenges and opportunities" J. Nucl. Mater.* **383** 189.
8. Yang M, Jee-Hwan Bae, Cheol-Woong Yang, Benayad A and Baik H 2013 *"Formation of an oxygen vacancy-dinitrogen complex in nitrogen-doped hafnium oxide" J. Anal. At. Spectrom., DOI: 10.1039/C3JA50034A;* Guha S and Narayanan V 2007 *"Oxygen Vacancies in High Dielectric Constant Oxide-Semiconductor Films" Phys. Rev. Lett.* **98** 196101.
9. Ryssel H 1978 *"The impact of ion implantation on VLSI" Electron Devices Meeting, 1978 International* **24** 583.
10. Robertson C, Panigrahi B K, Balaji S, Kataria S, Serruys Y, Mathon M –H and Sundar C S 2012 *"Particle stability in model ODS steel irradiated up to 100 dpa at 600 °C: TEM and nano-indentation investigation" J. Nucl. Mater.* **426** 240.
11. Karthik C, Kane J, Butt D P, Windes W E and Ubic R 2011 *"In situ transmission electron microscopy of electron-beam induced damage process in nuclear grade graphite" J. Nucl. Mater.* **412** 321.
12. Moller W 2010 *"Fundamentals of ion solid interaction 1: Stopping and Ranges" SPIRIT Tutorial Ion implantation and irradiation Dresden Germany December 13-14 2010.*
13. Dresselhaus M S and Kalish R 1992 *"Ion implantation in Diamond, Graphite and related materials" Springer series in material science ed. Gonser U et.al.* (Berlin: Springer Verlag).
14. Chason E et. al. 1997 *"Ion beams in silicon processing and characterization" J. App. Phys.* **81** 6513.

15. Nakashima Y et.al. 2012 *"Phosphorous transient enhanced diffusion suppression and activation enhancement with cluster carbon co-implantation" AIP Conf. Proc.* **1496** 107.
16. Liu C T, Ma Y, Becerro J, Nakhahara S, Eaglesham D J and Hillenius S J 1997 *"Light nitrogen implant for preparing thin-gate oxides" Electron Device Letters, IEEE* **18** 105.
17. Nakai K et.al. 2001 *"Oxygen precipitation in nitrogen-doped Czochralski-grown silicon crystals" J. Appl. Phys.* **89** 4301.
18. Graf D, Lambert U, Schmolke R, Wahlich R, Siebert W, Daub E and von Ammon W 2000 *"300mm Epi PP Wafer: Is there sufficient gettering?" Electrochem. Soc. Proc.* **2000-17** 319.
19. Alpass C R 2008 *PhD Thesis Department of Materials Oriel College University of Oxford.*
20. Elman B S, Shayegan M, Dresselhaus M S, Mazurek H and Dresselhaus G 1982 *"Structural characterisation of ion-implanted graphite" Phys. Rev. B* **25** 4142.
21. Kelly B T 1969 *"Thermal annealing of pyrolytic graphite irradiated with fast neutrons at 40^0 C" Carbon* **7** *699.*
22. Mitchell E W J and Taylor M R 1965 *"Mechanism of stored-energy release at 200 C in electron-irradiated graphite*" *Nature* **13** 638.
23. Burchell T D, Pappano P J and Strizak J P 2011 *"A study of the annealing behaviour of neutron irradiated graphite" Carbon* **49** 3.
24. Ewels C P, Telling R H, El-Barbary A A and Heggie M I 2003 "*Metastable Frenkel pair defect in graphite: Source of Wigner energy?" Phys. Rev. Lett.* **91** 025505.
25. Urita K, Suenaga K, Sugai T , Shinohara H and Lijima S 2005 "*In situ observation of thermal relaxation of interstitial-vacancy pair defects in a graphite gap*" *Phys. Rev. Lett.* **94** 155502.
26. Krasheninnikov A V and Banhart F 2007 *"Engineering of nanostructured carbon materials with electron or ion beams" Nat. Mat.* **6** 723.
27. Ochedowski1 O, Kleine Bussmann B, Ban d'Etat B, Lebius H and Schleberger M 2013 *"Manipulation of the graphene surface potential by ion irradiation" arXiv:1301.1192 [cond-mat.mtrl-sci].*

28. Esquinazi P, Spemann D, Höhne R, Setzer A, Han K H, and Butz T 2003 *"Induced Magnetic Ordering by Proton Irradiation in Graphite" Phys. Rev. Lett.* **91** 227201.
29. Burchell T D 1999 *"Fission reactor applications of carbon" Carbon materials for advanced technologies* ed. Burchell T D (Oxford: Elsevier) 429.
30. Heggie M I, Suarez-Martinez I, Savini G, Haffenden G L and Campanera J M 2010 *"Radiation damage in graphite – A new model" Proc. IAEA consultancy 'Solution for graphite waste : A contribution to the accelerated decommissioning of graphite moderated nuclear reactors' Manchester U.K March 2007* IAEA-TECDOC-1647 39.
31. Atsumi H 2003 *"Hydrogen retention in graphite and carbon materials under fusion reactor envireonments" J. Nucl. Mater.* **313-316** 543.
32. Krause-Rehberg R and Leipner H S 1999 "*Positron Annihilation in Semiconductors: Defect Studies" (Springer series in solid-state sciences*) **127** ed Manuel Cardona et *al* (Berlin: Springer).
33. Knoll G F 2000 *"Radiation detection and measurement"3rd edition (New York : John Wiley and Sons).*
34. Kansy J 1996 *"Microcomputer program for analysis of positron annihilation lifetime spectra" Nucl. Inst. Meth. Phys. Res. A* **374** 235.
35. Mantl S and Triftshäuser W 1978 "*Defect annealing studies on metals by positron annihilation and electrical resitivity measurements" Phys. Rev. B* **17** 1645.
36. Costello D G, Groce D E, Herring D F and McGowan J Wm 1972 *"Evidence for the Negative Work Function Associated with Positrons in Gold" Phys. Rev. B* **5** 1433.
37. Fischer D A, Lynn K G and Gidley D W 1986 *"High-resolution angle-resolved positron reemission spectra from metal surfaces" Phys. Rev. B* **33** 4479.
38. Coleman P G 2000 *"The generation and transport of positrons" Positron Beams And Their Applications* ed. Coleman P G (Singapore: World Scientific) p 11-40.
39. Canter K F and Mills Jr. A P 1981 *"Slow positron beam design notes" Can. J. Phys.* **60** 551.
40. Ghosh V J and Aers G C 1995 *"Positron stopping in elemental systems: Monte Carlo calculations and scaling properties" Phys. Rev. B* **51** 45.

41. van Veen A, Schut H, de Vries J, Hakvoort R A and Ijpma M R 1990 *"Analysis of positron profiling data by means of VEPFIT" Positron Beam for Solids and Surfaces AIP Conf. Proc. No.* **218** ed Schultz P J, Massoumi G R and Simpson P J (New York:AIP) 171.
42. Clement M, de Nijs J M M, Balk P, Schut H and van Veen A 1996 *"Analysis of positron beam data by the combined use of the shape- and wing-parameters" J. Appl. Phys.* **79** 9029.
43. Amarendra G, Rajaraman R, Venugopal Rao G, Nair K G M, Viswanathan B, Suzuki R, Ohdaira T and Mikado T 2006 *"Identification of open volume defects in disordered and amorphized silicon" Phys. Rev. B* **63** 224112.
44. Yang X, Xia H, Qin X, Li W, Dai Y, Liu X, Zhao M, Xia Y, Yan S and Wang B 2009 *"Correlation between the vacancy defects and ferromagnetism in graphite" Carbon* **47** 1399.
45. Barbiellini B et.al. 2013 *"Surfaces of nanomaterials for sustainable energy applications: thin-film 2D-ACAR and PALS studies" APS March Meeting 2013 Monday–Friday, March 18–22, 2013; Baltimore, Maryland* **vol.58.**
46. Rowe B W, Pas S J, Hill A J, Suzuki R, Freeman B D and Paul D R 2009 *"A variable energy positron annihilation lifetime spectroscopy study of physical aging in thin glassy polymer films" Polymer* **50** 6149.

Chapter 2
Thermal evolution of defects in Nitrogen ion implanted Silicon

This chapter deals with the investigation of thermal annealing of open volume defects in silicon, implanted to a dose of 10^{14} and 10^{15} ions/cm^2 with 60keV nitrogen (N^+) ions using slow positron beam spectroscopy (SPBS). The evolution of the implanted nitrogen during this defect migration is traced using secondary ion mass spectrometry (SIMS). During the isochronal annealing studies, the lower dose sample showed near complete defect recovery by 873 K except for a marginally higher S-parameter near surface corresponding to nitrogen-vacancy (N-V) complexes. On the other hand, the higher dose sample showed a two-step annealing with removal of deeper defects by 473 K followed by agglomeration of vacancies near surface by 873 K, giving a small signal corresponding to N-V complex. Complete recovery is obtained for both samples by 1073 K. The implanted nitrogen shows no noticeable diffusion until 873 K but is beyond the traceable limit of SIMS by 1073 K for lower dose sample. For higher dose sample, non-fickian diffusion towards the surface has been seen for 30 minutes annealing at 1073 K with two peaks, one fixed at the implanted range. On further annealing to 1 hour at the same temperature, nitrogen signals are not observed in SIMS. Thus, a detailed study of migration of vacancies and implanted nitrogen in silicon is provided in this chapter using two complementary techniques.

2.1 Introduction

Ion implantation is a valuable tool used extensively in planar device fabrication because of its ability to provide reproducible impurity engineering at specific depths with greater control over purity. The primary drawback is the damage produced during implantation and its subsequent evolution during further treatment. A proper understanding of the dynamics of these defects can ensure improved device performance. For example, the residual damage like dislocation loops left behind after the high temperature annealing treatment affects the device yield and parameters [1]. Another detrimental effect is the transient enhanced diffusion (TED) of doped impurity (specifically boron) in the presence of implantation induced damages, during subsequent annealing process [2]. This reduces the ability to have electrically active defects at specific depth ranges for fabrication of ultra shallow junctions.

Of the many ions used in silicon, nitrogen (N) implantation is very important from technological point of view. Nitrogen implantation has been shown to retard the oxide growth [3]. This makes it useful for self aligned contact applications in MOS technology [4] and to get multiple oxide thickness for system on chip applications by using different nitrogen doses [5]. Nitrogen is found to be largely electrically inactive in silicon (Si) [6]. However some shallow thermal donors have been identified which form at specific temperatures. Certain deep levels have also been reported which form only at certain annealing conditions and these centres are yet to be identified with respect to their specific structure [7]. It is also found that its introduction can control vacancy concentration [8] and affects the vacancy agglomeration process [9]. It is found to prevent the formation of larger voids which are more detrimental to device performance and are difficult to remove. The physical interaction of nitrogen and open volume defects which achieves this is unclear but it has been suggested to be due to the formation of

nitrogen-vacancy complexes [10]. They even provide mechanical strength by immobilizing dislocations in FZ(float zone)-Si. This is thought to happen because of nitrogen segregation at dislocations thus forming Nitrogen-Oxygen complexes. Its role in Cz-Si (czhocralski) [11] where dislocation blocking is achieved by excess oxygen is yet to be understood. It also improves oxygen precipitation in Si thereby improving the gettering of metallic impurities in devices, as this oxide precipitates act as efficient getters of metallic impurities and prevent them from reaching the junction regions [12, 13].

The structure of nitrogen species in silicon has been intensely researched with a host of tools like Fourier Transform Infra Red (FTIR) spectroscopy, Electron Spin Resonance (ESR) and ab-initio modelling. The primary species has been identified as the di-interstitial pair in as grown as well as implanted silicon samples with substitutional nitrogen amounting to less than 1% in the implanted specimens [14, 15]. A range of values from ~ 2 – 4 eV has been suggested as its binding energy taking its stability close to melting point for the latter values. A highly mobile monomer also resides interstitially and certain local vibration modes are assigned to them [7]. However the fundamental interaction of these species with the open volume point defects and its temperature dependence which ultimately influences some properties like vacancy aggregation and its density distribution, nitrogen diffusion etc. is not well understood. Nitrogen-Vacancy complexes have been observed experimentally in annealed FZ-Si using positron annihilation spectroscopy [16] and deep level transient spectroscopy (DLTS) [17] though the specific signals were not attributed to any known defect types. Ab-initio modellers, however have considered various interaction routes like complex of interstitial nitrogen monomer with vacancy giving rise to a substitutional nitrogen or interaction of di-interstitial with vacancy giving rise to interstitial-substitutional nitrogen complex etc.

[17]. Various structures, where vacancy is near an interstitial or substitutional nitrogen was also considered and their vibrational frequencies were calculated, though these have not been seen experimentally. For example two possible scenarios for Nitrogen-Vacancy complexes N_s-V (substitutional Nitrogen-vacancy) and (N_s-N_s)-V are given in Fig. 1[10].

As the di-interstitial pair is the dominant nitrogen defect in silicon, the diffusion of nitrogen has been considered based on the movement of this species. However one of the models considers the di-interstitial pair as immobile and its dissociation into the highly mobile monomer as responsible for the transport process [18, 19]. To explain the anomalous diffusion of nitrogen preferentially towards surface in implanted samples, Adam et.al. [20] considered another model where the substitutional nitrogen is taken as immobile and nitrogen-vacancy reaction as diffusion limiting sinks for interstitial nitrogen. Such a wide variety of proposals shows how little understanding is there about nitrogen – vacancy interaction and its role in a phenomenon like diffusion.

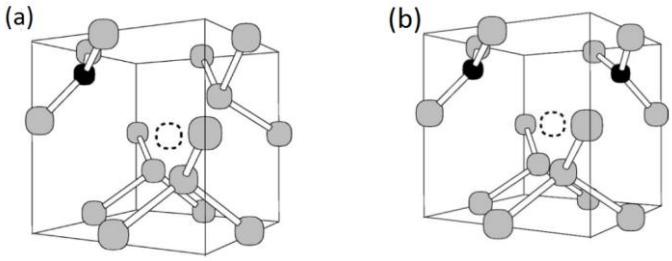

Figure: 1 Representation of (a) N_s (substitutional nitrogen)-V (vacancy) complex and (b) (N_s-N_s)-V complex (after Goss et.al [10]). Grey balls represent Silicon atoms and Black balls represent Nitrogen. The dashed circle represents the missing atom position.

Slow positron beam spectroscopy (SPBS) is sensitive to open volume defects in a material and to their local chemical environment, whereas secondary ion mass spectrometry (SIMS) gives nitrogen distribution and its movement with thermal treatment. Hence, these could be combined to look at thermal evolution of vacancy type

defects in nitrogen implanted silicon and the influence of nitrogen in the vacancy evolution. However, there are only a few studies [16, 21, 22] utilizing positron based techniques to understand the defect dynamics for nitrogen implantation in Si at medium doses where it is more important technologically. Two of the studies [21, 22] used nitrogen implantation in Si to compare the performance of the fitting routine ROYPROF which considers a composite Gaussian profile for damage instead of a box profile and obtained satisfactory results. Adam et.al.[16] used positron measurements to confirm the presence of N-V complexes in molecular ion implanted FZ-silicon. They could not find signature of these N-V complexes in the as irradiated state but were able to show their clear signals when the sample was annealed to 1023 K and thus, justified using N-V complexes in their nitrogen diffusion model though a structure of such a defect complex was not suggested. The study by Hao et.al [23] with 100 keV Nitrogen implantation in Cz-Si(111) invokes the concept of N-V complex in the as irradiated condition, and explained the shift in peak S parameter upon RTP (rapid thermal processing) at 923 K and 1023 K as movement of N-V complex to the surface. They could show the presence of O-V complexes very near to the surface at higher annealing temperatures of 1123 K using Coincidence Doppler broadening (CDB) studies.

In this chapter thermal evolution of defects in n-type Cz-Si (100), implanted with 60 keV Nitrogen to two doses in the medium range (10^{14} and 10^{15} N^{+}/cm^{2}) has been investigated from the as irradiated state until 1073 K using depth resolved positron annihilation studies. This would help to elucidate the dose dependent defect evolution, nitrogen-vacancy interaction and to look at the possible presence of N-V complexes from room temperature to 1073 K. Secondary ion mass spectroscopy has been used to look at nitrogen profile changes during these temperature treatments and thus, to understand the role, the implanted species play in vacancy evolution.

2.2 Experiments

A brief description of the sample preparation, implantation, thermal treatment, positron and SIMS characterization utilized for the present studies are given in the subsequent sections.

2.2.1 Nitrogen Ion Implantation

Implantation of nitrogen into silicon was performed using a 150 kV single ended ion accelerator where the source is maintained at the high potential and the target is grounded. A schematic of the accelerator is given in Fig. 2. Plasma of the gaseous element was produced by the application of RF potential in a quartz tube where the required gas was maintained at a pressure of ~10^{-3} to 10^{-2} mbar. Ions produced inside the plasma are extracted by biasing the plasma with respect to a narrow extraction canal. The extraction voltage (V_i) can be varied between 0 -5 kV.

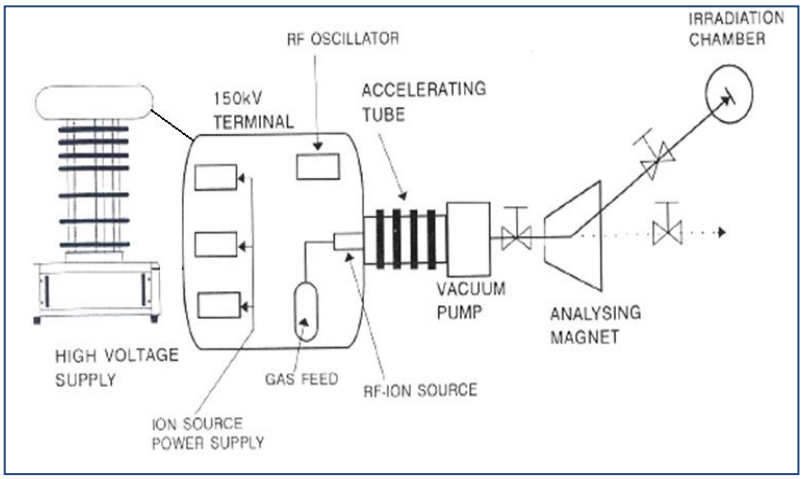

Fig. 2: Schematic arrangement of 150 kV ion accelerator

The entire assembly (ion source, power supplies, RF generator etc.) is kept inside a high voltage dome elevated to the required high potential generated by a solid-state power

supply. The extracted ions are accelerated using an accelerating column beyond which they are mass analyzed using a quadrapole magnet. The beam spot is fixed on the sample by a set of beam steering electrodes. The entire beam line is maintained in a vacuum better than $1x10^{-6}$ mbar. Thus the final energy of the particles will be a sum of the extraction (pre-acceleration) energy - eV_i of the ion source and the energy – eV_T attained by the application of the acceleration voltage V_T to the terminal. The implantation dose is found by integrating the beam current measured on the sample after applying proper correction using a Faraday cup.

In the present study Phosphorus doped n-type Cz-Si(100) wafers with a resistivity of 2.8 Ωcm (doping density of 1.63 x 10^{15} P/cm^3) were used. They were etched with hydrofluoric (HF) acid to remove the native oxide layer and implanted with 60 keV Nitrogen ions at room temperature to fluences of 10^{14} and 10^{15} N^+/cm^2. The implantation was carried out at an off–normal angle of 7^0 to reduce ion channeling effects. Low beam current of ~200 nA was used to avoid any effects due to heating of the samples.

The profile of implanted nitrogen in silicon and the corresponding damage produced was simulated using the monte-carlo simulation package TRIM [24]. The program simulates the transport and range of ions through an amorphous matrix using a quantum mechanical treatment of collision process with random selection of the impact parameters of the next colliding ion. As a zero Kelvin calculation is carried out the diffusion, recombination and clustering of the defect species are not taken into account and hence, the defect concentration predicted will always be higher than the actual situation. The temperature induced broadening of the profile of the implanted species is also not taken into account in these calculations.

2.2.2 Vacuum Annealing

The implanted samples were annealed in a vacuum better than 10^{-6} mbar using a vacuum system based on diffusion pump set up as shown in Fig. 3. The samples were cumulatively annealed for 30 minutes to different temperatures from 473 K to 1073 K in steps of 200 K. The measured temperature at the sample position with respect to time is shown in Fig. 4. The furnace is pre-heated to the required temperature and is inserted over the quartz tube containing the sample after the required vacuum is achieved.

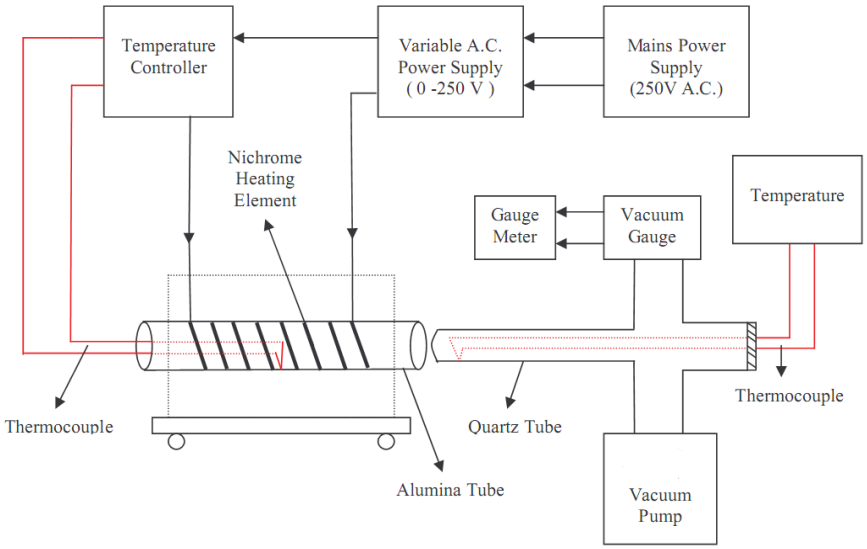

Fig. 3: Schematic representation of the vacuum annealing set-up.

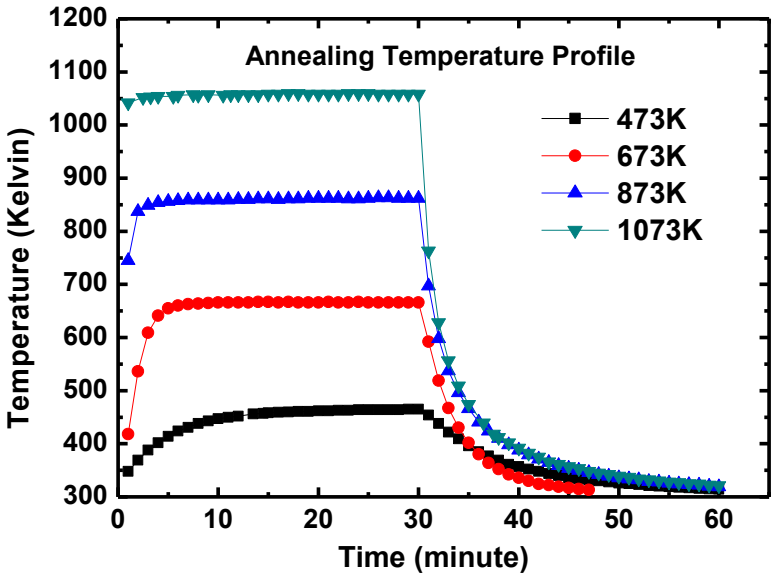

Figure 4: Variation of temperature at sample position with respect to time.

2.2.3 Slow Positron Beam Spectroscopy (SPBS)

Irradiated as well as pristine etched Si samples (taken as reference) were investigated using a magnetically guided variable low energy positron beam [25]. A schematic of the slow positron beam system is given in Fig. 5.

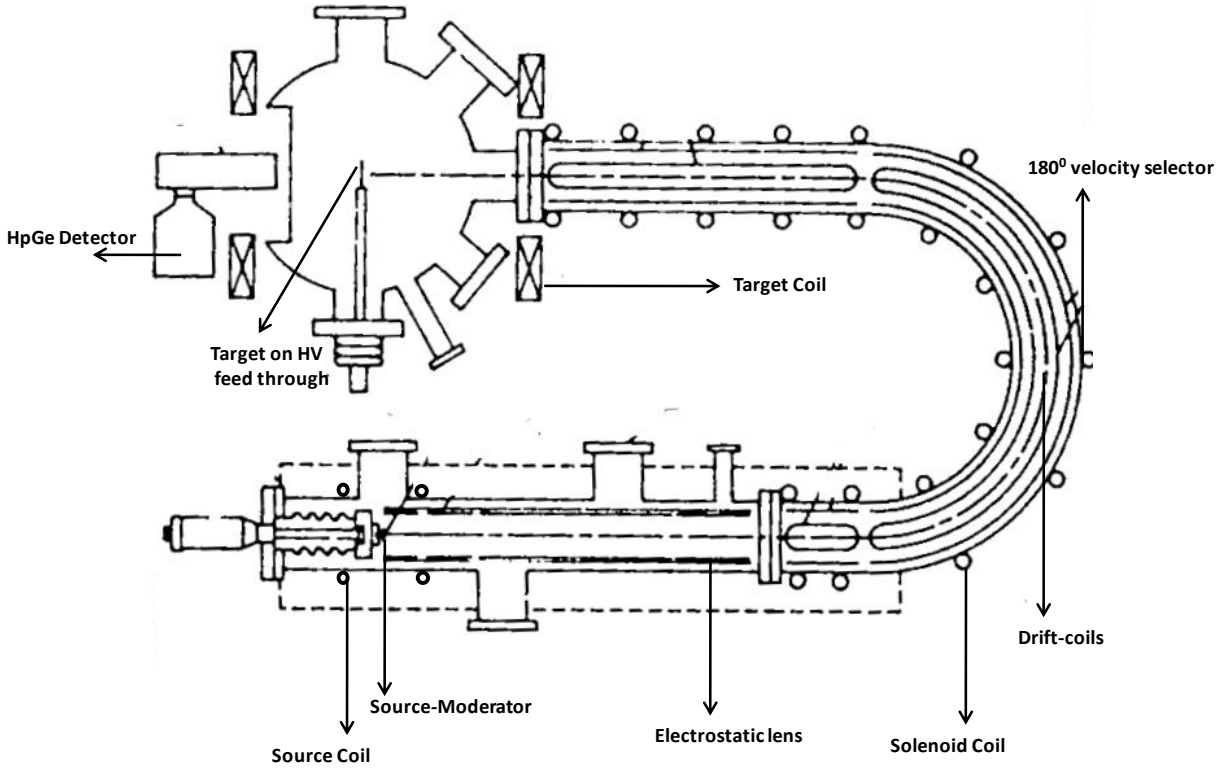

Fig. 5: Schematic of slow positron beam at IGCAR, Kalpakkam.

Radioactive ^{22}Na is used as the source of positrons which are moderated using W (100) micron thick single crystal. These are annealed at 2473 K to avoid any positron trapping by defects inside the crystal and also to improve the surface quality. The moderated positrons are brought to the magnetic guidance arrangement using a set of asymmetric einzel lens and a two tube lens system kept inside a UHV system. The slow mono energetic positrons are separated from the un-moderated fast positrons by bending the slow ones through 180^0 U-bend magnetic-solenoid tube. The slow positrons continue to the target through the field inside the solenoid tube. The energy of the positron beam,

and thus the mean positron implantation depth, was varied from 250 eV to 20 keV by applying the required high voltage to the sample mounted on a Cu holder. The annihilation γ-spectrum was recorded using an high purity germanium detector having an energy resolution of 1.45 keV at 662 keV γ line of Cs^{137} with a shaping time of 6 μs in the spectroscopic amplifier. Around 1.05 x 10^5 counts were collected in the main peak (511±10 keV) at a count rate of 29 cps using this detector. The 511 keV annihilation γ ray will be Doppler broadened as a result of the momentum of the annihilating electron-positron pair. This is quantified, as described in Chapter 1, in section 1.3.1, using a line shape parameter S defined as the ratio of counts in the central region of 511 keV peak (511±1 keV) to the total counts in the peak (511±10 keV) and a wing parameter (W) defined as the ratio of counts in the wing region of the peak (513.5 to 516 keV and 506 to 508.5 keV) to the total counts. With the accumulated counts in the main peak, central region and wing region, an error of ±0.002 is expected for S parameter and an error of ±0.0004 is expected on W parameter. VEPFIT [26] code is used to fit the experimental S vs E data so as to give the fraction of positrons annihilating in various trapping centres as a function of depth and the S or W parameters corresponding to each trapping centre. The S-W correlation plot with positron implantation energy as the running parameter [27] was also used to throw more light into the nature of implantation induced defects.

2.2.4 Secondary Ion Mass Spectroscopy (SIMS)

The implanted nitrogen profile in as-implanted samples and in those samples which were cumulatively annealed to 873 K and 1073 K were obtained by recording the secondary ion mass spectrum using a CAMECA IMS 7f magnetic sector SIMS instrument. The basic working principle of SIMS is based on the possibility of sputtering atoms from the top surface layer of target, when ions or neutral particles having energy

in the range of a few kilo electron volts are incident. Some of these ejected species have the probability of being charged, which can then be extracted using ion optics principles and can thus, be used to get the chemical map of the analysed area. The ejected species can be monoatomic, polyatomic or complex clusters and hence, a high mass resolution is required for careful selection of elements.

SIMS involves a primary ion source, which provides the ion species used for sputtering the sample. Some of the useful ion species are Cs^+, O^-, O^{2+}, Ar^+ and Ga^+, which are accelerated by a voltage bias of few tens of kV. Most SIMS systems consist of two sources –a duo-plasmatron which produces positive and negative ions and a themo-ionization Cs source. Sputtering process by these ions produces secondary ions with a range of translational energies which are narrower for molecular species. The fraction of the sputtered atoms which become ionized is called the ion yield or the ionization efficiency and it varies for different elements over orders of magnitudes. Hence, quantification in SIMS uses relative sensitivity factors for each element. The matrix in which the impurity is implanted is usually taken as the reference and during the trace element analysis, the concentration of the reference is taken as constant. In this condition, if I_R is the secondary ion intensity for reference element R, I_E & C_E is the secondary ion intensity of element E and its concentration respectively, then [28]

$$C_E \quad \alpha \quad \frac{I_E}{I_R} \tag{1}$$

Thus, if the secondary ion intensity of the required trace element is normalised with respect to the reference/matrix, then the profile obtained as secondary ion intensity becomes equivalent to a concentration profile.

In the CAMECA IMS 7f instrument, the duo-plasmatron source is biased to 2 - 17.5 kV and the Cs source is biased to 2-12 kV. The sample can be biased to ±10 kV and hence, a primary beam with an impact energy of ~ 0.5 – 10 keV can be obtained. These

ions are focussed and directed towards the sample which leads to the ejection of secondary ions. The secondary ions are transported through the secondary column where a selection for energy is made using an electrostatic analyser (ESA) and later a mass selection is made using the magnetic sector. The secondary ions are then steered towards the second ESA which gives good abundance sensitivity. The secondary ions are counted using an electron multiplier or a Faraday cup or can be directly imaged using phosphor screen attached with a CCD camera if the second ESA is grounded.

In the present study, Cesium source is biased to +10 kV whereas the sample is biased to +5kV. Hence, the impact energy of the primary beam would be 5 keV. A primary beam intensity of 10 nA is maintained throughout the experiment. A raster area of 200 µm was used for sputtering. The positive secondary ions obtained have a kinetic energy of 5keV. For samples implanted to a dose of $1x\ 10^{15}$ ions/cm^2, the analysis area was 62 µm but for samples implanted to a dose of $1x10^{14}$ ions/cm^2 the analysed area was set as 150 µm to get good statistics. The obtained intensity profile as a function of time was converted to a depth profile, by finding the average sputtering rate from the crater depth created by sputtering. A DEKTAK 6M stylus profilometer which works on the principle of linear variable differential transformer (LVDT) and with a stylus diameter of ~ 25 µm was used to get the crater depth.

2.3 Results & Discussion

2.3.1. TRIM

TRIM [24] simulation of 60 keV nitrogen implantation in silicon is shown in Fig. 6. The simulation yielded a defect profile with a maximum damage around 120 nm which extends up to around 280 nm. The implanted Nitrogen profile extends up to about 300 nm and has the highest concentration at a depth of 162 nm.

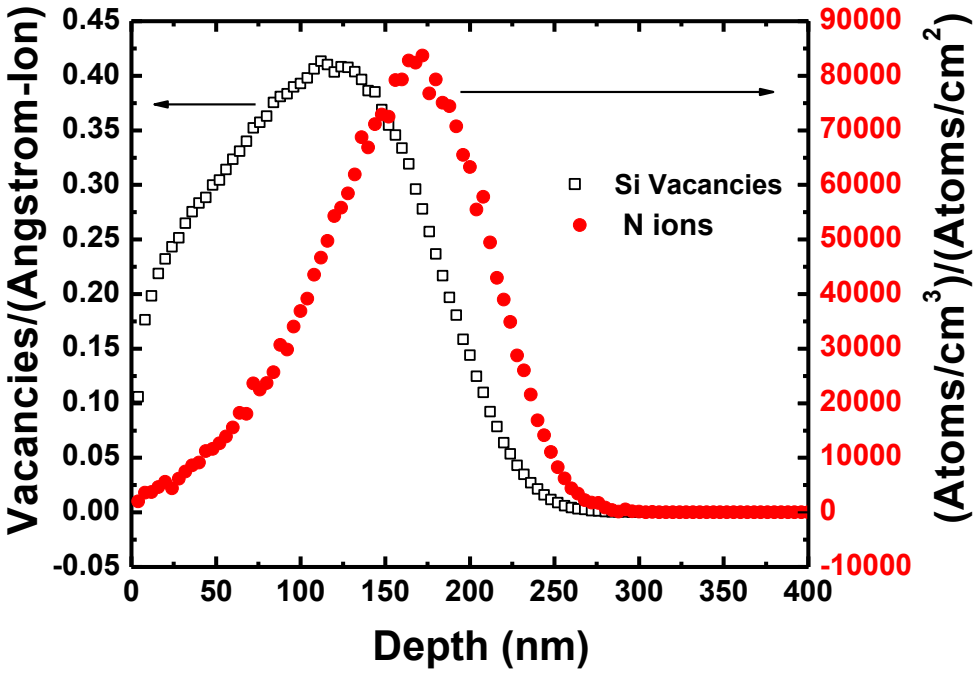

Figure 6: The depth profile of vacancies (left axis) and implanted Nitrogen ions (right axis) in Silicon calculated using TRIM code with 60 keV Nitrogen ion implantation.

2.3.2. SPBS

Depth-resolved S-parameter versus Positron beam energy (E) profiles are shown in Fig. 7 (a) and (b) for low dose and high dose samples respectively, along with the reference sample. Measurements taken after various stages of annealing are also shown. The solid line through the data points is a result of the analysis using VEPFIT [26]. The top axis shows the mean implantation depth of positrons in Si calculated using the relation for the mean implantation depth (equation (11) in Chapter 1). The S vs E profile of the reference sample shows a typical behaviour with a low S value near the surface region which gradually increases to a higher bulk value, which has been normalized to unity. Since we have removed the native oxide layer by etching, the S values at low positron energies are mainly due to the surface traps and hence, the S values are slightly higher than what is normally observed for samples with native oxide layer [29].

The sample implanted to a fluence of 10^{14} N^{+}/cm^{2} has a low S value at small positron energies (Fig. 7 (a)) and increases rapidly to a broad maximum around 4 keV

and beyond 6 keV, the S parameter decreases gradually to the bulk value. Positron energy of 4 keV corresponds to a mean depth of 140 nm which is close to the peak damage region as predicted by TRIM. The low S values in the initial positron energies is due to the positron annihilations in the native oxide layer; the broad maximum at intermediate energies is due to the open volume defects created by ion implantation and beyond 16 keV positron annihilations are entirely in bulk. Not much change is observed in this behaviour upon annealing the sample to 473 K. Upon annealing to 673 K there is a small decrease in the S parameter values in the energy range of 8 keV - 12 keV. By annealing to 873 K, the curve shows a drastic decrease in the peak S value but still lies higher than the reference sample. On further annealing to 1073 K, the S vs E profile resembles the reference sample except at the lower positron energies which is most probably due to the growth of thin native oxide layer into the sample during the final stage of annealing. A similar nature for S vs E profile is also obtained for the sample implanted to a higher concentration of 10^{15} N^{+}/cm^{2}, except for some important differences. In the case of high dose sample, the S values beyond 8 keV decreases slowly than in the case of lower dose sample and it's only beyond a positron energy of 18 keV that complete bulk annihilations could be seen. This sample too does not show much change in peak S-value upon annealing to 673 K except for a decrease in the S values at positron energies from 8 keV to 12 keV.

The major difference between higher and lower dose samples comes up during the annealing process at 873 K where the higher dose sample does not show a drastic reduction of S values in the peak damage region as seen in lower dose sample. Instead, upon annealing to 873 K there is a shift of the peak S value to lower positron energies and the S parameter in the energy ranges from 6 keV to 12 keV shows a considerable decrease compared to the as implanted stage. At 1073 K, the S vs E profile is similar to

what was obtained for low dose sample. The difference between the lower and higher dose samples is shown graphically in Fig. 8, where normalized average S values between positron energies of 1.25 and 6.25 keV is plotted as a function of the annealing temperature. This positron energy range corresponds to a depth of 25 to 300 nm where

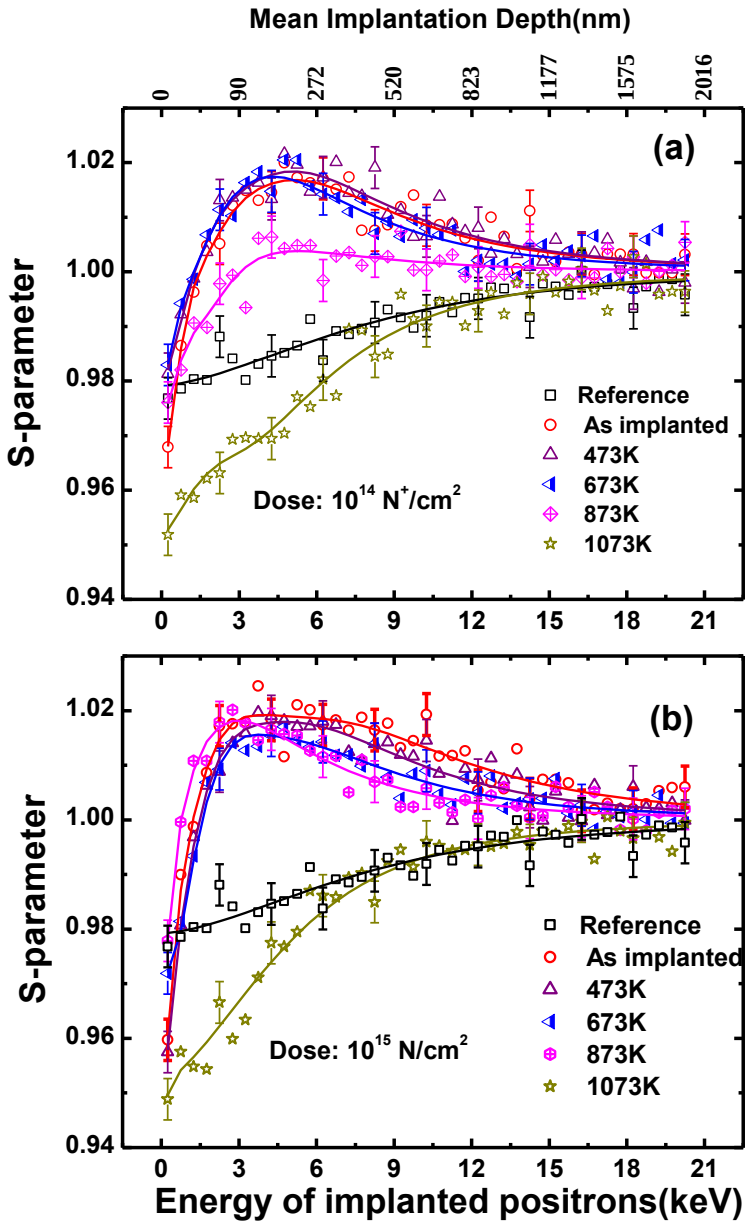

Fig. 7: Variation of normalized S-parameter with positron beam energy for (a) sample implanted with Nitrogen to a dose of 10^{14} N^+/cm^2 (b) for sample implanted with a dose of $10^{15}N^+/cm^2$ and annealed to various temperatures. The plot includes profile for reference Si (open-square). The line through the data points is a fit obtained using VEPFIT with 3-layer model.

TRIM [24] had predicted the presence of implantation induced defects. As can be clearly seen the S_{avg}/S_{bulk} for the two doses shows a similar behaviour except at 873 K. This aspect will be discussed later on.

Experimental S vs E profiles have been fitted using VEPFIT [26] code with a simple model consisting of a native oxide layer, a damaged layer and the bulk layer. The S parameters and widths of each layer are thus deduced. This is shown in Fig. 9 (a) and (b) for lower and higher dose samples, respectively. With 10^5 counts in the main peak and 0.5 keV step size for S vs. E curve, a best chi-square of less than 28 was obtained for all fits with 3 layers. The chi-square degraded for lower or higher number of layers. The diffusion length of bulk Si was obtained by fitting the data of reference Si to be 249±70 nm, which is very close to the value (245 nm) for Si [30]. This was the only parameter that was fixed while fitting the other data. The error on fitted S-parameter is less than 0.002 for all layers and for both the samples. The error on the boundary of the first layer generated using the fit for the lower dose sample laid between 8.62 to 37.67 nm, where as error on boundary of the second layer was between 33.60 to 70.62 nm. For high dose

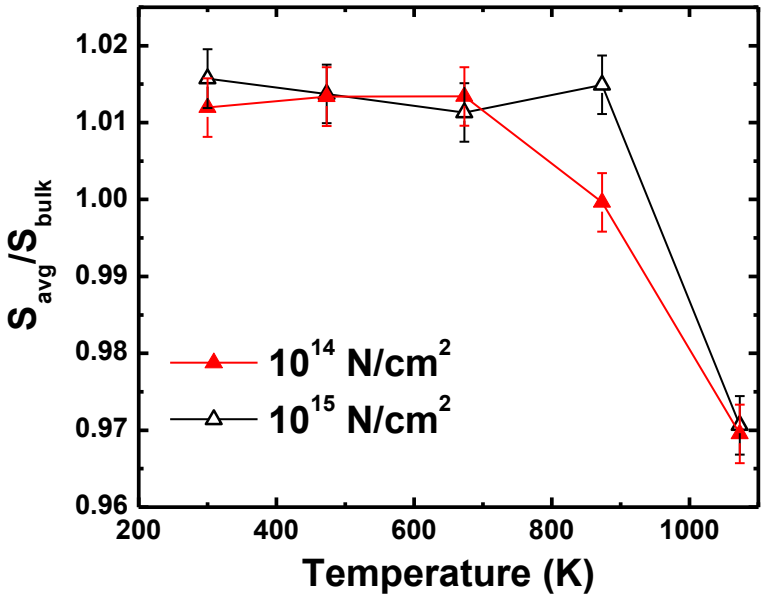

Fig. 8: Normalized average S-parameter is shown as a function of annealing temperature for Nitrogen implanted samples. The line through the data points is a guide to the eye.

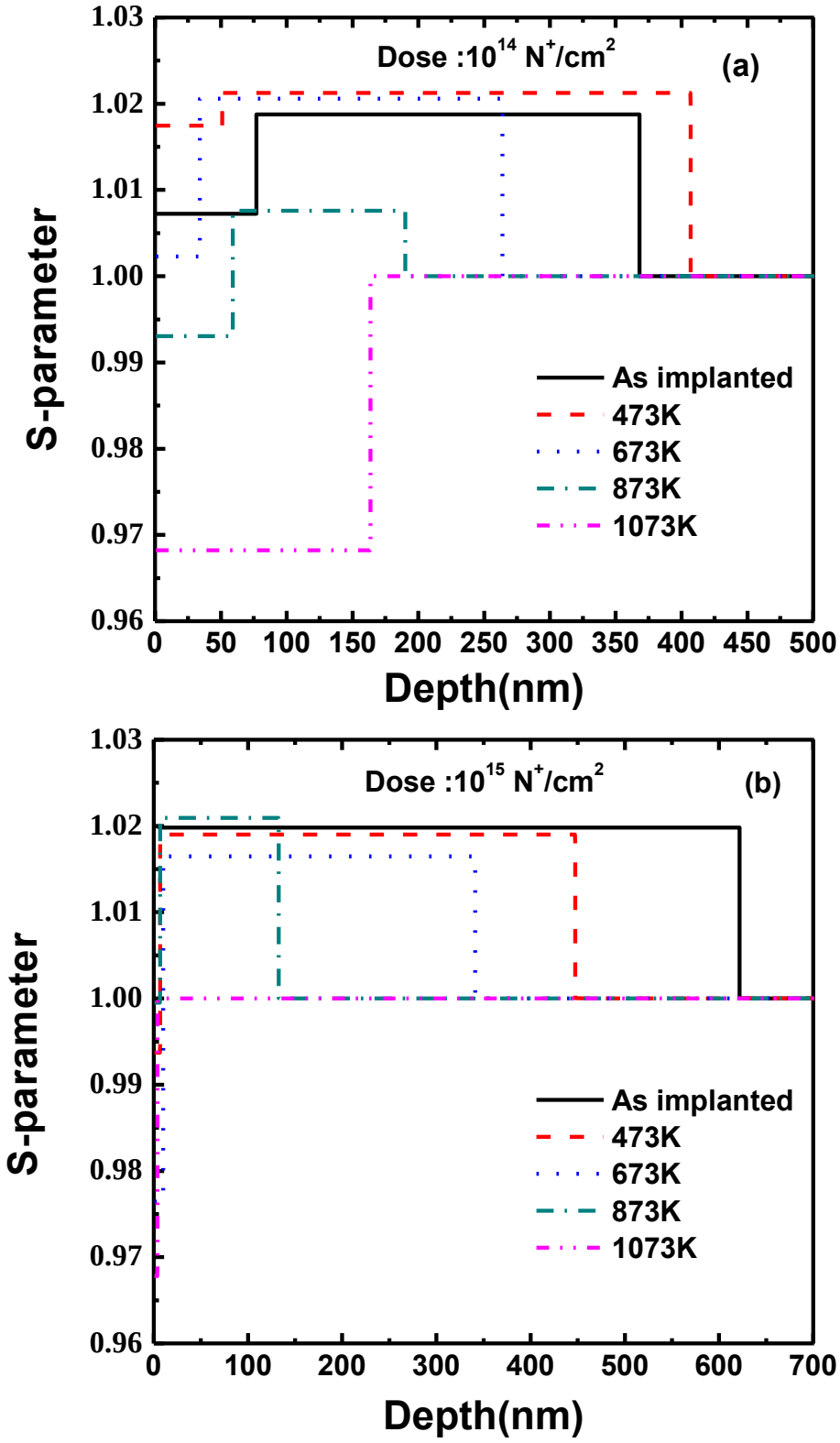

Fig. 9: Normalized S-parameter plotted as a function of depth (a) for sample implanted to a dose of 10^{14} N^+/cm^2 and (b) 10^{15} N^+/cm^2 considering a box profile for each layer. For all temperatures except 1073 K a three layer model is considered. A two layer model is considered for 1073 K.

sample the error on the boundary of the first layer is in between 0.5 to 27 nm and for second layer the error on boundary is between 25 to 54 nm. Errors on both the boundaries were considered while finding the width of the second layer and basic error propagation methodology was used to calculate the uncertainty on the width of the second layer. In the case of lower dose sample it was found that the damaged layer has an S value of around 1.02 until 673 K. At 873 K the S value of the damaged layer decreases drastically to 1.007 and upon annealing to 1073 K the damaged layer gets completely annealed out. Similar behaviour is seen for higher dose sample except for the differences highlighted in previous paragraph. Here the S value for damaged layer is also around 1.02. The S value of the damaged layer upon annealing at 873 K is 1.02 as opposed to the much lower value for lower dose sample and further annealing to 1073 K removes this damaged layer. As seen in Fig. 9 (a) and (b), the S parameter value of the damaged layer is around 1.02 for both samples which shows that there is near-saturation trapping at lower dose implantation itself. The S parameter values depend on the region chosen as the central region of 511 keV peak, on the energy resolution of the detector and on the orientation of the crystal [31] and S-parameters in the range of 1.02 to 1.045 have been assigned to divacancies in literature [30]. Based on this S-parameter value of 1.02 can be assigned to a predominant divacancy (V_2) type of defect.

In ion implanted silicon, mono-vacancies produced are highly mobile and unstable at room temperature. They cluster to form divacancies or associate with impurities like Oxygen (A-centres) or Phosphorous (E-centres) which are identified as possible traps for positrons that are stable at room temperature. The A-centres are shallow traps and will be visible only for positron measurements at lower temperatures. E-centres are stable till 423 K and are deep traps. Their formation depends on the concentration of Phosphorous and is predominantly formed for highly doped samples

[30]. However, the most prominent defects in irradiated silicon are divacancies [32]. Divacancies start to anneal out by 400 K and get completely removed from the system by 600 K. This is observed as the gradual disappearance of 1.8 μm line in the IR spectrum with annealing temperature [33]. The prominent annealing mechanism for divacancies at temperatures of 398 K to 523 K is attributed to the recombination of divacancies with interstitials which become mobile at these temperatures [34]. It has also been noted in earlier studies that annealing Si beyond 523 K results in divacancy agglomeration and such vacancy clusters are stable till 773 K but they anneal out completely for temperatures above that [34-36]. There have been suggestions of these being sponge-defects, a loose aggregation of vacancies [30] to account for divacancy disappearance with no change in peak S-parameters. It was later suggested by Makhov and Lewis [37] that the positron parameters need not show much change even when the divacancies get completely removed from the system as fourfold tetravacancies formed during the clustering process gives a positron signal similar to that of divacancy; the net effect being a marginal or no change in the peak S-parameter. Another positron trap that can develop with divacancy disappearance is the V_xO_y type defects where $x \geq 2$ [38]. The lifetimes assigned to various V_xO_y clusters can point to the behaviour of their corresponding S-parameter. For example V_2O which has been shown to dominate beyond 473 K has a lifetime which is slightly lower (~ 295 ps) than the divacancy value (~ 320 ps) and a similar behaviour could be expected for S-parameter. V_3O clusters which form beyond 673 K can give signals similar to divacancy as indicated by its divacancy like lifetime values (~ 325 ps). However, none of the V_xO_y clusters survive beyond 773K [38].

The variation of width of the damaged layer with annealing temperature is shown in Fig. 10 for lower and higher dose samples. The width of the damaged layer for lower

dose sample is 311 nm in the as implanted state, which shows a slight increase to 356 nm on annealing to 473 K. The width then decreases, up on annealing to 230 nm at 673 K and to 130 nm upon annealing at 873 K and finally, the layer disappears at 1073 K. The width of the damaged layer of the higher dose sample shows a steady decrease from 616 nm in the as implanted state at each level of annealing. Thus the boundary of the damaged layer (taking the width of oxide layer into account) of the sample implanted to the lower dose (370 nm) is slightly larger than the depth predicted by TRIM (280 nm) while the depth of this layer for the higher dose sample (621 nm) in the as implanted state is more than three times the depth predicted by TRIM. This has been observed in many previous studies [39-42] and has been attributed to various reasons. There were suggestions that it is related to the scattering angle of the implanted ion [43, 44], or an artefact of fitting by using a box profile for the damage caused [39]. Studies with differently doped Si samples showed that the depth profile of the damage deduced using variable energy positron beam spectroscopy is related to the internal electric field in the sample. Even then, it was found that the data could not be modelled properly without including deeper defects and the presence of such defects was suggested as due to the monovacancy migration and clustering at deeper regions at room temperature, ion channeling, or even impurities in the ion beam [41]. Experiment in which the surface damaged layers of Fluorine implanted Si were etched out in a controlled manner had confirmed the existence of such deeper defects. They have also observed that these deep level defects get annealed out by 573 K [40]. A similar behaviour is seen for the higher dose sample where there is a drastic reduction of the depth of the damaged layer from 620 nm to around 450 nm (Fig. 9(b)). The lower dose sample shows a slight increase in width which is within the average uncertainty (±40 nm) in the value of boundary generated using VEPFIT [26] and hence can be neglected. Hence, in the present study it

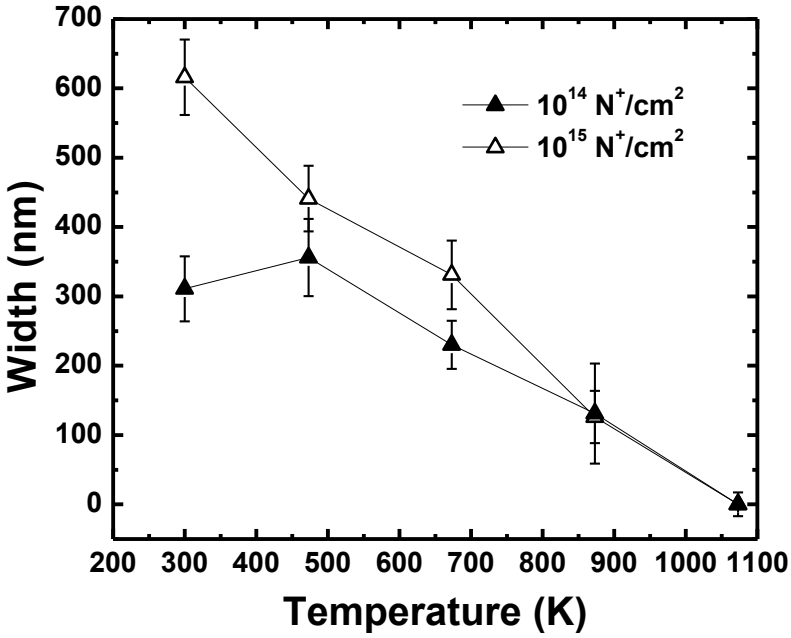

Fig. 10: Variation of width of the damaged layer obtained from VEPFIT analysis plotted as a function of annealing temperature for a dose of 10^{14} N^+/cm^2 and 10^{15} N^+/cm^2. The line through the data points is a guide to the eye.

is clear that for the higher dose sample, the defects in the deeper regions are getting annealed and this results in a decrease of width of the damaged layer at 473 K. It is difficult to pinpoint the exact nature of these deep level defects with Doppler broadening studies alone. As monovacancies are mobile at room temperature it is expected that some of these produced at the end of range migrate deeper before getting trapped in one of the stable forms. Since the number of monovacancies produced at the end of range will be smaller for the lower dose, the density of deeper defects formed will be small and hence the annealing stage at 473 K is not seen for the lower dose sample. Two processes where a decrease in S-parameter is expected by annealing up to 473 K are removal of divacancies by recombination with interstitials and removal of V-Phosphorous E centres. Any one of these or both could be identified as the deep level defects.

Upon further annealing to 673 K, both lower and upper dose samples show a decrease in the width of the damaged layer. At these temperatures the IR signal corresponding to divacancy is absent [33] but there is not much change in the peak

positron response, with the peak S value showing almost no change and the only change is in the width of the damaged layer. The decrease in the width indicate the removal of divacancies by recombination with interstitials or by collapsing to a surface sink or due to the formation of V_2O_2 complexes which have positron life time (~ 240 ps) close to bulk lifetime (~218 ps). The retention of the peak S-value at 1.02 for the damaged layer can be due to the formation of fourfold tetravacancies, sponge-defects or by the formation of V_3O complexes. From the decrease in the width it is also clear that the removal of divacancies happen close to projected range where the maximum density of interstitials and their clusters or loops are present.

By annealing to 873 K, the higher dose sample shows a shift in the peak S parameter towards the surface. However for lower dose sample there is a drastic reduction of S-parameter with values near surface (a small hump seen around positron energies of 2-4 keV) lying above the pristine silicon. Beyond 773 K, as shown by earlier studies, the clusters and oxygen complexes are not stable and may break into smaller vacancy clusters, divacancies or monovacancies and move towards the surface sink [35, 45, 46]. They are removed or get agglomerated into stable defect types during the cooling regime depending on the defect density. In such case, the observed variation in S-parameter for lower dose and higher dose sample may be due to a reduction in defect density alone. Hence for lower dose sample the removal of defects is dominating over agglomeration and for higher dose sample the annealing for 30 minutes has resulted in agglomeration of defects into stable forms near surface. It is also possible that the annealing at 873 K has resulted in the formation of new defect types or complexes for both lower and higher dose sample.

It is not possible to comment whether the variation in S-parameter reflects a variation in defect density or defect type just by using the S versus E plot. Hence the S-

W correlation plot and the idea of R parameter are used. Clement et.al. [27] has showed that S-W plots with implantation energy as running parameter can be used as an effective tool to identify various trapping layers, as different trapping layers have specific (S-W) co-ordinates. If there are only say, two trapping centers (*A*, *B*), each of them situated at different depths (let *A* be near surface and *B* in the bulk) then as we increase the implantation energy of the positrons, the effective S parameter at specific energy will vary as

$$S_m = f_A * S_A + (1-f_A) * S_B \quad (2)$$

$$W_m = f_A * W_A + (1-f_A) * W_B$$

where S_m and W_m are the measured S and W parameters and S_A,S_B and W_A,W_B correspond to S and W parameter of each trapping centre. *f* is fraction annihilating at the respective trapping centre. Hence, for very low energy positrons the contribution to the measured *S* comes mainly from the surface trapping centre *A* and as we increase the energy, S_m and W_m linearly increases towards the S_B and W_B values. Now if there is any other trapping centre in between *A* and *B*, then that will show up as turning point or inflexion [27] in S-W correlation plot. *R* parameter is defined as $\left|\frac{S-S_{bulk}}{W-W_{bulk}}\right|$ and is free of the effect of concentration of defects [47] provided there are only two trapping sites. From the definition of *R* parameter it is clear that it is numerically equal to the slope of the line joining the *S,W* coordinate of the defect and that of bulk. Thus different defect types show different slopes. Therefore if a turning point in *S - W* correlation plot represents a particular defect type, then a reduction in density of that particular defect type would result in turning points at lower *(S,W)* coordinates but which lies on the line joining the initial turning point and the bulk *(S,W)* coordinate. Any variation from this would signal the formation of new defect type or existence of equally dominating multiple defect types.

The S-W correlation plots for lower and higher dose samples for as implanted state as well as for annealing temperatures at 673 K, 873 K and at 1073 K are shown in Fig. 11(a) and (b) respectively. The (S,W) coordinate for all positron energies are plotted for as-irradiated sample whereas those near the turning point (1-8.5 keV) alone are shown for other temperatures for the sake of clarity. The straight lines are linear fits to the (S-W) coordinates belonging to specific energy groups. For higher dose sample the straight lines were fit for energies from 0 – 6 keV, 6.5 – 9.5 and from 10 - 20 keV. For lower dose sample however only two straight lines could be fit one from 0- 4 keV and 4-20 keV. The intersection point represents a particular type of defect according to the explanation by [27]. Hence, the deeper defect is detected in higher dose sample where as such defects are not visible in lower dose sample. If these deeper defects were divacancies then it would have had a (S,W) coordinate lying on the line joining the defect state and the bulk. Hence the most probable candidate for such defect type is the E centre which has stability only till 423 K. Its absence in lower dose sample could be directly attributed to the concentration of end of range vacancies produced. Even after annealing to 673 K, the turning point for both lower and higher dose sample shows only a marginal decrease. The arrow joining the turning point in the as – irradiated state, that at 673 K to the bulk state show that there is only a decrease in defect density. This was explained as due to the formation of defects which give positron parameters similar to divacancies. After annealing to 873 K, both lower dose and higher dose sample gives (S,W) coordinates which lie clearly outside the arrow. Hence the variation observed in the S versus E plot for both lower and higher dose sample cannot be attributed to change in defect density but to formation of a new defect type. For higher dose sample

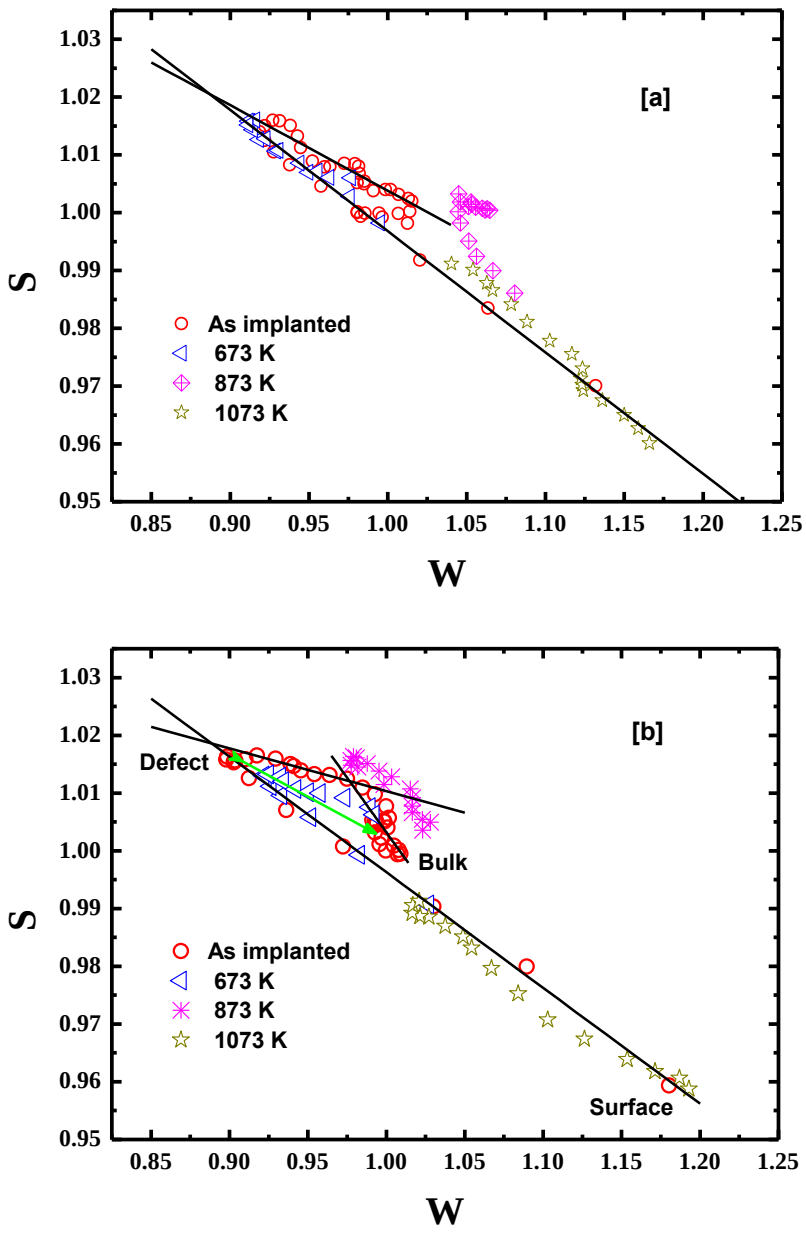

Fig.11: (a) S -W plot for as – irradiated (RT) and annealed samples (673 K, 873 K, 1073 K) for lower dose sample. The complete S-W correlation plot is given for as-irradiated sample with positron beam energy as running parameter. For other temperatures, only the inflexion or deviation points are shown for clarity (points from 1-8.5 keV). Different temperatures are identified in the figure by different symbols and colours. The black line is a linear fit to different energy regions identified in the text. (b) S-W plot for higher dose sample. The linear fits shown by black solid line identifies deeper defect in higher dose sample. The green arrow joins the inflexion point in as-irradiated state and at 673 K to the bulk S,W coordinate. The inflexion point corresponding to 873K lies outside of this showing a defect of different nature.

there is not much variation in S-parameter but there is an increase in W parameter. For lower dose sample there is reduction in S-parameter as well as an increase in W-parameter. Even at this stage it is not possible to identify the defect type. Adam et.al. [16] had defined the W parameter in two ranges from 513.3 - 514 keV (W1) and from 514.9 - 517 keV (W2), and assigned the first range to Nitrogen or Oxygen vacancy complexes and the latter to pure vacancies. By plotting the variation of W1 and W2 as a function of positron energy, it was argued that it was also possible to delineate between whether Nitrogen or Oxygen plays a role in the complex. If it was Oxygen – Vacancy complex, then W1 would be higher near surface due to the –OH terminated surface and would monotonically decrease towards bulk. If it were Nitrogen – Vacancy complex then there would be a constant value near the damaged region beyond which it would decrease towards bulk. In a similar fashion the W1, W2 parameters for as-implanted and sample annealed to 873 K for both higher and lower dose is given in Fig.12 (a) and (b). As seen in Fig.12 (a), W1 for as implanted sample shows a decrease from the surface to the bulk value. On annealing to 873 K, a large increase is seen in W1 value near the implanted region. Thus the small hump seen near 2 - 4 keV energy in S versus E plot in Fig. 7 (a) correspond to formation of N-V complexes. These would most probably be in V_2-N_2 format as V_2 is easily formed in Silicon during migration of monovacancies as well as by breakage of vacancy clusters and Nitrogen exists mostly as di-interstitial in Silicon. However such a large increase is not seen in higher dose sample after annealing up to 873 K. Hence, looking at high S-parameter near surface for higher dose sample at 873 K in Fig. 7 (b), the variation of (S, W) coordinate corresponding to 873 K in Fig. 11(b) and a small increase in W1 in Fig. 12 (b), two possible scenarios can be seen. In one scenario there can be a combined existence of both vacancy clusters and N-V complexes leading to higher S, deviated (S,W) coordinates and marginal increase in W1.

The second scenario being the formation of V_x-N_2 (x>2) which give rise to more of vacancy like signal with larger S-parameter, but also giving rise to deviated (S,W) coordinates and marginal increase in W1.

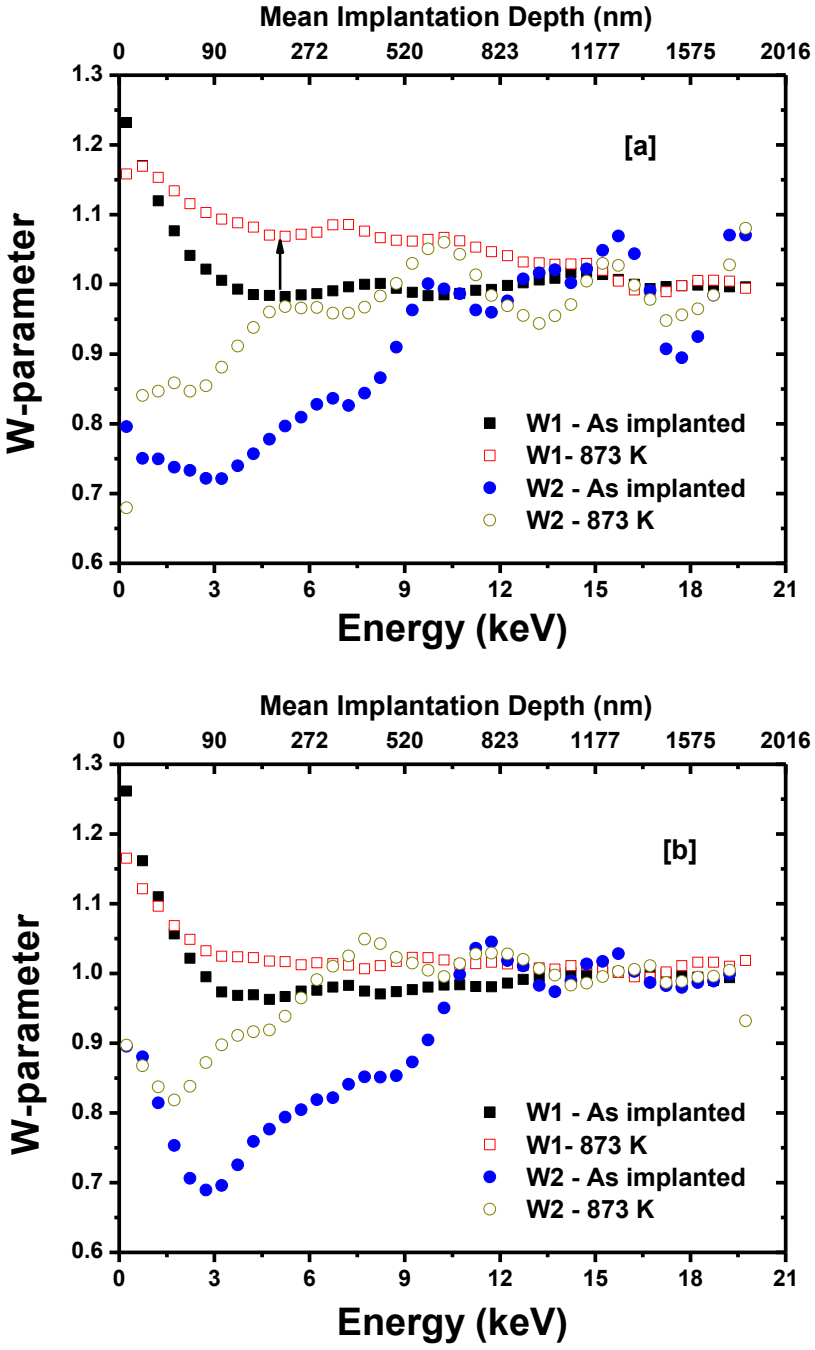

Fig.12: (a) W versus Energy plot for as – irradiated (RT) and annealed samples at 873 K for lower dose sample. W1 is defined between 513.3 to 514 keV and W2 is defined for 514.9 to 517 keV. Arrow mark indicates the increase in W1 parameter in the implanted region after annealing (b) W versus Energy plot for as – irradiated (RT) and annealed samples at 873 K for higher dose sample. Errors on both plots are equivalent to symbol size.

2.3.3 SIMS

The oxygen and nitrogen profiles for the low dose and high dose samples in the as implanted state and for those which were cumulatively annealed up to 873 K and 1073K are shown in Fig. 13 and 14 respectively. The oxygen profile for lower dose and higher dose sample validate the finding that for sample annealed at 1073 K, the oxide layer is wider for lower dose sample than that in higher dose sample. This is responsible for the lower than bulk S-value observed near surface in these samples. The oxygen profile grows into the sample only for a cumulative annealing for 60 minutes at 1073 K for higher dose sample where as it happens at the first 30 minutes itself for lower dose sample.

The nitrogen profiles given in Fig. 14 (a) and (b) are fit to single/double Gaussian peaks defined by the equation

$$y = y_0 + \frac{A}{w * \sqrt{\pi/2}} * \exp\left(-2 * \frac{(x-x_c)^2}{w^2}\right) \quad (3)$$

where y denotes the secondary ion intensity obtained as a function of depth, x gives the depth in nm, x_c gives the centroid of the Gaussian profile (in nm) and w is the standard deviation (nm). A is the amplitude of the Gaussian peak. The parameters obtained after fitting are given in Table 1. The nitrogen distribution for higher dose sample shows a non-symmetric movement towards surface at 1073 K and it alone has been fit to two Gaussian peaks. The difference in the peak position for lower dose sample when compared to the higher dose sample is due to the difference in acquisition area of secondary ions in the sputtered crater. The parameter variation was done to get reasonable counts for lower dose sample but has resulted in accumulation of data from the edge of the crater giving deeper nitrogen signals. This is also clear from the tailing

seen at higher depths for profiles obtained for lower dose samples. Comparison with the TRIM simulation data shows that the peak position values obtained for higher dose sample are close to the predicted values.

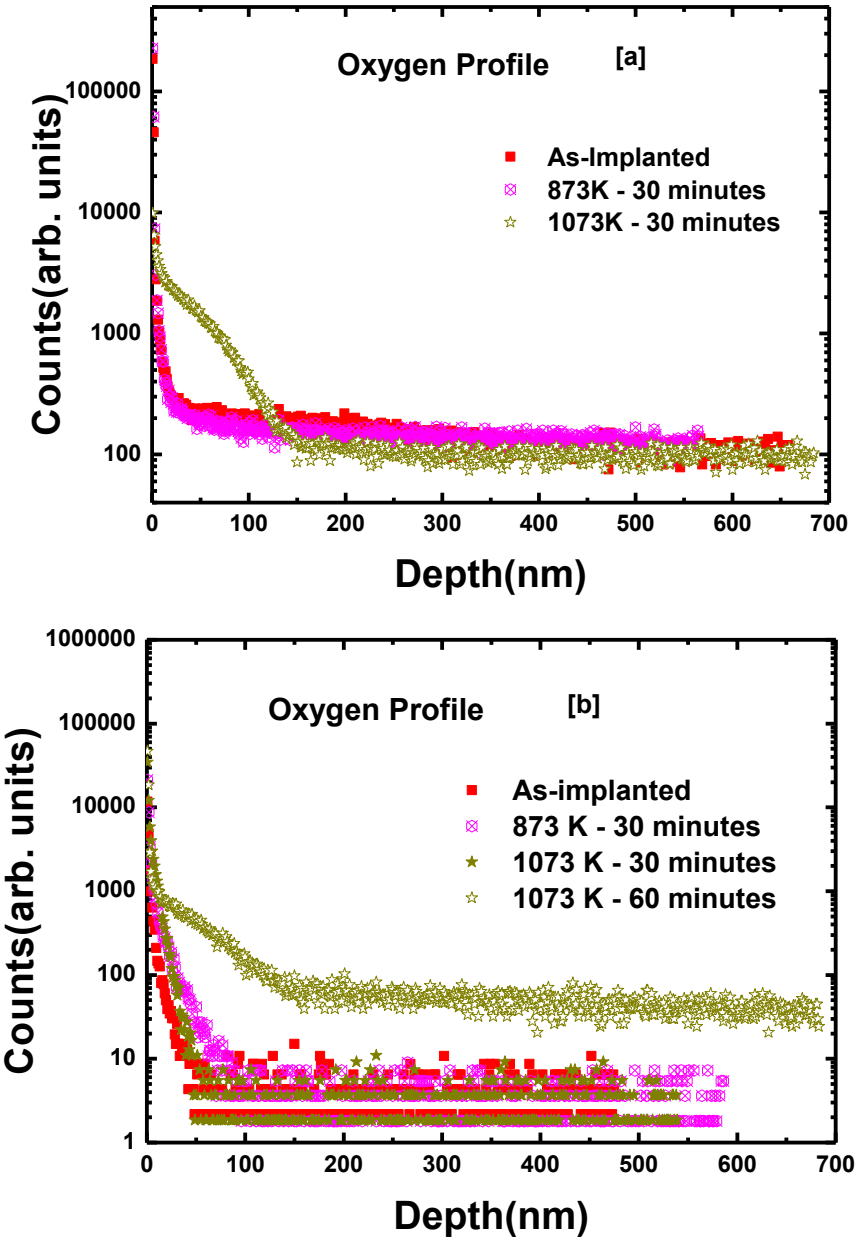

Fig.13: (a) Oxygen profile of lower dose sample in as – irradiated (RT) and 30 minute annealed samples at 873 K and 1073 K (b) Oxygen profile of higher dose as irradiated sample and those annealed at 873 K for 30 minutes, at 1073 K for 30 minutes and for 60 minutes.

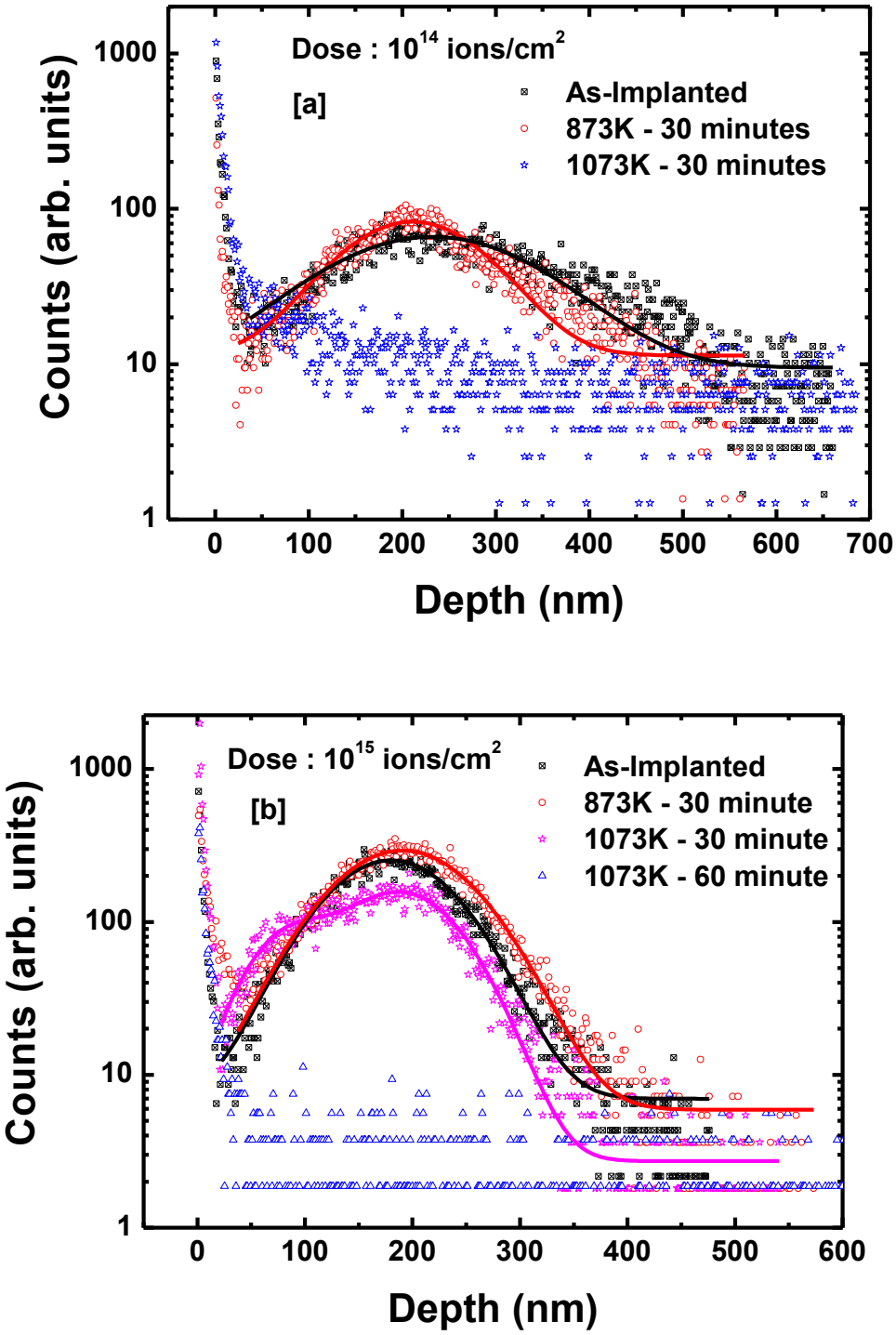

Fig. 14: (a) Nitrogen profile of lower dose sample in as – irradiated and 30 minute annealed samples at 873 K and 1073 K. (b) Nitrogen profile of higher dose as irradiated sample and those annealed at 873 K for 30 minutes, at 1073 K for 30 minutes and for 60 minutes.

Table 1: Parameters of the Gaussian profile after fitting them to the intensity plot.

Implantation Dose N^+/cm^2	**Annealing Temperature K**	**Number of Gaussians**	**Centroid (nm)**	**w (nm)**	**Height (counts)**
10^{14}	As-implanted	1	232±1.7	211±5	56
	873	1	211±1	142±3	71
10^{15}	As-Implanted	1	180±0.6	114±1.3	246
	873	1	191±0.5	124±1.13	287
	1073	1	189±2	101.5±3	153
		2	85±3	75±4.5	73

Comparing the thermal evolution of nitrogen for each dose separately, certain key features come out. They are

(a) For lower dose sample, there is only a little change in the implanted nitrogen profile on annealing to 873 K. The profile shows a small shift of nitrogen peak to the surface at 873 K. There is also a small reduction in width of the profile and it happens mostly in the deeper region than at the surface. However at 1073 K nitrogen has got completely redistributed into the sample beyond the detection limit showing that there is a temperature barrier beyond which the diffusion is extremely fast.

(b) For higher dose sample, there is no movement of nitrogen till 873 K. Only at 1073 K it shows an anomalous diffusion towards surface. The peak at the implanted range stays fixed (~189 nm) with reduction in its peak intensity and marginal change in width. A new peak appears at shallower depth close to the surface. Annealing at the same temperature for 30 minute more has resulted in the redistribution as seen before for lower dose sample.

(c) From the Oxygen profile it is clear that in-diffusion of oxygen starts only at that temperature where the Nitrogen signals are in traces.

As the Nitrogen profile shows marginal or no change by annealing at 873 K, the formation of Nitrogen – vacancy complexes as indicated by the positron beam results, is formed during the migration of open volume defects towards surface. From the anomalous diffusion profile at 1073 K for higher dose sample, it is clear that the Nitrogen becomes mobile at deeper regions than at the surface. It was also shown in earlier studies that the end of range Type 1 defects act as pinning centres for the Nitrogen interstitials [20]. Hence, near surface Nitrogen-Vacancy complexes and end of range dislocation loops act as barriers for Nitrogen diffusion giving rise to the observed behaviour with nitrogen being released near the peak of the implanted profile. It was also shown from the positron beam studies that open volume defects are not present after 1073 K annealing and hence, this also signals the presence of barrier for release of Nitrogen from its pinning centres before this temperature. Further annealing at same temperature has caused the Nitrogen to be diffused towards the surface or has got redistributed homogeneously. For lower dose sample, the lower concentration of pinning centres has resulted in the complete removal of Gaussian profile by annealing at 1073 K for 30 minutes only. It is of interest to note that the removal of Nitrogen has a role in the in-diffusion of oxygen as indicated by the results in Fig.13, which requires further investigation.

2.4 Summary

The thermal evolution of open volume defects and nitrogen impurity in nitrogen ion implanted Cz-Si is investigated using slow positron beam spectroscopy and SIMS. The major findings are as follows

- The sample irradiated to a dose of 1 x 10^{15} ions/cm^2 showed the existence of deeper defects which are removed by annealing to 473 K. Such an annealing step is not seen in the case of sample irradiated to 1 x 10^{14} ions/cm^2. The deeper defects are attributed to E centres formed as a result of migration of monovacancies during the dynamic process of irradiation.
- Indirect evidence is obtained using S-W correlation plot as well as using modified W parameter definition for the formation of nitrogen vacancy complexes in lower dose sample. However for higher dose sample, the formation of such a complex is not significantly brought out. It is argued that the result would have been due to the coexistence of other trapping centres like vacancy clusters along with nitrogen vacancy complex or due to the association of Nitrogen with larger clusters. Hence, the presence of larger vacancy density masks the formation of N-V complexes [48].
- The Nitrogen diffusion is found to be anomalous and is assigned due to the presence of pinning centres near surface (nitrogen vacancy complexes) and at end of range (Type 1 defects) [20].
- Oxygen in diffusion starts after the removal of Nitrogen from the system.

2.5 Conclusion & Future Outlook

A detailed investigation has been carried out on the thermal evolution of Nitrogen implantation induced defects in Silicon using slow positron beam spectroscopy and SIMS. It was possible to identify the presence of trans-projected range defects in higher dose sample and nitrogen-vacancy complexes after annealing to 873 K. The anomalous Nitrogen diffusion was attributed to pinning centres near surface and at end of range.

The study has to be continued for higher doses where there are high concentration of dislocation loops and amorphisation to investigate the action of pinning centres and Nitrogen diffusion through an amorphous structure. Isothermal studies can be carried out at temperatures near ~ 873 K to find out the activation dynamics of the Nitrogen-vacancy complex formation and at temperatures less than 1073 K to carefully look at their thermal stability. The role of Nitrogen on the in diffusion of Oxygen has to be investigated in detail with regard to the role of open volume defects. Even though slow positron beam spectroscopy could throw more light into thermal evolution of open volume defects, it was extremely hard to pin point the nature of defects especially in the case of higher dose sample annealed to 873 K. A positron beam based lifetime spectroscopy would have given a quantitative identification of the type of defects responsible for the observed behaviour near surface.

References:

1. Chelyadinskii A R and Komarov F F 2003 *"Defect-impurity engineering in implanted silicon" Physics-Uspekhi* **46** 789.
2. Fahey P M, Griffin P B and Plummer J D 1989 *"Point defects and dopant diffusion in silicon" Rev. Mod. Phys.* **61** 289.
3. Liu C T, Ma Y, Becerro J, Nakhahara S, Eaglesham D J and Hillenius S J 1997 *"Light nitrogen implant for preparing thin-gate oxides" Electron Device Letters, IEEE* **18** 105.
4. Josquin W J M L 1983 *"The application of nitrogen ion implantation in silicon technology" Nuclear Instruments and Methods in Physics Research* **209-210** 581.
5. Liu C T et.al. 1998 *"Multiple gate oxide thickness for 2 GHz system-on-a-chip technologies" Electron Devices Meeting, 1998.* ***IEDM '98****. Technical Digest., International* 589.
6. Mitchell J B, Shewchun J, Thomson D A and Davies J A 1975 *"Nitrogen implanted silicon. II. Electrical properties" J. Appl. Phys.* **46** 335.

7. Alpass C R 2008 *PhD Thesis Department of Materials Oriel College University of Oxford.*
8. Graf D, Suhren M, Lambert U, Schmolke R, Ehlert A, Von Ammon W and Wagner P 1998 *"Characterization of Crystal Quality by Crystal Originated Particle Delineation and the Impact on the Silicon Wafer Surface" J. Electrochem. Soc.* **145** 275.
9. von Ammon W, Holzl R, Virbulis J, Dornberger E, Schmolke R and Graf D 2001 *"The impact of nitrogen on the defect aggregation in silicon" Journal of Crystal Growth* **226** 19.
10. Goss J P, Hahn I, Jones R, Briddon P R and Oberg S 2003 *"Vibrational modes and electronic properties of nitrogen defects in silicon" Phys. Rev. B* **67** 045206.
11. Yonenaga I 2005 *"Nitrogen effects on generation and velocity of dislocations in Czochralski-grown silicon" J. Appl. Phys.* **98** 023517.
12. Nakai K et.al. 2001 *"Oxygen precipitation in nitrogen-doped Czochralski-grown silicon crystals" J. Appl. Phys.* **89** 4301.
13. Graf D, Lambert U, Schmolke R, Wahlich R, Siebert W, Daub E and von Ammon W 2000 *"300mm Epi PP Wafer: Is there sufficient gettering?" Electrochem. Soc. Proc.* **2000-17** 319.
14. Mitchell J B, Pronko P P, Shewchun J, Thomson D A and Davies J A 1975 *"Nitrogen implanted silicon. I. Damage Annealing and Lattice location" J. Appl. Phys.* **46** 332.
15. Jones R, Oberg S, Berg Rasmussen F and Bech Nielsen B 1994 *"Identification of the dominant nitrogen defect in silicon" Phys. Rev. Lett.* **72** 1882.
16. Adam L S, Law M E, Szpala S, Simpson P J, Lawther D, Dokumaci O and Hegde S 2001 *"Experimental identification of nitrogen-vacancy complexes in nitrogen implanted silicon" Appl. Phys. Lett.* **79** 623.
17. Fuma N, Tashiro K, Kakumoto K and Takano Y 1996 *"Diffused Nitrogen-Related Deep Level in N-Type Silicon" Jpn. J. Appl. Phys.* **35** 1993.
18. Voronkov V V and Falster R 2006 *"Multispecies nitrogen diffusion in silicon" J. Appl. Phys.* **100** 083511.
19. Voronkov V V and Falster R 2006 *"Nitrogen Diffusion in Silicon: a Multi-Species Process" ECS Trans.* **3** 113.

20. Adam L S, Law M E, Dokumaci O and Hegde S 2002 *"Physical integrated diffusion-oxidation model for implanted nitrogen in silicon" J. Appl. Phys.* **91** 1894.
21. Taylor J W, Saleh A S, Rice-Evans P C, Knights A P and Jeynes C 1999 *"Depth profiling of defects in nitrogen implanted silicon using a slow positron beam" App. Surf. Sci.* **149** 175.
22. vander Werf D P, Saleh A S, Towner A, Nathwani M, Taylor J, Rice-Evans P C and Bull S J 1997 *"Defect Profiling with Low Energy Positrons of Nitrogen Implanted Silicon" Materials Science Forum* **255-257** 500.
23. Hao X P, Yu R S, Wang B Y, Chen H L, Wang D N, Ma C X and Wei L 2007 *"Slow positron beam study of nitrogen implanted Cz-Si subjected to rapid thermal processing" Appl. Surf. Sci.* **253** 6868.
24. Ziegler J F, Biersack J P and Littmark U 1985 *"The Stopping Range of Ions in Solids"* (New York:Pergamon).
25. Amarendra G, Viswanathan B, Venugopal Rao G, Parimala J and Purniah B 1997 *"Variable low energy positron beams for depth resolved defect spectroscopy in thin film structures" Current Science* **73** 409.
26. van Veen A, Schut H, de Vries J, Hakvoort R A and Ijpma M R 1990 *"Analysis of positron profiling data by means of VEPFIT" Positron Beam for Solids and Surfaces AIP Conf. Proc. No.* **218** ed Schultz P J, Massoumi G R and Simpson P J (New York:AIP) 171.
27. Clement M, de Nijs J M M, Balk P, Schut H and van Veen A 1996 *"Analysis of positron beam data by the combined use of the shape- and wing-parameters" J. Appl. Phys.* **79** 9029.
28. Benninghoven A, Rudenauer F G and Werner H W 1987 *"Secondary Ion Mass Spectrometry: Basic concept, Instrumental Aspects, Applications and Trends"* (New York: Wiley).
29. Asoka-Kumar P, Lynn K G and Welch D O 1994 *"Characterization of defects in Si and SiO_2 – Si using positrons" J. Appl. Phys.* **76** 4935.
30. Krause-Rehberg R and Leipner H S 1999 "*Positron Annihilation in Semiconductors: Defect Studies" (Springer series in solid-state sciences*) **127** ed Manuel Cardona et *al* (Berlin: Springer).

31. Pi X D, Burrows C P and Coleman P G 2002 *"Optimization of measurement parameters in Doppler broadening spectroscopy" Applied Surface Science* **194** 255.
32. Watkins G D and Corbett J W 1965 *"Defects in Irradiated Silicon: Electron Paramagnetic Resonance of the Divacancy" Phys. Rev.* **138** A543.
33. Cheng L J, Corelli J C, Corbett J W and Watkins G D 1966 *"1.8-, 3.3-, and 3.9-μ Bands in Irradiated Silicon: Correlations with the Divacancy" Phys. Rev.* **152** 761.
34. Dannefaer S, Avalos V, Kerr D, Poirier R, Shmarovoz V and Zhang S H 2006 *"Annealing of electron-, proton-, and ion-produced vacancies in Si" Phys. Rev. B* **73** 115202.
35. Fujinami M, Tsuge A and Tanaka K 1996 *"Characterization of defects in self-ion implanted Si using positron annihilation spectroscopy and Rutherford backscattering spectroscopy" J. Appl. Phys.* **79** 9017.
36. Poirier R, Avalos V, Dannefaer S, Schiettekatte F and Roorda S 2003 *"Divacancies in proton irradiated silicon: Comparison of annealing mechanisms studied with infrared spectroscopy and positron annihilation" Nucl. Inst. Meth. Phys.Res. B* **206** 85.
37. Makhov D V and Lewis L J 2004 "*Stable Fourfold Configurations for Small Vacancy Clusters in Silicon from ab initioCalculations" Phys. Rev. Lett.* **92** 255504; Makhov D V and Lewis L J, *"Two component density functional theory calculations of positron lifetimes for small vacancy clusters in silicon" Phys. Rev. B* **71** 205215.
38. Kawasuso A, Hasegawa M, Suezawa M, Yamaguchi S and Sumino K 1995 *"An annealing study of defects induced by electron irradiation of Czochralski-grown Si using a positron lifetime technique" App. Surf. Sci.* **85** 280.
39. Eichler S, Gebauer J, Borner F, Polity A, Krause-Rehberg R, Wendler E, Weber B, Wesch W and Borner H 1997 *"Defects in silicon after B^+ implantation: A study using a positron-beam technique, Rutherford backscattering, secondary neutral mass spectroscopy, and infrared absorption spectroscopy" Phys. Rev. B* **56** 1393.
40. Chilton N B and Fujinami M 1993 *"Evidence of deep vacancy formation in fluorine implanted silicon" AIP Conf. Proc.* **303** 25.

41. Simpson P J, Knights A P, Goldberg R D, Aers G C and Landheer D 1997 "*Intrinsic electric fields in silicon" App. Surf. Sci.* **116** 211.
42. Amarendra G, Venugopal Rao G, Arora A K, Nair K G M, Ravindran T R, Sekar K, Sundarvel B and Viswanathan B 1999 *"Study of argon irradiation induced defects and amorphization in silicon using a positron beam, Raman spectroscopy and ion channelling" J.Phys: Condes. Matter* **11** 5875; Amarendra G, Rajaraman R, Venugopal Rao G, Nair K G M, Viswanathan B, Suzuki R, Ohdaira T and Mikado T 2006 *"Identification of open volume defects in disordered and amorphized silicon" Phys. Rev. B* **63** 224112.
43. Uedono A, Tanigawa S, Sugiura J and Ogasawara M 1989 "*A Study of Vacancy-Type Defects in B^+-Implanted SiO_2/Si by a Slow Positron Beam" Jpn. J. Appl. Phys.* **28** 1293.
44. Uedono A, Tanigawa S, Sugiura J and Ogasawara M 1990 *"Vacancy-Type Defects in As^+-Implanted SiO_2(43 nm)/Si Proved with Slow Positrons" Jpn. J. Appl. Phys.* **29** 1867.
45. Abdulmalik D A, Coleman P G and Al-Qaradawi I Y 2006 *"Self-implantation of Cz-Si: Clustering and annealing of defects" Appl. Surf. Sci.* **252** 3209.
46. Abdulmalik D A and Coleman P G 2008 *"Activation energies for the formation and evaporation of vacancy clusters in Silicon" Phys. Rev. Lett.* **100** 095503.
47. Mantl S and Triftshäuser W 1978 "*Defect annealing studies on metals by positron annihilation and electrical resitivity measurements" Phys. Rev. B* **17** 1645.
48. Varghese Anto C, Abhaya S, Magudapathy P, Amarendra G and Nair K G M 2010 *"Depth profiling of vacancy defects and their thermal stability in N-implanted Si: a positron annihilation study" J. Phys. D: App. Phys.* **43** 325401.

Chapter 3

Thermal evolution of defects in self ion irradiated Highly Oriented Pyrolytic Graphite

The investigation of the defect kinetics in 200 keV C^+ ion implanted highly oriented pyrolitic graphite (HOPG) is presented in this chapter. The thermal evolution of implantation induced defects is probed using three techniques sensitive at different depth levels. The dependence of the defect annealing on the implantation dose is brought out by implanting HOPG at two doses – 10^{14} & 10^{15} ions/cm^2, the higher one close to creating amorphisation near the projected range. The topography of the sample as seen by Atom force microscope (AFM) becomes highly ridged for higher dose implantation. The ridged surface is considered to be due to basal plane fragmentation followed by bending and curling of the surface sheets along the preferred/random directions depending on the damage produced. Defect recovery at near surface region has a small effect on surface topography with curvilinear ridges showing highly intricate network after annealing. The defect annealing mechanism at the near-surface region probed by Raman spectroscopy shows a fast and a slow process for both the doses; however difference among two doses lies in the recovery of the FWHM of the G-band. The slow positron beam spectroscopy shows vacancy recovery from 373 K and a clear movement of open volume defect towards surface by 623 K for lower dose sample. A particular defect type becomes visible in higher dose sample after annealing up to 523 K near the end of implantation range. This remains stable till 673 K showing a surface bound movement only at 723 K. Complete defect recovery also leads to a modified structure consisting of cross linking inter layer interstitial clusters at the projected range. This is brought to light by a lower than bulk S-parameter for the recovered region.

3.1 Introduction

Defect study in carbon allotropic materials is an area which has seen large amount of investigations owing to their importance to the industry and to the basic understanding of solids. Among the various carbon allotropes, graphite and diamond are often used as model materials and the inferences obtained from them are extended to their more exotic forms. For example graphite is a prototype for sp^2 hybridized group and for structures which show a layered nature. Graphite has been used extensively in the nuclear industry and is among the proposed materials for plasma facing wall of fusion reactors. This is because of its excellent high temperature properties (like high melting point and thermal shock resistance), low activity after neutron exposure and low Z [1]. This in turn has fuelled extensive research on defects in graphite to understand and control the after effects of radiation damage. Property changes like basal plane contraction, the *c-axis* expansion, the Wigner energy release, and the changes in electrical and thermal conductivity limit their long term use [2, 3]. Ion or electron beam induced structural transformations and phase transformations in graphitic materials are another area which drives the defect research industry. There has been demonstration of irradiation induced transformation of graphitic forms to diamond [4, 5], welding of Carbon nano-tubes with electron irradiation and formation of carbon onion structures [6]. The recent discovery of defect induced magnetism [7] and suggestions of doping/defect induced room temperature (RT) superconductivity in graphite [8, 9] has attracted the interest of basic physics fraternity as well. Ion beam based patterning of graphite surface is a major research area which seeks to understand and utilize the arrangement of defects on graphite surface as it is a common substrate for the growth of nanostructures and for various microscopic techniques [10, 11]. By extending the knowledge obtained about the

nature of defects on graphite surface, the electronic interaction of defects in 2D-graphene plane with electrons are now understood and are predicted to be magnetic [12].

In spite of all the effort over past five decades, the nature, formation, migration and interaction of even simple point defects like vacancies and interstitials in graphite remain sketchy. This is largely due to the highly anisotropic nature where different behaviour dominates parallel to the *c-axis* and that along the basal plane. Theoretical studies have predicted number of possible defect structures to explain the experimentally observed property changes and measured migration energies. To highlight one such discrepancy; the measured migration energy is ~ 3.1 eV for mono vacancies whereas the theoretically predicted value is ~1.7 eV [3]. The experimental investigations of defects in graphite has depended on Raman spectroscopy, Transmission electron microscopy (TEM), Scanning Tunnelling microscopy (STM), Atomic Force microscopy (AFM), Electron Paramagnetic Resonance, Ion Beam Analysis techniques like Rutherford back Scattering (RBS) and Channelling, Secondary Ion mass spectrometry and rarely on Hyperfine Interaction techniques. Many of these techniques are constrained by the fact that they are not directly defect related and depend on some property change with damage creation. Techniques like STM has been extremely successful in imaging mono vacancy structures on graphite surfaces, however difficulties arise in analysis due to probe-defect interactions or scan rate dependence etc. TEM studies on the other hand bring in sample preparation uncertainties as well as defect structure modification by the impinging electron beam. Hence there remains substantial uncertainty leaving space for further investigations using defect specific and non-interacting techniques.

Positron annihilation spectroscopy which is sensitive to vacancies or open volume regions in a material can be utilized to understand the atomic vacancy evolution in graphite effectively. This is achieved by self-probing of open volume defects by

positrons within its thermal diffusion length. In defect free graphite, the positron density distribution has a quasi two dimensional nature with the positron density being confined mostly to the inter-layer region .With the creation of vacancy type defects, this two dimensional confinement changes to specific trapping at the defect site. This results in variations in defect sensitive parameters like momentum distribution and positron lifetime [13, 14]. Hence, in the present investigation slow positron beam spectroscopy is utilized to understand the thermal evolution of vacancy like defects in graphite and thus try to bring out the dependence of thermally activated vacancy reactions on the type and density of defects produced. In the subsequent section we look at studies on different defect species in irradiated graphite and the understanding developed on the defect energetic in past six decades.

3.1.1 Literature Review

Ion implantation results in the deposition of the kinetic energy of the impinging ions on to the lattice and a cascade follows which results in the formation of lattice disorder and defect species like the Frenkel pair along the track of the implanted ion. At sufficiently high doses these disordered regions overlap and finally a non-crystalline or amorphous layer is formed [15]. This disorder can be recovered or relaxed by thermal annealing process. A large scatter in literature is observed in the proposed annealing processes, involved defect structures, their activation energies and temperatures of occurrence. Hence, some of the important studies are highlighted as shown in Table 1.

Table 1: Various annealing processes, defect structures involved, temperatures of occurrence and important remarks from literature. V,*v*- vacancy, I/*I*- interstitial, *a* – basal plane lattice vector, *c* –lattice perpendicular to basal plane, m-migration, 2D/3D →dimension. Red and Black denote experimentally determined values. Green and Blue are from ab-initio/theoretical calculations. α, β are un-equivalent sites in the unit cell.

Process/Defect structures assigned by authors	**Activation energy/ Temperature of occurrence/ Important Findings.**	**Authors**
V migration	**$E^m_{v,a}$ = 3.1 eV $E^m_{v,c}$ >5.5 eV**	[16,17]
I-V recombination	**$E_{barrier}$ = 0.24 eV. Occurring till 1523 K**	
I release from traps, weakly bound I-groups	**$E_{binding}$ = 1.2 – 1.7 eV.**	
I_2 (dimer) = 2I	**$E_{activation}$ > 1.2 – 1.7 eV. Hence cannot be a player in Wigner Energy release**	
Wigner Energy Release	**473 K, $E_{activation}$ = 1.2 – 1.7 eV**	
I-group migration and coalescence – nucleation of I-loop	**$E_{activation}$ = 1.17 eV.**	
V_2 (di-vacancy)	**Collapses to edge dislocation dipole or vacancy line.**	[18]
I migration	**$E^m_{I,a}$ = 0.45 eV**	
I binding to trap	**$E_{binding}$ = 1.38 eV, 473 K release from trap followed by I-V recombination.**	
V migration	**$E^m_{v,a}$ = 3.1eV $E^m_{v,c}$ > 5.5eV $E_{formation}$ = 7eV**	[19-20]
I migration	**$E^m_{I,a}$ < 0.1 eV, $E^m_{I,c}$ > 5 eV $E_{formation}$ = 7eV**	
I-loop/V-loop disappearance	**$E_{activation}$ > 8 eV**	
I migration (followed by I-V recombination)	**0.89 -1.0 eV, fast annealing second order process from 388 K**	[21-31]
I_2 migration (assisted I_2 – V recombination)	**1.8 eV, slow annealing process**	
V,I clustering/ Cluster migration	**>>1.8 eV. Slowest annealing process**	
I migration	**$E^m_{I,a}$ = 0.15 eV, > 573 K. Responsible for 2D-regrowth**	[15,32-36]

2D – re growth	**1773-2573 K, 0.67 eV**	
3D – epitaxial re growth	**> 2573 K, 0.78 eV/1.2 eV**	
c-axis random re growth	**1773-2573 K, 0.47 eV**	
I migration	$E^m_{I,a}$ **= 0.39 eV, >220 K**	[37-40]
V migration	$E^m_{v,a}$**= 3.1 eV, >1273 K**	
I-V recombination	$E_{barrier}$ **= 0.5 eV**	
I migration (followed by weak I-V pair and I-I pair formation in two annealing steps).	$E_{activation}$ **= 0.027 eV, 5-15 K & 0.05 eV, 15-45 K**	[41-53]
I (migration-long range – dispersion of weak pairs).	**0.09-0.11 eV, 45-65 K**	
I (migration-long range, trapped by stronger I-V and I-I pair)	**65-85 K**	
I-V pair → I + V I+I → I_2 / I-I pair	**0.27 eV, 85-125 K, at 100 K strong stored energy release peak & 0.40 eV, 120-180 K**	
n*I_2 → $(I_2)_n$ I+I → I_2 I_2 - 2V , I – V recombination	**0.55 eV, 165-230 K & 230-400 K**	
$(I_2)_2$ →2I_2 (rate limiting) I_2 - 2V recombination I_2+ $(I_2)_2$ → $(I_2)_3$ I_2+ $(I_2)_3$ → $(I_2)_4$	**1.34 eV, 448-513 K**	
$(I_2)_3$ →3I_2 (rate limiting) I_2 - 2V recombination I_2+ $(I_2)_3$ → $(I_2)_4$	**1.50 eV, 473-543 K**	
$(I_2)_4$ →4I_2 I_2 - 2V recombination	**1.78 eV, 533-593 K**	
I migration (Molecular Dynamics)	**0.01 eV**	
V migration to cluster/ loop formation	**> 1473-1573 K**	
Vacancy loop disappearance	**>1773 K**	
small I clusters→ large I	**373-773 K**	

clusters **I clusters break down →I, followed by I-V recombination** **I-loop disappearance**	**873-1173 K** **1473 K**	
Twin formation and Amorphisation **I migration (I-V recombination)** **I_2 migration**	**0.03-0.3 eV** **0.33 eV** **2 eV**	[54-66]
Disorder region growth (rate limiting factor is I migration)	**0.014 eV**	[66-70]
V migration **V_6**	**>1573 K** **Stable up to 1773 K**	[13]
V migration	**< 873 K**	[71]
V migration	**< 673 K**	[72]
V migration	**>348 K, 0.9-1.0eV**	[73]
I migration	**0.44 eV**	[74]
V migration	**1.6 eV**	[75]
V migration **I migration**	**$E^m_{v,a}$ = 1 eV $E^m_{v,c}$ = 4.7 eV** **$E^m_{I,a}$< 0.03 eV $E^m_{I,c}$ = 3.9 eV/2.3 eV** **(interstialcy mechanism)**	[76]
I migration	**> 1.4 eV**	[77]
Adatom migration	**0.47 eV**	[78]
Adatom migration **V migration**	**0.4 eV** **1.3 eV**	[79,80]
V migration **V→V_2 (5-8-5)** **V_2→V_2 (555-777)** **Adatom migration**	**0.94 eV** **1.6 eV** **5.74 eV** **0.4 eV**	[81]

I (A-ground state, B-barrier state, C-metastable state)		[82]
I (A-B-A) migration	**1.2-1.7 eV *(a-axis)***	
I(A-B-C) transition	**0.9 eV, 800K**	
I (B-C-B) migration	**0.5 eV *(c-axis* possible for irradiated HOPG)**	
I (c-axis migration along B-C-B, *aa*-stacking)	**0.7 eV (possible for irradiated HOPG)**	
Adatom migration	**0.84 eV**	
I migration	**1.27 eV *(a-axis)***	[83, 84]
	0.53 eV(sub-surface – *a-axis*)	
	0.42 eV(sub-surface – *c-axis*)	
V migration	**1.44 eV *(a-axis)*, 0.99 eV *(a-axis, on graphene)***	
V_2 (inter planar) migration	**3.2-3.5 eV**	
I-V pair recombination	**1 eV (perfect graphite)/ 0.5 eV (sheared)**	
	1.23 eV(sub-surface)	
V migration	**1.26eV*(a-axis)*, 1.37 eV *(a-axis*, on graphene)**	[85]
V→V_2 (5-8-5)	**2.17 eV**	
I migration(bridge)	**0.36eV*(a-axis)*, 0.53 eV *(a-axis*, on graphene)**	
I migration(spiro)	**2.12 eV**	
I(spiro)→I(bridge)	**1.88 eV**	
I-V_1 → I-V_2	**0.9 eV**	[86]
I-V_1 recombination	**>350K**	
I (C-dumb bell structure)→I (bridge)/I migration through this inter conversion	**0.9 eV *(c-axis migration)***	
V migration	**1.7 eV**	[87-96]
V_2 migration (in-plane)	**7 eV**	
inter-planar V_2 migration	**3.2-3.6 eV (inter conversion of various types or de trapping of V)**	
I-V pair recombination barrier	**1.4 eV**	
I (spiro) migration	**~1eV**	
I_2→I	**3 eV**	
$V_2^{3(trans)}$ third neighbour planar divacancy in –trans form migration	**2.8 eV**	
$V_2^{3(trans)}$→ V_2 (planar)	**3.5 eV**	

Thus the vacancy migration barrier has values from 0.90 – 3.1 eV and activation from temperatures as low as 348 K to as high as 1473 K. Similarly the interstitial migration has values from 0.027 eV – 2.1 eV. The defect annealing mechanism is also complicated

by large number of stable and meta stable structures possible for vacancies and interstitials. This is due to the property of C-atom to bind in different forms (sp to sp^3). There is also a difference in defect energetics near to surface and away from it influencing the experiments which are surface sensitive or bulk sensitive. The scatter is also due to different type of implantation conditions used like species and temperature. Yet certain generally accepted features can be brought out from the literature surveyed.

- It is now accepted that there is a recombination barrier between interstitial (I) and vacancy (V) and this stems from the existence of I-V meta stable state which has been experimentally shown [97]. It is also accepted that since Wigner energy peak at 473 K is due to I-V recombination, the meta stable state has a role in it.
- There is large evidence theoretically and some experimental proof that the migration barrier for vacancy along basal plane is not 3.1eV but much lower.
- Though there is no consensus on migration energy of interstitials, there is a wealth of evidence pointing to recovery taking place from temperatures as low as 10K. Hence if a higher migration barrier for I is correct, the observed low temperature recovery needs explanation.
- Once they are mobile, interstitials do cluster to form I_2 as they are more stable.
- V_2 (first nearest neighbour planar) is immobile with very high migration energy. There seems to be evidence in favour of barrier for divacancy formation from aggregation of monovacancies. Hashimoto et.al [98] has seen through HRTEM three single vacancies in the nearest neighbour position, yet stable enough not to form higher clusters (di- or tri-).
- There is a mixed phase hybridization (sp^2-sp^3) developed due to bridging, bending and cross linking of the adjacent layers.
- Annealing mechanism has a dependence on the amount of damage produced.

In spite of a certain level of understanding as mentioned above, the basic methodology of defect recovery remains vague from the activation numbers mentioned above. A positron based study could clarify some of the discrepancies as they are vacancy specific and non-destructive.

There has been previous studies which have utilized positron lifetime technique to identify the nature of bulk defects formed by electron or neutron irradiation in graphite [13, 51-53]. But to our knowledge the only experiment which looked at the vacancy profile and its annealing in a depth resolved manner using positron beam was by Yang et.al. [99]. They used beam based positron lifetime and Doppler broadening spectroscopy to identify the defect structures produced by RT irradiation of HOPG samples with 70keV $^{12}C^{+}$ ions to a fluence of 10^{15} ions/cm^2 and to understand their thermal recovery. From depth resolved lifetime values (obtained by simple lifetime decomposition with no larger lifetimes) they had concluded that the major defect produced is of V_6 type with some V_9 clusters very near to the surface and V_4, V_2 & V_1 near the implantation range where V_n represent n-vacancies clustered together. They found that when annealed to 373 K, all defects except V_1 had moved out and that by 473 K through I-V recombination even the single vacancies have been removed. They assumed that the larger clusters were formed due to the agglomeration of mono vacancies during the dynamics of irradiation. These results were correlated with the disappearance of ferromagnetic behaviour up to ~75% by 373 K and complete disappearance by 473 K. V_1, V_4 (some stable structures) and V_6 were found to have a net magnetic moment through spin averaged VASP calculations. They argued that for a particular vacancy concentration, the deformation field surrounding the vacancy was larger than the separation between the vacancies and that helps in local magnetic coupling with electrons transferred between two in-equivalent atom positions in 2D graphite. They

ruled out Hydrogen-Vacancy complexing in their samples through the observed positron lifetime. There was a discrepancy though in their Doppler broadening data which showed larger S-parameter (defect sensitive) even at 473 K and complete defect recovery only by 773 K where S-parameter values were lower than that in the un-implanted reference samples. This discrepancy was said to be due to complex defect structures with higher lifetimes, not visible in slow positron beam lifetime measurements though reflecting in S-parameter measurements. However it has to be pointed out here that the highest lifetime measured in graphitic samples was ~ 477 ps in glassy carbon [51].

There are other studies which used similar irradiation conditions as used in the present chapter. One such study utilised RBS in channelling mode on HOPG samples irradiated with 230 keV $^{12}C^{+}$ ions to a dose of $10^{15}/cm^{2}$. The recovery of the damaged region as a function of isochronal heat treatment was followed [36] and is given here in Fig.1 (a) and (b). Fig.1 (a) contains data from samples annealed up to 1373K for 20 minutes and Fig. 1(b) contains samples annealed up to 2573K. It can be seen that even for annealing temperatures at 573K there is a recovery from the surface region as well as a small epitaxial re-growth from the back interface. Major change at the projected range is observed only for annealing above 1373K as shown in Fig.1 (b).

This results shows that the sample is highly disordered at the projected range but only to a lesser extent near the surface. The annealing taking place for temperatures up to 2573K was assumed to be due to migrating interstitials resident between the graphite planes. By making an Arrhenius plot of the re-grown interface in this temperature regime, the activation energy was deduced to be around 0.15eV and hence the assumption that the interstitials play a major role was justified. It was also found that in this regime, the growth is diffusion limited and as soon as the growth reaches the highly

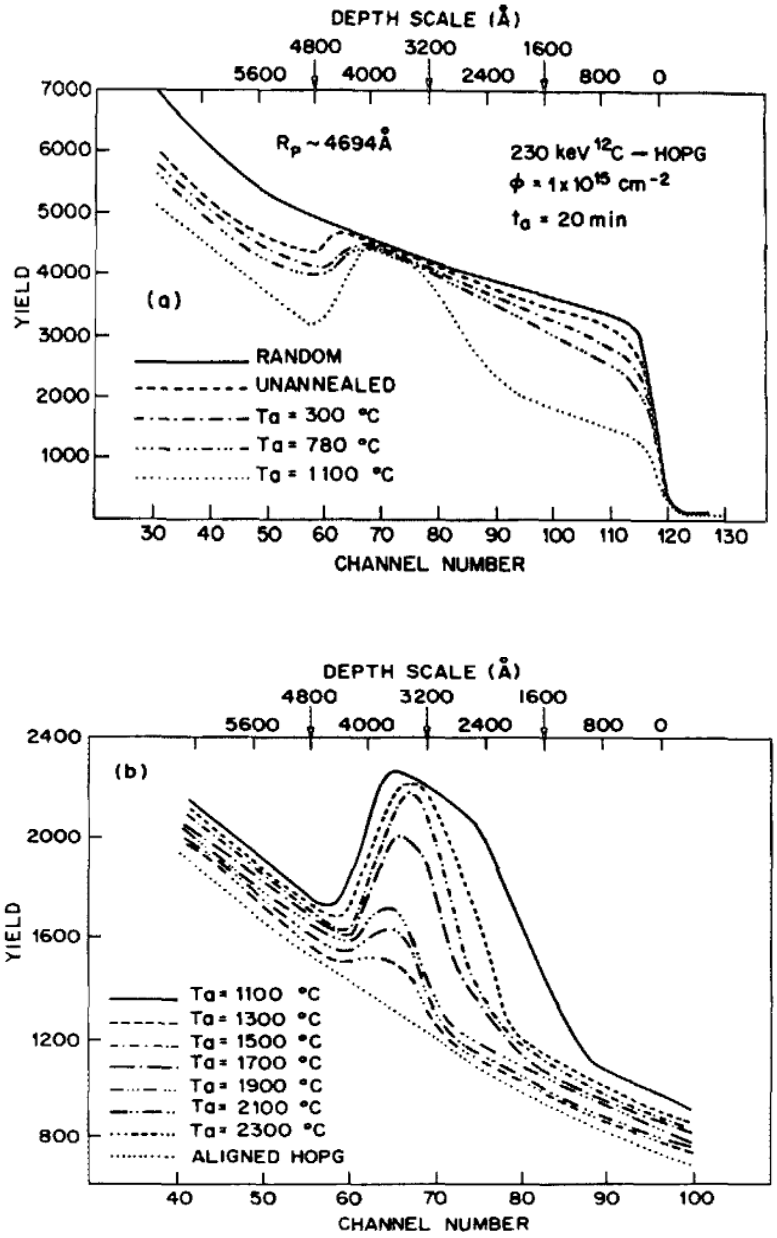

Fig.1: Back scatter yield from channelling study on samples irradiated with 10^{15} $^{12}C^{+}$ ions/cm^2 and annealed between (a) 573-1373K and (b) annealed between 1373-2573K. Reproduced from [36].

disordered region, the kinetics becomes complicated and is not dominated only by diffusion or by epitaxial re-growth. For the epitaxial 3D growth occurring in temperatures above 2573K, the activation energy was found to be ~ 1.2 eV. Such a small value was explained by an epitaxial recovery mechanism with crystalline substrate (the

crystalline region below the damaged surface) providing the nucleation sites and/or due to the presence of oriented crystallites even in highly damaged top layer.

Annis et.al. [74] utilized 165 keV C^+ ion irradiation at various doses from $6x10^{13}$ ions/cm^2 to $3x10^{15}$ ions/cm^2 to understand the surface damage creation mechanism and identified two type of defect feature at higher doses – rectilinear ridges running across the HOPG surface and highly networked and curvilinear ridges. Since the energy and dose are similar to the present investigation, images from the study are reproduced here which shows both type of ridge structures mentioned above in Fig. 2 (a-c).

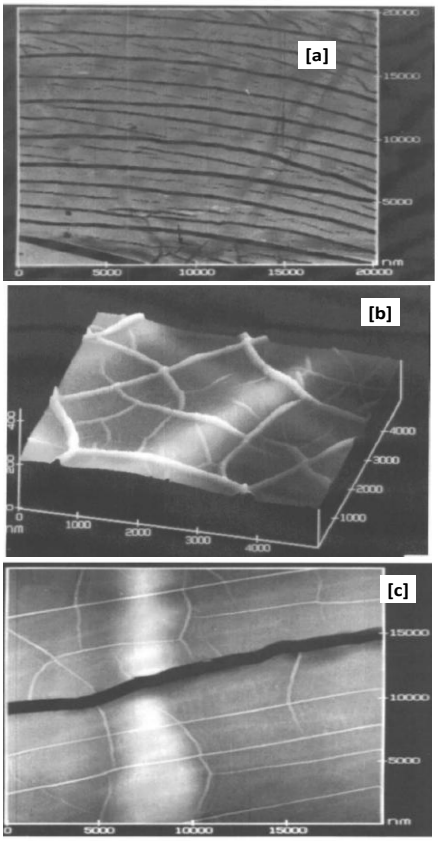

Fig.2: AFM images from two regions of sample irradiated to (a & b) $3x10^{15}$ ions/cm^2 and (c) to $6x10^{14}$ ions/cm^2 with 165 keV C^+ ions. (Reproduced from [74]).

Their study showed that for all the doses used, patches of ordered basal plane remained on the sample surface and that it maintained the crystallinity to give the corresponding Raman features. They argued a possibility of buried amorphous layer for

the highest dose implantation after comparison with a sample irradiated to same dose, at the same rate but with 35 keV ions. For lower dose sample (< $6x10^{14}$ ions/cm^2) they observed patches of disordered as well as normal structures. Linear defects in $\langle 10\bar{1}0 \rangle$ direction which were associated to a line of eight vacancies were seen in the lower dose samples. Apart from this surface protrusion which is a few nano-meter high was also observed and was assigned to interstitial clusters below the surface layer and to fragmentation and rotation of basal plane. The latter was assumed to provide easy migration path for the interstitials across the c-axis. For higher doses, dendrite like cracks were seen and some of them were deeper than the implantation depth. This was explained to be due to heavy contraction near surface layer by fragmentation or by vacancy collapse resulting in large amount of stress. The stress is released by cracking along the crystal direction and/or along the weak spots like grain boundaries. For the highest dose they observed ridges or wrinkles on the surface where one set was rectilinear possibly along $\langle 10\bar{1}0 \rangle$ direction and the other curved. No twin boundaries were associated with these ridges though such identification had been done earlier [54,55]. Calculating the number of carbon atoms in the ridges and its surface coverage, they argued that migration energy of 0.44 eV would be required to carry interstitials (part of Frenkel pair) from the bulk to the surface. This as argued earlier was aided by the fragmentation of the basal plane leading to easy migration path. The carbon atoms thus reaching the surface could accumulate at the fragment intersections (stress centres) and the ridges grow. In the initial stage of irradiation fragmentations occurs along crystallographic directions and thus explain the linear ridges. As dose increase fragmentation becomes random and this could explain the curvilinear random ridges seen. Another possible mechanism that they proposed was basal plane slip like tectonic plate movement giving rise to observed ridges preferentially along the step edges.

High resolution TEM (HRTEM) studies on certain forms of graphite (graphene, CNT etc.) have helped in identifying & understanding the dynamics of some of the exotic defect species possible in graphite. Hashimoto et.al. [98] had showed the existence of pentagon-hepatagon Stone Wales defect on a SWNT after electron irradiation. They had also identified up to three single vacancies lying next to one another showing that damaged region is more prone to further damage than the undamaged region and that there is a possible barrier for clustering to higher vacancies. While searching for adatoms on single walled CNT (SWNT) surface, they found three adatoms attached very close to a divacancy again giving evidence for I-V recombination barrier. The structure they assumed implied that the adatom migration energy is ~0.47 eV. Similar study by the same group [97] on double walled (DWNT) showed the existence of intimate I-V pair (one I with V or I with V_2 – it was not possible to distinguish between these two) after electron irradiation which was the first experimental identification of an inter-layer defect with partial sp^3 character. At low temperatures (~93K) clustering of vacancies and interstitials were observed due to knock outs near an earlier defect which did not get enough time to recover. Very important observation is that even for higher temperature they did not find much movement by interstitials or vacancies showing that the interlayer migration has higher barrier than surface atoms. By counting the number of I-V pairs at different irradiation temperatures, the energy dynamics of this particular defect was given which is reproduced below in Fig 3. There is a steep decrease in the number of I-V pairs formed with increasing irradiation temperature; however, a plateau is seen to occur beyond 473 K which is indicated by a broken line. The start of this threshold has closeness to the Wigner energy peak at 473 K.

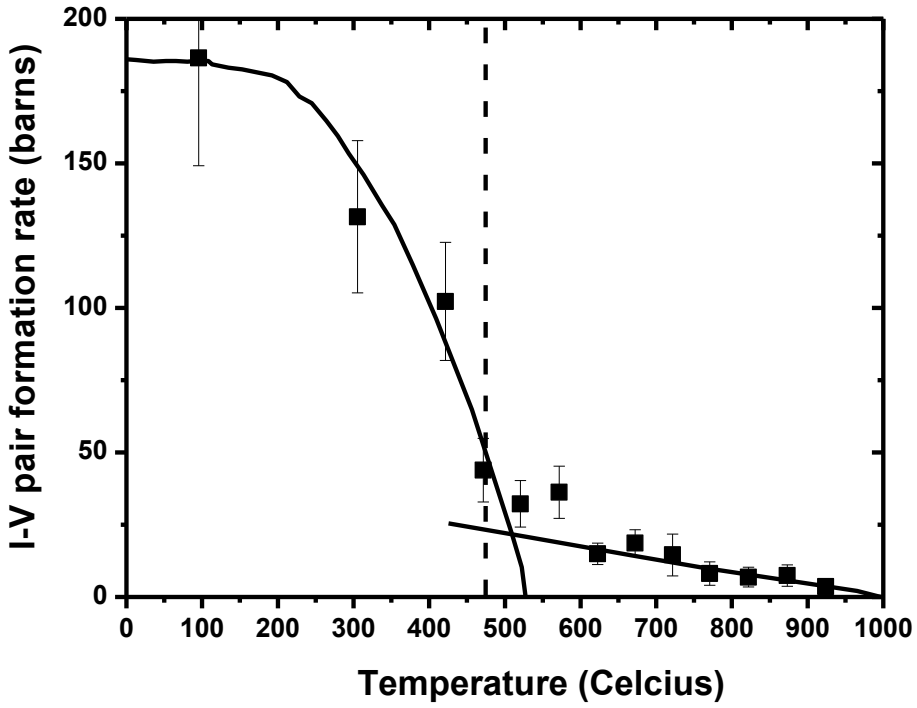

Fig.3: Number of intimate I-V pair counted for different irradiation temperature. (Reproduced from [97]).

By techniques which are sensitive at different depth levels a comprehensive know how on defect evolution can be built as given by the results above. Here channelling gives depth resolved information on the thermal evolution of interstitial (I) like defects, STM & AFM shows how surface structure develops through defects and TEM provides proof for specific nature of atomistic defects. In this scenario, the present study tries to throw more light into the annealing mechanism of vacancies using positron beam based Doppler broadening spectroscopic measurements on samples which are irradiated with $^{12}C^{+}$ ions of 200 keV energy along with Raman spectroscopy and AFM. Since Doppler broadening study is used, the defect structures at specific depths cannot be identified but the qualitative change with temperature will bring out the activation channels in the damage recovery and possible defect structures involved can be pointed out based on already existing activation energy data.

3.2 Experiments

Highly Oriented Pyrolytic Graphite Samples of SP-1 grades (equivalent to ZYA grade) were obtained from SPI supplies. This grade has very high crystalline order and exhibits properties close to single crystal graphite. The mosaic spread is as low as 0.4 ± 0.1^0 and the lateral grain size is usually higher than 1µm and can be typically up to 3mm. All the samples were freshly cleaved before implantation and the surface would consist of steps of several atomic layers with height of single step ~ 0.34 nm. The density is 2.27 g/cc and the samples were of dimension 10x10x1 mm. The impurity levels in the sample are at 10 ppm ash or better [100].

3.2.1 Carbon Ion Implantation

Carbon ions ($^{12}C^+$) were implanted into the samples using a 1.7MV Tandetron accelerator at IGCAR, Kalpakkam, whose details are given elsewhere [101]. In the present study, HOPG samples were irradiated at room temperature with 200 keV C^+ ions parallel to the *c*-axis to a fluence of 10^{14} and 10^{15} C^+ ions/cm^2. A beam diameter of 10 mm was used to get uniform damage across the sample. The beam current was kept around 55 nA to avoid beam heating of the sample. The beam energy was selected so as to be equivalent to a damage creation by a 1MeV neutron as well as have the damaged region inside the optical skin depth of 514.5 nm laser light. If a non–relativistic head on collision of hard spheres is considered, the maximum energy that can be transferred to a primary knock on atom (PKA) (T_{max}) is given as

$$T_{max} = \frac{4MM_pT_p}{(M+M_p)^2} \quad (1)$$

where $M = 12M_p$ mass of carbon nucleus and M_p is the mass of neutron with energy T_p. This amounts to about 300keV energy for PKA created by 1MeV neutron. The

particular ion was also chosen to avoid any impurity based effect during defect evolution. Keeping in mind the optical skin depth (~ 50-70 nm), a lower but closer value to 300 keV i.e. 200 keV was chosen. This is the minimum energy possible for singly charged carbon ions in this accelerator. The higher dose was selected to achieve a highly disordered region close to amorphisation near to the projected range and a lower dose was selected to look at the variation in defect evolution with damage density and defect type.

3.2.2 Vacuum Annealing

The implanted samples were annealed in a vacuum better than 10^{-6} mbar using a vacuum system described in section 2.2.2. The samples were cumulatively annealed for 60 minutes to different temperatures from 373 K to 773 K in steps of 50K. They were also annealed at 973K and at 1273K for the same time. The furnace is pre-heated to the required temperature and is inserted over the quartz tube containing the sample once the required vacuum is achieved. After the prescribed time, furnace is removed and the tube is quenched into liquid nitrogen bath to speed up the temperature drop. For all temperatures, the rise time and the fall time between 373 K and ~0.95*final temperature is less than 300 s. Relaxation below 373 K was shown to be very slow and for temperatures like 473 K, the fastest relaxation process had a characteristic time constant of ~450 s [30, 31]. Hence the processes occurring during the rise and fall time could be ignored compared to that at the set temperature. The set temperature was attained within an accuracy of $+5^{0}$C for all temperatures.

3.2.3 Slow Positron Beam Spectroscopy (SPBS)

Implanted and annealed samples were investigated with magnetically guided variable energy slow positron beam [102] in order to track the recovery of the damaged region of graphite surface with isochronal annealing and the role played by open volume defects in the process. The details of the slow positron beam as well as the defect characterisation methods are discussed in section 1.3.1 of chapter 1 and in section 2.2.3 of chapter 2. However for the sake of completion the parameters used for the present experiment are discussed here. The positron annihilation γ-spectrum from the sample was recorded using an high purity germanium detector having an energy resolution of 1.42 keV at 662 keV γ line of Cs^{137} with a shaping time of 6 μs in the spectroscopic amplifier. Around 3 x 10^5 counts were collected in the main peak (511±10 keV) at a count rate of 27 cps using this detector for annealing temperatures up to 473K. For higher temperatures, ~ 8.5 x 10^5 counts were collected in the main peak at a count rate of 450 cps. This rise in count rate was due to the installation of a new 50 mCi source into the beam line.

The Doppler broadening of the 511 keV annihilation γ ray is quantified, as described in 1.3.1, using a line shape parameter S and a wing parameter W (wing region of the peak is defined in this case as 513.5 to 518.5 keV and 503.5 to 508.5 keV). With the total counts in the main peak, central region and wing region, an error of < ±0.002 is expected for S parameter and an error of < ±0.0004 is expected on W parameter. VEPFIT [103] code is used to fit the experimental S vs Energy of positrons (E) data and give the fraction of positrons annihilating in various trapping centres as a function of depth as well as the S parameter corresponding to each trapping centre. It has to be specifically mentioned here that the positron beam direction was parallel to c-axis and the implantation depth of positrons given with each data is with respect to the c-axis.

Directionality is not important for the obtained S-parameter versus Energy spectrum for isotropic materials because of the three dimensional random diffusion of positrons post thermalisation. However in a layered structure like perfect graphite where there is a quasi 2D confinement and a pointed confinement at nearby defect sites, the obtained information is sensitive to lattice direction but with a resolution equivalent to positron diffusion length along the c-axis. When vacancies are created on the basal plane, the diffusion length reduces drastically to values equivalent to the inter-planar distance and hence the technique does become highly direction sensitive.

3.2.4 Positron lifetime spectroscopy

Unlike slow positron Doppler broadening spectroscopy, conventional positron lifetime spectroscopy gives quantitative information on the defect nature of the bulk of the sample. The lifetime of positrons inside the sample is proportional to the local electron density at the site of annihilation and hence variation induced in this by the formation of atomistic open volume defects can be quantified with characteristic lifetimes and their intensities. A brief theory of positron annihilation spectroscopy is covered in 1.3.1, though for sake of completion experimentally relevant points are discussed here. The experiment is carried out by placing a ^{22}Na source encapsulated 1µm thick Nickel foil in between two identical samples in the sandwich geometry and by using a fast-fast positron lifetime setup. The obtained positron decay spectrum is fit to multiple exponential decay schemes using LT9 [104] program which takes care of Gaussian resolution functions and subtracts the self-annihilation events from the source.

In the present study, two HOPG samples of the same grade (SP-1) were used for sandwich mounting. Around 10^6 counts were collected in the region of interest. The Gaussian resolution function and the contribution from source annihilations were found

using similar measurement on Silicon (100) single crystal. The data is fit to two components using LT9 and a variance close to 1 signals a very good fit.

3.2.5 Raman Spectroscopy

Raman spectroscopy is a powerful non-destructive technique to understand the symmetries and bonding nature of the solids. Through symmetry forbidden Raman lines and their intensities, it is also possible to understand degree of disorder of the system. Raman spectrum of various carbon forms provide specific signatures which makes it a most commonly used tool in the characterization of various allotropic and disordered forms of carbon like HOPG, diamond, glassy carbon, carbon fibres, carbon nanotubes, graphene, graphitic foams etc. [2, 105]. Raman spectroscopy is a powerful non-destructive tool in the case of ion implanted studies through the presence of crystallinity and defect specific modes such as the zone centre ($k=0$) E_{2g2} allowed mode of frequency shift 1582 cm^{-1} (G) and through the disorder induced double resonant modes at around 1360 cm^{-1}(D) and 1620 cm^{-1}(D'). Three dimensional correlations of the two dimensional graphene planes can also be tracked using the overtone mode at 2720 cm^{-1} (G'). The dispersive behaviour of the D and G' modes and the difference of the Stokes and anti-Stokes spectra are also used to understand the complexity of the double-resonant process.

As known, in Raman spectroscopy an intense beam of laser of frequency ω_0 is irradiated on to the sample. The scattered light consisting of the Rayleigh scattering part (ω_0) and the Raman scattered part ($\omega_0+\omega'$*-Stokes &* $\omega_0-\omega'$*-anti_Stokes)* is measured using a system consisting of light source, transmission optics and light counting system. As the intensity of stokes lines are greater than the anti-stokes ones, the characterization is usually carried out using the measurement of Stokes lines. Any measurement system consists of four major components (1) Excitation source (2) Sample illumination and

collection (3) wavelength selector and (4) Detection, acquisition and control system [106]. For the present measurements a Renishaw μ-Raman spectrometer was used, whose description is given elsewhere [107].

In the present measurement, a 50X objective lens at the microscope was used to illuminate the sample and the scattered light was accumulated normal to the sample in the backscattering geometry. The data was acquired for 120 s with a power of ~100 mW to have good signal to noise ratio. The spectral range was chosen from 100 cm^{-1} to 4000 cm^{-1}. The spot size was ~ 2μm. The Raman shift in wave number was calibrated using 520.5 cm^{-1} Raman line from Silicon single crystal. It should also be emphasized here that for a wavelength of 514.5 nm the optical skin depth is of the order of ~50 nm and hence, present Raman characterization would be looking at the tail of the implantation induced damage profile. The obtained spectrums was background corrected using linear fit at selected frequency ranges and the resultant spectrum was fit to multiple Lorentzians using PeakFit.

3.2.6 Atom Force Microscopy

The topography of the freshly cleaved pristine samples as well as that of implanted samples was mapped using NT-MDT Solver PRO atom force microscope. The measurement was done in the semi-contact mode using the standard silicon cantilever which is maintained at a constant force. The details of the instrument are given elsewhere [108]

3.3 Results

3.3.1. TRIM

The profile of vacancies produced by the implantation of 200 keV C^+ ions parallel to the c-axis is shown in Fig.4. This was generated using the monte carlo simulation package TRIM [109]. The displacement energy (E_d) required to produce isolated Frenkel pair (I-V) is taken to be 34 keV [3]. This will decide the number of vacancies/interstitials produced per ion.

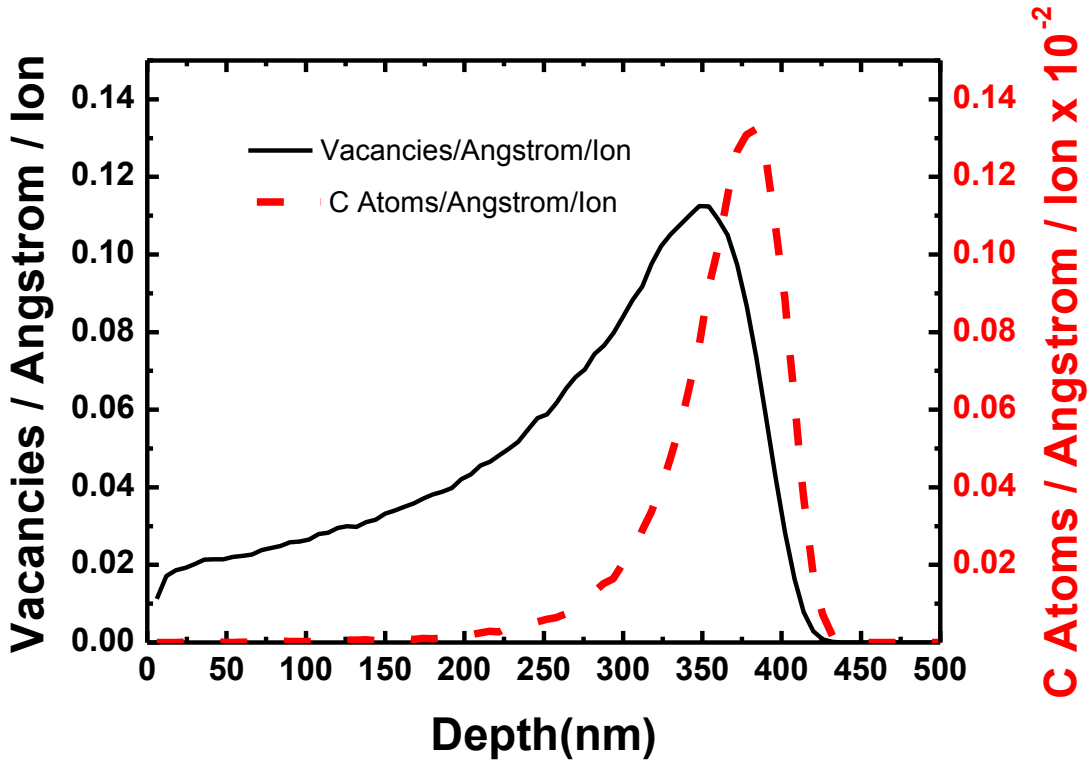

Fig.4: Profile of damage produced and implanted C^+ ions (200 keV) generated using TRIM [109]. The displacement energy was taken to be 34keV for implantation along *c-axis*.

The peak damage is predicted to be around ~350 nm deep and it is shown to extend till ~425 nm. The peak of the projected range (R_p) of the implanted C^+ ions is around 375 nm. Elman et. al.[15] has shown that the theory which is generally used for non-crystalline solids is applicable to a certain extent to a crystalline and layered material like graphite. Though some caution is required when taking the values generated as

absolute quantities because an amorphous structure proportional to the material density is assumed in this code and hence, certain features like channelling is not taken into account. It also doesn't allow for vacancy-interstitial recombination or structural relaxation to a new phase, since zero Kelvin calculations are performed. Hence, the damage predicted by TRIM is always overestimated [2].

The vacancies produced per ion (*Vpi*) is predicted to be 210 for the taken displacement energy. Since a 1 cm^2 beam was used, and as the damage extends till ~ 400 nm (as predicted by TRIM), the damage volume (V_d) can be taken as 4 x 10^{-7} cm^3. The atomic density (*N*) of HOPG is ~ 1.25 x 10^{23} atoms/cm^3. Therefore using relation

$$dpa\ (displacement\ per\ atom) = \frac{D}{N} = \frac{\varphi(Vpi)}{V_d N} \qquad (2)$$

where *D* is the total damage and φ is the fluence; the damage produced in dpa can be calculated. Hence for the fluence used here, 10^{15} and 10^{14} C^+ ions/cm^2 the damage produced is 0.04 and 0.004 dpa respectively.

3.3.2. Pristine HOPG

Atom Force Microscopy

Topography of the freshly cleaved pristine HOPG sample measured using AFM in semi-contact mode is given in Fig. 5. The topography looks mostly featureless with sharp multiple step edges due to cleaving. Large patches of graphitic basal planes with sizes > 3µm can be seen which coincides with the in plane crystallite size of >1µm as suggested by the supplier [100].

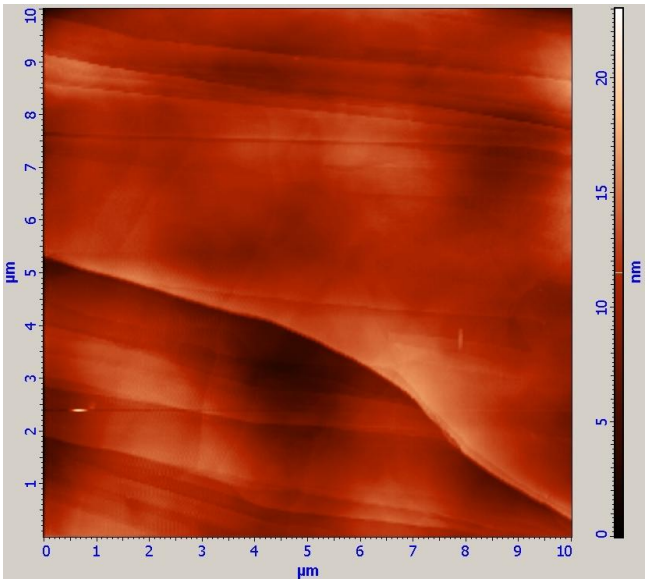

Fig.5: AFM image of pristine freshly cleaved surface of HOPG taken at semi-contact mode. The topography is mostly featureless with sharp step edges due to cleaving.

Positron Lifetime Spectroscopy

Positron lifetime measurements on as received freshly cleaved samples (2 nos) of HOPG SP-1 grade resulted in a lifetime spectrum as shown in Fig.6. The fit data and the deduced lifetime components are also shown in the figure. The obtained values are tabulated in Table 2. The spectrum could be fit to two components after fixing the resolution function and source correction. The values are very close to that obtained by Iwata et.al. [51] for Pyrolytic graphite annealed at 3273K for 4 hours.

The obtained lifetimes could be interpreted in terms of two – state trapping model. If τ_f is the defect free lifetime, λ_f the corresponding annihilation rate, κ_1 the specific trapping rate of a defect species, τ_2 the defect lifetime of that species, λ_d the corresponding annihilation rate then the bulk annihilation lifetime obtained by experiments would be

$$\tau_1 = \frac{1}{\kappa_1 + \lambda_f} \qquad (3)$$

where $\tau_f = \frac{1}{\lambda_f}, \tau_2 = \frac{1}{\lambda_d}$. The specific trapping rate κ_1 is related to the obtained intensities as

$$I_1 = 1 - \frac{\kappa_1}{(\kappa_1+\lambda_f)-\lambda_d} \tag{4}$$

and

$$I_2 = \frac{\kappa_1}{(\kappa_1+\lambda_f)-\lambda_d} \tag{5}$$

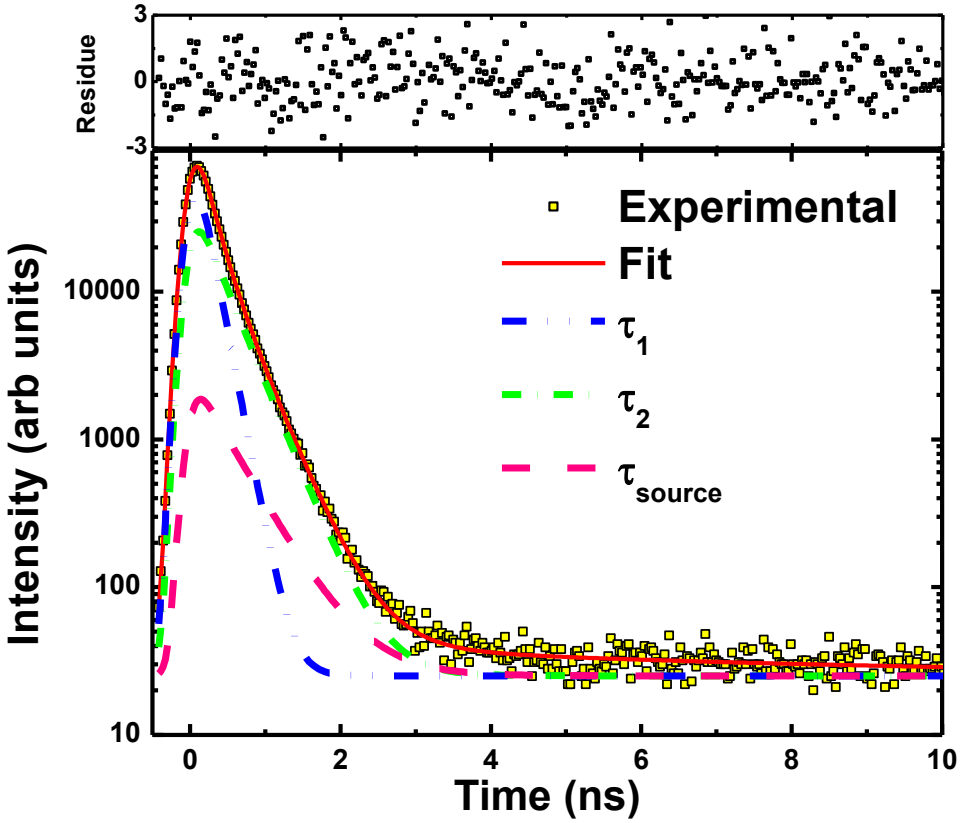

Fig.6: Positron Lifetime spectrums for pristine HOPG samples. Also shown are the fit line (solid red line), the lifetime components (blue dash dot dot and dash dot green line) and the source component (pink dashed). The residue of the fit is shown in the same time scale above.

combining these we can write τ_1 as

$$\frac{1}{\tau_1} = \frac{1}{\tau_f} + \left(\frac{1}{\tau_f} - \frac{1}{\tau_d}\right)\frac{I_2}{I_1} \tag{6}$$

Table 2: Positron Lifetime results for pristine HOPG samples. Probability for annihilation in trap is a measure of the crystalline quality [51].

Sample	**τ_1 (ps)**	**I_1 (%)**	**τ_2 (ps)**	**I_2 (%)**	**τ_{mean} (ps)**	**τ_1 (calculated) (ps)**	**Probability for annihilation in trap**	**Variance**
HOPG SP-1	**160±2**	**54±1**	**344±3**	**46±1**	**245±5**	**158**	**0.24**	**1.12**

The probability for annihilation in the trap (P_d) is given by,

$$P_d = \frac{\kappa_1}{\kappa_1+\lambda_f} \quad (7)$$

By assuming the bulk lifetime in highly oriented pyrolytic graphite as 210 ps [13], the calculated values of τ_1 is very close to the experimentally observed value showing that the two state trapping model works well for the as received samples. Therefore the pristine sample contain defect free crystallites with random *a- axis* orientation. The inter-crystallite surfaces act as effective trapping sites giving rise to the second component which is close to the surface state lifetime (350 ps) of HOPG [110]. The probability of annihilation is a measure of such trap sites i.e. of the area of the internal surfaces. Hence ~25% of the implanted positrons annihilate at these internal surfaces.

Slow Positron Beam Spectroscopy

S-parameter for the pristine samples shows a gradual decrease with increase in positron energy from a high S-value very near to the surface reaching the bulk S-parameter by 8keV as shown in Fig.7 (a). The high value at the surface is due to the phonon assisted positronium (Ps) formation and the relative Ps yield for 200 eV

positrons at 300K was shown to be as high as 16% [111]. They had also speculated that in HOPG, either the surface trap state is not present or the electrons sampled by the surface-bound positrons are very similar to those seen by interlayer positrons. They had calculated the energy at which the Ps yield falls off by half as 2.4 KeV. By fitting the S vs E data to a simple monolayer model using VEPFIT (description is given in 1.3.1), the diffusion length of positrons in graphite is found to be 209±11 nm, which is close to the value for Silicon (245 nm). The bulk positron lifetimes for both materials are also close (210 ps for HOPG and 220 ps for Silicon) and through the relation between diffusion length and bulk positron lifetime, the fit value looks good provided they have similar positron diffusion co-efficient at 300 K. This value is fixed for subsequent fits in irradiated samples for the defect free bulk layer. As there are no depth specific traps, the linearity of the S-W correlation plot as given in Fig.7 (b) is conserved. Hence, this can be used to look at defects at specific depths in irradiated samples. The error bar on S and W parameter are also provided in the S-W correlation plot, to identify the specific inflexion points when going from surface to bulk in irradiated samples beyond experimental errors. It has to be emphasized here that the position (S=1, W=1) correspond to bulk annihilations which encompasses both annihilations in defect-free bulk as well as in internal surfaces as shown by positron lifetime measurements. In the range of the present annealing temperatures, though no change is expected to the grain size as 2D grain growth starts for temperatures >1773 K and 3D ordering takes place only above 2573 K [32]. As the major contributor to the second lifetime does not show any change during the present annealing regime, changes appearing in the S-parameter can be interpreted independent of them.

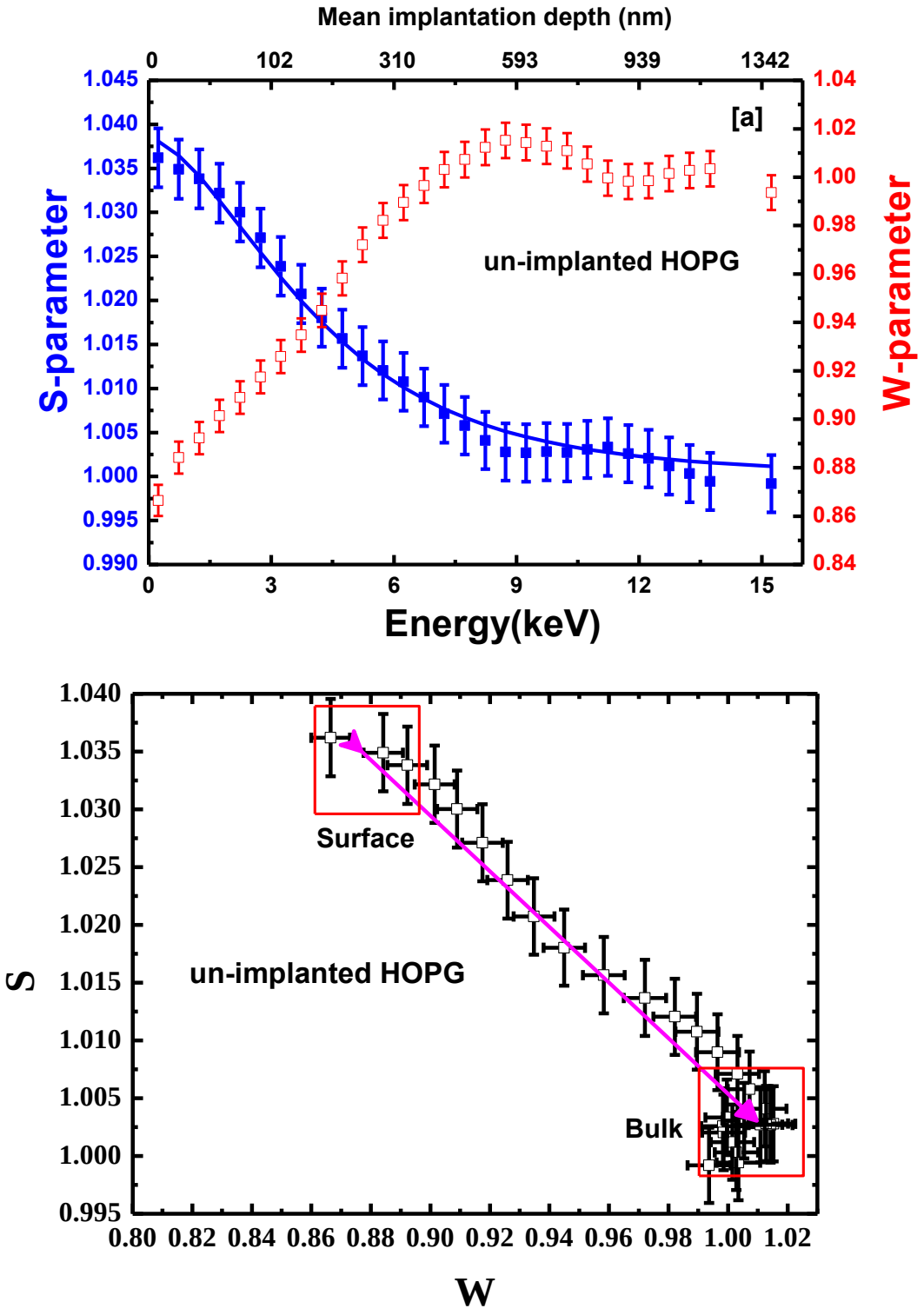

Fig.7: (a) S and W parameter variation with implanted positron energy for pristine HOPG sample. The mean implantation depth of positrons is also given in the top axis. The solid line through the S vs. E curve is the fit to the data considering a simple monolayer model using VEPFIT. (b) The linearity of S vs W correlation plot as positron goes deeper in to the sample shows the absence of a third annihilation site other than bulk and surface of the sample. The arrow shows increasing positron energy. The scales of the axes are chosen to be constant throughout this chapter for better comparison with irradiated samples.

Raman Spectroscopy

The first and second order Raman spectrum of the pristine HOPG sample is shown in Fig.8 (a) and (b) respectively. Also shown are that obtained for irradiated samples which are up shifted in scale for clarity. The first order spectrum is fit to four Lorentzians for pristine HOPG sample. The major peak is the G-band at 1583 cm^{-1} which is the Raman active mode for sp^2 carbon network. This mode is degenerate at the brillouin zone (BZ) centre (the in plane transverse optical (iTO) mode and the Longitudinal optical (LO) mode) with E_{2g2} symmetry. The degeneracy disappears for general points inside the BZ. The full width at half maximum (FWHM) of the fit Lorentzian to this peak is 13.93 cm^{-1}. There is a very weak disorder peak at ~1361 cm^{-1} (D) whose origin has been recently ascribed to double resonance through an elastic scattering process via defect [105]. Though it has a doublet structure it is not visible in this case due to very low intensity. The integrated intensity ratio I_D/I_G is as small as 0.00862 where as the peak intensity ratio of these two modes is only about 0.0019. Using the empirical relation put forward by by Tuinstra and Koening [112] connecting the in plane crystallite size L_a to the intensity ratio as

$$L_a(nm) = \frac{4.4}{(I_D/I_G)} \qquad (8)$$

we get the in plane crystallite size to be around 510 nm and using the relation by Pimenta et.al [105] which utilizes the integrated intensity ratio and the energy of the excitation laser light (E) as

$$L_a(nm) = \frac{560}{E^4}\frac{1}{(I_D/I_G)} \qquad (9)$$

the in plane crystallite size is around 1925 nm. As the two values differ, one of them could be used to get a qualitative (as both are empirical) picture during thermal evolution.

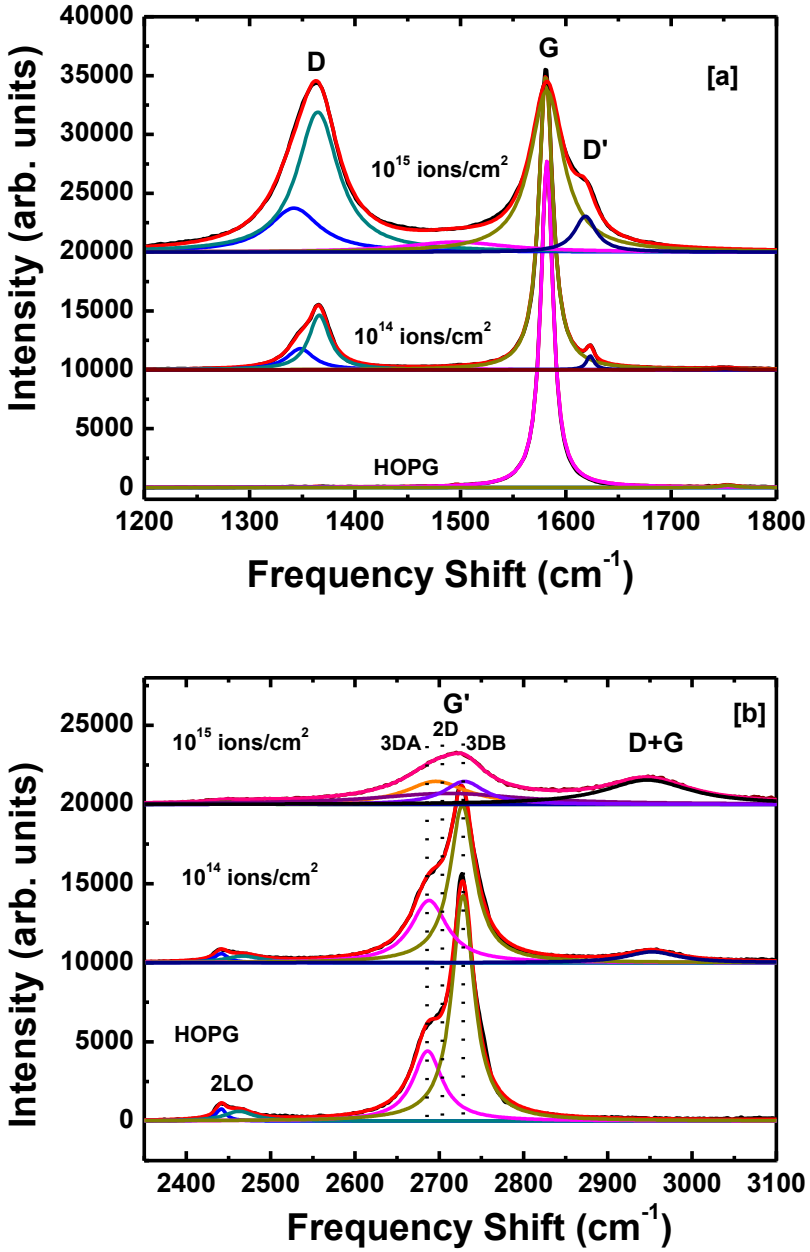

Fig.8: (a) The first order Raman spectrum of pristine HOPG shows the double degenerate G band at ~ 1583 cm^{-1} (E_{2g2} symmetry) from the zone centre which is active for sp^2 carbon networks. Also shown are the Raman modes obtained for low dose and high dose samples for comparison which are up shifted for clarity. The defect induced double resonance Raman process generated D band at ~ 1360 cm^{-1} and D' band at ~ 1620 cm^{-1} and they can be seen emerging with the increase in dose. (b) The second order Raman spectrum for pristine HOPG and implanted samples are shown. The symmetry allowed G' band along with the deconvoluted G'$_{3DA}$ and G'$_{3DB}$ Lorentzian peak positions are shown in them. For higher dose sample, there is also weak G'$_{2D}$ peak at ~2707 cm^{-1} corresponding to 2D graphite. The feature around 2450 cm^{-1} corresponds to overtone of LO mode where as the feature at ~ 2950 cm^{-1} is defect induced D+G mode. The symbols are explained in detail in the text.

L_a can also be looked upon as the phonon correlation length as defects/grain boundaries tend to change the lattice atom interaction. Thus considering L_a as the average distance between in plane defects, Nakamura et. al [21] has shown that the defect density (N_d) is related to the intensity ratio as

$$N_d = constant * \left(\frac{I_D}{I_G}\right)^2 \quad (10)$$

for lower irradiation doses. The other two weak Lorentzians observed for pristine HOPG are around 1496 cm^{-1} and 1754 cm^{-1}. The latter is named M^+ mode and is assigned to be the overtone of the out of plane Transverse optical mode (oTO) where as the earlier one is close to 1450 cm^{-1} LO mode [113].

The second order Raman spectrum of pristine HOPG shows the presence of symmetry allowed overtone of the defect induced D mode (i.e. ~2*D), though here conventional naming system is followed and is named as G' band. It has a doublet structure and can be fit using two Lorentzians – G'_{3DA} at 2686 cm^{-1} and G'_{3DB} at 2728 cm^{-1}. The relative intensity ratio of G'_{3DB} to G'_{3DA} is constant and for measured spectrum it was obtained to be about 2.4. The changes in the number of peaks in this band are a measure of the stacking order of the graphitic planes. For turbostratic graphite samples where there is no stacking order along *c-axis* this band is composed only of one Lorentzian around 2707 cm^{-1} (G'_{2D}) and as the stacking order improves (on annealing) the band goes from one peak to two peak via three peak regime which shows combined existence of 2D as well as 3D structure in the system. The introduction of intercalants or interstitials by ion implantation in the interlayer region causes an expansion of the layer spacing from 3.35 Å up to 3.45 Å when the interaction between the layers is destroyed and a 2D graphitic structure form. Thus variation in the relative intensity ratio of G'_{3DB} and G'_{2D} with thermal treatment could be followed to understand interlayer species arrangement and the recovery of the stacking order in ion implanted samples. Another

weak feature in the pristine HOPG spectrum is around 2450 cm^{-1}, whose origin has been assigned to the overtone of the LO mode [114].

The presence of the D-peak and the D' peak (~1620 cm^{-1}), with intensity comparable to G-peak, differentiates the spectrum obtained for irradiated samples from that for pristine HOPG. Both the peaks have their origin in the double resonance process but are understood as inter-valley (for D mode) and intra-valley (for D' mode) process involving electronic states at K and K' points (for D mode) or those involving electronic states around the same K (or K') point (for D' mode) in the brillouin zone of graphite [113]. The D-peak shows a doublet structure with two peaks around 1347 cm^{-1} and 1367 cm^{-1} for the irradiated samples. The doublet nature becomes difficult to resolve for higher dose and is some time ascribed to the loss of 3D ordering i.e. increase in turbostraticity [115]. The FWHM of all the peaks show an increase with the dose. The peak position of G-band shows only a marginal change of < 2.5 cm^{-1} with irradiation. The irradiated samples also have a weak and broad peak around 1500 cm^{-1} characteristic of amorphous carbon with double bonding, though it has appreciable intensity only for higher dose sample. In the frequency shift range from 100cm^{-1} to 1200cm^{-1}, a low intensity peak at ~1085cm^{-1} (which is not seen in un-irradiated graphite) appears (not shown here). This is assigned to hydrogenated carbon with chains of alternate single and double bonds [116].

The second order spectrum of irradiated sample shows the defect induced peak D+G mode at ~ 2950cm^{-1} (absent for the pristine HOPG) which increases in intensity and broadness with dose. This feature is considered to be a combination of D and G modes. The 2*LO mode around 2450 cm^{-1} is not resolvable for higher dose sample. The G' band shows broadening for lower dose sample and goes to a three peak regime

(G'_{3DB}, G'_{3DA} and G'_{2D}) for higher dose. Parameters deduced from Raman spectrum would be discussed for each dose in respective sections.

3.3.3. Low Dose implantation (10^{14} C^+/cm^2)

Atom Force Microscopy

The changes in the topography of the sample with low dose carbon ion implantation and after the complete annealing cycle are given Fig.9 (a-d). The images are taken at two different positions on the sample. The AFM image shows that there are locations with flat patches of ordinary graphitic surface with sharp edges due to cleaving with no indication of any implantation induced disordering except for the smaller size of basal fragments compared to the pristine surface (Fig. 9(a)). Whereas at a different location of the same sample disordered protrusions are visible among patches of graphitic basal planes. The protrusions are ~ 20 nm high and ~ a few 100 nm wide. The protrusions are too large to be due to sub-surface interstitial clusters as seen in other low dose irradiation [117], but are more likely to be the nucleation phase of the ridge structures as documented by Annis et.al. [74] (shown in Fig.2). Muto et.al. [118], using TEM studies of the ridge structure, argued that the ridges are curled graphitic planes due to sp^3 defects on a sp^2 matrix similar to the ones observed by Hiura et.al. [119], though the nucleation phase of this phenomenon is not very clear. The electronic transformation from sp^2 to sp^3 was invoked as the ridges formed within few seconds of irradiation. As seen here, the protrusions have a rather irregular structure and do seem to be along the edges of basal plane fragments. After the annealing cycle up to 1273 K, the topography looks similar to the pristine sample however with wavy nature at some locations. The regions where there are ridges or folding, remains after the annealing.

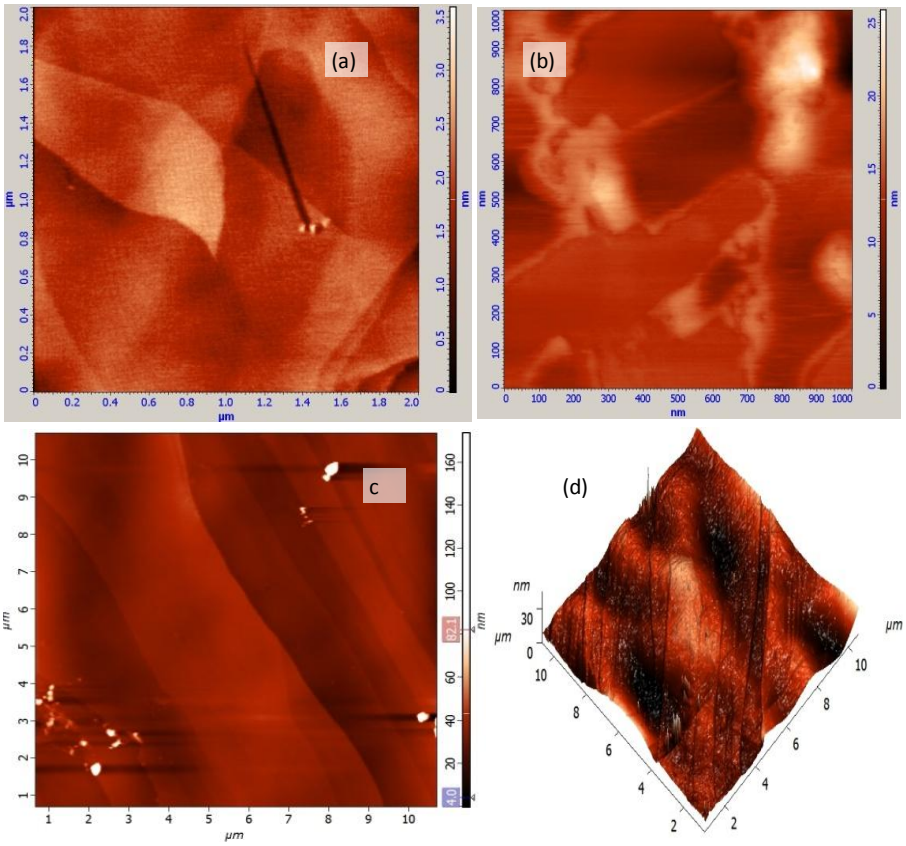

Fig.9: AFM image of HOPG implanted with 200 keV $^{12}C^{+}$ with a dose of 10^{14} ions/cm^2 taken at two different regions. (a) The surface shows flat basal plane with sharp step-edges produced by cleaving similar to what was observed in un-implanted specimen (b) Another region on the same sample which shows small protrusions along the sharp step edges. The protrusions are ~ 20 nm high and ~ a few 100 nm wide. (c) and (d) Topography after going through the complete annealing cycle which again shows defect free regions as well as curls running through the surface.

Raman Spectroscopy

Raman spectrum of the sample irradiated to low dose was fit in three different regimes – 100 to 1200 cm^{-1}, 1200 to 1900 cm^{-1} and 2350 to 3100 cm^{-1}. The measurements were taken at two different locations within the implanted zone and the maximum variation among different measurements is given as the error or deviation possible on the data points. The presence of a weak mode at ~ 1085 cm^{-1} differentiates the first region from that in pristine graphite. The intensity of the peak was weak but yet was compared with another intense mode in the same region which was present in un-

irradiated graphite at 805 cm^{-1}. It shows an increase in relative intensity (with respect to 805 cm^{-1}) from ~0.30 (for 300 and 373 K) to 0.6 at 423 K. There after the peak does not show any change in relative intensity till 773K. The relative intensity shows a marginal reduction to 0.42 at 973 K and remains at a similar value for 1273K annealing. Since it has very less intensity and does not show appreciable change with annealing from 423K it will not be discussed here. The region from 1200-1900 cm^{-1} is fit to 6 peaks, among which, four have appreciable intensity which are the D peak doublet, D' and the G peak. The important parameters deduced from Lorentzian fit are shown in Fig. 10(a-b). It has been observed that FWHM of the G band is more responsive to amorphization and shows a sudden jump with very small rise in the intensity ratios [59]. Here FWHM of irradiated sample is higher than but close to the pristine value, which shows that the density of defects in the probe volume is small and that the sub-surface still maintains a high degree of crystalline nature. It can also be seen that the FWHM of the G band shows a tendency to recover with annealing. However, even after annealing up to 1273 K, FWHM remains higher than that for pristine sample. The intensity ratio of the D-peak with the G – peak on the other hand shows a rapid decline and reaches a minimum by 523 K, thereafter there is a small increase at 623 K which again undergoes a decrease. Here too, the D-peak remains in the spectrum and does not reach the condition of pristine sample even on annealing to 1273 K. The correlation length increases from ~10 nm to ~30 nm by the end of annealing cycle as shown in the Fig.10 (b). D' intensity ratio also shows exactly the same trend as in D-peak (not shown here) but the increase at 623 K is much more pronounced. By taking the Raman spectrum along the graphite edge it was shown that the D-peak intensity shows a variation even with nature of the edge (zig-zag or armchair) whereas D' intensity remained constant [105]. Hence the, difference in

amount of variation in D and D' could be understood in terms of the influence of factors other than defects on the D-peak, like the region of the probed surface. The main point

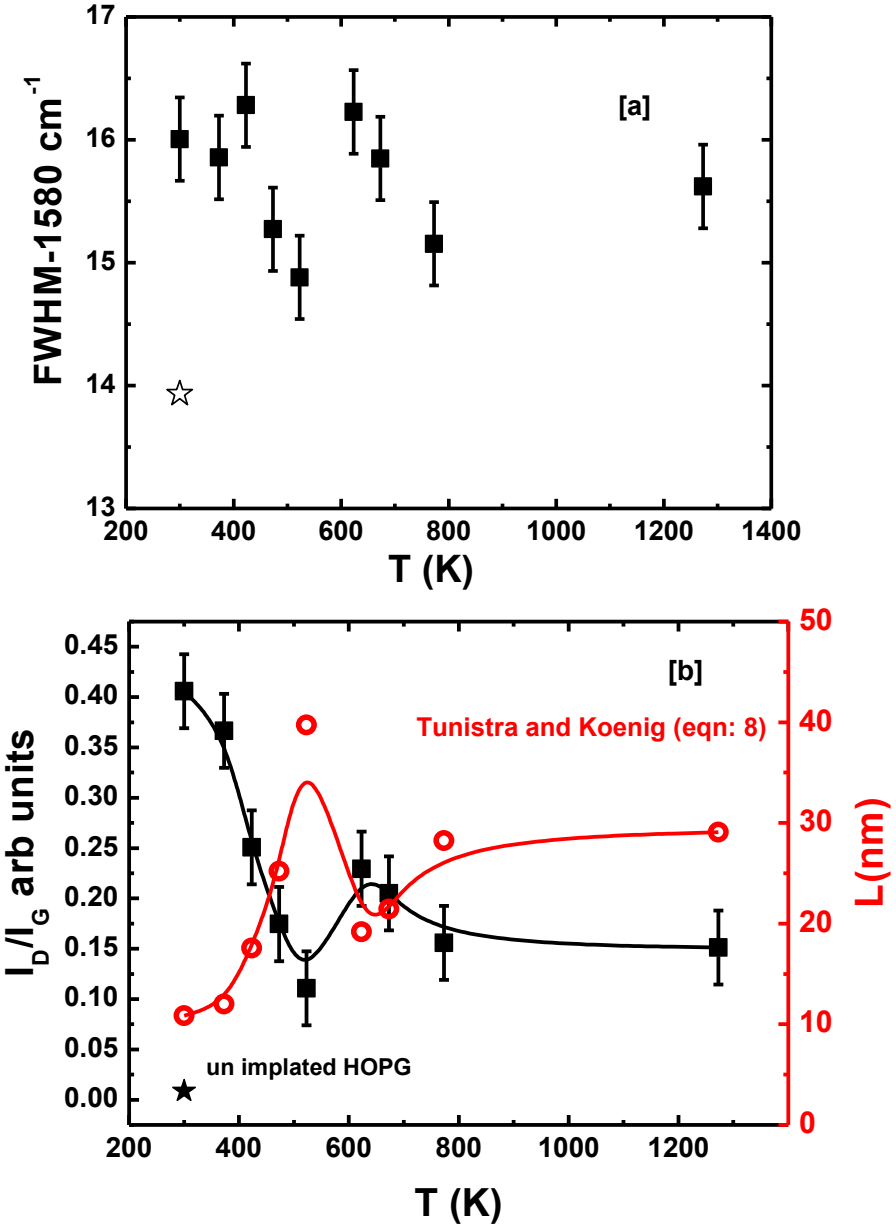

Fig.10: (a) FWHM of the G band in the as-irradiated sample and its variation with annealing. The FWHM of the pristine sample is also shown as open star.(b) Annealing behaviour of the relative intensity ratio of D peak with the G peak (I_D/I_G) shown as black squares and phonon correlation length (L) shown as red circles calculated using the empirical relation in equation (8).

however is that both D and D' peak shows a rapid decrease from 373 to 523 K which is similar to the fast process seen in other implantation studies [30,59.] The drop at the second instance from 623 K to 1273 K is slow compared to the first drop and it reflects a

complex process reported by [31]. The two processes are separated by an increase in the range of 523-623 K, which indicates an increase in the defect concentration in the sub-surface region. It has to be emphasized here that the defect can be any structural modification which can provide an elastic scattering centre in the double resonance process and need not necessarily be the ones created by irradiation. However its origin will be discussed later in the chapter. An additional broad and weak peak at 1500 cm^{-1} has to be invoked to get a get good chi-square for the fit. The intensity of the peak is very low and does not show any particular trend. This peak is usually attributed to be present in amorphous carbon and its weak presence shows that the damage in the probed depth is not close to amorphisation. The second order spectrum near the G' band could only be fit with two peaks corresponding to $3D_A$ and $3D_B$ with frequency shift 2687 and 2727 cm^{-1} respectively. These peaks showed marginal increase in their FWHM and remained as such during the entire annealing period. The intensity ratio between them I_{3DB}/I_{3DA} fluctuates around 1.8 – 2.4 which is the expected value for these peaks. This shows that in the volume which is investigated by the laser light disordering along the c-axis is very small.

Slow Positron beam spectroscopy

The variation of S-parameter with implanted positron energy (E) for the low dose sample in the as irradiated state is shown in Fig 11(a). The variations in S vs. E after annealing for 60 min to different temperatures are also given. The data points are 5-point smoothened with fixed boundary condition and normalised with respect to the bulk value. A fit to the experimental points are obtained using VEPFIT [103] assuming a two layer model – a defected surface layer and an un-defected bulk. In the as implanted sample, the S-parameter shows a slow decrease from the surface maximum, to reach a

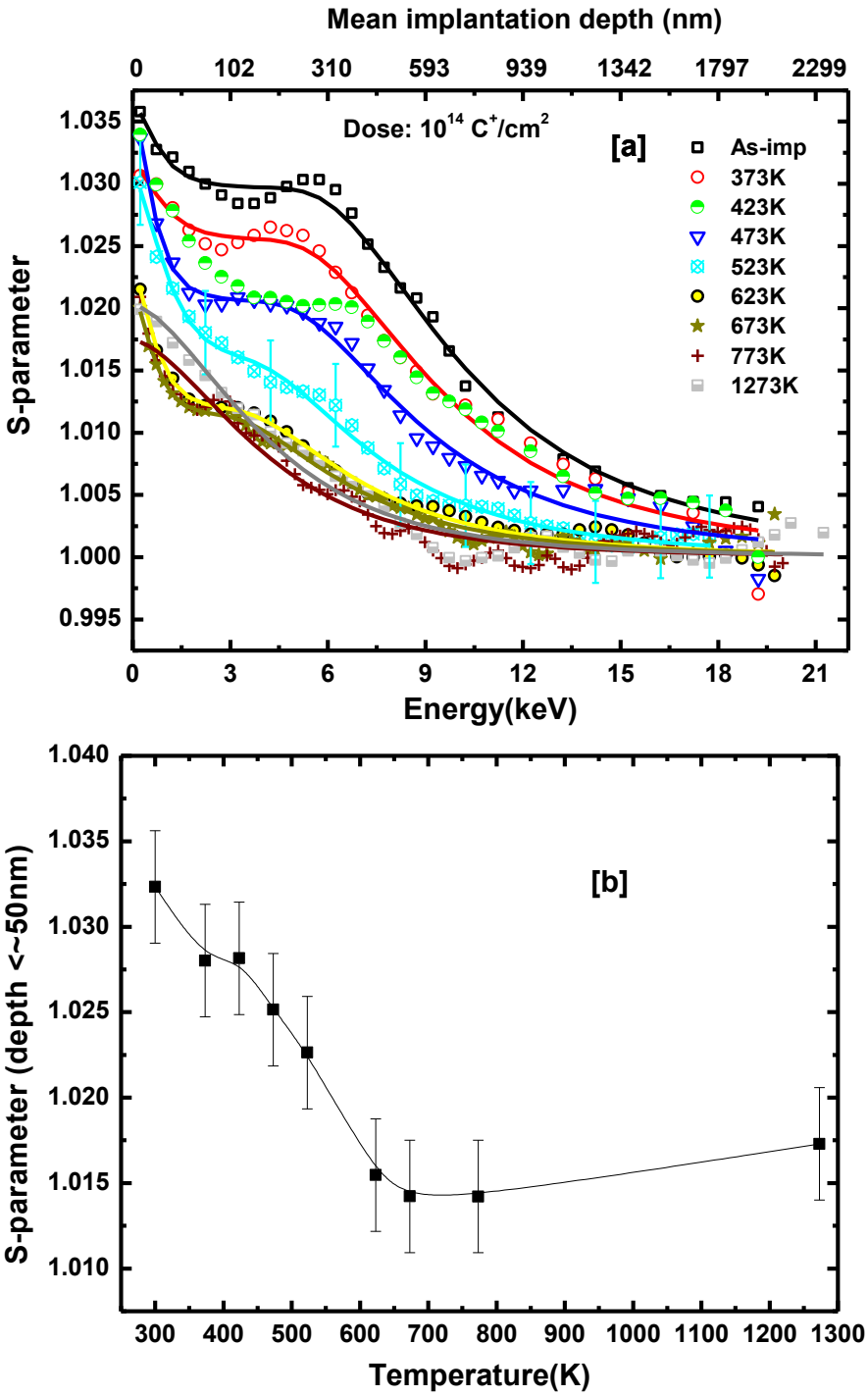

Fig.11: (a) S parameter versus Positron beam energy (E) for the as implanted and isochronally (60 minutes) annealed samples. Only representative curves are shown for clarity. The top axis shows the mean implantation depth. The error bars are shown on the data for 523 K at equally spaced points. The data points are 5-point smoothened with fixed boundary. The line through the data points are fit using a two-layer model in VEPFIT [103]. With annealing, the S-parameter at the peak damaged area shows a decrease and interface between the damaged layer and the un-defected bulk shows a re-growth towards the surface. (b) The variation of the average of S-parameter till 2keV as a function of the annealing temperature is shown.

"flat" region extending from ~ 3 keV - 7 keV (i.e. ~ 100 - 400 nm) followed by a shoulder. Beyond this, the S-parameter shows a gradual decrease towards the bulk. The peak damaged region (identified as the "flat & shoulder" region) agrees well with the vacancy profile predicted by TRIM [109]. The damage is highest near the projected range with decreasing disorder towards the surface, which is evident from the closeness of the trend of the curve to that of the pristine sample near surface. The higher S-parameter at the surface is due to Ps formation as well as due to surface restructuring after irradiation with protrusions. In the sub-surface region (< 2 keV, 50 nm), the defects created by irradiation are not trapping positrons as efficiently as in the projected range and hence, they are able to escape to the surface giving a greater contribution from surface S-parameter. By thermal treatment of the sample at 373 K for 60 minutes, the "shoulder" or the interface between the defected layer and the pristine layer move towards the surface accompanied by a decrease in the S-parameter of the damaged region. At 423 K the curve looks same as that of 373 K, except for a pronounced lower S-parameter at the peak damage region with same boundary. For 473 K, the interface moves towards the surface with little change in S-parameter. The trend of decreasing S-parameter and increasing recovered region continues for isochronal treatments at higher temperatures and by 773 K there is a near complete (a small hump is seen very near to surface) removal of the defected (open volume) region. On annealing the sample further at 973 K and at 1273 K, the gradual decreasing trend in S-parameter observed for pristine sample is repeated. It is also noted that there is a decrease in the surface S-parameter (< 2keV/50nm) with annealing, the maximum change at 373 K, which gradually slows down at 523 K. There is a second large decrease beyond 523 K, after which the surface S-parameter remains more or less constant. To make this point clear, this variation is shown in Fig.11 (b), where average of S-parameter from 0 to 2 keV is

plotted as a function of annealing temperature. Another factor is the existence of definite flat region where S-parameter is more or less constant in the as irradiated sample and up to 423 K annealing. The flat region suggests that in spite of positron implantation profile broadening and positron diffusion after thermalisation, positrons are seeing similar open volume region in this depth range and the S-parameter is solely that of the damaged region from 100-300 nm and is free from diffusion related contribution from surface or bulk. It is also clear that there is a definite motion of open volume region towards the surface at 623 K.

The experimental S versus E data is fit using VEPFIT and the results are shown as a box profile in Fig. 12 (a). The S-parameter derived for the defected layer is now corrected for positron-diffusion after thermalisation. The width of the box represents the width of the defected region as seen by positrons. Fig.12 (b) shows the variation of derived S-parameter and width with thermal treatment. An ideal model for VEPFIT, could have been one with three layers instead of two as shown above, the additional layer representing the sub-surface defects. A three layer model, however produced un-realistic results with poor chi-square values. This is due to the difficulty in delineating the surface from the near or sub-surface region due to the large diffusion length of positrons in graphite. Hence even though a single value is given for the defected layer from surface, the value is more representative of the defected region 100 – 300 nm. The values are very close to that obtained in flat region of the S versus E curve (Fig.11(a), giving proof for the earlier argument that the S-parameter at flat region is a true representation of the defected layer. The data for 423 K could not be fit to good chi-square with fixed values of bulk diffusion length and physically significant width of damaged layer and hence not shown here. Though taking clue from the other fits it is

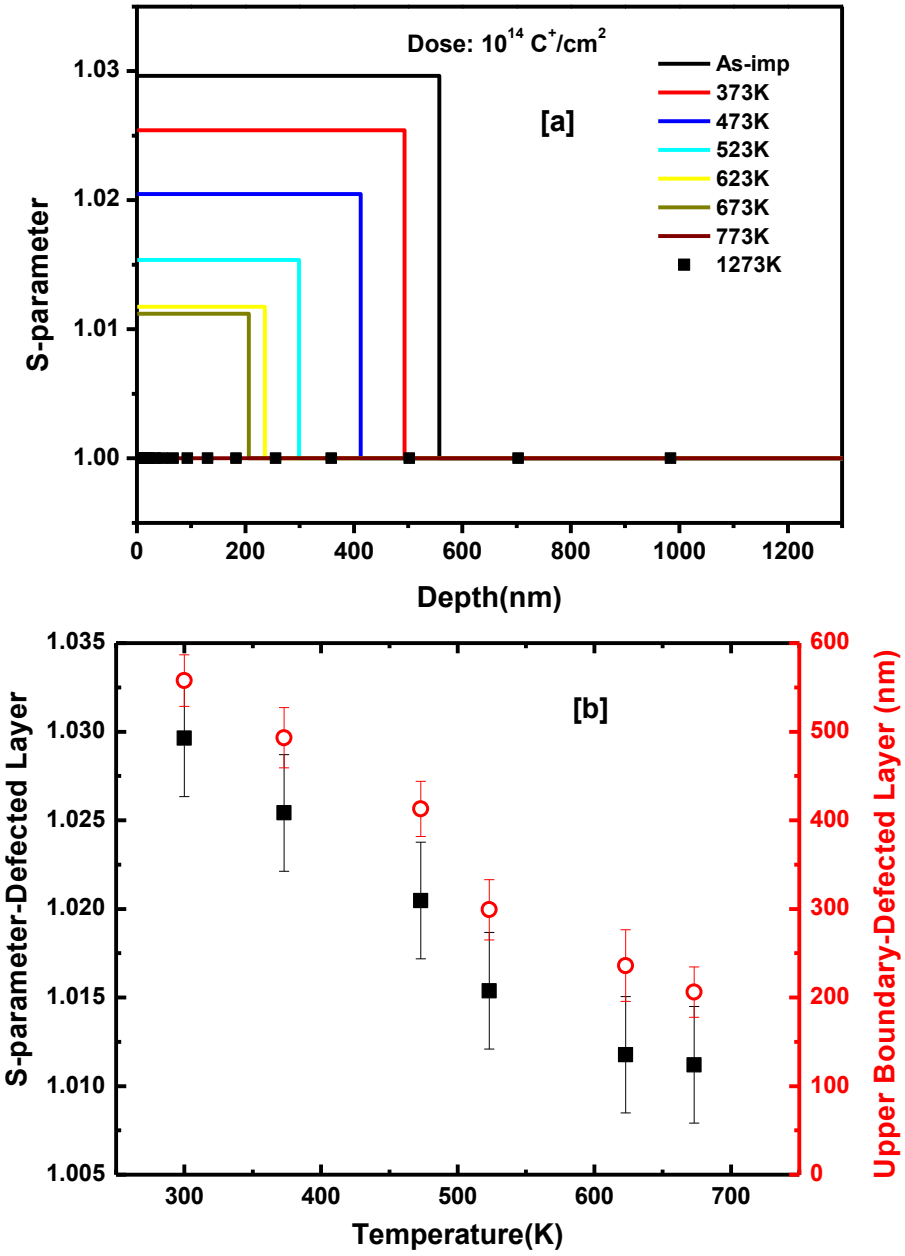

Fig.12: (a) S parameter versus depth as derived from VEPFIT using a two layer model for as implanted and annealed samples. (b) The values of derived S-parameter and upper boundary of the defected layer with error bars.

clear that the S-parameter would be exactly same as that in the flat region i.e. same as that for 473 K and upper boundary of damaged layer would be close to that for 373 K, though the surface restructuring is pronounced in this case making the total width of the damaged region smaller. It was also difficult to fit the data for 773 K to two layers as the

small hump like feature is very close to the surface occurring at around ~ 50 nm (2 keV), and hence was only fit to bulk layer.

R-parameter which is defined as $\left|\frac{S-S_{bulk}}{W-W_{bulk}}\right|$ is free of the effect of concentration of defects [120] provided there is only one type of defect. For bulk measurements R parameter can be calculated correctly if there is homogeneous distribution of defects in the probe volume. In case of beam measurements, S-W correlation plot gives a similar qualitative picture as R-parameter calculated for specific positron energies will not be a correct indicator with a dependence on positron diffusion and possibility of trapping at other sites away from region of interest. R-parameter can then be considered as a slope in the S-W plot and a change in slope will point to a change in defect character and not concentration. The S-W correlation plot of the as-implanted sample is given in Fig. 13. The plot also contains the inflexion points of annealing at 373,423 and 473 K. This is done to keep the clarity of the figure. Each temperature is identified by a different colour and different symbol. The pink arrow (with head and tail) passing through the yellow squares gives the direction of increasing energy, with arrow head at (S,W) of pristine sample close to (1,1). Yellow squares lying outside this arrow represent the damaged region in the as implanted state. Similar deviations for other temperatures are given. It is clear that the (S,W) co-ordinates corresponding to inflexion or deviation for annealing temperatures from 373 – 473 K lie on a line joining them to the bulk (S,W) value, where as the as irradiated sample lie outside this line. Thus, at 373 K there is a definite change in defect type, and for annealing up to 473 K, a change in concentration of this defect type is expected. For higher annealing temperatures the deviation from the straight line denoted by the pink arrow is too small or too close to the surface making such analysis difficult.

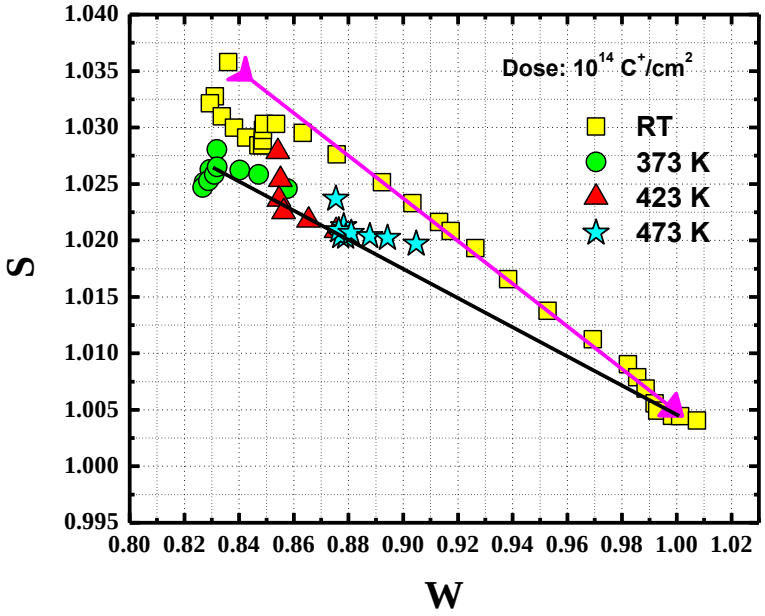

Fig.13: S vs W parameter for as – irradiated (RT) and annealed sample (up to 473 K). The complete S-W correlation plot is given for as-irradiated sample with positron beam energy as running parameter. The pink arrow represents the increasing positron energy. For other temperatures, only the inflexion or deviation points are shown for clarity. Different temperatures are identified in the figure by different symbols and colours. The black line is an aid to the eye to identify that inflexion points of 373, 423 and 473 K lie on straight line joining them to the un-defected bulk (S,W) co-ordinate.

Thus to summarize, the sub-surface S-parameter (≤ 50nm) shows a major drop at 373 K, with a maximum decrease at 623 K. Beyond this there is not much change in sub-surface S-parameter. The defected region S-parameter shows a decrease starting from 373 K with maximum drop at 423 K and at 523 K with a little change (factoring the statistical error) at 473 K. At 623 and 673 K, the defected region is close to surface signalling a migration of open volume region towards surface. The maximum recovery of the damaged region (in terms of width) happens at 523 K. Complete recovery takes place for annealing at temperatures more than 773 K. The S-W correlation plot gives a hint that there is a change in defect character at 373 K and from 423-473 K, change in S-parameter is due to change in concentration of the defects rather than a change in its type.

3.3.4. High Dose implantation (10^{15} C^+/cm^2)

Atom Force Microscopy

AFM images of the sample irradiated to 10^{15} C^+/cm^2 are given Fig.14 (a-c). The images taken after the annealing cycle is given from Fig. 14(d-e). The images are taken at different positions on the sample. The AFM image shows structures similar to the ones given in Fig.2, with ridges on the sample. The first image shows the existence of linear ridges running across the sample. The second image shows curvilinear ridges apart from the linear ones. The third image gives evidence of linear ridges going in opposite directions giving a square grid structure with oriented flat basal plane inside each grid. The ridges are of the order μm in length. These were considered to be associated with twin bands due to its development along crystallographic directions [54]. It was later assigned to the fragmentation of basal plane followed by adatom aggregation along the stress centres at the fragment interface [74]. These were also assigned to curls on graphite sheet due to sp^3 hybridisation and speculated its development along twin directions [118]. From XPS studies, there is evidence of mixed sp^2-sp^3 nature at least in the sub-surface (~3 nm) region giving credence [121] to the idea.

For the aggregation mechanism, an activation barrier of 0.47 eV [78] has to be crossed for surface migration. Such large scale ridge formation becomes hard unless the migration parallel and perpendicular to the basal plane becomes faster in the dynamics of irradiation and the migrating atoms avoid other possible traps. For low dose implantation also, μm level irregular protrusion were seen in Fig. 9 along the step edges and such structure becomes difficult to be explained by adatom aggregation mechanism alone as the entire irradiation lasts only for a short time. It is known that with increasing dose there is an enhanced fragmentation of basal plane leading to bending and cross linking of the planes with added stress along the fragment interface. This would lead to an

increased sp^3 character of the graphite sheet and hence there will be an added curling of the surface sheets to relieve stress accumulated in the surface and sub-surface layers. Depending on the amount of irradiation dose the fragmentation can be along the weak

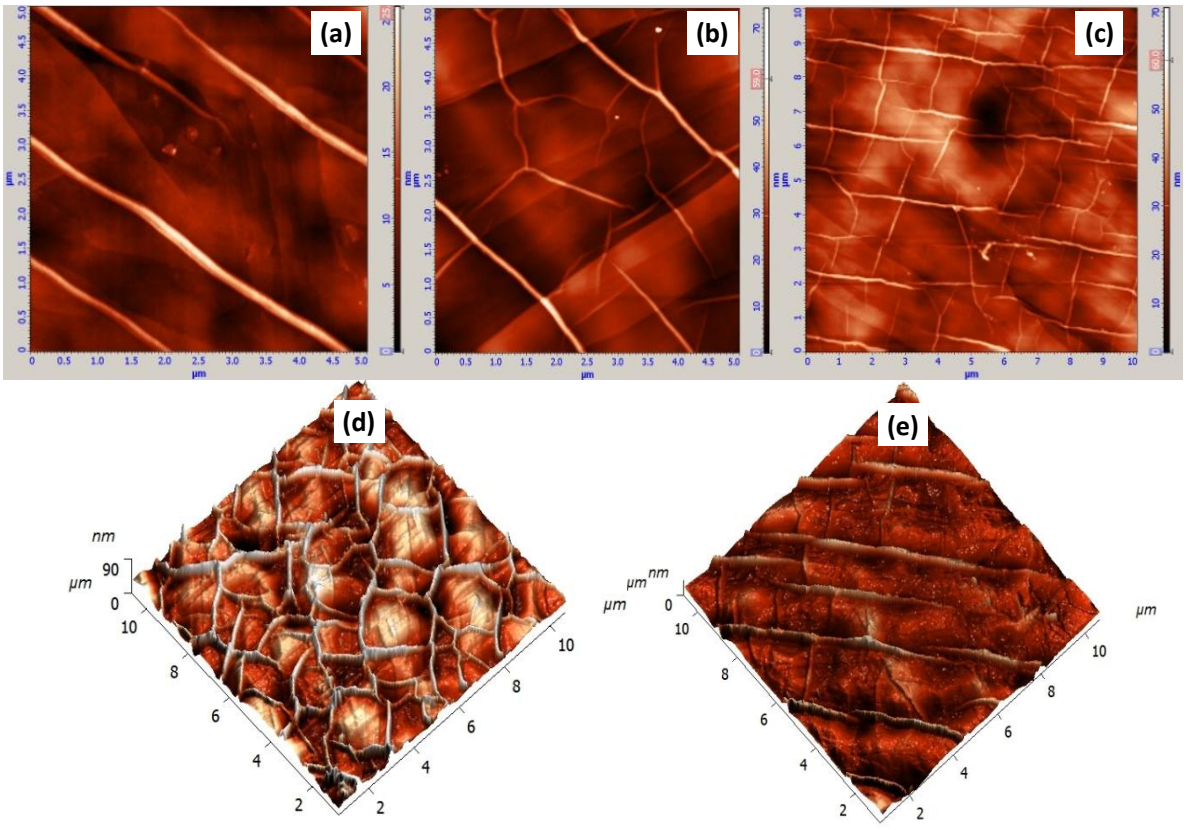

Fig.14: AFM image of HOPG implanted with 200 keV $^{12}C^{+}$ with a dose of 10^{15} ions/cm^2 taken at three different regions. (a) The surface shows oriented basal plane strips separated by linear ridges running across the sample in a roughly periodic manner (b) Another region on the same sample which shows curvilinear ridges. (c) Square grids with linear ridges running across in perpendicular directions. (d) Topography after the full annealing cycle. 3D plot shows an intricate network structure. Small change is observed by annealing with increase in cross networking and ridges could be seen running inside each grid as well. (e) Regions where only linear ridges are present remain even after annealing.

centres like the grain boundaries, step edges etc. or along certain preferred orientation or at random sites. Thus low dose implantation leads to fragmentation along the already existing random step edges in the pristine sample with bending and curling leading to irregular μm level protrusions. Small amount of wrinkling, recovery and waviness is

seen after annealing up to 1273 K, thus showing that point defect recovery at the surface does play a role during their subsequent evolution by annealing. At medium doses fragmentation and curling progress along certain preferred orientation [77] leading to linear ridges and at higher dose random directions start to fragment and curl leading to curvilinear ridges and wrinkling. Annealing treatment does not show appreciable change, however the curvilinear ridges exhibits a little more intricate structure showing an enhanced stress release by curling during vacancy recovery near surface. Such surface features are also an indication of large scale damage extending from the projected range up to the surface as is evident from slow positron results below showing the importance of sub surface disorder and their recovery on surface topography.

Raman Spectroscopy

Raman spectrum obtained at two different regions of the sample implanted to high dose is given in Fig.15 (a-c). Unlike in the case of low dose sample the measurement at two points did not always give the same parameters and this is represented as two sets of points in the graphs – solid squares and open circles. It shows that the sample sub-surface has highly disordered regions close to amorphisation which is represented by FWHM of G-band > 45 cm^{-1}. There are also other less disordered regions with FWHM < 40 cm^{-1}. These regions show different annealing behaviour for FWHM where the highly disordered region not showing any significant recovery till 973 K where as for regions with lower FWHM the recovery starts by 423 K. For latter, there is a fast drop beyond 423 K, a threshold region is seen between 573 K – 723 K and a slow decrease thereafter. In the case of the intensity ratio of D-peak with the G-band (Fig. 15(b)), both sets show a similar trend even though the values are different. There is fast decrease in the intensity ratio from 373 K itself with a slowing down near 573 K –

723 K beyond which there is a slow drop. The phonon correlation length calculated increases from ~ 2.5 nm to 25 nm by the end of annealing cycle as given in Fig. 15(c). As in the case of low dose sample, the FWHM and the intensity ratio does not reach the pristine values even after annealing to 1273 K. Apart from the these four peaks, the broad peak at 1500 cm^{-1} has to be introduced to get a good fit. Here the integrated intensity ratio of 1500 cm^{-1} peak with G-band remains constant throughout the annealing cycle at around 0.25±0.11, which is appreciable compared to other peaks in the region. Its presence shows high level of disordering close to amorphisation in the sub-surface/surface region, which is also corroborated by high FWHM of the G-band at some regions of the sample.

The second order spectrum from 2350 – 3100 cm^{-1} was fit to 6 peaks. Three of them constituted the G' band, one of them was the D+G band and the other two belonged to the band at 2450 cm^{-1}. The G' band was now found to consist of a broad peak a round 2704 cm^{-1} with a standard deviation of 5 cm^{-1}. This is very close to the G' peak assigned to turbostratic or 2D graphite. Hence the implantation dose is such that in the sub-surface region there is a loss of c-axis ordering. The intensity of this peak with respect to the more intense 3DB peak at ~ 2727 cm^{-1} fluctuates around 0.2-0.6 and does not show any decreasing trend by annealing up to 1273 K. However the FWHM of both 3DA and 3DB peaks show an overall decreasing trend from values as high as 150 cm^{-1} to 50 cm^{-1}. The intensity ratio between 3DB to 3DA is smaller than that obtained for low dose and pristine sample but shows a higher value of 1.8 - 2.2 for the final annealing temperature of 1273 K.

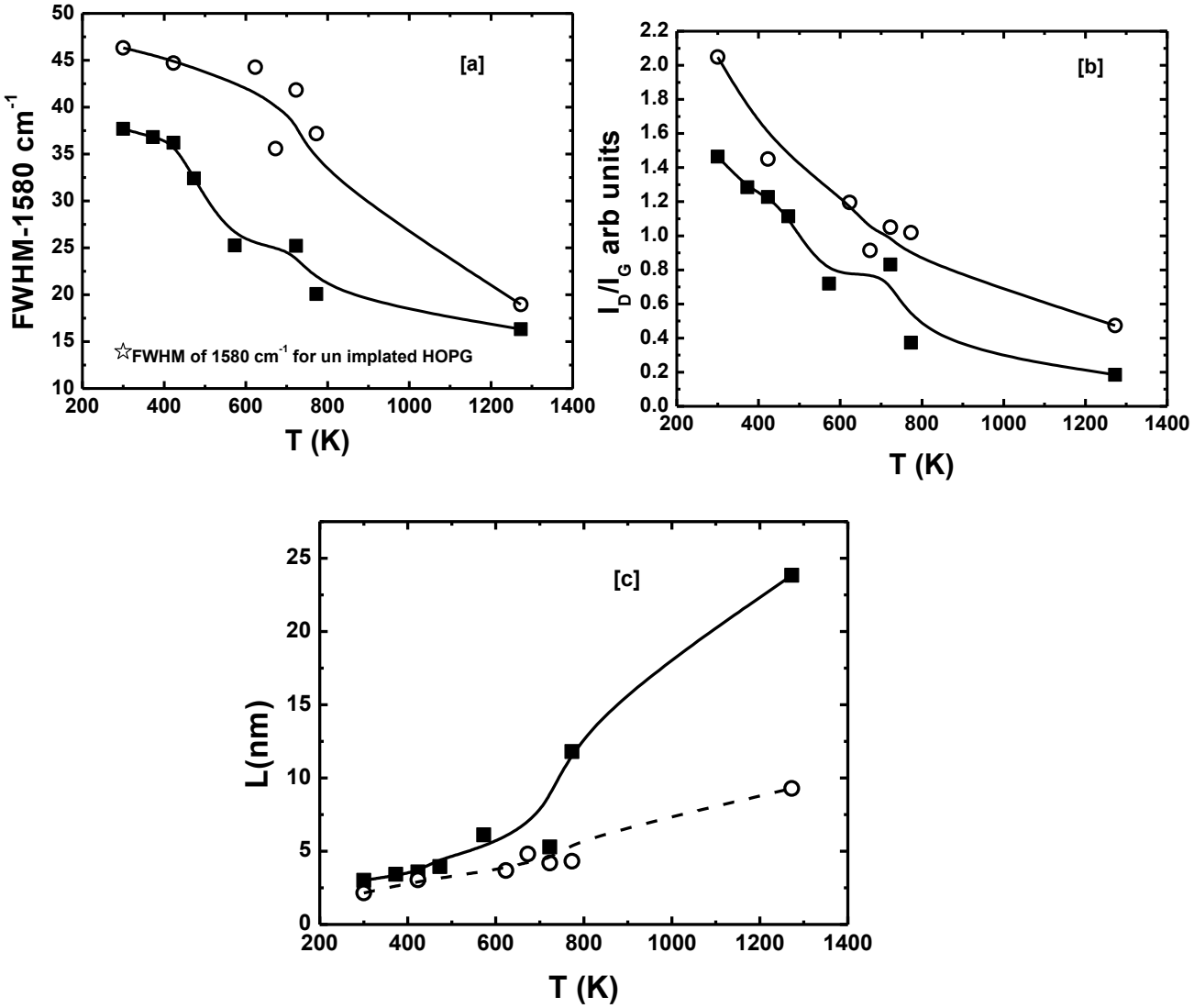

Fig.15: (a) FWHM of the G band in the as-irradiated sample and its variation with annealing. (b) Annealing behaviour of the relative intensity ratio of D peak with the G peak (c) phonon correlation length calculated using the empirical relation in equation (8). Solid squares and open circles represent measurements at different positions on the implanted zone.

Slow Positron beam spectroscopy

The dependence of the defect annealing mechanism on the irradiation dose is brought out by the S vs. E curves for the sample irradiated to higher dose and its thermal evolution in comparison to that for low dose sample. The curves are given in Fig 16 (a). It should be mentioned that only representative temperatures are shown for clarity. The curves obtained for as irradiated sample and after annealing at 373 K was exactly the

same. The S parameter curves showed no difference between annealing temperatures 423 and 473 K. Similar trend was also seen at 573 K and 623 K. The observed defect annealing mechanism can be better conveyed through Fig. 16 (b-c) which plots the S-parameter at specific energies (5 keV & 2 keV) as a function of temperature where interesting features were seen, one representing a peak in S vs E curve and another a local minimum in the same curve. The as irradiated sample shows an increase in S-parameter from the surface to a high value between ~ 3 keV - 5 keV beyond which there is a drop to the bulk S – value in S vs E curve as given in Fig. 16 (a). The sub-surface (1-2 keV) shows a small recovery on annealing to 423 K. At 523 K two interesting features arise, one a local minimum around 2keV and another a peak at around 5 keV. The peak at 5 keV has lesser S-parameter compared to the as irradiated state and it decreases on further annealing to 573 K as also shown in Fig. 16 (b). The S-parameter at 5keV remains at around the same value on further annealing till 673 K, after which the peak in S vs E curve disappears (at 723 K) and the curve resembles that of the low dose sample at 523 K with a shoulder. There is a definite movement of the peak towards the surface, with a shoulder now appearing at lower energy as compared to the peak position. The S-value corresponding to the shoulder shows a decrease on annealing to 773 K and shows a complete disappearance by 973 K. Annealing at 1273 K takes the S-parameter near the projected range to values lower than bulk S-parameter. The small recovery seen near surface at 423 K becomes the local minimum at 523 K, and it shows further decrease only at 673 K as also shown in Fig. 16(c). With the appearance of the shoulder near surface, the local minimum disappears and the S-parameter of the region now represents this higher S-parameter which decreases on annealing to 973 K. There is not much change in sub-surface S-parameter on further annealing to 1273 K, however the surface S-parameter at 0 keV (i.e. 235 eV beam transport energy) shows a decrease at 1273 K

from the earlier values. Unlike the low dose sample, here the back interface between the damaged and the pristine region shows a sluggish recovery for temperatures greater than but near 523 K, making a major shift only at 723 K.

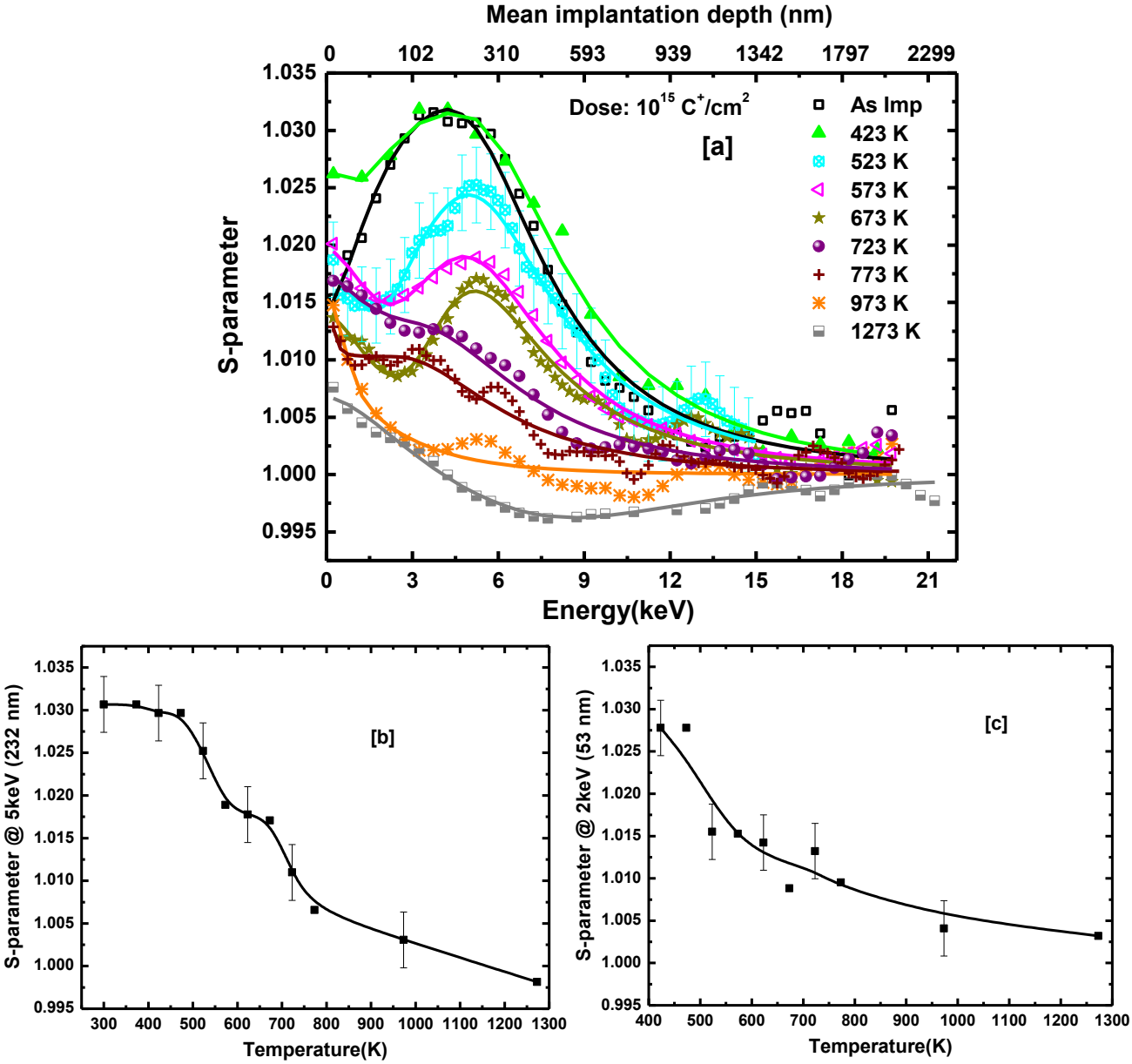

Fig.16: (a) S parameter versus Positron beam energy (E) for the as implanted and isochronally (60 minutes) annealed samples. Only representative curves are shown for clarity. The top axis shows the mean implantation depth. The error bars are shown on the data for 523 K at equally spaced points. The data points are 5-point smoothened with fixed boundary. The line through the data points are fit using a two-layer model in VEPFIT [103]. (b) Variation of S-parameter at 5 keV (implantation depth ~ 232 nm) with temperature where a peak appears in Fig. 16 (a) after annealing up to 523 K. (c) S-parameter at 2 keV (implantation depth of 50 nm) with temperature where a local minimum appears in Fig. 16 (a) after annealing up to 423 K.

The data for as – irradiated sample is fit to a two layer model and for annealing treatments from 423-673 K a three layer model is used in VEPFIT to account for the local minimum. For annealing temperatures from 723 K, again a two layer approach gives the best fit. The results are shown as a box profile in Fig. 17. The recovery near surface which starts at around 423 K, grows towards the damaged region till 673 K and S-parameter of the region is even lower than the bulk value from 523 K onwards. The S-parameter of the damaged region represented here is free from diffusion related contributions and thus is higher than the experimental S-parameter at 5keV plotted in Fig. 16(b), but the trend remains same. This is true for S-parameter of the sub-surface region. The width of the damaged region decreases with annealing mostly due to the recovery at the surface before moving towards the surface.

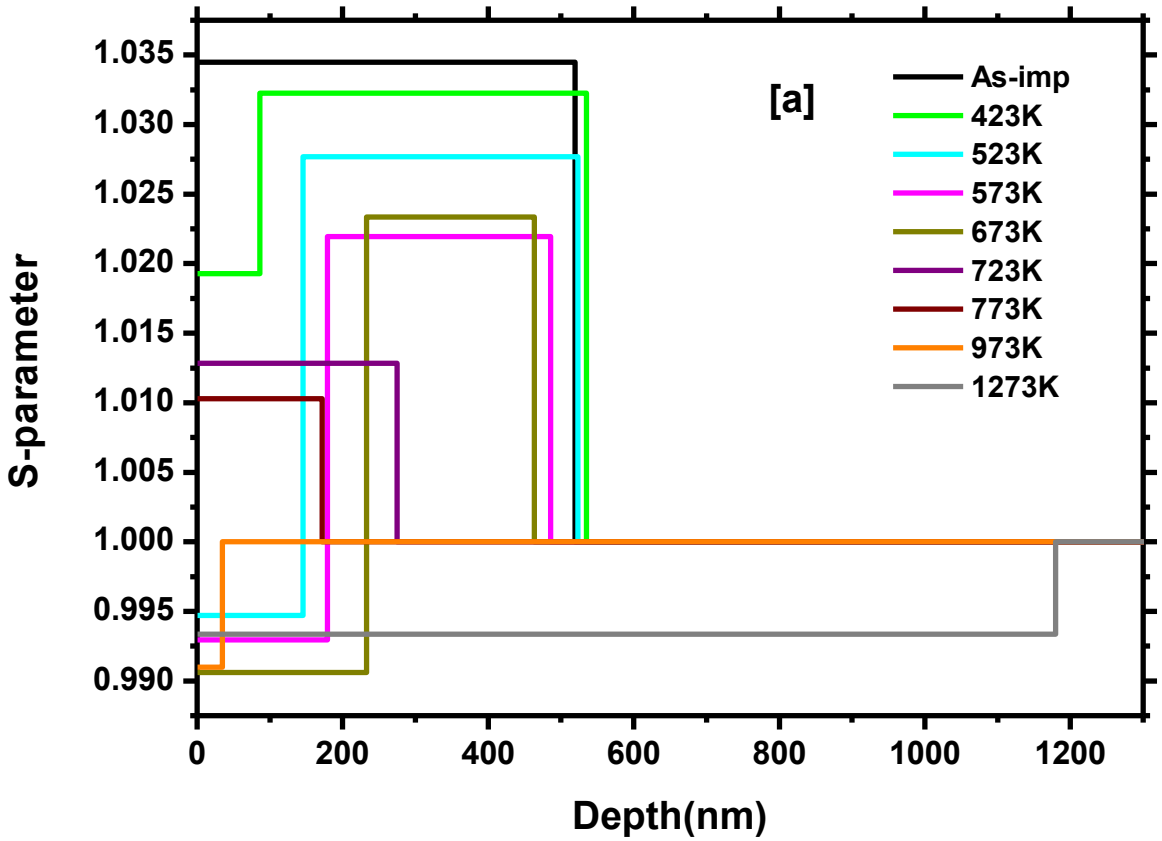

Fig.17: S parameter versus depth as derived from VEPFIT using a two layer model for as implanted and for thermal treatments at 723 K, 773K, 973 K & 1273 K. A three layer model is used for other temperatures.

The S-W correlation plot for as-irradiated sample is shown in Fig. 18(a), with linear fits to three regions, showing three slopes near the inflexion point. Fig. 18(b) shows the same curve along with S,W co-ordinates corresponding to the inflexion points alone for annealing temperatures from 523 – 623 K. The details of the curve are given in the figure caption. The key information from Fig. 18(a) is the presence of two separate positron trapping regions, one near surface and the other at around 5keV represented by intersecting straight lines. The near surface trap region could not be brought out by VEPFIT but appeared as a separate minimum from 423 K. The S-parameter of damaged layer got from VEPFIT represents the deeper trap which is evident from the closeness of this to the value at intersection i.e. ~ 1.035. Annealing brings out its presence by a peak around the region. The peak region appearing at 523,573 and 623 K lie along a straight line through bulk S,W value. This shows over thermal treatment, the concentration of this defect decreases till 623 K. From as irradiated state to 523 K, however the change of slope is small and hence it is not possible to say conclusively whether there is an actual change of defect type. In the as irradiated state, there will be different type of defects because of high dose of implantation. It is possible that the particular defect type is distinguishable when others are removed through thermal treatment as seen by the drop of S-parameter near surface. Hence evidence is presented for the first time for spatially separated defect types in as – irradiated state of HOPG which has different thermal stabilities. The one which is dominant near surface starts to anneal out from 423 K itself. The prominent defect near the projected range is stable up to 673 K, which most probably disintegrates and moves towards the surface at later annealing temperatures.

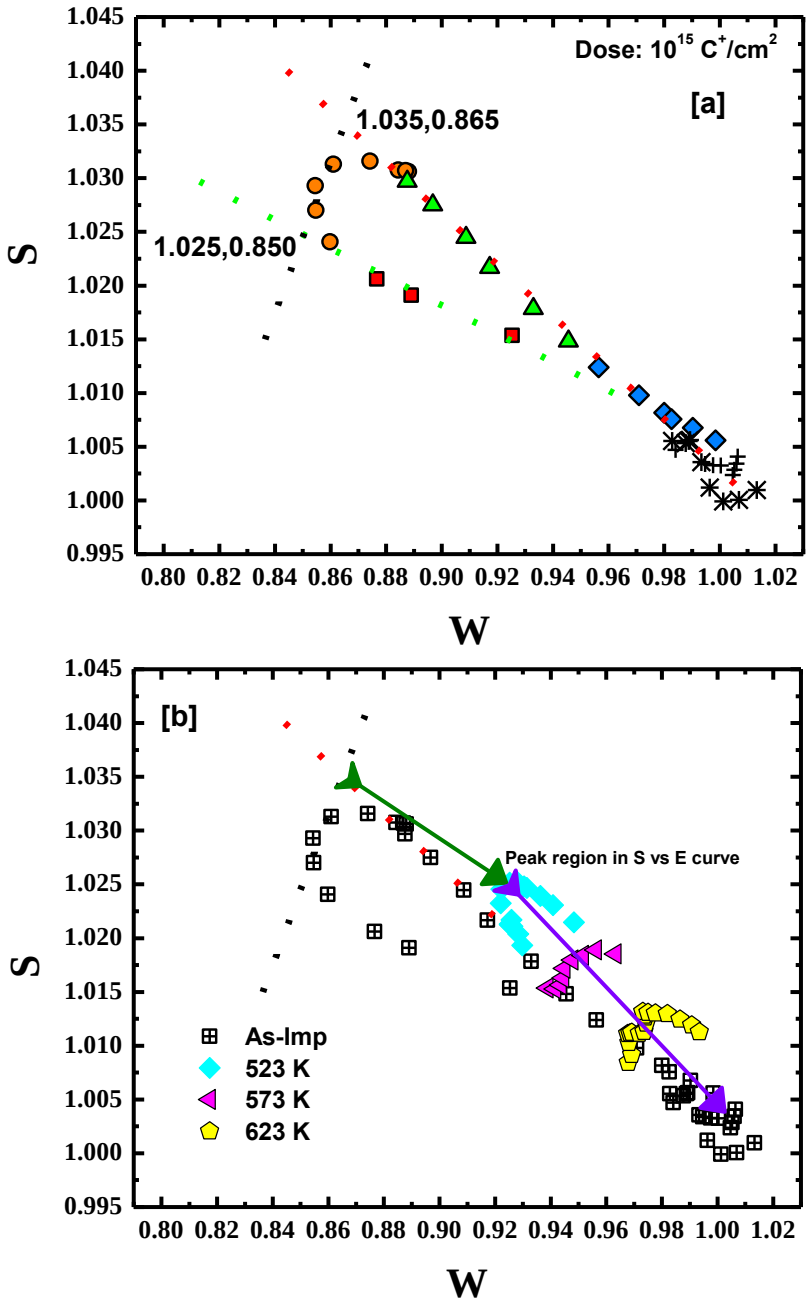

Fig.18: (a) S vs W correlation plot for as – irradiated (RT) sample with positron beam energy as running parameter. The increasing positron energy is represented through different symbols as given here. Red squares for 0-1 keV, orange circles for 1.5-5 keV, green triangles from 5.5 -8 keV, blue kites for 8-11 keV, and others for higher energies. Three straight lines are linear fits to three slopes near inflexion point, surface to ~ 2keV (green), 2.5-4.5keV (black) and 5 keV- 20 keV (red). The S,W coordinates corresponding to the intersection of straight lines are given near each crossing. (b) S-W correlation plot as in (a) but with inflexion points (alone) of other annealing temperatures identified by different symbols. The peak region in S-E curve is identified here. The violet arrow is an aid to eye showing a near straight line passing through S,W coordinates of the peak region of temperatures from 523-623 K to bulk S,W values. The olive green arrows connects one of the intersection points derived for as-irradiated state to the peak region of 523 K, showing small change of slope with respect to the violet arrow.

Hence to summarize, the as – irradiated sample shows two trapping sites for positrons, one dominant near surface and the other near projected range. The near surface defect starts annealing by 423 K; however the major change happens at 523 K (just beyond 473 K) creating a local minimum in S vs E curve. There is further decrease in near surface S-parameter with annealing up to 673 K, the layer S-parameter going below bulk value as derived from VEPFIT. The recovery up to 673 K mostly happens near surface decreasing the width of the damaged region as the back interface motion is slow till 673 K, showing a boundary motion to surface only at 723 K. The defect near projected range shows a decrease in concentration till 673 K, beyond which it most probably disintegrates or/and moves to surface. The defect thus accumulated near surface undergoes complete recovery by 973 K. However the S-parameter of the recovered region lies below the bulk S-value.

3.4 Discussion

Broadening of FWHM of the G-band has been related to vibration excitation lifetime near a defect [26, 64] or to C-C bond length/nature variation by irradiation. For the low dose sample, inside the Raman probe volume there is not much disorder along the c-axis as evidenced by the absence of any major parameter shift in the second order spectrum. However there are point defects as well as fragmentation of basal plane and nucleation of the ridge structures which would cause an increase in FWHM of the G-band due to the limited lifetime of phonons starting at the fragment interfaces or at point defects inside of the basal fragments. The amount of broadening is low in this case as seen from the values obtained. It is known that the 2D re-growth with a-axis alignment for pyrolytic graphite starts above 1873 K [36], hence no variation is expected in FWHM by annealing up to 1273 K, even when point-defects contributing to the broadening have

been removed. The relative intensity ratio on the other hand is related more to the in plane defect density prior to clustering and hence shows a sharp drop during annealing from even 373 K signalling a fast defect recovery process in the sub-surface region inside each fragment. The subsequent slow drop beyond 623 K shows that a slow complex defect recovery process dominates. The non attainment of the pristine value for 1273 K also signals that the intensity ratio has its share from the fragment interfaces as edge of graphite sheets are also defect states that give rise to the D-peak. Hence, the intensity ratio would reach zero only beyond 1873 K when actual grain growth starts along a-axis and later along c-axis.

In the case of higher dose sample too the intensity ratio behaves in the exactly same way with decrease from the first annealing temperature. However, the intensity ratio is much higher now and the decrease is not as sharp as in the case of low dose sample. There are different intensity ratios obtained from different regions of the same sample, however both show similar two-slope decrease with a relatively faster drop followed by threshold around 573-623K, and a slow decrease. The difference in behaviour from low dose sample is evident from FWHM of G band, which is much higher than that of low dose sample. There are also different values obtained from different regions of the same sample showing inhomogeneous distribution of disorder and different annealing behaviour. It has been shown that there is a slow recovery when there is near amorphization by implantation [25]. Hence, in this case the little change in FWHM of G band till 973 K would point to highly disordered region, probably belonging to broken, bent and curled and cross linked sheets, which are responsible for ridged and cracked formations on the graphite surface. The 3D disorder along the c-axis which is shown by the presence of weak 2704 cm^{-1} band, also require temperatures as high as 2573 K to be removed by recrytallisation along that direction. The presence of

ridged surface may also be responsible for peaks at 1500 and 1085 cm^{-1} going by their stability till 1273 K. Inter and intra planar defects or clusters which can affect the planarity of graphene sheets also contribute to FWHM rise by changing the bond nature and length. But these can recover at much lower temperature as and when the defects responsible are removed; hence FWHM of G-band from such regions show a decrease with annealing from about 423 K and shows a trend similar to the intensity ratio. Hence for both lower and higher dose sample there is a fast recovery process at low temperatures and then a slowing down across the similar temperature range from 473-723 K, followed by a slow decrease. The difference among them points to the complexity of the defect structure involved in the surface and the sub surface region.

The difference arising from the type and density of defects is also reflected in the annealing process as imaged by the open volume defect sensitive S-parameter. For the low dose there is recovery of the damaged region from the projected range and from the front surface from 373 K itself with a marked reduction in S-parameter. However the drop is significant beyond 473 K signalling the importance of some process which enhances the open volume defect or vacancy removal after this thermal barrier. There is also a movement towards surface from 623 K - 773 K, which is an extremely low temperature for all sorts of defect migration along the c-axis with the reported migration energies for c-axis diffusion. For higher dose sample however there is no recovery at the projected range till 673 K. Near surface recovery starts only at 423 K and the barrier at 473 K is significantly visible with large drop in S-parameter at the first temperature (523 K) beyond this point. The surface bound movement is from 723-773 K. For both low dose and high dose sample complete recovery is achieved by 973 K, but the structure to which recovery happens is different with higher dose sample giving a lower than bulk S-

parameter which was also reported by Yang et.al.[99], however no explanations were provided.

The 473 K annealing temperature which seems important here is linked to the Wigner energy release process and is attached to I-V recombination [50]. However the process which leads to recombination has many possible candidates. Many of the earlier studies has considered the possibility of I getting released from a trap whose binding energy is of the order of 1.3 eV, though the exact nature of trap was not identified [16-18]. Some others utilized the lower migration of I to account for I-V recombination at temperatures lower than 473 K and disassociation of I_2 clusters for recombination beyond 473 K [50]. Accumulation of I_2 and vacancy loop at temperatures lower than 573 K, disassociation and migration of I_2 above 573 K and migration of vacancies to form vacancy loop at 773 K are another set of processes speculated to explain the recovery process at temperatures which is much lower than the recrystallisation in 2D or 3D [61]. An intimate I-V pair which was first theoretically predicted and later experimentally seen [91, 97] is also held responsible for the sudden jump near 473 K. It was also shown theoretically that I-V pairs did not form in all cases and depended on the approach of I near a α-site (atom on top and bottom) or a β-site (hexagon centre top and bottom). I-V pair was shown to form only near β-site and no barrier was seen for recombination at α-site. I-V pair recombination barrier was also depended on its nearby structure – perfect, sheared or near-surface [84]. The vacancy is assumed to be immobile in many of these speculated processes and hence required a mobile I. Telling et.al. [89] also assumed structures like inter-planar divacancy to explain the observed immobility of otherwise mobile (~ 1.7 eV) vacancy and attached its existence to vacancy density. The slow recovery was always associated with I released from large clusters or dislocation loops of I type, and vacancy clustering to or collapsing to dislocation loop of V type.

The channelling result by Venkatesan et.al. [36] reflects (Fig.1) I movement and it can be seen that I is released near surface even at 573 K. It could be also assumed from the known migration energies that I migrates before a vacancy and hence the initial recovery at 423 K for higher dose sample could be due to I migrating to α-sites leading to I-V recombination without any barrier or to β-sites leading to I-V intimate pairs. When the 473 K barrier is over come I migration followed by enhanced I-V recombination could explain the observed large reduction of S-parameter near surface. Theoreticians have predicted at least three type of interstitial positions-bridge, y lid and spiro- their stability depending on the existence of sheared graphitic order [93]. The defects, I and V which recovered from 423-523 K near surface also caused large increase in FWHM and defect peak intensity ratio in Raman spectrum. Hence those structures which could cause an interlayer bonding with basal plane buckling could be responsible here rather than simple bridge structures. Hence the migration of single I which cause interlayer bonding is thought to start from 423 K. The recovered vacancy defect may also be of larger type like the V_6 or V_9 as predicted by pulsed positron lifetime [13].

The lack of recovery at the end of range is due to alternate I and V structures which are more stable against migration or recombination. The S-W correlation plot (Fig. 18) gives evidence that the vacancy structure in the as irradiated state and that in 523 K annealed condition are different. It could be thermally produced by vacancy clustering. This is possible if the vacancy migration barrier is in the range as predicted by most of the theoretical studies i.e. 1-1.7 eV. The new structure formed should also be energetically more favourable than its isolated components. If any barrier for structure transformation is involved then that should be achievable in this thermal treatment. For example the first neighbour in-plane divacancy formation from migrating monovacancy has to undergo a barrier of at least 1.6 eV to collapse to 5-8-5 structure [81]. Since there

is an indication of c-axis migration at 723 K, a-axis migration which would involve lesser structural barriers could happen at earlier temperatures. Larger vacancy clusters could also be produced athermally by knock out near a vacancy which does not get enough time to relax. Such defect formation was experimentally demonstrated by in-situ HRTEM measurements where vacancy loops were imaged during the dynamic condition of electron irradiation [122]. These loops were thought to originate from the in plane divacancy that collapses to a vacancy line and which later leads to dislocation dipoles as predicted by Niwase et.al [66]. Another possible vacancy structure which is stable against migration and recombination and which can be formed thermally or otherwise is the inter-planar cross linking di-vacancy. When other vacancy structures in the end of range are removed in the relaxation process prior to 523 K, these stable entities come to the fore as prominent trapping sites. Vacancy loops of appreciable size are shown to exist till very large temperatures like 1773 K. Also the migration energy for in-plane divacancy has been consistently modelled to be large of the order of 7 eV and hence once it forms in the temperature range of present annealing there is only possibility for its growth and no chance of any movement. However beyond 723 K there is marked movement of the structure towards surface. Thus the most possible structure giving a separate peak from 523 – 673 K is inter-planar divacancy. This is the first time any evidence is given for such structure and a temperature range where it could exist is shown. It has greater probability to form at the end of implantation range when the primary knock on has only enough energy to create at most one more secondary. Along the c-axis, it is only when the primary knock on is displaced at acute angles forcing it travel through the inter layers that the vacancies in corresponding layers be widely separated. Otherwise the vacancies can be at least in second nearest neighbour position in adjacent layers causing it to interact and form interlayer bonds via the John-Teller

distorted atom near a vacancy. Its presence is also related to vacancy density i.e probability of having two nearby vacancies at adjacent layers reduce with reduced density thereby not making them homogeneously distributed to efficiently trap positrons.

The interlayer divacancy structure becomes unstable beyond 723 K and this result in release of vacancies at adjacent planes. The released vacancies are seen to move towards the surface. This is surprising given the high barrier for c-axis migration for vacancies. It could be noted in the channelling data there is no movement or drop of disorder at the implanted range even at 1373 K annealing and hence the drop here in the peak S-parameter near to R_p at 723 K has to be due to divacancy disassociation. The observed migration towards surface warrants a theoretical relook at vacancy diffusion along c-axis. The observed threshold in the "intensity ratio" and "FWHM" recovery near 523-723 K could be attributed to this transition from the first to the second recovery phase. In the first phase maximum possible near surface defect recovery has been achieved till 523 K and in the second phase at 723 K there is vacancy migration towards surface thereby maintaining the D-peak intensity at around the same value. The surface bound vacancy recovery process is slow due to the complexity of c-axis migration. After complete removal of vacancies by annealing up to 1273 K, the S-parameter in the damaged region is lower than the bulk S-value. It was assumed that single I migrate beyond 423 K above. This may also lead to the formation of highly stable di-interstitials or their clusters which form very strong interlayer bonds. The densification due to such sp^3 natured clusters could explain the occurrence of lower than bulk S-value in the damaged region as well as in near surface region. It has to be remembered that when basal plane vacancies are removed positrons annihilate mainly from interlayer regions. Similar argument was given before for the observed positron lifetime drop in neutron irradiated samples [69].

In the case of low dose sample however the vacancy annealing mechanism is much simpler because of the presence of mostly isolated Frenkel defects. Through Raman spectroscopy and AFM it is clear that there is not much disorder along the c-axis and hence interlayer cross linking defects (I and V) will be less dense. Thus I would be mostly bridge type and vacancies would have John Teller distortion however little cross linking. This is evidenced by sharp drop seen in Raman intensity ratio as well as S-parameter recovery both from the front and back surface that could be attributed to the I-V recombination from 373 K. Compared to 373 K, there is larger S-parameter recovery at 423 K and no change at 473K. Taking clue from the recovery in high dose sample from 423 K, it can be argued that recovery from 373-423 K is due to migrating isolated bridge interstitials where as from 423 K – 473 K the cross linking interstitials also become mobile and contribute to recombination. However, the little S-parameter change at 473 K shows that for further large scale annealing the recombination barrier has to be overcome. This is found true by the pronounced drop at 523 K. The S-W correlation plot had shown a change of defect pattern at 373 K from as irradiated state which is followed up only by decrease in its intensity with annealing signalling the existence of different vacancy states in as-irradiated state. From 623-773 K there is a movement of defects towards surface (again showing a c-axis migration) and this coincides with the increase seen in the Raman intensity ratio. Thus the threshold region seen for intensity ratio recovery at 523-723 K is again associated with fast recovery followed by the complex process of c-axis migration of defects towards surface and hence is slow.

Here no mention has been given when the basal plane migration of vacancies start. No such indications of basal plane migration were obtained from the positron beam measurements; however an intelligent guess can be made based on the following arguments. Since basal plane migration is energetically and structurally more simple than

c-axis migration, the basal plane migration has to be before 623 K i.e. before *c-axis* migration. If vacancy migration starts before the recombination barrier is achieved then pronounced vacancy and interstitial clustering would be there which would not result in the observed S-parameter drop seen at 523 K for higher dose sample. Hence the migration should be after 473 K. This agrees well with the theoretical value of around 1.7 eV [89].

3.5 Summary

The defect annealing mechanism has been investigated at different depth scales in HOPG samples irradiated to two different doses. AFM, Raman and Slow positron spectroscopy has thrown light on the microstructural changes due to irradiation and their thermal recovery. The major findings of this study are

- For higher dose implantation a highly ridged structure is obtained which is due to the breaking, bending and curling of the graphitic sheets. Recovery of sub-surface defects at surface sink has some effect on topography with enhanced stress relief via wrinkling. Low dose shows near flat surface after sub-surface defect recovery although small amount of curling remains.
- The integrated intensity ratio obtained from Raman spectrum shows a fast recovery process followed by a threshold region and a slow recovery up to 1273 K for both high and low dose sample. Recovery via I-V recombination is responsible for the fast near surface recovery. Threshold region is due to the transition from fast I-V recombination process to a slow defect migration process where there is migration of vacancies to surface.
- For low dose sample open volume defect recovery as seen by positron Doppler broadening spectroscopy, starts from 373 K itself and is due to I-V recombination

as pointed out before. Isolated point defects which do not contribute to inter layer bonding like the bridge interstitials and monovacancies play a major role here. After the recombination barrier is overcome an enhanced S-parameter recovery is seen. c-axis migration starts from 623-773 K, which is much less than the migration barrier reported.

- For high dose sample surface recovery starts at 423 K which gets enhanced beyond the I-V recombination barrier at 473 K. Cross linking single interstitials and vacancy clusters which could absorb interstitials play a major role here. Such structures was assumed to account for observed large FWHM of G-band and its fast recovery in Toto with near surface S-parameter drop. Interlayer divacancy is shown to trap vacancies near the projected range from 523-673 K, beyond which they break and show a migration towards surface from 723 K, the existence of which is shown for the first time. The migration also correlates well with threshold region seen in both FWHM and intensity ratio recovery seen in Raman spectrum. Complete recovery is obtained after 973 K.
- An indication of when the basal plane migration starts was obtained indirectly to be between 473 and 623 K.
- When compared to channelling data by Venkatesan et.al. [36], it becomes clear that interstitials are locked up in stable structure near the implanted range and are responsible for the low S - value obtained at 1273 K. As interstitials are mobile from 423 K, cross linking di-interstitials could be responsible for S-parameter values lower than that in the bulk.

3.6 Conclusion & Future outlook

A comprehensive vacancy annealing mechanism in irradiated HOPG was brought out by using slow positron beam, Raman and AFM measurements. It was shown that the defect annealing mechanism is dependent on the dose of implantation and the density as well as type of defects produced at different implantation. New theoretical studies have to be invoked on c-axis migration of vacancies as surface migrations at lower temperatures were reported here. Experimental evidence for vacancy trapping defect types was also provided for the first time along with their thermal stability.

It is possible to identify pin-pointedly the various defect process reported here by the identification of defect structures involved by carrying out beam based positron lifetime experiments. Isothermal annealing studies can be carried out to find the activation energies of various processes reported here. It is also important to track surface restructuring using STM which provides much higher resolution than AFM with each annealing step. The studies could be complemented by ab-initio calculation to find positron parameters – lifetime as well as momentum distribution – for various exotic defect structures like the interplanar divacancy, intimate I-V pair and cross linking interstitial clusters which can be compared with the obtained experimental values.

References:

1. Shimotomai M, Takahashi T, Fukushima H, Doyama M and Iwata T 1981 *"Irradiation Behaviour of Graphite probed by Positrons" J. Nucl. Mat.* **103 - 104** 779.
2. Dresselhaus M S and Kalish R 1992 *"Ion implantation in Diamond, Graphite and related materials" Springer series in material science ed. Gonser U et.al.* (Berlin: Springer Verlag).

3. Telling R H and Heggie M I 2007 "*Radiation defects in graphite*" *Phil. Mag.* **87** 4797.
4. Niwase K, Nakamura G K, Yokoo M, Ken-ichi K and Iwata T 2009 *"Pathway for the transformation from highly oriented pyrolytic graphite into amorphous diamond*" *Phys. Rev. Lett.* **102** 116803.
5. Zaiser M and Banhart F 1997 *"Radiation-Induced Transformation of Graphite to Diamond" Phys. Rev. Lett.* **79** 3680.
6. Krasheninnikov A V, Nordlund K, Keinonen J and Banhart F 2002 *"Ion-irradiation-induced welding of carbon nanotubes" Phys. Rev. B* **66** 245403.
7. Esquinazi P, Spemann D, Höhne R, Setzer A, Han K H, and Butz T 2003 *"Induced Magnetic Ordering by Proton Irradiation in Graphite" Phys. Rev. Lett.* **91** 227201.
8. Scheike T, Böhlmann W, Esquinazi P, Barzola-Quiquia J, Ballestar A and Setzer A 2012 *"Can Doping Graphite Trigger Room Temperature Superconductivity? Evidence for Granular High-Temperature Superconductivity in Water-Treated Graphite Powder" Adv. Mater.* **24** *5826.*
9. Larkins G and Vlasov Y 2011 *"Indications of superconductivity in doped highly oriented pyrolytic graphite" Supercond. Sci. Technol.* **24** 092001.
10. Nordlund K, Keinonen J and Mattila T 1996 *"Formation of ion irradiation induced small-scale defects on graphite surfaces" Phys. Rev. Lett.* **77** 699.
11. Dolbec R, Irissou E, Chaker M, Guay D, Rosei F, and El Khakani M A 2004 *"Growth dynamics of pulsed laser deposited Pt nanoparticles on highly oriented pyrolitic graphite substrates" Phys. Rev. B* **70** 201406(R).
12. Jian-Hao C, Cullen W G, Williams E D and Fuhrer M S 2011 *"Tuneable Kondo effect in graphene with defects" Nature Physics* **7** 535.
13. Tang Z, Hasegawa M, Shimamura T, Nagai Y, Chiba T, Kawazoe Y, Takenaka M, Kuramoto E and Iwata T 1999 *" Stable vacancy clusters in neutron-irradiated graphite: Evidence for aggregations with a magic number*" *Phys. Rev. Lett.* **82** 2532.
14. Berko S, Kelley R E and Plaskett J S 1957 "*Angular correlation of annihilation radiation from oriented graphite" Phys. Rev.* **106** 824.
15. Elman B S, Shayegan M, Dresselhaus M S, Mazurek H and Dresselhaus G 1982 *"Structural characterisation of ion-implanted graphite" Phys. Rev. B* **25** 4142.

16. Kelly B T 1969 *"Thermal annealing of pyrolytic graphite irradiated with fast neutrons at 40^0 C" Carbon* **7** 699.
17. Kelly B T 1977 *"The theory of irradiation damage in graphite" Carbon* **15** 117.
18. Mitchell E W J and Taylor M R 1965 *"Mechanism of stored-energy release at 200 C in electron-irradiated graphite*" *Nature* **13** 638.
19. Thrower P A and Loader R T 1969 *"Interstitial atom energies in graphite*" *Carbon* **7** 467.
20. Thrower P A and Mayer R M 1978 *"Point defects and self-diffusion in graphite*" *phys. stat. solid.* (a) **47** 11.
21. Nakamura K and Kitajima M 1992 *"Ion-irradiation effects on the phonon correlation length of graphite studied by Raman Spectroscopy" Phys. Rev. B* **45** 78.
22. Nakamura K G, Asari E and Kitajima M 1992 "*Thermal relaxation of lattice disorder in graphite induced by He+ irradiation" Solid State Comm.* **82** 569.
23. Kitajima M and Nakamura K 1992 "*Initial damage in graphite under ion irradiation studied by real-time Raman measurement*" *J. Nucl. Mat.* **191** 356.
24. Kazutaka G, Nakamura and Kitajima M 1993 "*Time-resolved Raman measurements of a graphite surface under ion irradiation*" *Surf. Sci.* **283** 255.
25. Asari E,Kitajima M and Nakamura K G 1993 "*Thermal relaxation of ion-irradiation damage in graphite" Phys. Rev. B* **47** 143.
26. Nakamura K, Fujitsuka and Kitajima M 1990 "*Disorder-induced line broadening in first-order Raman scattering from graphite" Phys. Rev. B* **41** 260.
27. Nakamura K and Kitajima M 1992 "*Raman studies of graphite lattice-disordering kinetics under low-energy He-ion irradiation*" *Phys. Rev. B* **45** 5672.
28. Asari E, Kamioka I, Nakamura K G, Kawabe T and Lewis W A 1994 *"Lattice disordering in graphite under rare-gas ion irradiation studied by Raman spectroscopy" Phys. Rev. B* **49** 1011.
29. Kitajima M, Asari E and Nakamura K G 1994 *"Real-time observation of thermal relaxation of initial damage in graphite under ion irradiation" J. Nucl Mater.* **212-215** 139.
30. Asari E, Nakamura K G, Kawabe T and Kitajima M *1997 "Observation of relaxation processes of disorder in ion-irradiated graphite using Raman spectroscopy*" *J. Nucl. Mater*. **244** 173.

31. Asari E, Kitajima M and Nakamura K G 1998 "*A kinetic study of the recovery process of radiation damage in ion-irradiated graphite using real-time Raman measurements*" *Carbon* **36** 1693.
32. Elman B S, Braunstein G, Dresselhaus M S, Dresselhaus G, Venkatesan T and Gibson J M 1984 *"Observation of two-dimensional ordering in ion-damaged graphite during post-implantation annealing" Phys. Rev. B* **29** 4703.
33. Elman B S, Dresselhaus M S, Dresselhaus G, Maby E W and Mazurek H 1981 *"Raman scattering from ion-irradiated graphite" Phys. Rev. B* **24** 1027.
34. Elman B S, Braunstein G, Dresselhaus M S and Venkatesan T 1985 *"Retention of Impurities in Ion Implanted Graphite" Nucl. Inst. Meth. Phys. Res. B* **7/8** 493.
35. Elman B S, Braunstein G, Dresselhaus M S, Dresselhaus G, Venkatesan T and Wilkens B 1984 "*Channeling studies in graphite*" *J. Appl. Phys.* **56** 2114.
36. Venkatesan T, Elman B S, Braunstein G, Dresselhaus M S and Dresselhaus G 1984 "*Ion channelling studies of regrowth kinetics of disordered surface layers on graphite" J. Appl. Phys.* **56** 3232.
37. Roth J, Moller W, Poker D B and Wittmaack K 1986 "*Ion induced self diffusion of carbon" Nucl. Inst. Meth. Phys. Res.B* **13** 409.
38. Soder B, Roth J and Moller W 1988 "*The influence of the grain size on the mobility of irradiation induced self-interstitials in graphite" Nucl. Inst. Meth. Phys. Res. B* **32** 160.
39. Soder B, Roth J and Moller W 1988 "*Anisotropy of ion-beam-induced self-diffusion in pyrolytic graphite" Phys. Rev. B* **37** 815.
40. Siegele R, Roth J, Scherzer B M U and Pennycook S J 1993 *"Damage and deuterium trapping in highly-oriented pyrolytic graphite*" *J. Appl. Phys.* **73** 2225.
41. Iwata T, Fujita E F and Suzuki H 1961 *"On the energy of the interstitial atom in graphite" J. Phys. Soc. Jpn.* **16** 197.
42. Iwata T, Nihira T and Matsuo H 1968 "*Recovery of electrical resistivity below 80 K in electron-irradiated pyrolytic graphite*" *Physics Letters* **28A** 146.
43. Iwata T, Nihira T and Matsuo H 1972 "Low *temperature electron-irradiation damage and recovery in pyrolytic graphite" J. Phys. Soc. Jpn.* **33** 1060.
44. Iwata T, Nihira T and Matsuo H 1974 *"Irradiation and annealing effects on the c-axis electrical resistivity of graphite" J. Phys. Soc. Jpn.* **36** 123.
45. Nihira T and Iwata T 1975 "*Thermal resistivity changes in electron-irradiated pyrolytic graphite" Jpn. J.Appl. Phys.* **14** 1099.

46. Maeta H, Iwata T and Okuda S 1975 *"Recovery of c-axis spacing in pyrolytic grahite after neutron irradiation at 5 K" Physics Letters* **53A** 295.
47. Maeta H, Iwata T and Okuda S 1975 *"c-Axis spacing changes in pyrolytic graphite after neutron irradiation at 5 K" J. Phys. Soc. Jpn.* **39** 1558.
48. Iwata T and Nihira T 1976 *"Stored energy release in electron-irradiated graphite*" *Jpn. J. Appl. Phys.* **15** 575.
49. Taji Y, Yokota T and Iwata T 1986 "*Dynamic simulation of interstitial atom in graphite*" *J. Phys. Soc. Jpn.* **55** 2676.
50. Iwata T 1985 *"Fine structure of Wigner energy release spectrum in neutron irradiated graphite" J. Nucl. Mat.* **133 - 134** 361.
51. Iwata T, Fukushima H, Shimotomai M and Doyama M 1981 "*Characterisation of Graphites by Positron Lifetimes*" *Jpn. J. Appl. Phys.* **20** 1799.
52. Shimotomai M, Iwata T, Takahashi T and Doyama M 1983 *"Vacancy in Graphite: Positron Studies" J. Phys. Soc. Jpn.* **52** 694.
53. Shimotomai M, Takahashi T, Fukushima H, Doyama M and Iwata T 1981 *"Irradiation Behaviour of Graphite probed by Positrons" J. Nucl. Mater.* **103 - 104** 779.
54. Niwase K, Sugimoto M, Tanabe T and Fujita 1988 *"Electron microscope study of radiation damage in graphite produced by D^+ and He^+ bombardment" J. Nucl. Mater.* **155-157** 303.
55. Niwase K, Tanabe T, Sugimoto M and Fujita F E 1989 *"Modification of graphite structure by D^+ and He^+ bombardment" J. Nucl. Mater.* **162-164** 856.
56. Niwase K, Nakamura K, Tanaka I, Miyamoto Y and Tanabe T 1991 *"Laser Raman microprobe analysis of the modified surface of He^+-irradiated graphite" J. Nucl. Mater.* **171-181** 214.
57. Niwase K and Tanabe T 1991 "*Modification of graphite structure by D^+ and He^+ bombardment-II" J. Nucl. Mater.* **179-181** 218.
58. Tanabe T, Niwase K, Tsukuda N and Kuramoto E 1992 "*On the characterisation of graphite*" *J. Nucl. Mater.* **191** 330.
59. Niwase K, Tanabe T, Tanaka 1992 "*Annealing experiment of ion-irradiated graphite by laser Raman spectroscopy" J. Nucl. Mater.* **191** 335.
60. Niwase K and Tanabe T 1993 *"Defect structure and amorphization of graphite irradiated by D^+ and He^+" Materials Transactions, JIM* **34** 1111.

61. Niwase K 1995 "*Irradiation-induced amorphization of graphite*" *Phys. Rev. B* **52** 15 785.
62. Niwase K, Atou T, Nakamura K G and Iwata T 2012 "*Effect of dose and pressure on the transformation from neutron-irradiated graphite to amorphous diamond*" *J. Phys: Conf.* Ser. **377** 1.
63. Hirai T, Compan J, Niwase K and Linke J 2008 *"Laser Raman microprobe analysis of graphite exposed to edge plasma in the TEXTOR tokamak" J. Nucl. Mater.* **373** 119.
64. Niwase K 2012 *"Raman spectroscopy for quantitative analysis of point defects and defect clusters in irradiated graphite*" *International Journal of Spectroscopy* **2012** 1.
65. Niwase K 2004 "*Formation of dislocation dipoles in irradiated graphite*" *Materials Science and Engineering: A* **400-401** 101.
66. Niwase K 2002 *"Irradiation induced amorphization of graphite: A Dislocation accumulation model" Phil. Mag. Lett.* **82** *401.*
67. Tanabe T, Maruyama T, Iseki M, Niwase K and Atsumi H 1995 "*Radiation Damage of graphite: degradation of material parameters and defect structures" Fusion Engineering and Design* **29** 428.
68. Muto S and Tanabe T 1997 "*Damage process in electron-irradiated graphite studied by transmission electron spectroscopy.I.High-resolution observation of highly graphitized carbon fibre*" *Phil. Mag.* **76** 679.
69. Tanabe Tetsuo 1996 *"Radiation damage of graphite-degradation of material parameters and defect structures" Physics Scripta* **T64** 7.
70. Muto S, Takeuchi M and Tanabe T 1997 "*A new microscopic model of electron irradiation damage in graphite" J. Surf. Analysis* **3** 420.
71. Hinman W G, Haubold A and Gardner J O and Layton K J 1970 *"Vacancies and interstitial clusters in irradiated graphite*" *Carbon* **8** 341.
72. Burchell T D, Pappano P J and Strizak J P 2011 *"A study of te annealing behaviour of neutron irradiated graphite" Carbon* **49** 3.
73. Paredes J I, Solis-Fernandez P, Martinez-Alonso A and Tascon J M D 2009 "*Atomic vacancy engineering of graphite surfaces:Controlling the generation and harnessing the migration of the single vacancy*" *J. Phys. Chem. C* **113** 10249.
74. Annis B K, Pedraza D F and Withrow S P 1993 *"Topological changes induced by high carbon-bombardment of graphite" J. Mater. Res.* **8** 2587.

75. Kaxiras E and Pandey K C 1988 "*Energetics of defects and diffusion mechanisms in graphite*" *Phys. Rev. Lett.* **61** 2693.
76. Xu C H, Fu C L and Pedraza D F 1993 "*Simulations of point-defect properties in graphite by a tight-binding-force model*" *Phys. Rev. B* **48** 13273.
77. Li L, Reich S and Robertson J 2005 "*Defect energies of graphite: Density-functional calculations*" *Phys. Rev. B* **72** 184109.
78. Lehtinen P O, Foster A S, Ayuela A , Krasheninnikov A, Nordlund and Nieminen R M 2003 *"Magnetic properties and diffusion of adatoms on a graphene sheet" Phys. Rev. Lett.* **91** 017202.
79. Krasheninnikov A V, Lehtinen P O, Foster A S and Nieminen R M 2006 "*Bending the rules: Contrasting vacancy energetic and migration in graphite and carbon nanotubes*" *Chemical Physics Letters* **418** 132.
80. Krasheninnikov A V, Nordlund K, Lehtinen P O, Foster A S, Ayuela A and Nieminen R M 2004 *"Adsorption and migration of carbon adatoms on zigzag carbon nanotubes*" *Carbon* **42** 1021.
81. Gun-Do L, Wang C Z, Yoon E, Nong-Moon H, Doh-Yeon K and Ho K M 2005 "*Diffusion, coalescence and reconstruction of vacancy defects in graphene layers*" *Phys. Rev. Lett.* **95** 205501.
82. Ma Y 2007 "*Simulation of interstitial diffusion in graphite*" *Phys. Rev. B* **76** 075419.
83. Teobaldi G, Ohnishi H, Tanimura K and Shluger A L 2010 *"The effect of van der Waals interactions on the properties of intrinsic defects in graphite" Carbon* **48** 4145.
84. Teobaldi G, Tanimura K and Shluger 2010 *"Structure and properties of surface and subsurface defects in graphite accounting for van der Waals and spin-polarisation effects" Phys. Rev. B* **82** 174104.
85. Zhang H, Zhao M, Yang X, Xia H, Liu X and Xia Y 2010 *"Diffusion and coalescence of vacancies and interstitials in graphite: A first-principles study" Diamond and Related Materials* **19** 1240.
86. Yazyev O V, Tavernelli I, Rothlisberger U and Helm L 2007 "*Early stages of radiation damage in graphite and carbon nanostructures: A first-principles molecular dynamics study*" *Phys. Rev. B* **75** 115418; Yazyev V O and Helm Lothar 2007 *"Magnetism induced by single-atom defects in nanographites"* J. Phys: Conf. Ser. **61** 1294.

87. Ewels C P, Heggie M I and Briddon P R 2002 "*Adatoms and nanoengineering of carbon" Chemical Physics Letters* **351** 178.
88. Telling R H and Heggie M 2003 "*Stacking fault and dislocation glide on the basal plane of graphite" Phil. Mag. Lett.* **83** 411.
89. Telling R H, Ewels C P, El-Barbary A A and Heggie M I 2003 *"Wigner defects bridge the graphite gap" Nat. Mat.* **2** 303.
90. El-Barbary A A, Telling R H, Ewels C P, Heggie M I and Briddon P R 2003 "*Structure and energetic of the vacancy in graphite" Phys. Rev. B* **68** 144107.
91. Ewels C P, Telling R H, El-Barbary A A and Heggie M I 2003 "*Metastable Frenkel pair defect in graphite: Source of Wigner energy?" Phys. Rev. Lett.* **91** 025505.
92. Telling R H and Heggie M I 2007 "*Radiation defects in graphite*" *Phil. Mag.* **87** 4797.
93. Latham C D, Heggie M I, Gamez J A, Suarez-Martinez I, Ewels C P and Briddon P R 2008 *"The di-interstitial in graphite*" *J. Phys: Cond. Matter* **20** 395220.
94. Heggie M I, Suarez-Martinez I, Davidson C and Haffenden G 2011 "*Buckle, ruck and tuck: A proposed new model for the response of graphite to neutron irradiation" J. Nucl. Mater.* **413** 150.
95. El-Barbary A A 2005 *"First principles characterization of defects in irradiated graphitic materials" School of Life Sciences University of Sussex.*
96. Heggie M I, Suarez-Martinez I, Savini G, Haffenden G L and Campanera J M 2010 *"Radiation damage in graphite – A new model" Proc. IAEA consultancy 'Solution for graphite waste : A contribution to the accelerated decommissioning of graphite moderated nuclear reactors' Manchester U.K March 2007* IAEA-TECDOC-1647 39.
97. Urita K, Suenaga K, Sugai T , Shinohara H and Lijima S 2005 "*In situ observation of thermal relaxation of interstitial-vacancy pair defects in a graphite gap*" *Phys. Rev. Lett.* **94** 155502.
98. Hashimoto A, Suenaga K, Gloter A, Urita K and Lijima S 2004 *"Direct evidence for atomic defects in graphene layers" Nature* **430** 870.
99. Yang X, Xia H, Qin X, Li W, Dai Y, Liu X, Zhao M, Xia Y, Yan S and Wang B 2009 *"Correlation between the vacancy defects and ferromagnetism in graphite" Carbon* **47** 1399.

100. http://www.2spi.com/catalog/new/hopgsub.php
101. Arunkumar J 2011 *Doctoral Dissertation Department of Physics University of Madras.*
102. Amarendra G, Viswanathan B, Venugopal Rao G, Parimala J and Purniah B 1997 "*Variable low energy positron beams for depth resolved defect spectroscopy in thin film structures" Current Science* **73** 409.
103. van Veen A, Schut H, de Vries J, Hakvoort R A and Ijpma M R 1990 *"Analysis of positron profiling data by means of VEPFIT" Positron Beam for Solids and Surfaces AIP Conf. Proc. No.* **218** ed Schultz P J, Massoumi G R and Simpson P J (New York:AIP) 171.
104. Kansy J 1996 *"Microcomputer program for analysis of positron annihilation lifetime spectra" Nucl. Inst. Meth. Phys. Res. A* **374** 235.
105. Pimenta M A, Dresselhaus G, Dressselhaus M S, Cancado L G, Jorio A and Saito R 2007 *"Studying disorder in graphite-based systems by Raman spectroscopy" Phys.Chem.Phys.* **9** 1276.
106. Ferrero J R, Nakamoto K and Brown C W 2011 *"Introductory Raman Spectroscopy" second edition* (San Diego CA: Elsevier).
107. Mishra K K 2012 *Doctoral Dissertation IGCAR, Kalpakkam Homi Bhabha National Institute.*
108. Kamalakannan R 2012 *Doctoral Dissertation IGCAR, Kalpakkam Homi Bhabha National Institute.*
109. Ziegler J F, Biersack J P and Littmark U 1985 *"The Stopping Range of Ions in Solids"* (New York:Pergamon).
110. Ohdaira T, Suzuki R, Kobayashi Y, Akahane T and Dai L 2002 *"Surface analysis of a well-aligned carbon nanotube film by positron-annihilation induced Auger-electron spectroscopy" App. Surf. Sci.* **194** 291.
111. Sferlazzo P, Berko S, Lynn K G, Mills A P, Roellig L O, Viescas A J and West R N 1988 *"Evidence for phonon-assisted positronium emission from graphite" Phys. Rev. Lett.* **60** 538.
112. Tuinstra F and Koenig L J 1970 "*Raman spectrum of graphite*" *J. Chem. Phys.* **53 3** 1126.
113. Dresselhaus M S, Dresselhaus G, Saito R and Jorio A 2004 "*Raman spectroscopy of carbon nano tubes" Physics Reoprts* **10** 006.

114. Shimada T et.al. 2005 *"Origin of the 2450 cm^{-1} Raman bands in HOPG, single-wall and double-wall carbon nanotubes" Carbon* **43** 1049.

115. Ferrari A C 2007 "*Raman spectroscopy of graphene and graphite: Disorder, electron-phonon coupling, doping and nonadiabatic effects" Solid State Communications* **143** 47.

116. Watanabe H 1993 "*Structural characterisation of ion implanted HOPG and glass – like carbon by laser Raman spectroscopy" Nucl. Inst. Meth. Phys. Res. B* **80 – 81** 489.

117. An Bai, Fukuyama S, Yokogawa K and Yoshimura M 2000 *"Surface structure of Ar^{+} - ion irradiated graphite by scanning probe microscopy*" *Jpn. J. Appl. Phys*. **39** 3732.

118. Muto S, Tanabe T, Takeuchi M, Kobayashi Y, Furuno S and Hojou K 1999 *"TEM analyses of surface ridge network in an ion irradiated graphite thin film" J. Nucl. Mater.* **271 & 272** 285.

119. Hiura H, Ebbesen T W, Fujita J, Tanigaki K and Takada T 1994 *"Role of sp^3 defect structures in graphite and carbon nanotubes" Nature* **367** 148.

120. Mantl S and Triftshäuser W 1978 "*Defect annealing studies on metals by positron annihilation and electrical resitivity measurements" Phys. Rev. B* **17** 1645.

121. Mathew S ,Joseph B, Sekhar B R and Dev B N 2008 *"X-ray photoelectron and Raman spectroscopic studies of MeV proton irradiated graphite" Nucl. Inst. Meth. Phys. Res. B* **266** 3241.

122. Karthik C, Kane J, Butt D P, Windes W E and Ubic R 2011 *"In situ transmission electron microscopy of electron-beam induced damage process in nuclear grade graphite" J. Nucl. Mater.* **412** 321.

Interlude

The previous two chapters discussed about defect creation via ion implantation and their thermal evolution using slow positron beam Doppler broadening spectroscopy. Even though this technique could give a qualitative idea on the vacancy annealing mechanism including possible impurity complex formation, the exact nature of defects remained sketchy. This is because of the inability of defining a proper defect related functional form for the Doppler broadening of the 511 keV γ curve. These are two example cases were positron lifetime as a function of temperature would have given a more rigorous proof for some of the defect structures proposed. There are many other possible applications like in thin film technology where it is important to identify open volume defects in a depth resolved manner. In these applications a positron beam based lifetime system would be a good tool to supplement the findings of a beam based Doppler broadening results.

In the following chapters, an attempt at the design and development of a pulsed positron beam is described starting from the development of a slow positron beam for Doppler measurements. A methodology based on radio frequency pulsing, which has been successfully used for getting a beam based lifetime system worldwide has been utilized here.

If we don't see failure as a challenge to modify our approach, but rather as a problem with ourselves, as a personality defect, we will immediately feel overwhelmed. – Anthony Robbins

Chapter 4
Design of a Pulsed Positron Beam System

The design of a pulsed positron beam system which uses a ^{22}Na source and a magnetic transport has been described in this chapter. The pulsing system has three main components, a chopper and two bunchers. The design is based on positron trajectory calculations under the influence of time varying electric fields and static magnetic field using SIMION. Important design parameters like the frequency combination of pre-buncher and main buncher and the required magnetic field were tested in the simulation and validated. Some other parameters like the amplitude of the time varying voltage and the drift correction voltages were derived from the simulation. Based on these parameters a UHV system to house the pulsed positron beam has been designed, fabricated and tested. The solenoid and the Helmholtz coils for the guiding magnetic fields, the mechanical assembly of the pulsing electrodes, sample mounting and high voltage connections, as well as the arrangement to mount the source and the positron moderator were fabricated as a part of the design. The required RF components were identified and procured. The design of the impedance matching box as well as the timing circuit were also made.

4.1 Introduction

The ability of positron lifetime spectroscopy to identify the nature of defects and to quantify their concentration when combined with a slow positron beam can be an effective tool for problems such as those discussed in Chapters 2 and 3 [1]. Such a combination is possible, if a signal can be generated which indicates the entry of a positron in to the solid, the signal for its annihilation being the 511 keV γ. Number of methods has been employed for time tagging each positron entry into the solid [2-32]. In one technique, positrons were time tagged by the scintillation photons produced by the passage of positrons through a thin plastic scintillator [2], while some others used LINAC for positron generation and the inbuilt timing signal from LINAC as the time tag [3,4]. Yet another method detected the secondary electron ejection from the sample surface during the implantation of positrons to know the time at which positrons enter the solid [5-8]. Through this method Gidley et. al. [8] was able to get a time resolution of ~500 ps for their lifetime experiment which is very good for measurements involving o-Ps like lifetimes. The method suggested by Mills et.al. [9] where a harmonic potential is applied periodically to the incoming slow positron to modulate its voltage has been attempted in number of labs [10-30]. This is due to the conventional like time resolutions achievable with the method. Trapping of positrons in a magnetic bottle or Penning trap also gives reasonable time resolutions [31, 32]. The trigger signal to release the positron from the trap acts as the time tag here.

Among various techniques listed above, radio frequency potential assisted modulation of positron energy has been employed to probe problems in metals and semiconductors due to its superior resolution and repeatability. The differences among various attempts start with the source of positrons like ^{22}Na, LINAC or from reactor based neutrons [17, 23, 24, and 27]. The last two give high intensity positron beam

which can be re-moderated to get sub-mm or μm beam spot with positron beam intensity of the order of 10^8 s^{-1} and a lifetime event rate of ~10^3 s^{-1}. The radioactive source based lifetime beam is however suitable for small laboratories with a table top arrangement. The next difference among them comes from the number and relative arrangement of the key elements i.e. chopper and buncher. Chopper and buncher have been adapted into the positron beam from its use to produce nanosecond pulses in high energy ion beams [33]. Some pulsed positron systems have used just a two element model of one chopper and one buncher to attain lifetime spectrum [19, 24] while some others have achieved better resolutions with one chopper and two bunchers [25]. There are also differences in their relative positions. For example, a chopper can be put in front of two bunchers [11] whereas in some systems a pre-buncher is put first followed by a chopper and main buncher [16]. The design of chopper and buncher adopted are also different. Chopper can be reflection type grid based chopper or the deflection type. Similarly the buncher can be the λ/4 resonator cavity or a drift based double gap buncher. Since the implementation of buncher in a double gap form is simple and is as effective as the cavity, this was chosen for the beam designed in the thesis. The important parameters to be tuned once the base frequency and the higher harmonic are chosen are the length of the buncher tubes and the peak to peak value of applied radio frequency (RF) voltage depending on the time focal point. The phase difference between the signals which makes sure that each positron sees a particular region of the modulating signal can also be optimized; however this has to be tuned during the actual installation due to number of delays incorporated during RF coupling. Thus in this chapter a pulsed positron beam system based on RF pulsing is designed; the starting point however has to be with a slow positron beam.

4.2 Slow Positron Beam Physics

The primary components in any slow positron beam are a source, a moderator, a velocity selector and an accelerator. A beam focussing system with electrostatic lenses are also included, however this is not mandatory [34]. The first step is the moderation of positrons falling on to the moderator from the source. The moderator can be arranged in number of geometries [35] like the transmission geometry where positrons enter through one face while moderated positron emission is through the opposite face. In backscattering geometry the source is in front of the moderator surface from which remission takes place. There are still others which are quasi-transmission. Examples for such geometries are the moderators in the form of Venetian blinds or W polycrystalline mesh. This geometry requires a small potential on the source which is higher than that on the moderator to reflect the positrons emitted towards the source into the beam direction. With the availability of thin tungsten single crystals, the transmission geometry has become efficient and popular [36]. The thickness of the W (100) single crystals are chosen such that the maximum density of positrons in the β^+ spectrum reach the opposite surface when used in transmission geometry. Once on the surface, there are possibilities of getting trapped in the surface state or defect states near surface. There is also possibility of reemission as Ps. These processes happen in equal probability with the free positron emission. Hence the moderator has to be thermally treated to remove surface trap states like the native oxide layer or the near surface defects. It has also been observed that the free-positron emission increases when the moderator is thermally treated in oxygen atmosphere which was attributed to the inhibition of Ps formation by adsorbed oxygen [37]. The free positron is emitted from the moderator surface with an energy spread and an angular spread which is consistent with the thermal broadening

[38] at 300 K. The angular spread Δθ (FWHM) is about 10^0 with thermal spread in the range of 100's of meV for a mean positron work function of 2.8eV for W(100) [38].

The emitted positron can be extracted into the transport region by applying a small positive potential to the moderator with respect to the ground electrode which causes the positron to acquire a net momentum towards the ground electrode. The positron thus acquires an energy equal to work function energy plus *e* (charge) times the moderator potential. The confinement of positron to the beam axis can be achieved by magnetic field and hence the trajectory can be defined using the Lorentz force equation in the non relativistic regime as

$$m\frac{dv}{dt} = e(\boldsymbol{E} + \boldsymbol{v}\ \mathrm{X}\ \boldsymbol{B}) \qquad (1)$$

Where *m* is the mass of positrons, *e* is its charge $\boldsymbol{E}$ and $\boldsymbol{B}$ are the applied fields and $\boldsymbol{v}$ its initial velocity. A combination of electrostatic lenses can be used along with the simple extraction method for beam focussing [34]. As conservative forces are applied, Liouville's theorem is applicable to the phase space trajectory of the group of positrons. In a cylindrically symmetric electrostatic particle beam, the phase space of the beam in an area perpendicular to the beam axis is given by the r-θ diagram as shown in Fig.1 [39]. Extending the Liouville's theorem to this diagram the expression for phase space conservation becomes

$$4x\theta\sqrt{E} = constant \qquad (2)$$

where *x* and θ represents the spatial and angular co-ordinates and *E* is the energy of the beam. Thus a reduction in *x* would result in greater divergence, unless it is overcome by re-moderation.

An axial magnetic field with a bend is usually used to transport the emitted slow positrons from the source to the target. The bend, filters the slow positrons from the fast positrons and prevents the direct line of sight of the 1280 keV γ to the detector [39].

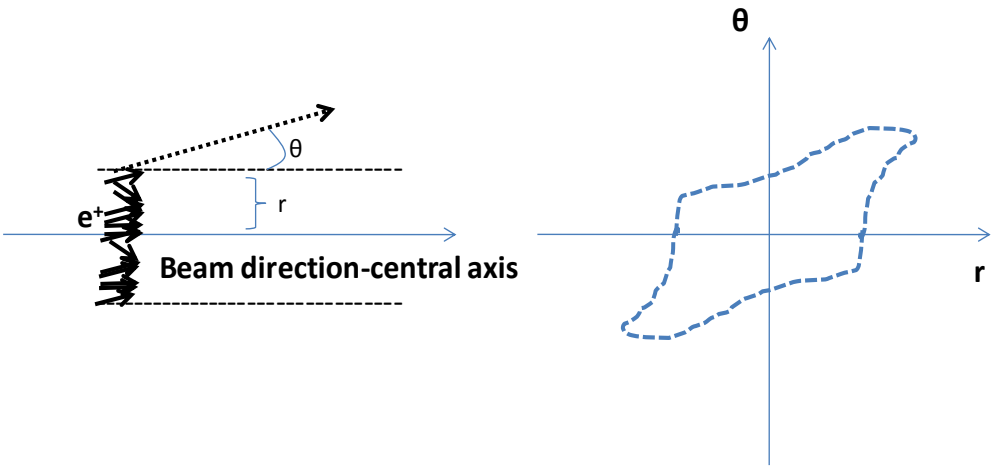

Fig. 1: Definition of r and θ for a beam and an example for an r-θ phase space area which is conserved by Liouville's Theorem [39].

Important factors that need to be considered here are field uniformity and its variation over one Larmor radius of positron. The importance of field uniformity and strength is evident from the relations

$$\frac{Sin\theta}{B} = constant \;\; ; \;\; tan\theta = \frac{v_{||}}{v_p} \tag{3}$$

where θ is the pitch, $v_{||}$ is the velocity component parallel to field and v_p is the velocity component perpendicular to the field $\boldsymbol{B}$. If field is too strong it can result in reflection of positrons having large pitch. Hence the field should be such that it confines the beam to centre without much effect from external fields like earth's magnetic field and it should not be too strong to squeeze the beam into reflection. Usually a field of 100 Gauss is employed which satisfies this condition [35]. If the beam is adiabatically varying over the bend then the positron will follow the field. However there are possibilities for off-axis drift given as

$$v_D = 2 * 10^8 \frac{E_{||}}{R*B} \tag{4}$$

where v_D is the drift velocity in cm/s, $E_{||}$ is the energy parallel to the field in eV, R is the radius of curvature of the bend and $\boldsymbol{B}$ is the field in gauss. Therefore, if R and B are

large, v_D will be small. If v_D is large, then correction has to be applied in form of external drift correction coils to kick the beam back to the axis [39]. Sharp bends can be used for similar velocity filtering but is based on a principle of making the Larmor radius equivalent to the radius of curvature of the bend by applying a transverse field at the bend instead of an axial one. The working of such a sharp 90^0 bend is given in Fig.2 simulated using SIMION [40]. However, this has been found to be difficult to achieve practically when compared to the axial field. In purely electrostatic beams, the beam diameter is controlled by focussing and the velocity selection is through deflection

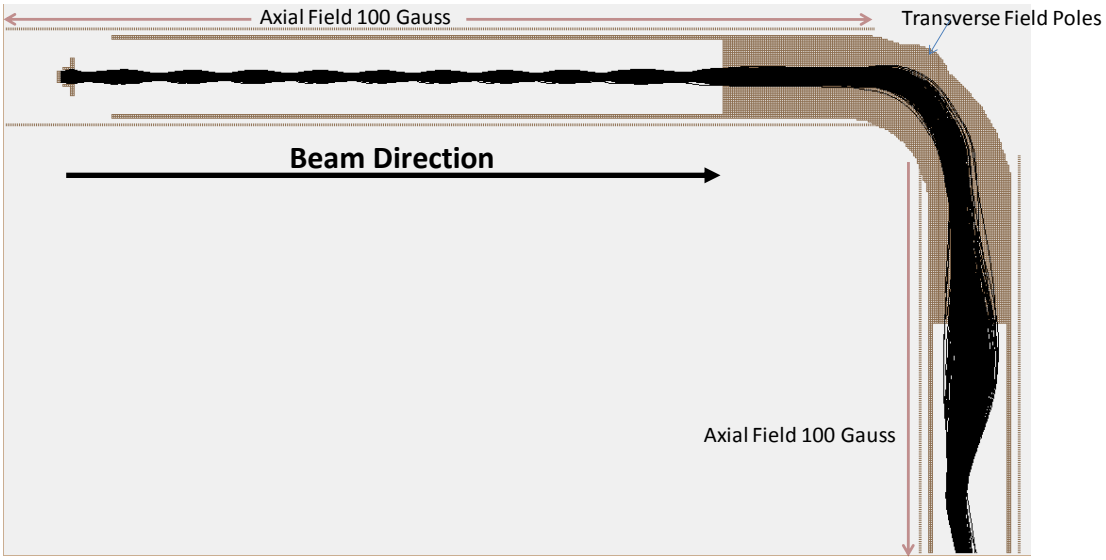

Fig. 2: Bending of positrons of selected energy through the 90^0 baffle by applying transverse magnetic fields. The field values are such that the Larmor radius is equal to the curvature radius. By careful positioning of the transverse field at the bend region, more than 95% transmission can be achieved.

mirrors. Special care has to be taken to avoid even small magnetic fields near the beam line and compensation coils has to be provided to negate any magnetic field along the beam direction [35]. Velocity selection is also achieved in magnetic beams using "E x B" filter where the electric field is applied perpendicular to the axial magnetic field. In the present thesis a magnetic bend based slow positron beam has been devised for its

ease and to avoid any electric field in the beam direction causing any unsolicited energy spread.

4.3 Pulsed Positron Beam Physics

The principle of RF potential assisted time focussing can be understood in terms of the classical problem of three particles travelling at different speeds one after the other, the faster particle going first and the slowest particle going last. If the middle particle is taken as reference, it is possible to calculate the amount of deceleration to be given to the first particle and the amount of acceleration to be given to the last particle such that after a certain travelling distance all three will be crossing at a point i.e. all of them take same amount of time from the start of acceleration/deceleration to travel a fixed distance. Thus if the start of acceleration/deceleration and the crossing time is known then the time of flight can be calculated. If any addition delay to the time of flight is added due to a different process, then it is also possible to calculate this delay as the fixed time of flight is known. This additional delay happens to be the annihilation rate in case of positrons. Pulsing is nothing but time focussing by moderation of particle energy and in terms of Lagrangian dynamics, energy and time are the conjugate variables in this problem. Thus the phase space area defined by them would be conserved under the action of a conservative force as was the case with spatial focussing. To start with we have a mono-energetic beam with large time spread as given in Fig. 3 (a) which is acted upon by conservative force because of which the time spread shortens. As the area is conserved this becomes a spread in energy as shown in Fig. 3(b) which at the focal point becomes a minimum possible time spread with a maximum possible energy spread (Fig. 3(c)).

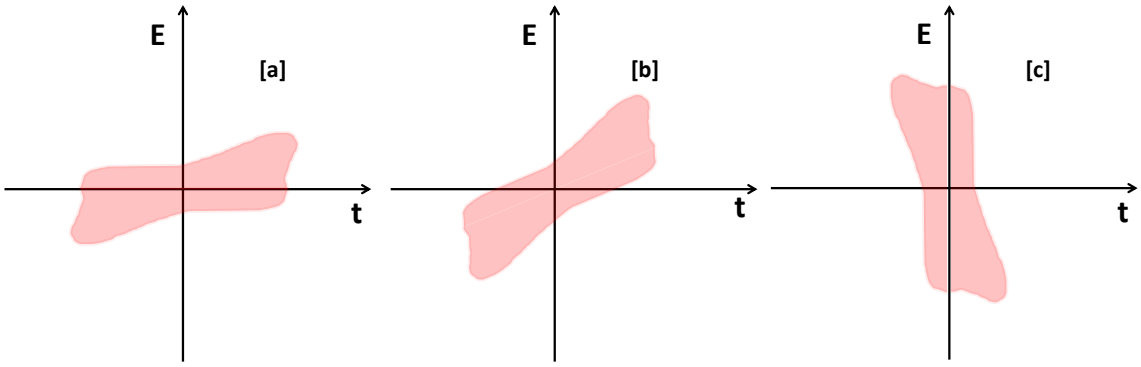

Fig. 3: Phase space defined by the conjugate variables Energy and Time during the time focussing of the charged particle. (a) phase space of a mono energetic beam (b) phase space after the action of an energy modulation to beam (c) phase space at the time focal point.

The time focussing or beam bunching described above can be achieved by the application of a time varying potential to particles arriving at a gap between two electrodes at random times. This is the working principle of bunchers. The exact potential to be applied can be got as follows [16]. If τ_0 is the time taken by reference or un-moderated particle to reach from the centre of the bunching gap to the target (L), then for any other particle at an instant t at the bunching gap, the time

$$t + \tau(t) = \tau_0 \tag{5}$$

where $\tau(t)$ is the time of flight of the modulated particle to the target. Now the time taken to travel from bunching gap to target (L) is

$$\tau(t) = \frac{L}{v(t)} \tag{6}$$

where $v(t)$ is the modulated velocity by the modulating voltage $V(t)$. The energy of the modulated particle would be $E_0 + eV(t)$, where E_0 is the incoming energy of the beam. Thus by using non relativistic expression for kinetic energy $v(t)$ is $\sqrt{\frac{2(E_0 + eV(t))}{m}}$ where m is mass of positron. Therefore substituting the expression for $v(t)$ in (6) and then in (5) it is possible to derive an expression for $V(t)$ as

$$V(t) = \frac{E_0}{e}\left(\frac{1}{\left(1-\frac{t}{\tau_0}\right)^2} - 1\right) \tag{7}$$

which is a parabolic potential and is difficult to achieve in practical scenarios at MHz frequency. This when approximated to the first term becomes a saw tooth wave given as

$$V(t) = \frac{2E_0}{\tau_0 e} t \tag{8}$$

which once again is approximated using a sine wave near the zero crossing as $V(t) = V_0 Sin(\omega t) \approx V_0\, \omega t$ near zero. Then

$$V_0 = \frac{2E_0}{\tau_0 e \omega} = \frac{2}{e\sqrt{m}} \frac{\sqrt{2E_0^3}}{\omega L} \tag{9}.$$

This expression can be used to find the peak voltage V_0 once the frequency ω and the focal point L from the buncher is fixed for a beam of positrons with energy E_0. A double gap buncher is kept to improve the bunching efficiency such that one more velocity modulation is applied at the second gap. However the length of the tube should be such that the reference positron of energy E_0 reaches the second gap at the second zero-crossing of the sine wave as indicated in the schematic below in Fig. 4. Thus, the length of the buncher electrode can be calculated in the non relativistic regime as

$$l_{buncher} = \frac{T}{2} v_0 \tag{10}$$

where T is the period of the applied sinusoidal voltage and v_0 is the unmoderated positron velocity. Hence, for an initial energy of 263 eV, a 50MHz sine wave would require a bunching electrode of length 95 mm and for 200 MHz sine wave the bunching electrode length would be 23 mm. As the ideal bunching potential is saw tooth, adding multiple harmonics of sine wave to a bunching electrode has been shown to improve the bunching efficiency. However it was later shown by Pandit et.al. [41] that using two separated electrodes with harmonically related frequencies is more efficient than having up to six harmonics at the same electrode. The base frequency selected should be such

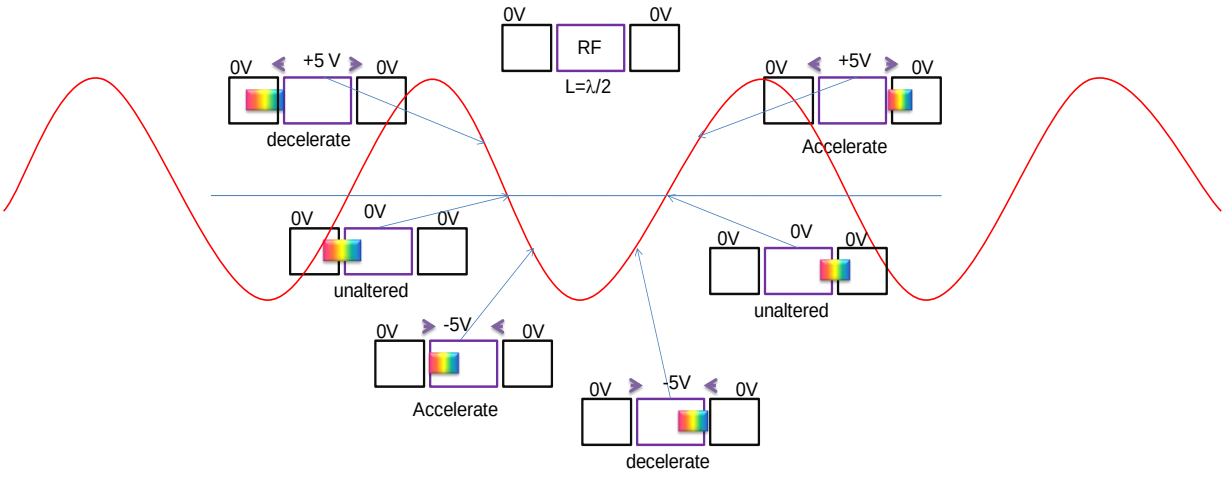

Fig. 4: The schematic shows the working of a double gap buncher. The necessity for the length of the bunching electrode to be equivalent to the distance travelled by the particle in half time period is clear as the reference positron has to come at zero crossing in both gaps.

that the time gap between positron pulses should be high enough for the acquisition of long lifetimes and the second frequency should be high enough to produce efficient compression at the time focal point. It was based on these considerations that a combination of 50 MHz – 200 Mhz has been chosen for the present beam.

However it is not possible to have infinite bunching efficiency with all positrons bunched into a particular pulse. The unbunched positrons between pulses will show up as long components in the positron lifetime spectrum. To avoid this, it is necessary to cut out the positrons between the pulses. This is done by the chopper, which chops the beam into pulses of base frequency. The chopping voltage should be equal to the incoming beam energy. For example for a moderator biased at +10V, positrons will have a mean kinetic energy of ~ 13eV. Thus the chopping voltage should have an amplitude of at least 13 V. The ideal function for the chopper potential is a square pulse which however will be difficult to couple to a load. The chopper can come before the buncher or after it. If it comes before the buncher the distance between them should be such that pulses reach the buncher without a large time broadening with drift. If it is after the buncher, then the time focus of the first buncher should be at the chopper such that the bunched pulses

reach the chopper at its “allow” phase and the unwanted positrons in between the pulses arrive at the “stop” phase. Thus the chopping frequency decides the time gap between the pulses and hence, some beams [23] employ variable frequency at the chopper to have variable time gaps to include both large and short positron lifetimes. The chopper can be achieved as a deflection type chopper, where the periodic potential deflects the positrons to an orifice or a reflection type three grid chopper where the middle grid reflects the positrons during the “stop” phase. Both have been introduced in the pulsing systems around the world. With the present design, the three grid chopper is selected.

4.4 Optimization of pulsing parameters – SIMION simulations

Based on the principles described above a positron pulsing system has been designed and optimized in SIMION [40]. SIMION is a finite difference based approach which calculates the 2D/3D electrostatic and scalar magnetic fields solving the Laplace equations and then the trajectories of charged particles through it by constant step integration using a highly modified 4^{th} order Runge-Kutta method. SIMION also follows a work-bench protocol where the physical entities making up the system could be placed on a gridded work bench. The electric potential as well as the magnetic field to the various electrodes could then be given and trajectory of the particle can be simulated. The user programming capabilities of SIMION using LUA [42] to set static (dc) as well as quasi static (RF) potentials for the electrodes was utilized. The magnetic field was set at 100 Gauss throughout the beam line. The beam was designed in a 2D geometry and hence the magnetic bends were not introduced and it was simulated as a straight section. The design used is shown in Fig. 5 (a-d). Fig. 5 (a) shows the moderator and the extraction grid, 5 (b) shows the chopper in three grid geometry where the third grid is given to the pre-accelration electrode. The pre-acceleration bias is -250 V. It also shows

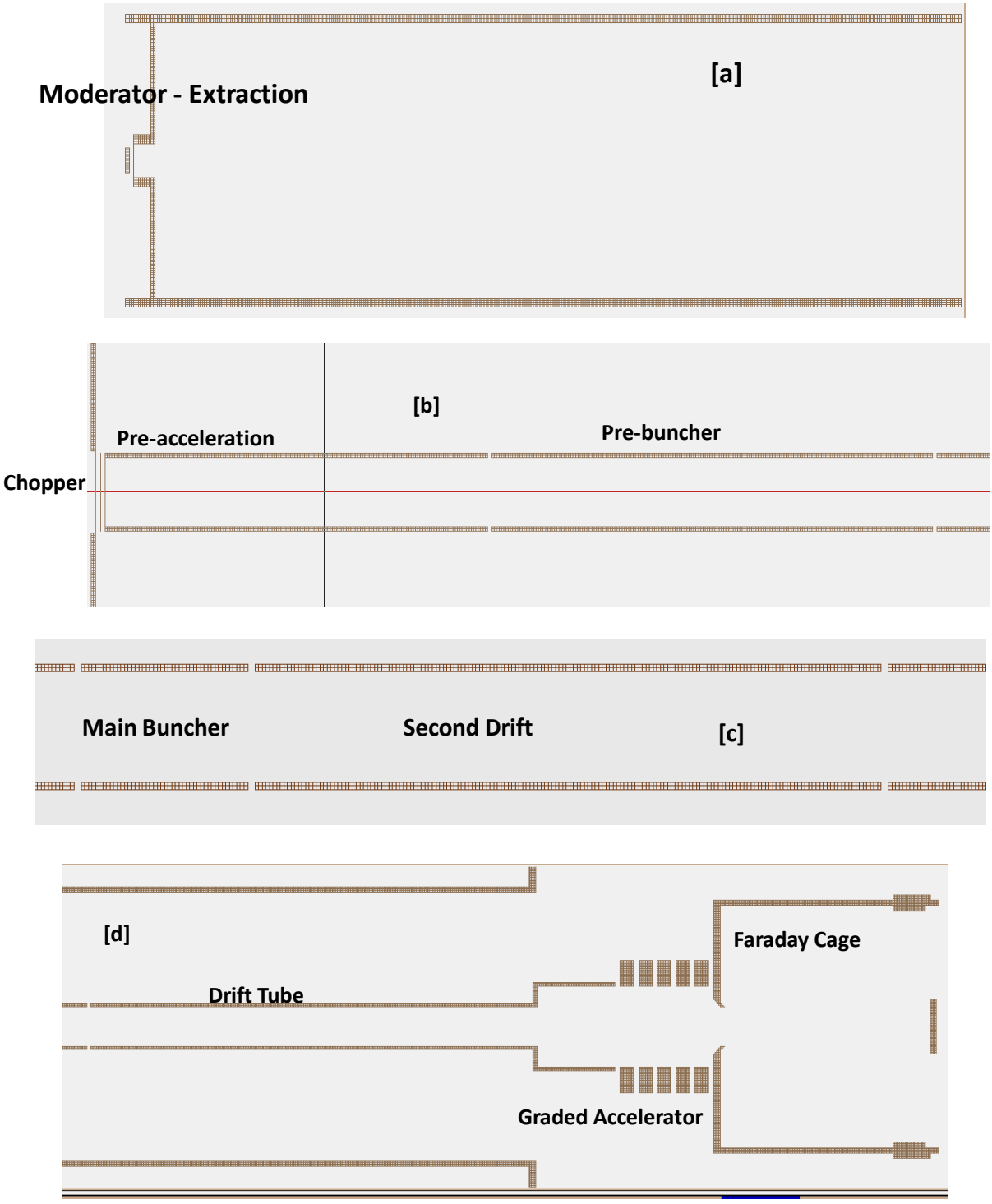

Fig. 5: The design used in simulating the pulsing electronics in SIMION [40] is shown. (a) shows the moderator and the extraction grid. (b) shows the chopper in three grid geometry where the third grid is given to the pre-accelration electrode. After pre-acceleration, the positron energy is 263 eV. It also shows the first buncher tube followed by the first drift tube. (c) shows the main buncher and the second drift tube. (d) shows the drift tube where variable voltage is applied and the graded accelerator including the Faraday cage.

the first buncher tube followed by the first drift tube. Fig. 5 (c) has the main buncher and the second drift tube. Fig. 5 (d) shows the drift tube where variable voltage is applied and the graded accelerator including the Faraday cage. The graded accelerator gradually increases the energy and helps to control the beam diameter where as the Faraday cage suppresses the contribution of back scattered positron induced gamma to the lifetime spectrum.

The moderator is given a bias +10V and hence the positrons would have an initial energy of 13 eV beyond the extraction grid. The initial energy due to the work function of moderator is given a Gaussian distribution centered at 3 eV with a standard deviation of 0.6 eV. The moderator is 6 mm in diameter and the positrons came out with an angular deviation of $\pm 15^0$ which was close to the reported value [38]. The time of birth is taken to be random inside 20 ns. These input parameters are shown in the Fig. 6 (a-d). These values were recorded at a plane near the moderator. At the chopper grid, a positive voltage of 15V prevents the positrons from entering into the pulsing column. However the negative going square pulse added to this bias makes the potential go to zero at a frequency of 50 MHz. The chopping action by this arrangement is shown in Fig. 6(e) which was recorded at the entrance gap of the pre-acceleration stage. The chopped pulses are pre-accelerated by 250 eV, taking the energy to 263 eV. These then go through the pre-buncher which is given a sinusoidal voltage of 50MHz with peak to peak amplitude of 14V in addition to the dc bias of -250 V. The sinusoidal variation in the amplitude of the potential to the pre-buncher electrode is with respect to the two tubes on either side of the buncher electrode which are also given a dc bias of -250 V. The phase of the applied potential is adjusted such that the reference positron arrives at the zero of the negative going sine pulse. The phase here is given with respect to the moderator position. The reference positron is taken as the one which is born at zero time, which is emitted

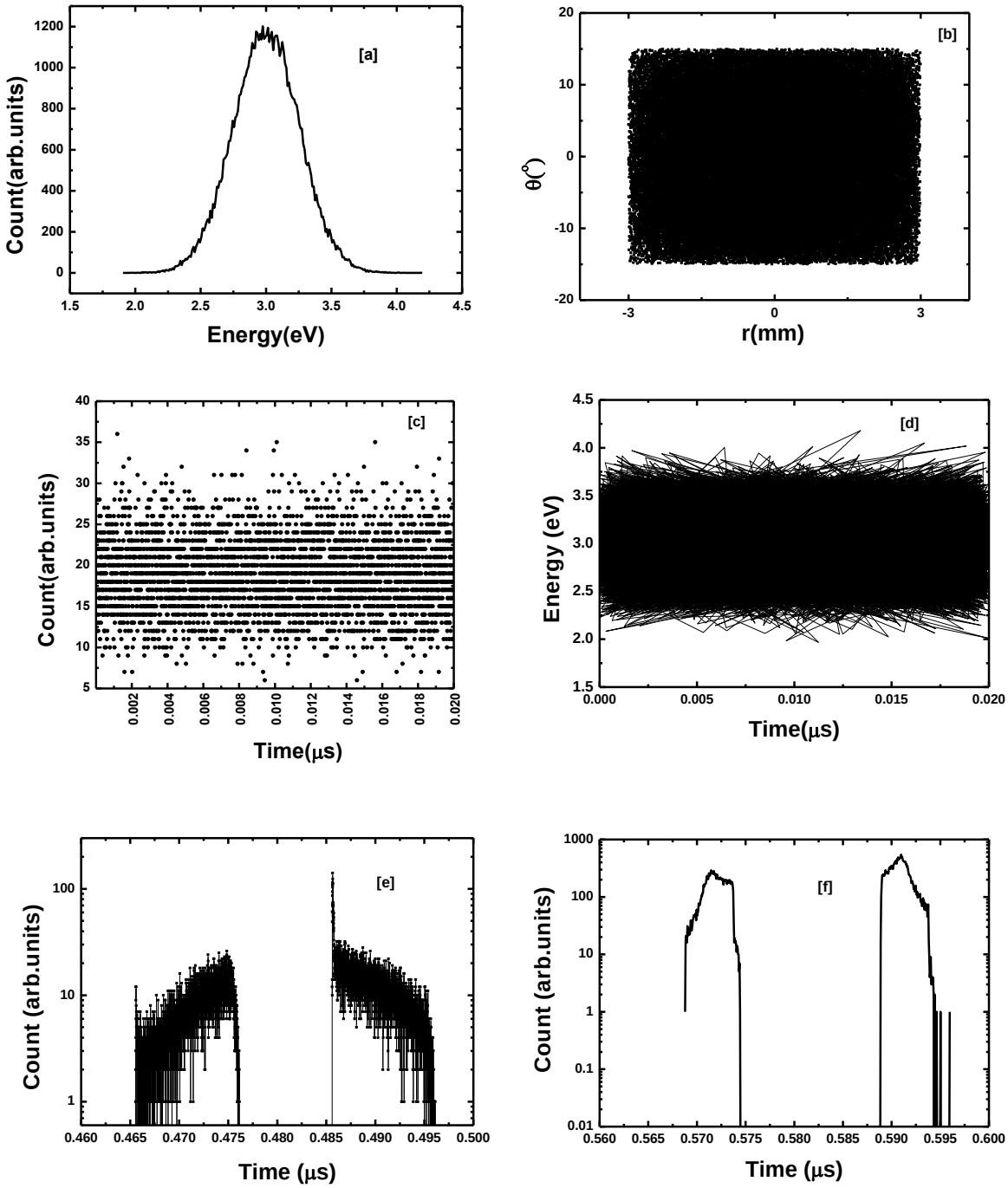

Fig. 6: The input parameters of the SIMION simulation (a) The energy spread of the positrons emitted from the moderator (b) r-θ phase space plot showing the diameter of the beam and the starting divergence given (c) Time of birth of the positrons from the target is given a random distribution with uniform sampling. With large counts, it resembles a continuous distribution from 0-20ns. (d) E-T phase diagram (e) Chopping action seen at the entrance of pre-accelerator (f) Reduction in time spread seen at the first gap of main buncher as a result of pre-buncher modulation.

along the central axis of the magnetic field and which has energy equal to 3eV. In practice the phase has to be optimized with respect to the chopper, however there is no loss of physics in giving like this. In practical beam optimization the the phase of the pre-buncher will be adjusted with respect to the chopper till maximum counts within the time pulse are obtained at the target as any out of phase situation will cause some of the positrons to be modulated in the non-liner region of the sine wave. The output of the pre-bunching action was recorded at the first gap of main buncher and is given in Fig. 6(f). The bunching potentials and phases were optimized for a drift tube bias at -250 V and target high voltage at 10kV. A small RF voltage (7V amplitude) was enough for the pre-buncher because of the large distance at which focussing happens from the first buncher. The target is at ~126 cm from the middle of the pre-buncher electrode; however this is also not the focal point of pre-buncher. At the target, the positron pulse will be under-focussed by the action of pre-buncher alone. This focus is brought to the target by the action of main-buncher as shown in schematic given in Fig. 7. Thus the RF power required becomes low and thus, the complications associated with high RF power can be avoided. This aspect is highlighted in the Fig. 8 (a-c) where the action of pre-buncher alone, pre-buncher and main-buncher and all three components activated is shown. For the main-buncher, a sinusoidal modulation voltage of only 3V (amplitude) is required for getting the optimum bunching. This also is given in addition to the dc bias of -250 V with respect to the -250 V dc biased tubes on either side of the main buncher. It can be seen in Fig. 8 (c) that the chopper removes the positrons in between the bunched pulses. After the main buncher the positrons go through two drift tubes both of which were biased to -250 V. A five stage graded accelerator setup gradually increases the energy of the positrons from 263 eV to 10 kV by the time it reaches the target. The potential gradation is given between the last drift tube and the Faraday cage.

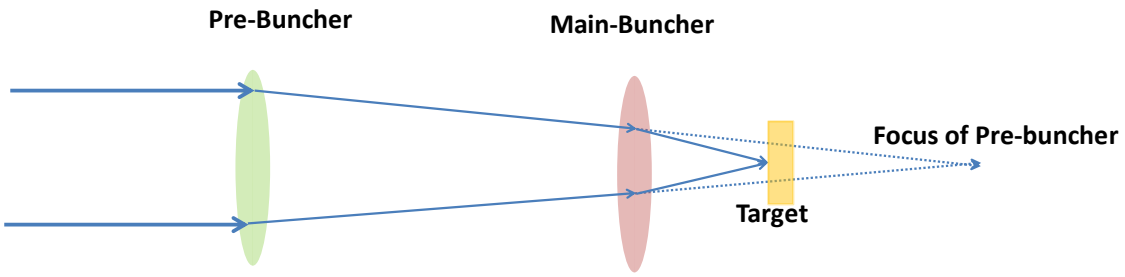

Fig. 7: Time focussing by pre-buncher and main buncher – analogy with optics. The focal point of pre-buncher is at distance >126 cm. Hence the velocity modulation to be provided is less as more distance is there for the catch up or crossing. The action of main buncher is to forward the focal point to target. The higher frequency ensures larger compression rate giving pulses with fwhm in the range of few 100 ps's.

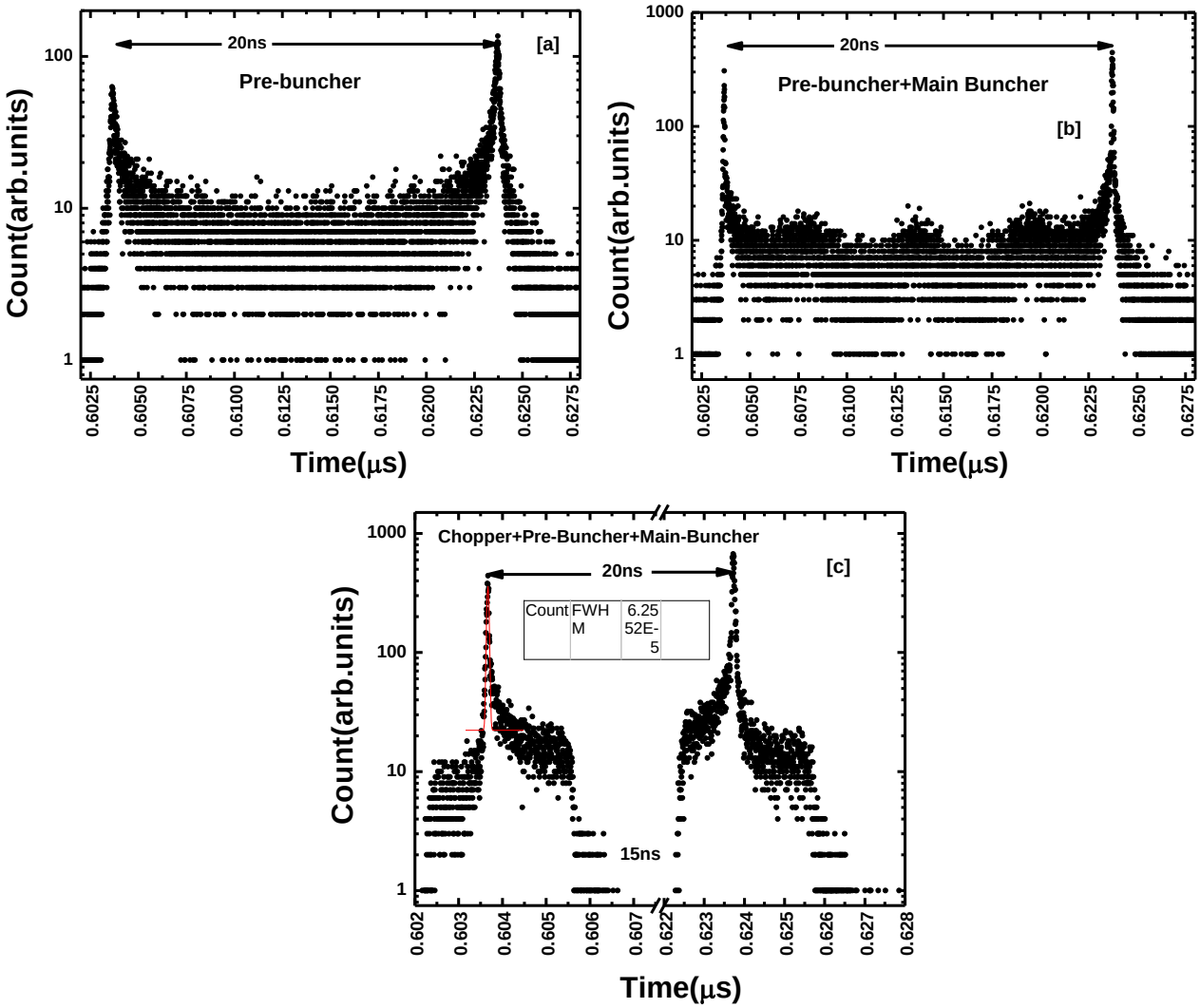

Fig. 8: (a) Time focussing with pre-buncher working at 14 V peak to peak (b) pre-buncher and main buncher are working but chopper is not in action (c) All three working to give a pulse width in the range of 100 ps.

The variation in energy, r-θ and E-T phase diagrams as a result of this bunching and chopping process is given in Fig. 9 (a-c). The marked reduction in divergence is a result of the graded accelerator set up which does not induce spatial focussing effect during the final acceleration. It could be seen that with energy spread of 60eV a time bunching of 100 ps can been achieved. When compared to the energies that would be used in the beam based measurement (1keV-20keV), this energy spread is negligible compared to the depth resolution possible with the Makhovian implantation profile of the positrons. The phase space evolution shows that a few positrons are lying outside the time focussing and are responsible for the tailing seen especially on the higher time side.

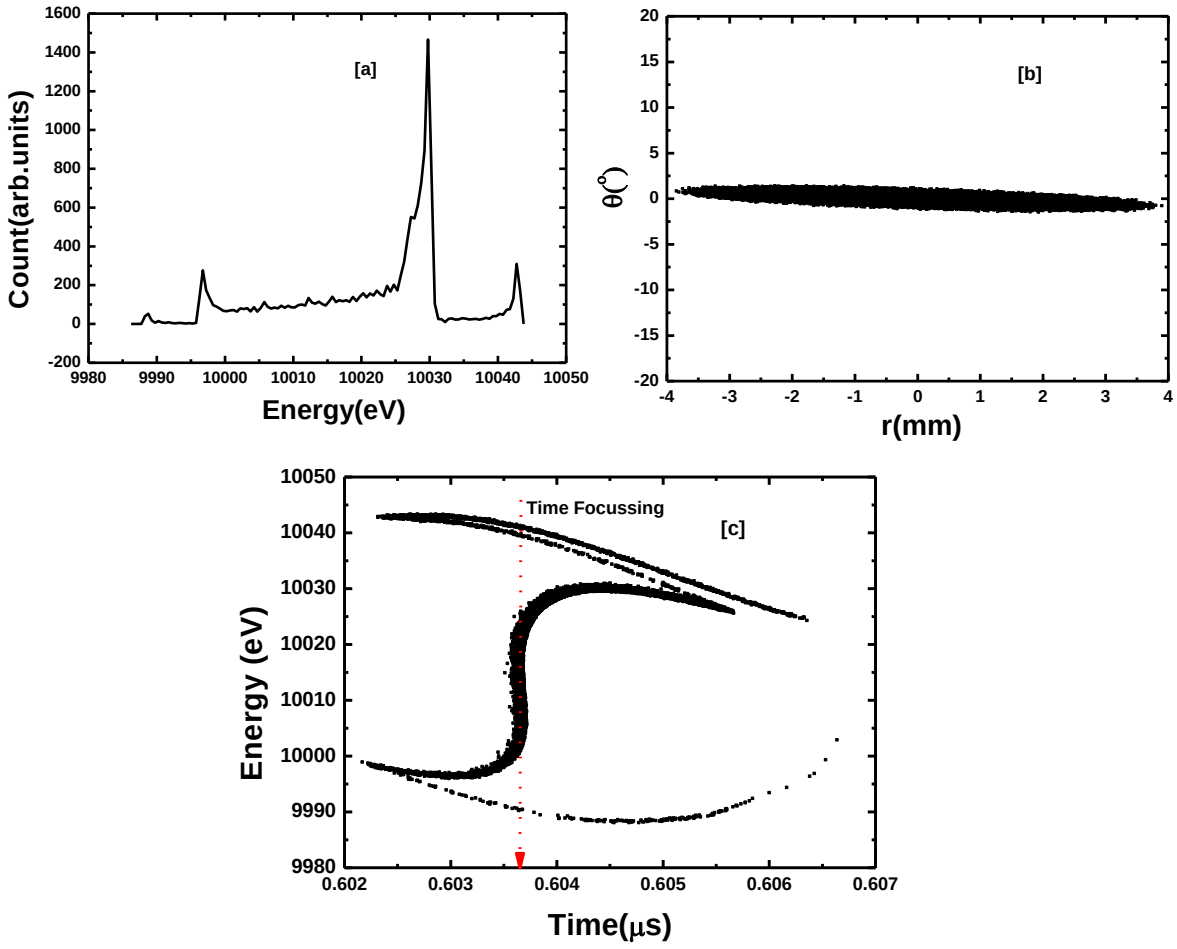

Fig. 9: The output parameters of the SIMION simulation (a) The energy spread of the positrons reaching the target (b) r-θ phase space plot showing the diameter of the beam and the final divergence (c) E-T phase diagram which shows time focusing at ~ 0.6037μs. The positrons lying outside the focusing causes the tailing seen at the ends.

To make sure that the bunching action was reproducible for other high voltages, simulations were carried out at energies such as 1,5,15 and 20 kV. Initially the same RF power and the same drift bias were given to the buncher electrode and the final drift tube attached to the graded accelerator respectively. However except for 5 kV, other energies did not show focussing. While some showed under focussing, others like 1 kV where over focussed. This was expected as drift time from the last drift stage to the target changed depending on the high voltage applied and hence for higher voltages, positrons were reaching the target before they could focus or for lower voltages the drift time was longer than the actual focal time. This was corrected by applying a variable drift voltage to the final drift tube such that the drift time becomes same for all the accelerating voltages. The required drift voltages were found using the Nelder-Mead downhill type simplex optimization routine available with the SIMION [40]. The optimization is done by equating the time of flight of the reference positron in each case with that during 10 kV acceleration. In spite of this adjustment it was also required to fine tune the modulation voltages applied in each case to get similar positron pulse widths. The optimization for the drift tube voltage was done with the modified bunching voltages. Fig. 10 (a) shows the effect of having a constant drift voltage. It can be seen that for each accelerating voltage, positron pulse arrives at different times leading to over focussing and under focussing. Fig. 10 (b) shows uniform bunching action for all accelerating voltages after the application of variable drift correction. The variation in beam diameter with accelerating voltage is shown in Fig.11. It can be seen that the maximum diameter would be around 10 mm and the introduction of the variable drift has not induced any additional focussing or defocusing effects than before.

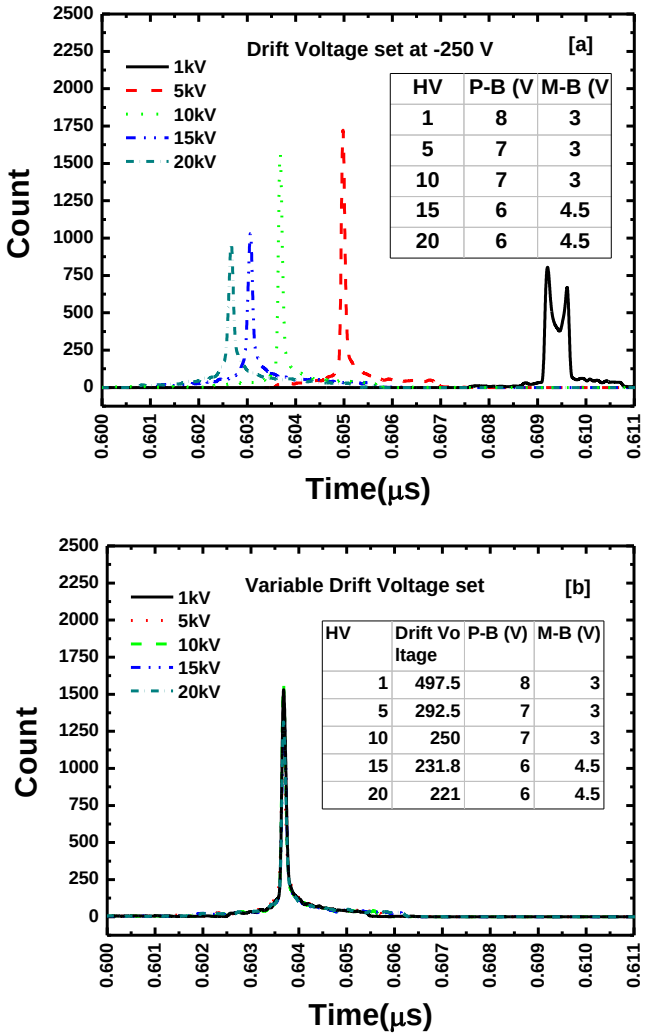

Fig. 10: (a) Time of arrival at the target for various accelerating voltages with constant drift tube voltage. The inset shows a table which gives the applied bunching voltages. (b) Uniform time of arrival for all accelerating voltages by applying varying drift voltages. The voltage values are given in the inset.

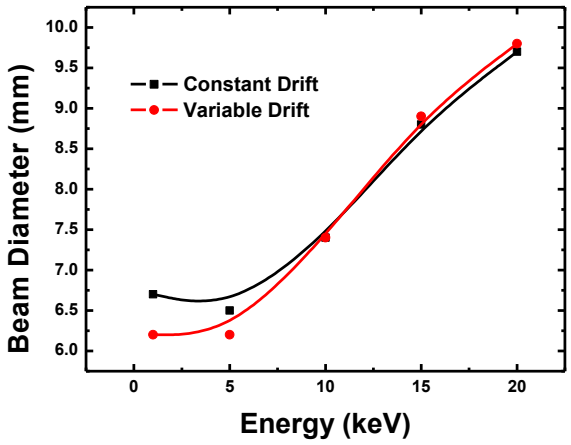

Fig. 11: Variation of beam diameter with applied accelerating voltage with constant drift voltage and different drift voltages. The maximum beam diameter is about 10 mm .

Thus a complete design of the positron pulsing system has been simulated and important fabrication parameters were deduced. Based on these simulations the development of the UHV housing system and other electrodes are taken up in the subsequent sections.

4.5 Design and fabrication of an Ultra High Vacuum (UHV) system and related components

A high vacuum environment of better than 10^{-6} mbar is necessary for the efficient transport of positrons from the source up to the target position. The vacuum should be such that the mean free path of the molecules in the system should be larger than the dimensions of the UHV system reducing its chance to meet positrons and increasing its interaction with walls of the system. It can be shown that to make the mean free path of molecules equal to the dimensions (here ~350 cm) travelled by positrons through the UHV tube, then the vacuum has to be of the order $2x10^{-6}$ mbar [24]. Hence, the transport length of the positrons with a few keV energy increases with better vacuum conditions because of the reduced collision with atmospheric atoms and thus, reduced probability for annihilation with their electrons. Better vacuum condition is also necessary for the prolonged usability of the moderator whose surface properties decide the fast to slow positron conversion efficiency. Hence, a UHV system has been designed to have a source and moderator mounting arrangement, a slow positron filter and a long tube to hold the pulsing electronic components viz. chopper, pre-buncher, main-buncher, drift tube and a target assembly with graded acceleration. The design also takes into account the requirement for placing the detector as close as possible to the target assembly. The entire UHV system has been fabricated using SS-316L to avoid any stray magnetic field along the path of the positron beam. This material is also important from a

UHV system point of view with low out gassing even for unbaked systems. The non magnetic precaution was also taken for the welding joints and all fasteners used. The entire system was designed to be on a flat non-magnetic beam table with 12 mm thick aluminium table top with height adjustable bolt arrangement. The design of the table also included space for important electronic components and two ion pumps.

Two designs were conceptualized for the transport until the magnetic bend which acts as the velocity filter. A design where both source and moderator are mounted together, followed by a gradual bend of ~ 60^0 for slow positron extraction was one of them. The second one consists of a source – moderator mounting arrangement where moderator could be removed without removing source and thus results in lesser radiation exposure. Here the slow positron filter is a sharper 90^0 bend similar to the one used by Reurings et.al [43]. The linear section beyond the magnetic bend houses ports to vacuum pumps, pulsing system and target chamber. A schematic of the beam with the parts marked for the design with 90^0 bend is shown in Fig. 12. The detailed design of each part is discussed in subsequent sections.

4.5.1 Source – Moderator mounting

The source moderator mounting arrangement is designed after taking into account number of factors. They were ease of source-mounting, less handling time, easy insertion into beam line, proximity between source and moderator, future removal of moderator for annealing, possibility of incorporation of an in-situ moderator annealing set-up, effective extraction of monoenergetic positrons emitted by moderator into the transport field and radiation shielding around the source.

In one design the source is mounted on a 6’ linear transporter. The transporter end is attached with mating arrangement for the ^{22}Na source capsule [44]. The linear

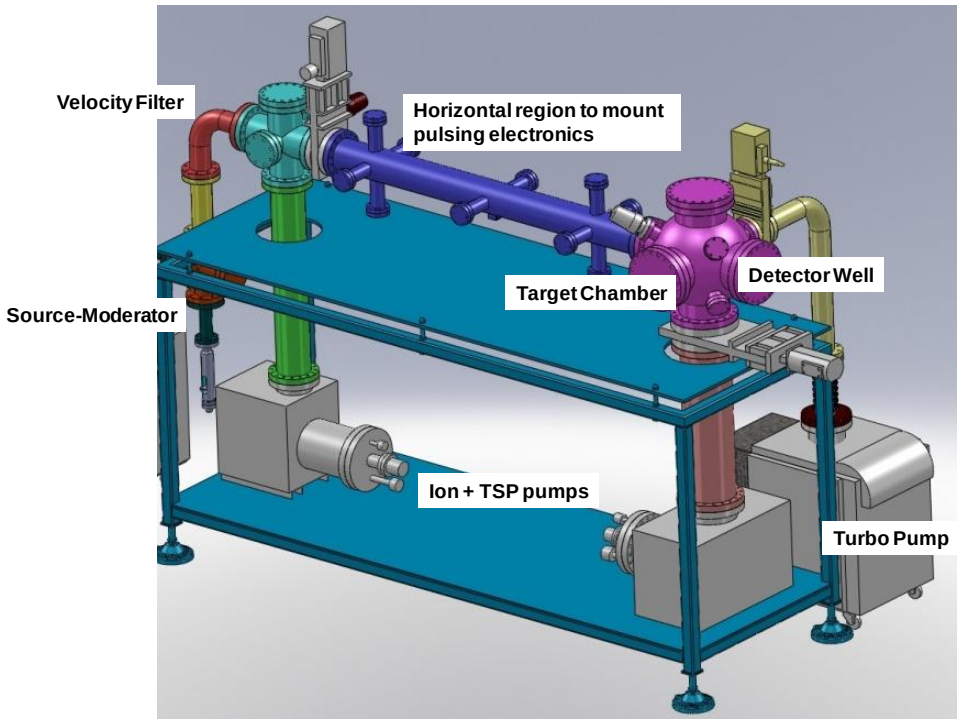

Fig. 12: A 3D schematic representation of the UHV system with 90^0 bend.

transporter is attached to a ConFlat Flange (CF)-63 cross tube. On one of the perpendicular ports of the cross tube, the moderator mounting arrangement is attached with proper biasing such that it extends up to the centre of the tube as shown in Fig. 13 (a). There are provisions for minor adjustment of the moderator position in forward and backward direction. This design can be easily modified for a possible in-situ moderator annealing set-up with the moderator system mounted on a motion manipulator. The source could be moved up by pre-designated distance and could be brought to a touching position with the moderator. The arrangement described is shown in Fig. 13 (a-e). Fig. 13 (b) shows a dummy source made to similar dimensions of the available source capsule [44] mounted on to a MACOR cylindrical block with proper mating i.e. M4 female tapping to go with M4 screws of the source which then is attached to liner transporter. Fig. 13 (c) shows the moderator mounting and Fig. 13 (d) shows the arrangement inside the cross tube seen through one of the view ports. The biasing is given through a CF 35 voltage feed through attached to the CF 63 – 35 zero length

adapter on which the moderator mounting is held. Since the source touches the moderator, both of them would be in the same potential. The top plate of the moderator arrangement is grounded to complete the positron extraction optics as given in schematic Fig. 13 (e).

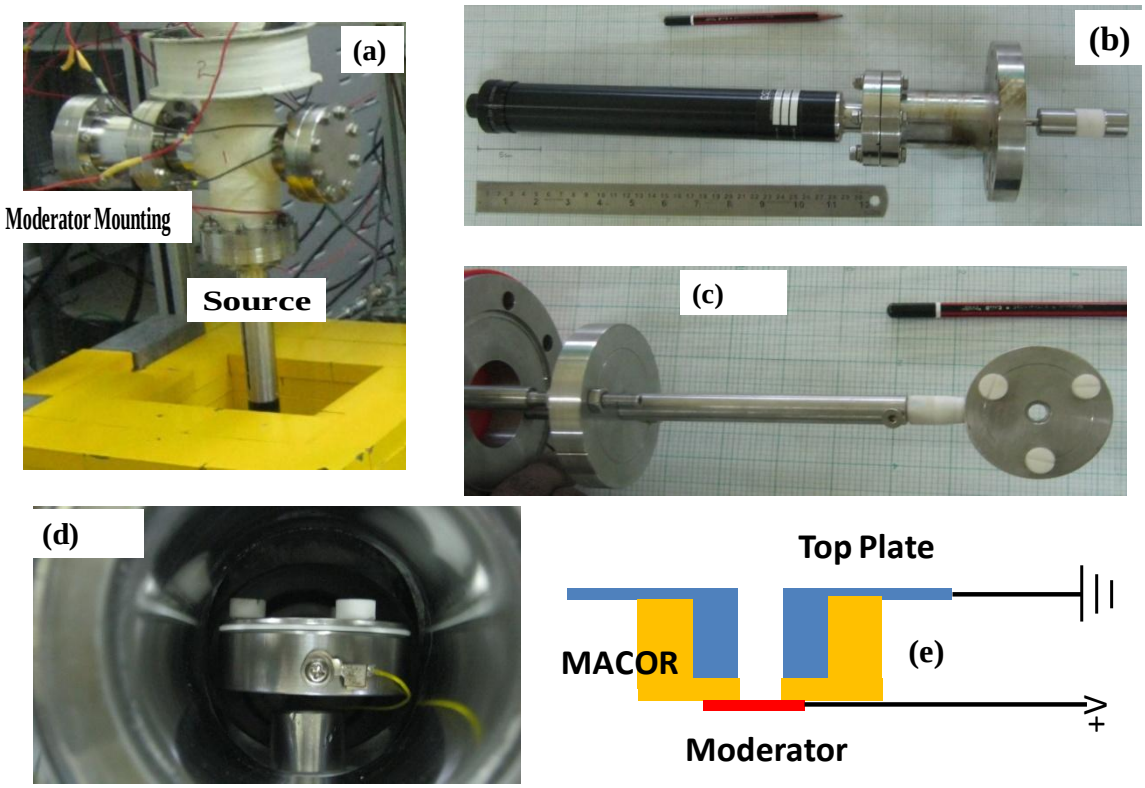

Fig. 13: (a) Cross tube arrangement on which the source and moderator are attached in perpendicular directions with moderator reaching exactly at the middle of the cross tube (b) Dummy source mounted on MACOR insulator. The whole assembly is mounted on a 6' linear transporter. (c) Moderator mounting on a CF 63 – 35 zero length adaptor flange. (d) Source – Moderator assembly inside the CF 63 cross tube seen from a view port. (e) Schematic of extraction optics of the monoenergetic positrons.

The second design uses the CF 63 – 35 zero length adaptor flange as above but now the entire source-moderator assembly sits on it. The zero length adaptor and the mounting disc as shown in Fig. 14 (a) holds the source mounted on Teflon holder (Fig. 14 (b)). The Teflon tube carrying both the moderator holder (Fig. 14(c)) and the

extraction electrode (Fig. 14 (d)) is put over the source so that the source touches the moderator. Hence the source and moderator are in same potential and the extraction electrode is grounded with respect to the moderator as shown in schematic in Fig 14 (e). The biasing is again through CF 35 voltage feed through and the entire assembly goes into a CF 63 I-tube. The I-tube connects to the velocity filter section (i.e. the 60^0 bend). An aperture of 16 mm is attached at the joint between the I-tube and velocity filter which cuts off diverging high velocity positrons and helps to limit the beam diameter entering the high magnetic field region.

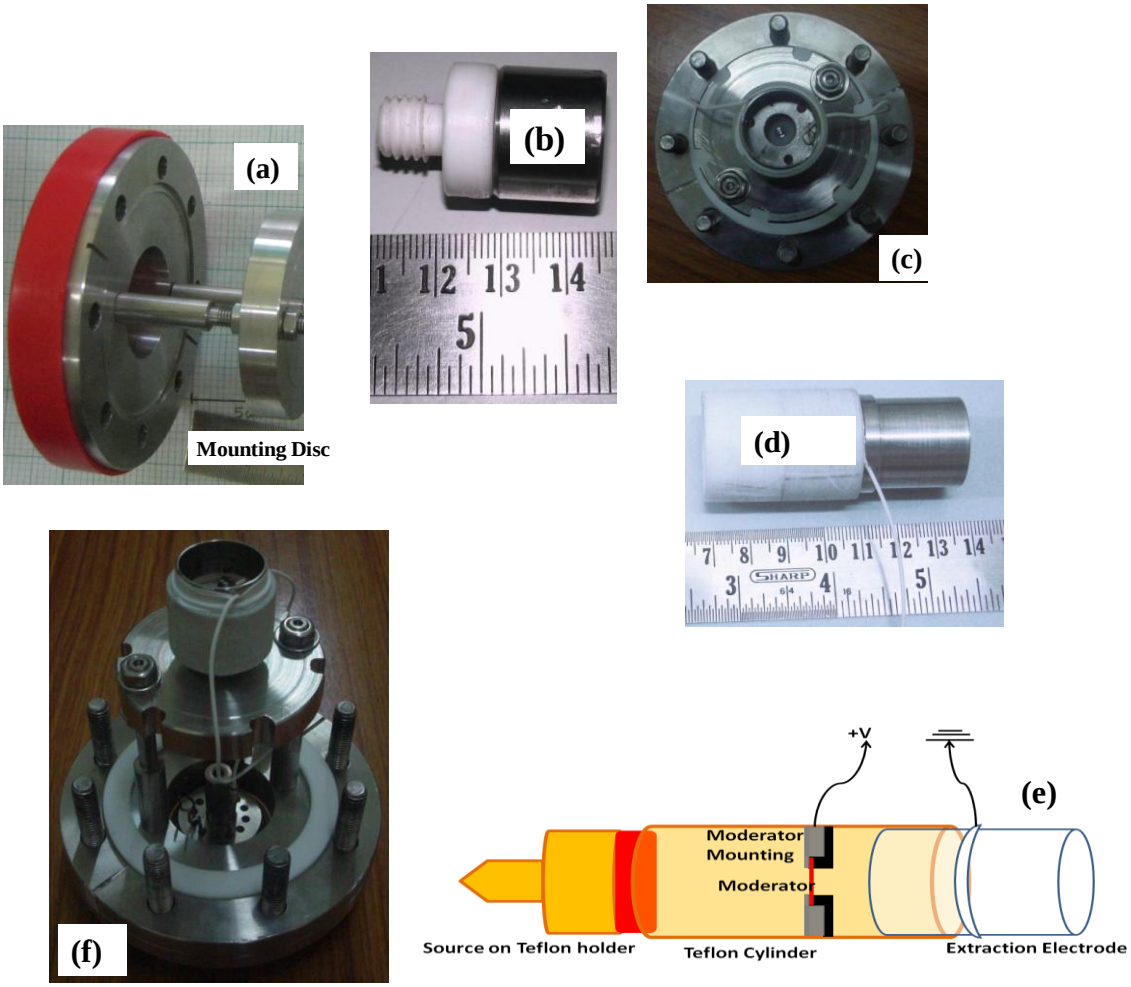

Fig. 14: (a) The zero length adaptor and the mounting disc (b) the dummy source mounted on Teflon holder (c) Moderator assembly inside the Teflon cylinder seen from top. (d) Teflon Tube holding the extraction electrode (e) Schematic of the arrangement (f) Assembled unit – side view with biasing.

4.5.2 Magnetic Bend – Velocity Filter

The separation of monoenergetic positrons from the unmoderated fast positrons is achieved through a magnetic bend. The bend can be shallow [45] or it can also be a complete 180^0 turn [34]. Here two designs were made, one with 90^0 bend and another with 60^0. Fig. 15 (a) and 15 (b) shows 90^0 and 60^0 bends respectively both of which are having dimensions of a CF 63 tube. The 90^0 was highly compact though extraction was difficult, while 60^0 bend is longer though velocity separation was attained easily.

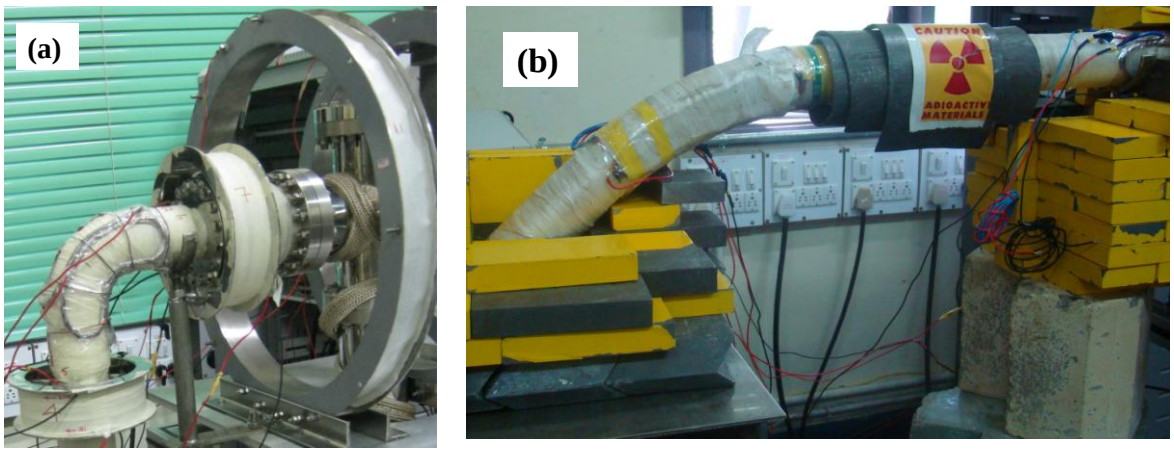

Fig. 15: (a) The 90^0 magnetic bend and (b) the 60^0 bend.

4.5.3 Linear Region and Target Chamber

Beyond the magnetic bend there is a horizontal region which houses the ports for vacuum pumps as well as a 120 cm long tube with multiple inlet ports for holding the pulsing electrodes and the drift tube. The diameter of the UHV chamber changes from CF 63 to CF 100 in this region. The long I tube ends at a spherical chamber of 12' diameter manufactured by M/s Kurt J. Lesker with multiple ports of various dimensions. One of the CF 150 port of the spherical chamber is attached with a detector well such that the detector sits right behind and as close as possible to the target. The high voltage is applied to the target via a CF 35 high voltage feed through attached to the top port.

The detector well arrangement attached to the spherical chamber and the long tube is shown in Fig. 16 (a) and (b) respectively.

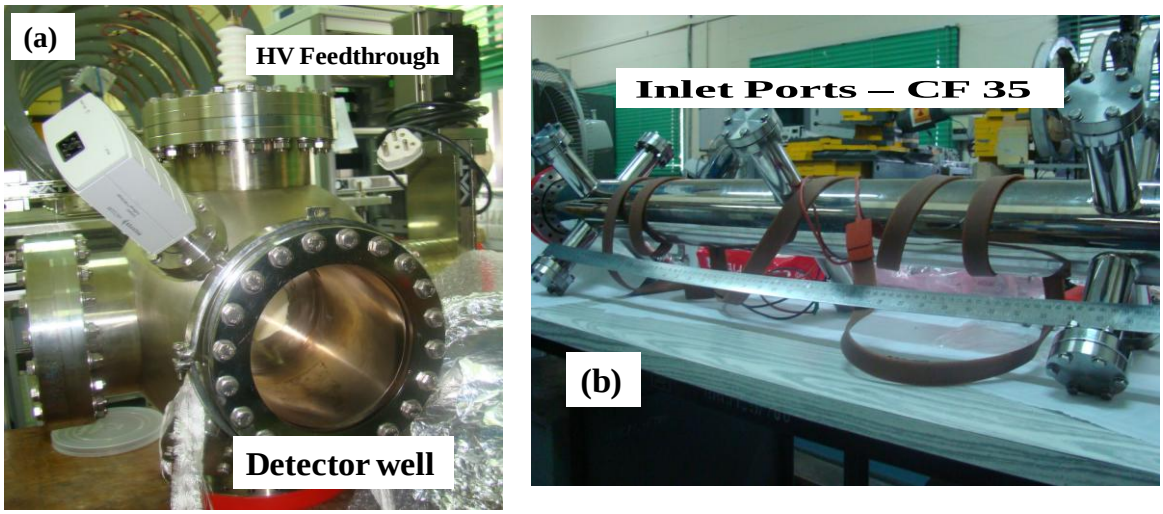

Fig. 16: (a) The 12' spherical chamber with detector well attached. The depth of the detector well is such that the detector sits at a distance of 1.75 cm from the target. (b) The 120 cm long CF 100 I tube

4.5.4 Assembly, pumping system and testing

The entire system was assembled on an aluminium beam table top as shown by various stages of assembly in Fig. 17 (a-d). The vacuum pumping system which is used to pump the entire UHV system from atmosphere down to ~10^{-8} mbar is a combination of Turbo molecular pump and Ion-Titanium sublimation pump (TSP). Turbo molecular pump with a backing scroll pump would be used to get a base vacuum of 10^{-6} mbar in the entire chamber after which two Ion-TSP's take over. Once this happen, the Turbo part is cut off using a gate valve. There is provision for the region; which includes the source-moderator, magnetic bend and one of the Ion – TSP pump, to be isolated using a gate valve when the sample is changed at the target side. This helps to increase the lifetime of the moderator by avoiding air exposure and maintaining the moderator at ~ 10^{-8} mbar. During the sample mounting the target side Ion – TSP would also be cut-off with the

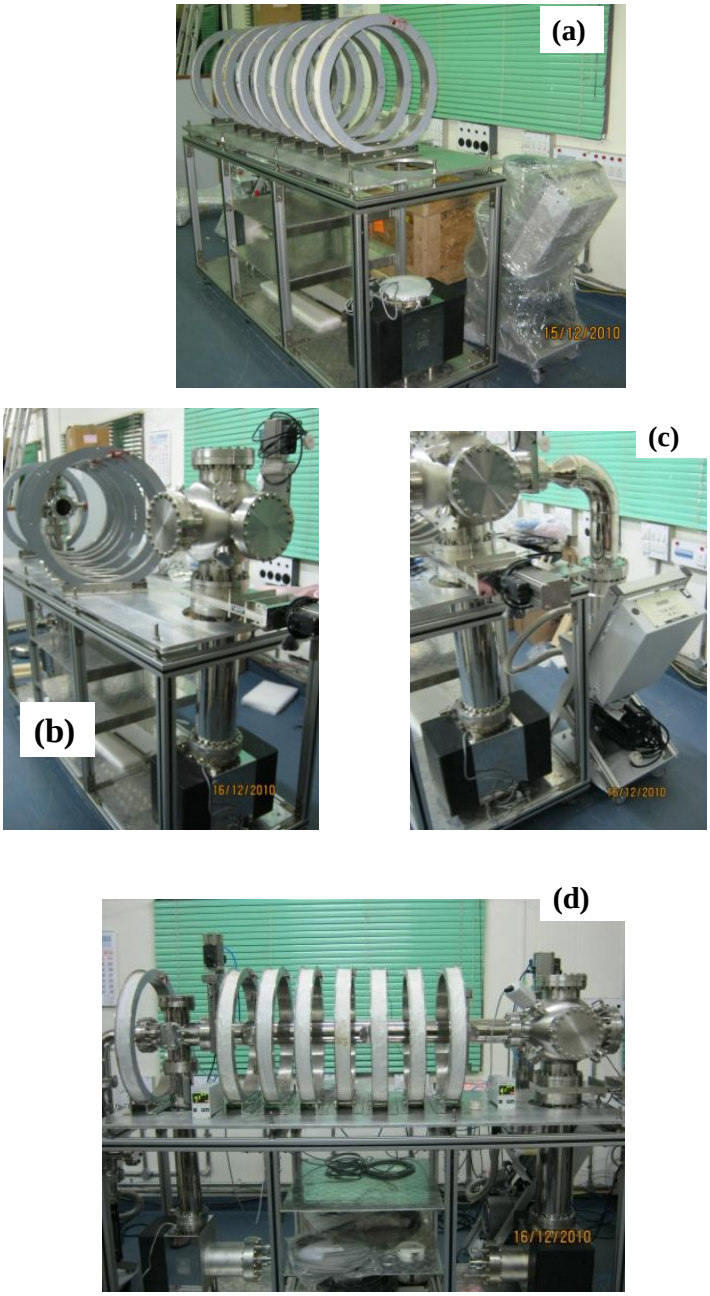

Fig. 17: (a) The Helmholtz coils arranged on the beam table. The height adjustment of the beam table helps to centralize the magnetic axis and the beam axis within a few mm. (b) The Ion – TSP pumps attached (c) The Turbo molecular pump for the initial pump down (d) The full assembly.

gate valve provided. The pressure is measured at the source side and the target side separately using a combination Pirani – Bayard Alpert (BA) gauge. BA type gauge is preferred for its non-magnetic working and accuracy.

The volume pump down time depends only on the total volume of the system and smallest conductance in the system as is evident from the equation of the effective pumping speed.

$$\frac{1}{S_{effective}} = \frac{1}{S} + \frac{1}{C} \tag{11}$$

where $S_{effective}$ is the effective pumping speed, S is the pumping speed for the pump at its mouth and C is the conductance of the port attached. Hence whatever be the pumping speed of the pump used, the smallest conductance becomes the maximum pumping speed possible. For the 60^0 magnetic bend, a CF 63 tube of length 140 cm determines the effective pumping speed with a conductance of 21 l/s calculated from the formula

$$C = \frac{12D^3}{L} \tag{12}$$

where *D* is the diameter of the tube of length *L* expressed in centimetre. This formula is valid only in the molecular flow regime. The pump down time from 10^{-3} to 10^{-6} mbar would be minimal as the total volume to be pumped is only ~ 54 litres. The pump down time is found using the equation

$$t = 2.303\frac{V}{S}\log\frac{P_0}{P_i} \tag{13}$$

where *t* is the pump down time in second, *V* is the volume in litres, *S* is the effective pumping speed in litres/second and P_0 and P_i are the initial and final pressures after pumping. This is again valid only in the molecular flow regime and does not take into account the surface load. To make use of the maximum available conductance, a pump with a pumping speed which is more than one order higher than the calculated conductance is used. Thus for the initial pump down, a Turbo molecular pump assembly (V-550) of pumping speed 550 l s^{-1} (for Nitrogen) from M/s Varian is used. The required pumping speed of the ion pumps depends on the gas load of the system, which can be

calculated from the out gassing rate of SS 316L when the surface behaves as the primary load after the initial volume pump down. Here the primary vacuum equation of

$$QA = SP \tag{14}$$

becomes handy where Q is the out gassing rate of the material exposed to vacuum, A is the surface area exposed to vacuum, S is the effective pumping speed and P the pressure to be achieved when in equilibrium. Considering only the region beyond the bend and excluding the port connected to the Turbo molecular pump, the total surface area is ~ 8600 cm^2. The electrodes and the electrical connections for the timing optics are inserted in this region. The electrodes are manufactured with SS 316L, but it would be difficult to get a correct value of the internal surface area. Hence we take a conservative estimate of three times the calculated surface area which is around ~ $2.5x10^4$ cm^2. By using equation (14), it could be seen that with an out gassing rate of 10^{-11} mbar l $s^{-1}cm^{-2}$ (for SS 316L baked at 150^0C for ~ 4 days) an effective pumping speed of 25 l s^{-1} is required to maintain a vacuum of 10^{-8} mbar in equilibrium. For a 178 cm long tube with diameter of 10 cm, the conductance is of the order of 53 l s^{-1} using equation (12) and in order to get this conductance as the maximum pumping speed a Ion-TSP pump with one order higher pumping speed of 300 l s^{-1} (Vac Ion Plus 300 - Starcell) from M/s Varian is used. The frequency of firing the TSP pump is determined based on the pressure and time involved. Using similar considerations an Ion – TSP pump with a pumping speed of 150 l s^{-1} (Vac Ion Plus 150 - Starcell) is used near the source side.

During the initial vacuum testing of the assembly, the system was pumped down to a vacuum of ~10^{-5} mbar using the Turbo molecular pump. The pump was baked at ~ 150^0C for ~ 48 hours as shown in Fig. 18. After proper bake out of the system and the Ion pump (using the in-situ heater available), the system was loaded on to the two Ion-TSP pumps. At 10^{-6} mbar the TSP pump was fired every 1 hour which was reduced to

once every 36 hours after the vacuum improved to better than 10^{-8} mbar on both the source and the target side. An ultimate vacuum of 10^{-9} mbar was achieved on the source side and a vacuum of 5.5 x 10^{-10} mbar was achieved near the target side. However this was without any pulsing electrodes, source-moderator mounting or target mounting inside the system and such low values were attained because of proper baking and extended pumping. However, considering the higher pumping speeds of the Ion pumps and the TSP, the incorporation of these components will not affect the achievable ultimate pressure.

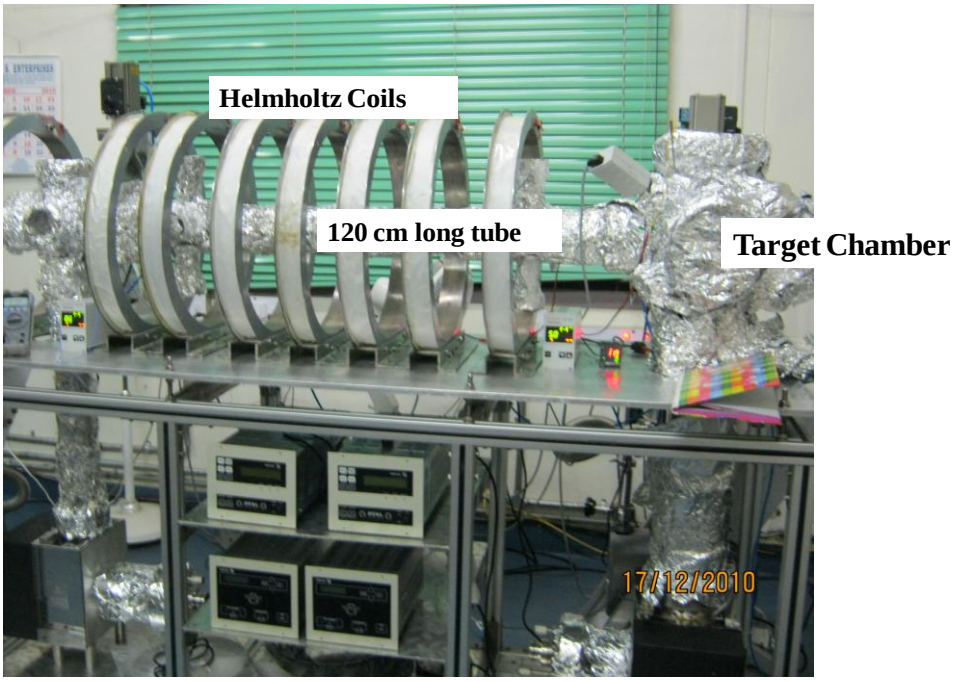

Fig. 18: The UHV assembly during baking. The gauge meters and temperature sensors are visible.

4.6 Magnetic Field for transport

The transport of the positrons from the moderator to the target side is achieved using magnetic field of the order of 100 Gauss as modelled in SIMION [40]. The field is generated using a combination of solenoid and Helmholtz coils arrangement. The

solenoid coils were put near the source side whereas Helmholtz coils were utilized near the linear region where ports for RF electronics connection and the target chamber cause hindrance for solenoid winding.

4.6.1 Helmholtz coil design and testing

Nine Helmholtz coils were designed and fabricated to provide the required magnetic field of ~ 100 Gauss in the linear region. The mechanical structure for winding the coils was made from SS 304L sheets as aluminium sheets buckled under winding. The diameter of the coils was set at 50 cm in order to avoid any influence from the edge and from curving of the field. Approximately thirteen (12.7 to be exact) layers of SWG-17 super enamelled Cu wire were wound over a width of 5.4 cm. The measured room temperature resistance was ~ 7.5Ω for each coil. Each layer was separated by Nomex Kapton sheets which provided the necessary interlayer electrical insulation with high thermal stability. A thermal cut off was provided as the insulation on the Cu wire had a temperature stability of ~ 130^0C. The thermal cut off had a bimetallic strip with the set point temperature of 90^0C. This was fixed near the bottom most layers. A reverse current protection during sudden current failure was provided to the voltage source through a reverse biased diode. These coils were also provided with an L-bend stand with fixers to position them tightly on the Aluminium table. These Helmholtz coils are shown in the previous section in Fig. 18.

Normally for a pair of Helmholtz coils, the distance between their centres is set as equal to the radius and thus a constant field is obtained between them. Hence the distance between the coils has to be set at 25 cm here. However depending on the distance available between the target chamber and the magnetic bend as well as the position of various vacuum ports; in this case the distances between the individual coils

were tweaked, to get a constant wriggle free field, which is near to ~ 20cm. The first Helmholtz coil near the magnetic bend is powered separately whereas other eight coils are paired. Required number of 150 V, 10 A constant current sources were used for powering these coils. Before testing, the magnetic centre and the mechanical centre of the horizontal UHV tube in the top-down direction were matched by adjusting the height of the Aluminium table top. The lateral centring was done by matching distances from the coil inner edge and the UHV tube. The orientation of the magnetic axis with respect to the mechanical axis was adjusted by ensuring the flatness of the table top using spirit level and by visually aligning the coil edges parallel to the UHV tube edge. During testing, the field generated at the magnetic centre was measured using a three probe (hence B_x, B_y and B_z can be measured simultaneously) gauss meter operating in the 300 Gauss range from magnetic bend up to the target level. The testing was done without the ninth coil near the target and hence the last coil is not paired during testing. Thus, a monotonous drop is expected near the sample. The measured values were compared as shown in Fig. 19 with the analytically calculated field for such an arrangement using the equation for a field due to a finite straight thin shell air core solenoid [46] given as

$$B = \frac{\mu_0 NI}{2l}\left[\frac{x_2}{\sqrt{x_2^2+r^2}} - \frac{x_1}{\sqrt{x_1^2+r^2}}\right] \quad (15)$$

where μ_0 is the permeability of free space, N is the total number of turns, I is the current through the coils, l is the width of the air core solenoid and r is the radius of the solenoid. x_1 and x_2 are the axial distance of the point at which field is calculated from the near edge and far edge of the solenoid. It can be seen that the measured values closely follow the required trend as given by the analytical equation. The long term stability of the Helmholtz coils were also tested and showed that proper cooling was required for the

coils. Hence, to dissipate the heat, temperature near the UHV beam line has been reduced and extra fans were provided for cooling the coils by air circulation.

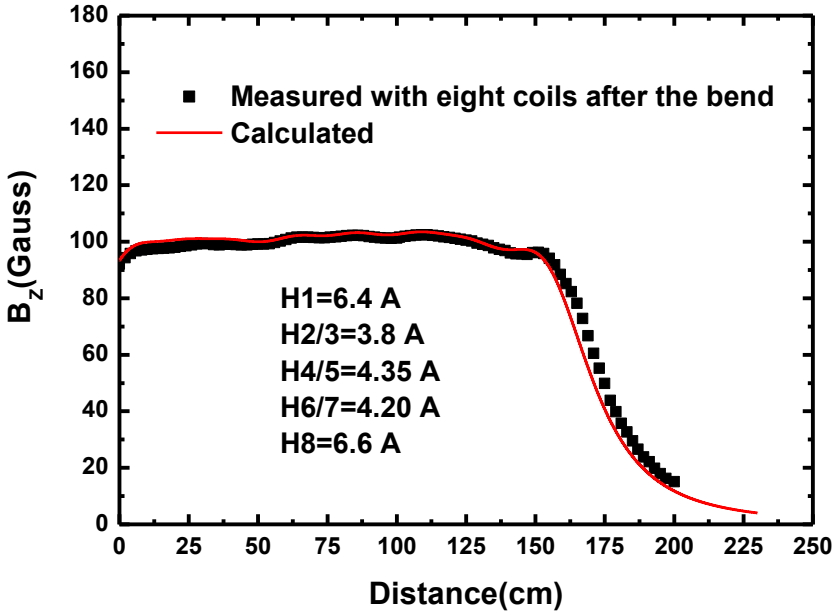

Fig. 19: The magnetic field intensity along the central axis of the Helmholtz coils measured in the direction of the beam propagation. The solid red line is the calculated values using equation (15). Also given in the legends are the current applied to each coil where coils are identified as H1-H8. It can be seen that except for first and last, all other coils were paired. The origin of this plot is the 100 CF flange immediately after the magnetic bend and the target is located at 175 cm.

4.6.2 Solenoid and Flange Coils

Solenoids play a major role in the filtering and subsequent transport of extracted slow positrons beyond the magnetic bend, feeding them into the field due to the Helmholtz coils. Solenoid coils were wound directly on to the UHV tubes after proper insulation. Insulation to the stainless steel tube was provided by electrically insulating adhesive tapes with thermal stability up to 150^0C. These were also used for the interlayer insulation. Five layer of coil were wound over the available width of each UHV attachment. Care was taken to provide enough width for the easy removal and attachment of nuts and bolts. For design with 90^0 bend, solenoids were wound on the

four-way CF 63 cross tube, CF 63 I tube of length 21 cm and the 90^0 bend. For 115 cm long 60^0 bend SWG 16 super enamelled Cu wire was used. Here only two layers were wound. Each of them were tested separately and compared with the analytically found field given by equation (15). The field measured for 60^0 bend at a few locations for multiple currents and that for the I tube is shown in Fig. 20 (a-b) as specimen. The CF 63 I-tube on which solenoid is wound is also shown in Fig. 20 (c). All of them were tested for long term stability. To account for the drop of field at each flange joint, a solenoid coil setup was designed and fabricated which could be mount on the flange joints as shown in Fig. 20 (c). The design is such that the coil could be removed from the flange joints without much difficulty and the central hold makes sure that the coil remains centred with respect to the mechanical axis. The magnetic field measured and tested for these coils is shown in Fig. 20 (d). As the analytically calculated fields represent the magnetic field of each component to high degree of accuracy, the field due to the entire assembly was calculated by superimposing the calculated field due to each one of them. The field used for the extraction and transport of the slow positron beam was thus calculated and is presented in Chapter 5.

Apart from the transport field, there are drift correction and steering fields to maintain the positron beam along the mechanical tube central axis, guide it through the pulsing electrodes of 1.5 cm diameter kept concentric with the CF 100 tube and to make it fall centrally on the sample mounted on the Faraday cup. The field required is small of the order of few Gauss for such steering. The drift at the magnetic bend as given by equation (4) can be corrected by providing small transverse field additions to the guiding field. Small solenoid coil pair with 10 layer winding and which covers the curvature of the magnetic bend are fixed perpendicular to the central axis of the CF 63 tube exactly at the magnetic bend. The drift coils are provided in two perpendicular directions -

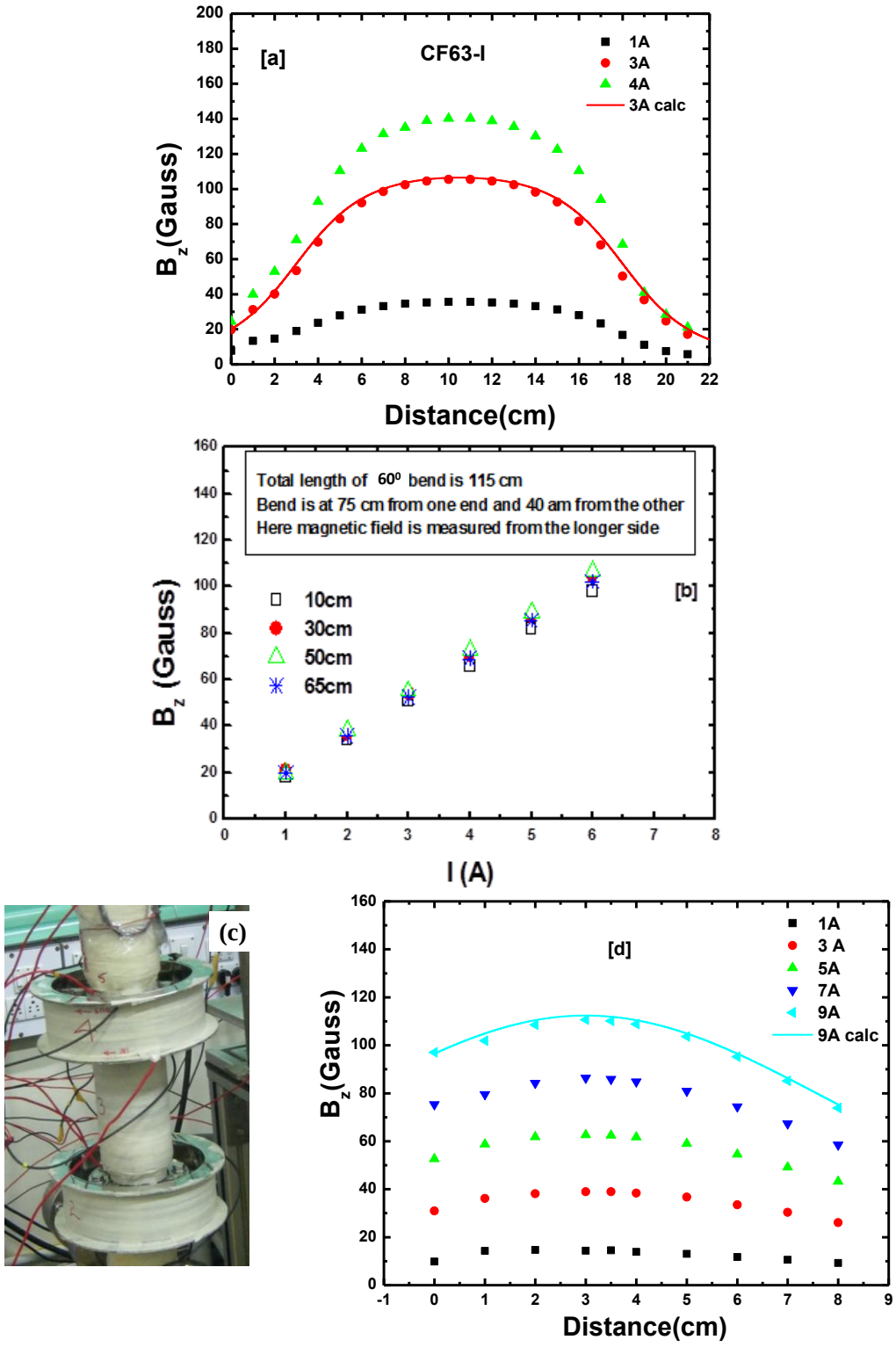

Fig. 20: (a) The magnetic field intensity along the central axis of the solenoid wound on CF 63 I tube measured in the direction of the beam propagation. The solid red line is the calculated values using equation (4). Also given in the legends are the current applied to each coil. (b) Field measured at different positions of the 60^0 bend for different applied current. The distance is measured from the longer side. (c) The flange coils attached to avoid the drop in magnetic field intensity fixed at two flange joints of the CF 63 I tube. (d) The measured field along the central axis of the flange coil for various currents.

top-down and left-right with respect to central axis; however only one of them will be more effective. A field intensity of 1.5 Gauss is obtained for 1A at the centre of a pair of coils when separated by a distance equal to the outer diameter of the CF 63 magnetic bend. In a similar way, steering coils wound on square frames were mounted at the exit of the magnetic bend, one near the entrance to pulsing electrodes and one at the entrance of the target chamber. Pair of coils was put in top-down position and another pair in left-right position with respect to the central axis at each of the above mentioned positions. All of them gave 1.4 - 1.82 Gauss for 1A current.

4.7 Mechanical Design of RF pulsing electrodes, graded accelerator and target mounting assembly

The main design parameters for the pulsing electrodes were the chopper – ground grid arrangement, length for the pre-buncher electrode tube which works at 50MHz and that of the main-buncher electrode which works at 200MHz. The calculated lengths for the buncher electrodes are 9.5 cm and 2.3 cm respectively as seen from the calculations and the simulations above. Other important design parameters were diameter of the tube as well as the separation between each electrode. Apart from the pulsing electrodes, a drift tube arrangement, a graded accelerator and a Faraday cage with target assembly arrangement had to be fabricated. The design has to be such that these electrodes remain concentric with the containing CF 100 UHV tube. The design should also take care of the insulation between the electrode tubes at specific separation and the insulation of the pulsing electrodes from the outer tube. The arrangement should not reduce the vacuum conductivity drastically and should be mechanically sturdy and stable during and after installation. Taking all these factors into account the design of the chopper, pre-acceleration, bunchers, drift tube and final accelerators were designed and fabricated. An

isometric design view of the assembled system is given in Fig. 21 where as the fabricated parts are shown from Fig. 22 (a-g).

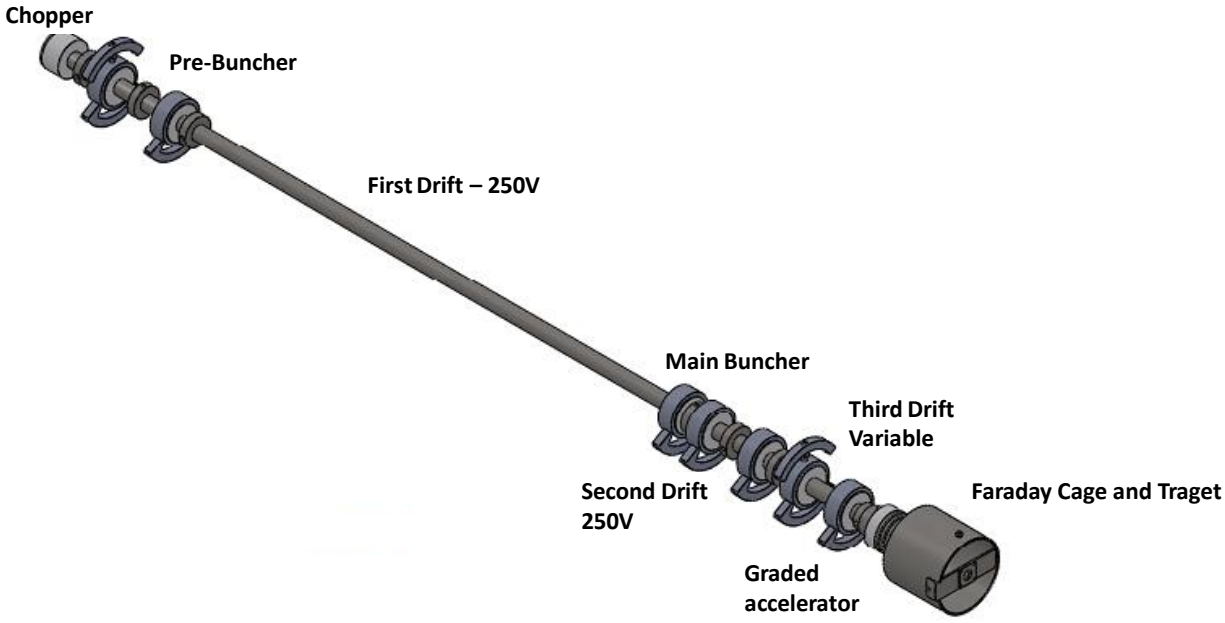

Fig. 21: The isometric design view of the entire pulsing system with the support and insulation. Various parts are marked for identification.

The primary supports for the entire assembly are the triangular stainless steel-MACOR holders which make sure that the assembly is properly centred as well as insulated from the outer tube. Two such arrangements have a locking mechanism which fixes the entire assembly inside the CF 100 I tube. One such arrangement is shown in Fig. 22 (b) on which the 9.5 cm pre-buncher tube is put. The chopper and the ground grids are spot welded on stainless steel rings which are held together by a MACOR cup arrangement as shown in Fig. 22(a), and this could be mounted in a snug fit manner to the pre-acceleration tube. The chopper, pre-acceleration tube and the central pre-buncher electrode are put together as shown in 22 (c). The MACOR cup as well as other MACOR holders has a groove arrangement which maintains the distance between the tubes and

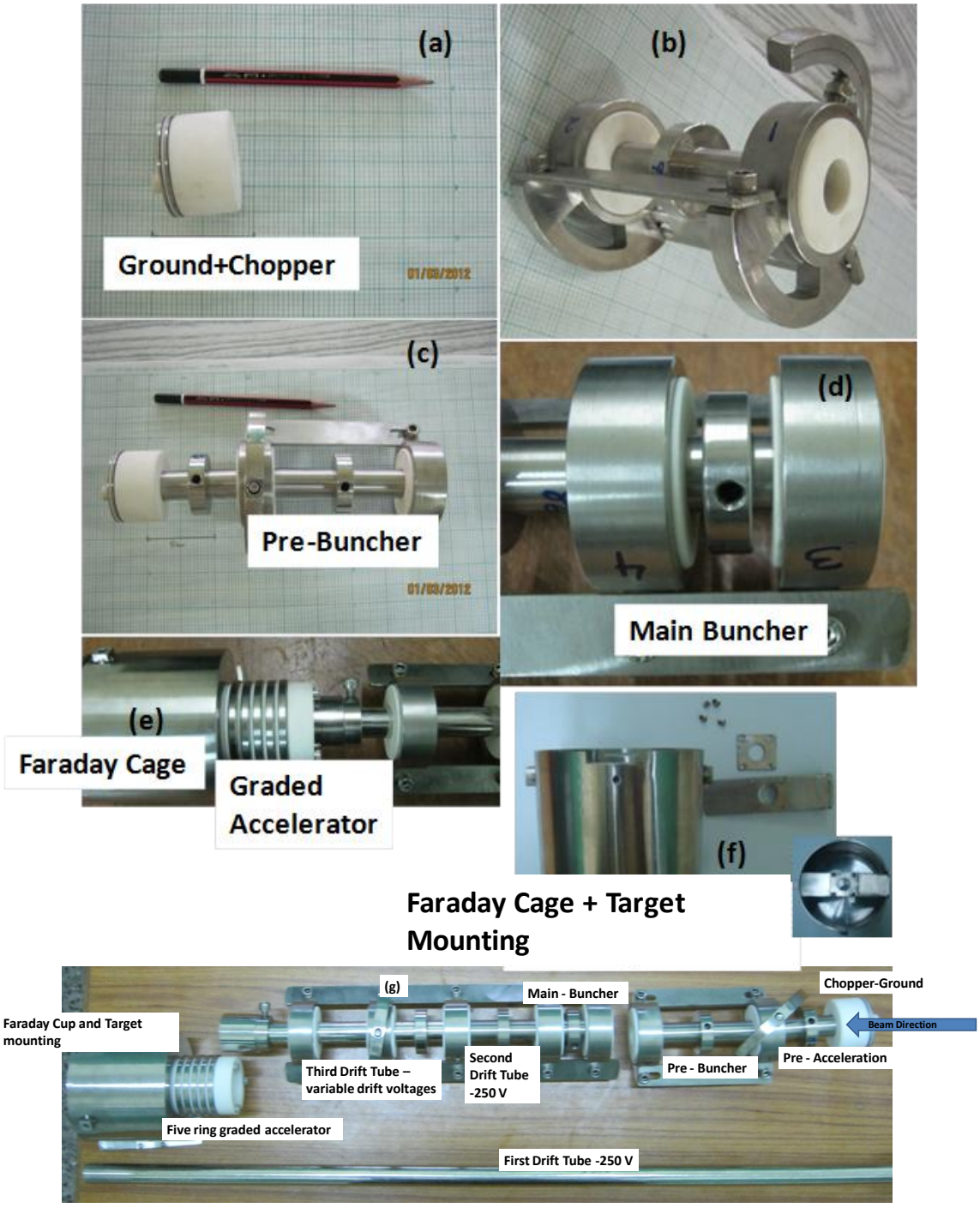

Fig. 22: (a) The chopper and ground grid mounting stainless steel discs held together on the MACOR cup arrangement. (b) Pre-buncher tube mount on the triangular stainless steel-MACOR holders with fixers to the outer tube visible. (c) Chopper, pre-acceleration and the pre-buncher tube arranged together. (d) The main buncher tube snug fit in the MACOR holders. (e) The drift tube inside the MACOR holders on one side and fit into the MACOR cup of graded accelerator on the other. The MACOR cup holds the five ring graded accelerator set up and is attached to the Faraday cup through a screw and bolt arrangement. (f) The L shaped target mounting assembly with Faraday cup and after connecting to the Faraday cup. (g) The entire assembly arranged in order from right to left with important parts marked and the beam direction given

hence provides the necessary electrical insulation between the two. The main-buncher and the drift tube are mount in a similar way as shown in Fig. 22 (d) and (e). The end of the drift tube goes into another MACOR cup which holds together the five stainless steel and MACOR rings for graded potential drop and is attached to the Faraday cup using a screw and bolt arrangement completing the six stage graded acceleration from the drift tube potential to the Faraday cup potential as shown in Fig. 22 (e). The L-shaped target mounting strip is attached to the Faraday cup as shown in Fig. 22 (f). The full assembly arranged in order is shown in Fig. 22 (g). All the electrodes are provided with M5 tapping holes for electrical connections.

4.8 Voltage Divider for Graded Acceleration

As described in section 4.4, the drift tube voltage has to be modified in order to get uniform time bunching for all the accelerating voltages. A graded accelerator is provided to avoid large and sudden spatial focussing/de-focussing of the positron beam due to abrupt change in the potential usually associated with single step acceleration as well as to have enough travel length for the drift tube correction. The graded acceleration is applied from the drift tube electrode to the Faraday cup in six steps as shown schematically in Fig. 23. Vacuum compatible 100 MΩ (non-magnetic/high precision) resistors are used for the graded voltage division.

4.9 Waveform generator, amplifiers and testing

The 50 MHz square wave for the chopper, 50 MHz sine wave for pre-buncher and the 200 MHz sine wave for main-buncher are derived from the 2.1 GS/s dual channel Arbitrary Waveform Generator (AWG) WX2182 (M/s Tabor Electronics Ltd).

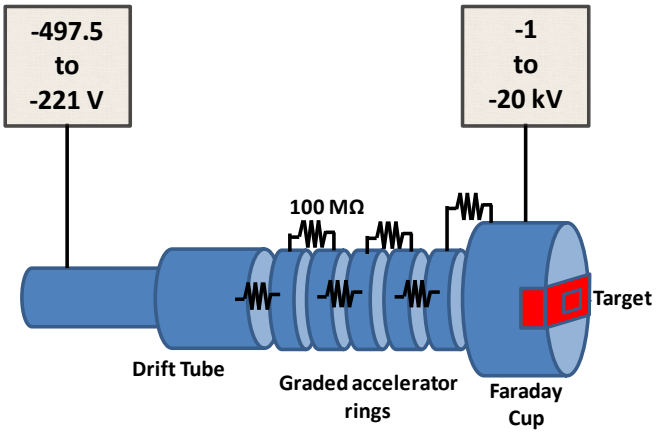

Fig. 23: The six-stage graded accelerator set up with 100 MΩ resistors. The drift tube voltage is varied from ~ -500 to ~ -220 V for target high voltage of -1 to -20 kV respectively.

The DC coupled output from each channel was provided at an output impedance of 50 Ω. Using Kapton insulated 50 Ω coaxial cable with SMA connectors, the power is transferred to the amplifiers, to other RF peripherals like the DC blocks and then to the impedance matching network. Grounded UHV electrical feedthrough with SMA type single pins or dual pins which can take up to 700V mounted on CF 35 flanges are used for the atmosphere to vacuum connection. Vacuum compatible coaxial cables are used to couple RF power to the pulsing electrodes inside the UHV chamber.

Single ended output from the AWG can give a maximum of $2V_{p-p}$ at each channel. Using common sample clock for both channels, the delay between the channels can be adjusted up to 3 ns. As the same sample clock is used for both channels, standard sine waves available with the function generator cannot be used to produce different frequencies. Instead, using a wave composer sine waves are generated as arbitrary waves and are fed into the generator. For 50 MHz sine wave at a sampling rate of 2 GS/s, 40 points can be generated per cycle whereas for 200 MHz sine wave only 10 points per

cycle represent one cycle of the wave. Less number of points affects the signal reproduction and can be checked with a high sampling digital oscilloscope. The RF modulation voltage varies from ~ 13-16 V_{p-p} depending on the final acceleration of positrons. Hence to get the required modulation voltage for the bunchers, the output from the AWG are amplified using coaxial amplifiers with a maximum of 2W output obtained from M/s Mini circuits. It can give a minimum gain of +29dB in the operating frequency range with a flatness of ±1db. The amplifier has a maximum power input of +10dBm which correspond to a sine wave of 1V amplitude at 50 Ω. Marker (square wave) output available corresponding to each channel from the AWG is utilized as the square wave source. The delay between the channel output to the corresponding marker output can be adjusted to a maximum of 3ns. Maximum amplitude of 1 V_{p-p} is available at the marker. The marker output is taken with respect to the channel from which 50 MHz sine wave is drawn. This output is also generated as square pulses in the wave composer and is fed into the memory of the generator. A high bandwidth amplifier (11.5GHz) with minimum rise/fall time (31-36 ps) is used as the square wave amplifier and is obtained from M/s Picoseconds Lab with a maximum input of 1.5 V and a maximum output of 11.5V. Fig. 24 (a) shows the testing of AWG and the amplifiers using a 2.5 GS/s, 1GHz digital oscilloscope. Fig. 24 (b) shows the screen captured image of the wave composer output of 50 MHz sine wave and 200 MHz sine wave. It also shows the bit editor to create a square wave.

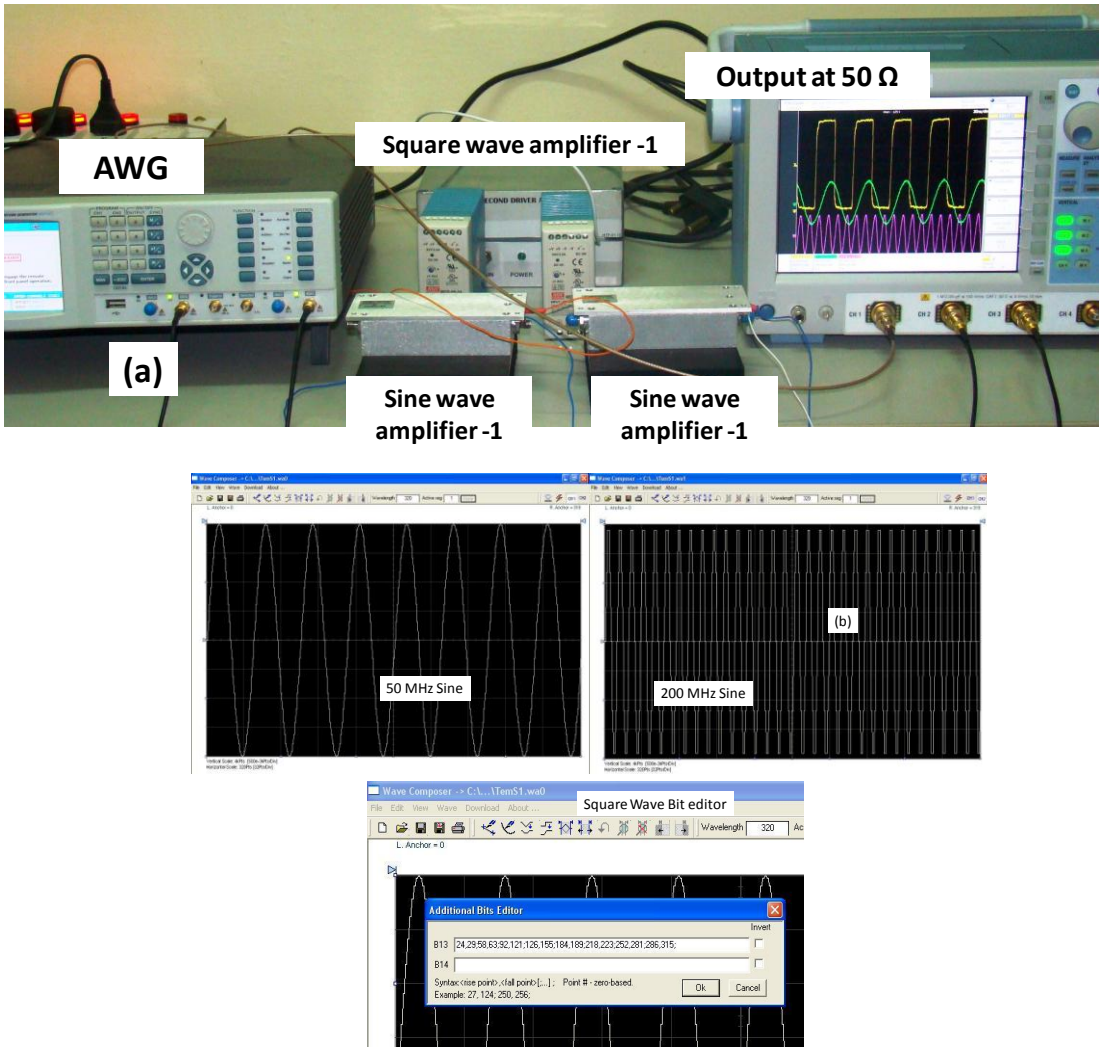

Fig. 24: (a) Testing of AWG along with the amplifiers for two sine waves and a maker output square wave. (b) Screen captured images of the wave composer output to get 50 MHz and 200 MHz sine waves. It also shows the bit editor for getting the 50 MHz square as the marker.

The testing results of two sine wave amplifiers are shown in Fig. 25 (a) and (b), where signals before and after an amplification of +32dB are shown respectively. Also shown are the possibilities for adjusting the time delay between the signals and its effectiveness after amplification. The smoothness of the sine wave is not available with digitally produced sine wave because of the finite sample points; however the amplification does not introduce additional noise. The square wave is given as a reference; though the 50MHz sine wave was the trigger for the oscilloscope.

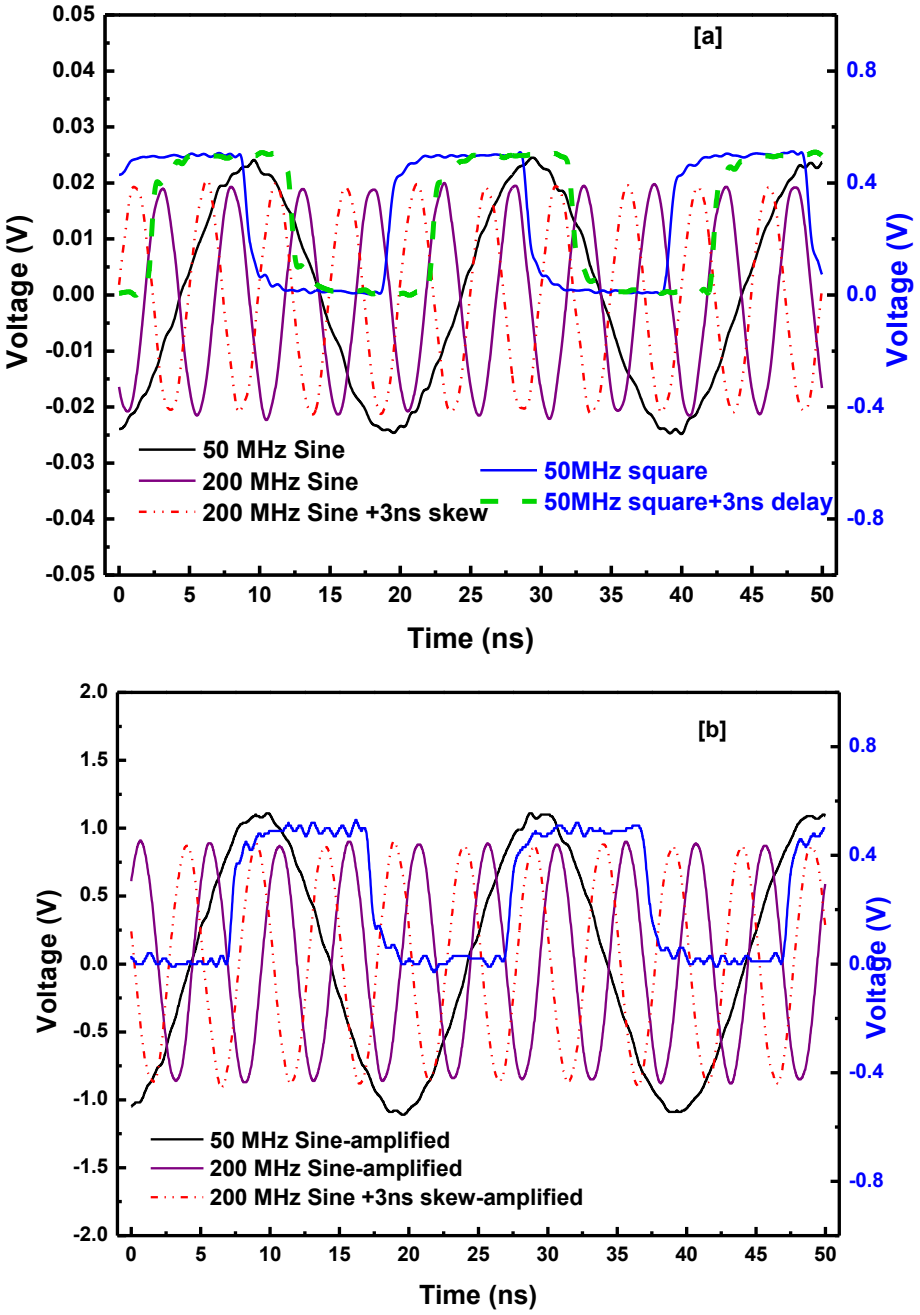

Fig. 25: (a) 50 mV_{p-p} sine wave of frequency 50 MHz and 200 MHz as well as a 50 MHz square wave with 0.5 V amplitude captured in a digital oscilloscope using the 50 MHz sine wave as the trigger. Also shown are the 200 MHz sine wave and square wave after introducing a time delay with respect to the 50 MHz Sine wave reference. (b) Shows the output after amplification. The un-amplified square wave is shown for comparison with earlier result. Here again the a time delay is given to the amplified 200MHz sine wave with respect to the lower frequency sine wave.

The amplification of the square wave is difficult without distortion of wave shape owing to finite bandwidth of any linear amplifier and because of the rise time increase after amplification. To get a negative going square wave pulse of required amplitude, a DC offset bias is given to the amplifier. A maximum of -17 V could be given in the present model and Fig. 25 (c) shows the output after amplification up to +17 dB as well as after the maximum possible amplification (11.5V) using the selected amplifier. To capture the maximally amplified square signals in the digital oscilloscope at 50 Ω coupling, a DC offset of -5V was applied and hence only a part of the signal from -3V to -6 V is visible. A negative going pulse of -15 volt is envisaged for use as chopper pulse and presently work is going on to achieve this. One way to get over the difficulty in getting fast rising, high amplitude square waves is to apply sine wave of similar frequency of required amplitude instead. However this results in a much reduced open chopper window leading to reduced counts. Other problems which are seen in the amplified signals are the increase in rise time and the significant pulse shape variation which would result in positrons entering the bunching column at off state and unwanted velocity modulation at chopper leading to satellite peaks in the lifetime spectrum and positron pulse broadening. The pulse shape distortion is due to the non linear amplification of the harmonics of the square wave. The time delay which can be achieved between 50 MHz sine wave and square wave is demonstrated in this case as well.

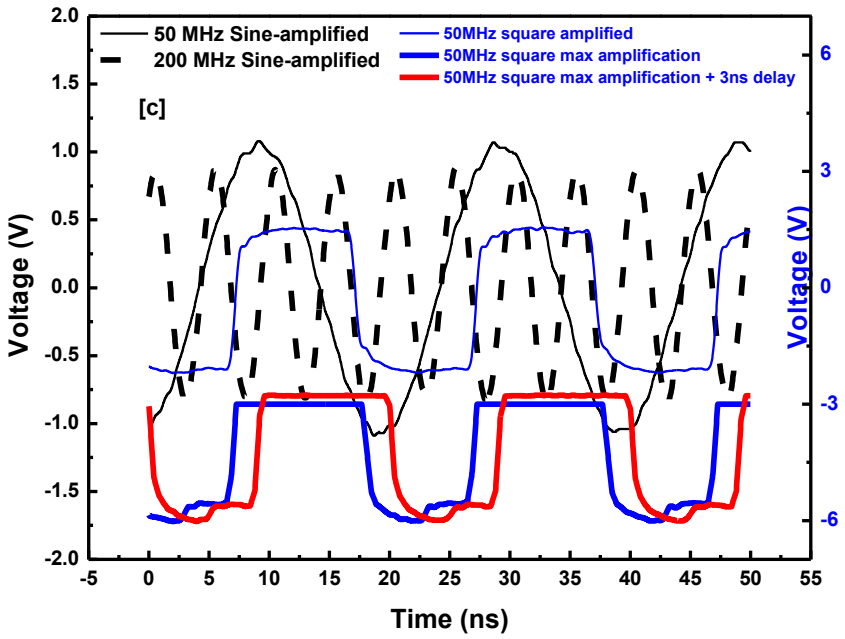

Fig. 25: (c) Along with the amplified sine waves, amplified DC offset negative going square waves are shown after +17dB amplification and also after the maximum possible amplification (V_{amp}= 11.5V). To obtain the output after maximum amplification, a DC offset has been introduced in the digital oscilloscope and hence values from -3 to -5.5 V alone are visible. Output after introducing a time delay between 50 MHz Sine wave and the amplified square wave is also shown.

4.10 RF power coupling

The required RF power to the load (here the bunching electrodes) has to be transferred through an impedance matching network to have minimum loss by reflection. The impedance matching unit can be a basic L-network with inductor in series and capacitance as shunt such that along with electrodes (which contribute a capacitive and/or inductive reactance) the net impedance of the load becomes 50 Ω. During testing, the matching can be checked by measuring the reflected power and the voltage standing wave ratio (VSWR). A very low VSWR implies good matching. The chopper grid is biased to +15V DC and is used as a reflector in the absence of the nullifying 50MHz -15V pulse. Similarly all the electrodes in the pre-buncher as well as in main-buncher will be floating at -250V DC bias to maintain the pre-acceleration of the positrons applied

immediately after the chopper up to the drift tube. The matching network hence also includes the arrangement for this DC bias and is similar to the working of a bias-tee. The AWG is protected from accidental DC flow using inner-outer DC blocks provided along all three output path of the AWG. The DC blocks for both sine wave and square waves were obtained from M/s Aeroflex Inmet taking into account the maximum DC bias to be protected against and the working frequency range. Fig. 26 shows the flow diagram of the pulsing electronics set-up starting from the AWG. Fig. 27 (a) and (b) shows the impedance matching network for the sine waves and coupling network for the square wave.

The matching network concept adopted in the NCSU pulsed beam buncher has been taken up here [24]. The buncher electrodes are all biased at -250V and hence a DC block is required at both inside and outside paths. This is achieved using C_2 in the bias tee and C_3 in the DC block as shown in Fig. 27 (a). The required bias tee for high voltage bias with the required bandwidth has been acquired from M/s Aeroflex and M/s Picoseconds Lab for square wave and sine wave respectively. The buncher could be considered as a capacitance C which is in series with C_2 and C_3. This net capacitance is in parallel with the variable capacitor C_1. Thus, the network boils down to a series LC circuit with a sine signal of a particular frequency f. The resonance condition ($f = 1/2\pi\sqrt{LC}$) is applied to obtain the value of L to be used here. The inductance coil is then wound using the parameters derived using the approximate coil winding formula for a single layer air-core coil as given here [24]

$$L = \frac{(rN)^2}{9r+10l} \tag{16}$$

where N is total number of turns, r is the radius in inches and l is the length of the coil in inches and L is the self inductance in micro henries. The expression is accurate to 1% of the value. The variable capacitor can be tuned to get minimum reflected power ensuring

maximum power transfer to the load. The matching and biasing box will be sitting right on top of the RF electrical feedthrough on the CF 35 flange and hence the net capacitive reactance of the buncher electrodes will be measured at 50 and 200 MHz at the SMA connector on the electrical feedthrough meant for RF coupling. The measurement is carried out at the operating vacuum as that too works as the dielectric for the buncher capacitor apart from the MACOR insulator. The measurement helps in the determination of all the capacitive and inductive values in the biasing box.

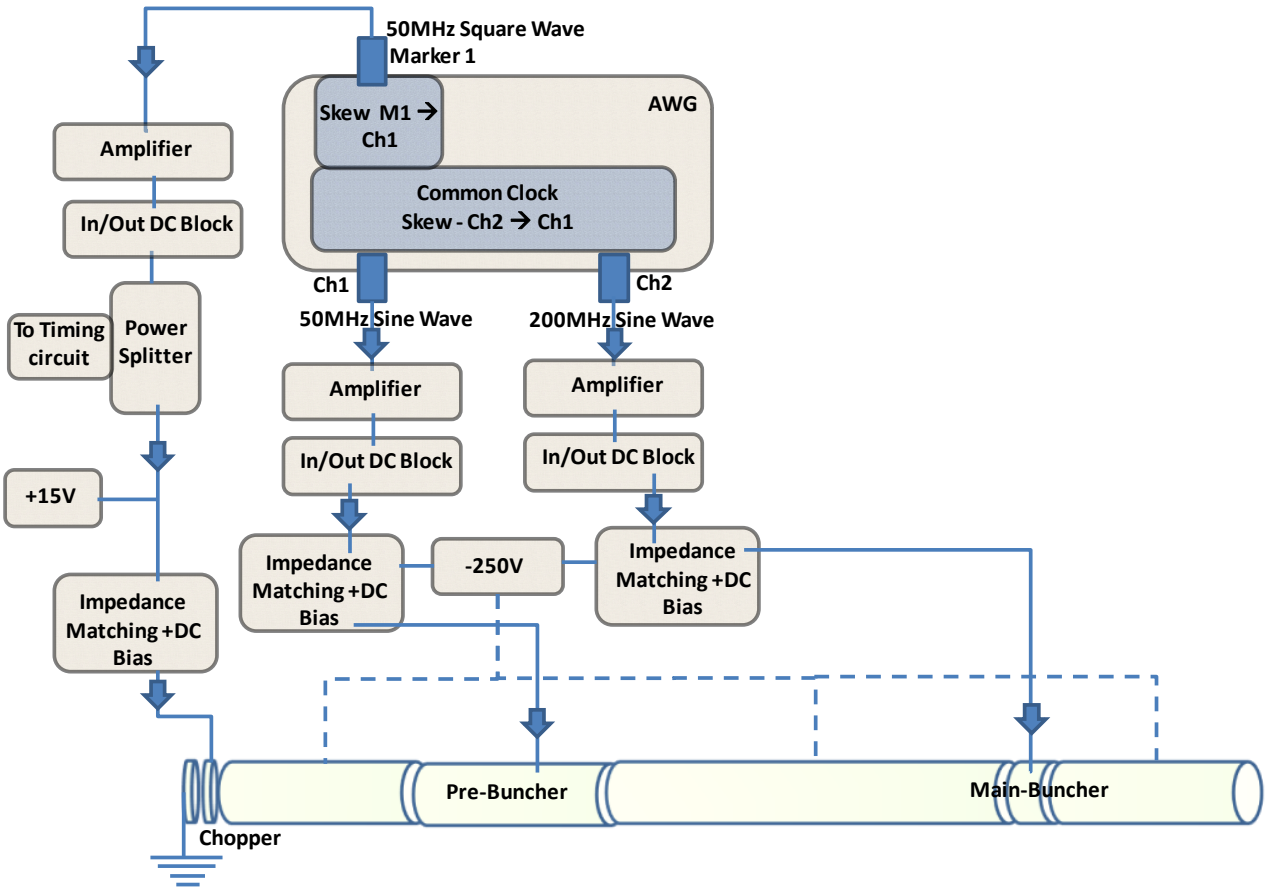

Fig. 26: Block diagram of the application of RF power on the chopper and the bunching electrodes using a single AWG. The beam proceeds from the chopper to the main buncher.

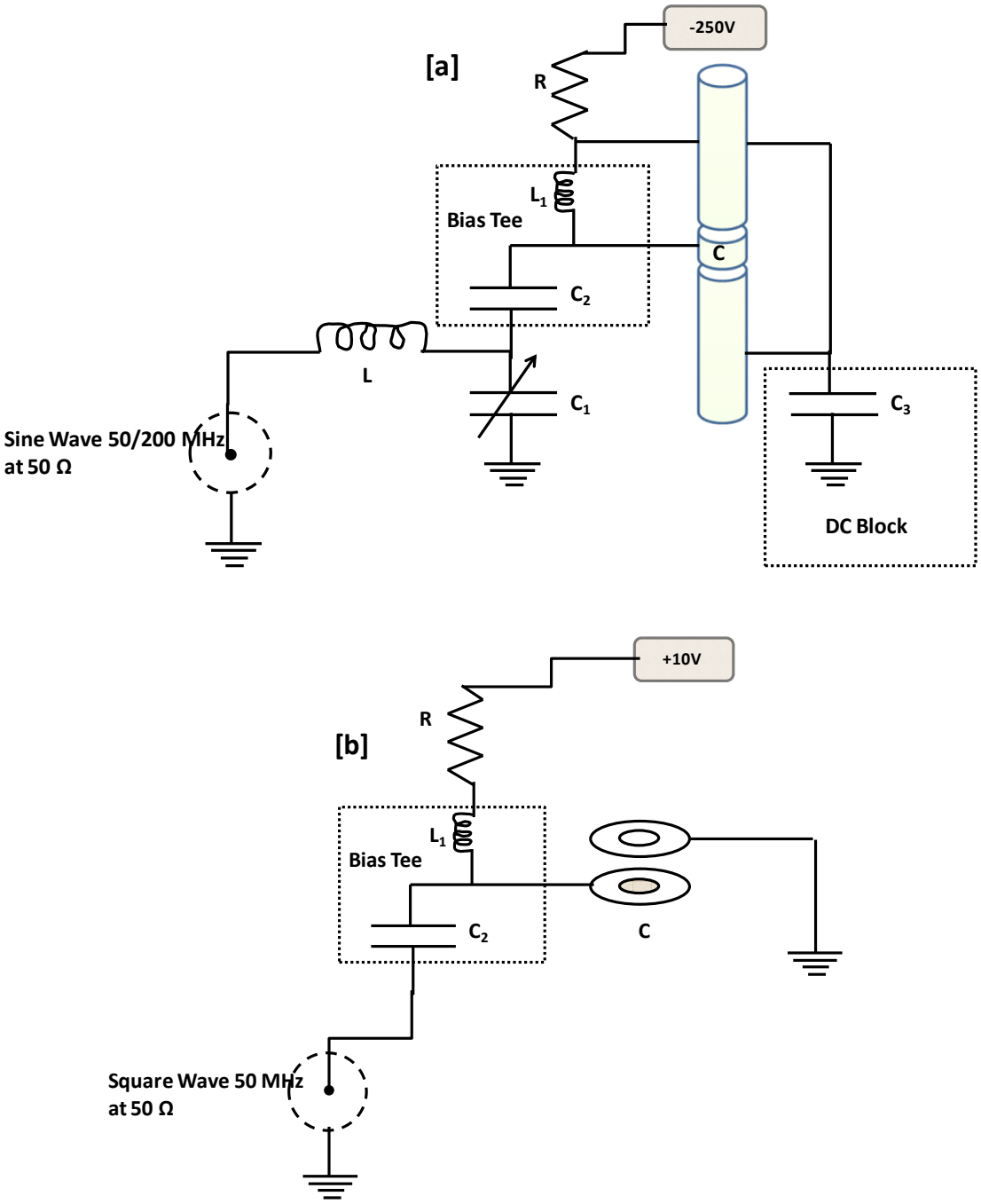

Fig. 27: (a) Impedance matching and biasing network for bunchers (pre as well as main). L and C_1 form the balancing L-network, whereas C_2 and C_3 are DC protection for RF components achieved using Bias Tee and DC block. (b) Coupling Network where C_2 forms DC protection achieved using Bias Tee.

4.11 Positron Lifetime measurement – Flow diagram

The timing signal which would be the stop pulse to the Time to amplitude converter (TAC) is derived after giving the amplified square wave signal to the constant fraction differential discriminator (CFDD). Since a two way connection is required from the square wave amplifier, a high band width power splitter from M/s Broad wave technologies and a resistive voltage divider arrangement [47] for attenuated input to CFDD will be used. The start signal is derived from CFDD to which the 511keV γ signal from the BaF_2 – XP2020Q Photomultiplier tube is given. This detector gives a time resolution of the order of 250 ps in the conventional bulk lifetime system. The two time pulses are additionally tagged by a fast coincidence setup, to ensure that both start and stop are corresponding to the same event. The fast coincidence timing condition is kept around 20ns which corresponds to the time difference between pulses of time compressed positrons. The time difference between the two is converted to voltage by TAC which then is sent to the multi channel analyzer (MCA) to generate the lifetime spectrum. The time delay between the signals has to be tuned so that the TAC works in its linear range. Additional delays are also provided in start and stop signal paths so that the start signal comes well inside the fast coincidence pulse at the TAC and the stop comes after the start but before the next fast coincidence pulse. The flow chart - block diagram of the timing circuit is given in Fig.28 where the final lifetime plot and its centroid are also shown.

As described above, since the 511keV γ signal is taken as start and chopping pulse is taken as stop, an inverted spectrum is obtained which needs to be corrected for further analysis. The lifetime spectrum generated can be understood as follows. A perfect chopping and bunching is assumed for the explanation. Hence no positrons exist in the drift column unless the chopper reflecting potential is lifted. All positrons could be time

bunched such that its time of flight from chopper to target is exactly equal to that of the reference positron whose description is given in the optimization section. The reference positron is assumed to be at the middle of the "on" phase of the chopper. The time difference between the centres of the open window of 10ns to the leading edge of the next open window is 15 ns as the time period of the square pulse is 20 ns. For perfect bunching, all positrons reach the target after a time τ_{drift} which is the time of travel of the reference positron from the chopper to the target. This produces the 511 keV Start pulse. Let the positron annihilate at the instant it reaches the target. Then the subsequent stop pulse comes at 15-τ_{drift} ns after the start pulse. Hence the zero of the inverted lifetime spectrum will be at 15-τ_{drift} ns. If the positron takes a slightly longer time to annihilate say τ, then the time difference between start and stop becomes 15-(τ_{drift}+τ) ns. τ follows the lifetime spectrum and hence, an exponential spectrum decaying from the zero is achieved after collecting the spectrum for sufficient counts. In case of perfect bunching the time resolution of the experiment is only determined by that introduced by the lifetime detection system. A finite width ($\Delta\tau$) of the positron pulse at the target reflects as 15-(τ_{drift}+τ ± $\Delta\tau$) and hence the positron pulse width gets integrally summed to the detector resolution. Positrons entering the bunching column in the off-period results in reduction of time difference between the start pulse and the stop pulse which shows up as peaks (called as satellite peaks) on the decay spectrum in the lower time side or as long lifetime tails. Therefore the chopping potential and the bunching electrode phases have to be well tuned to get good time resolution from the pulsed positron system.

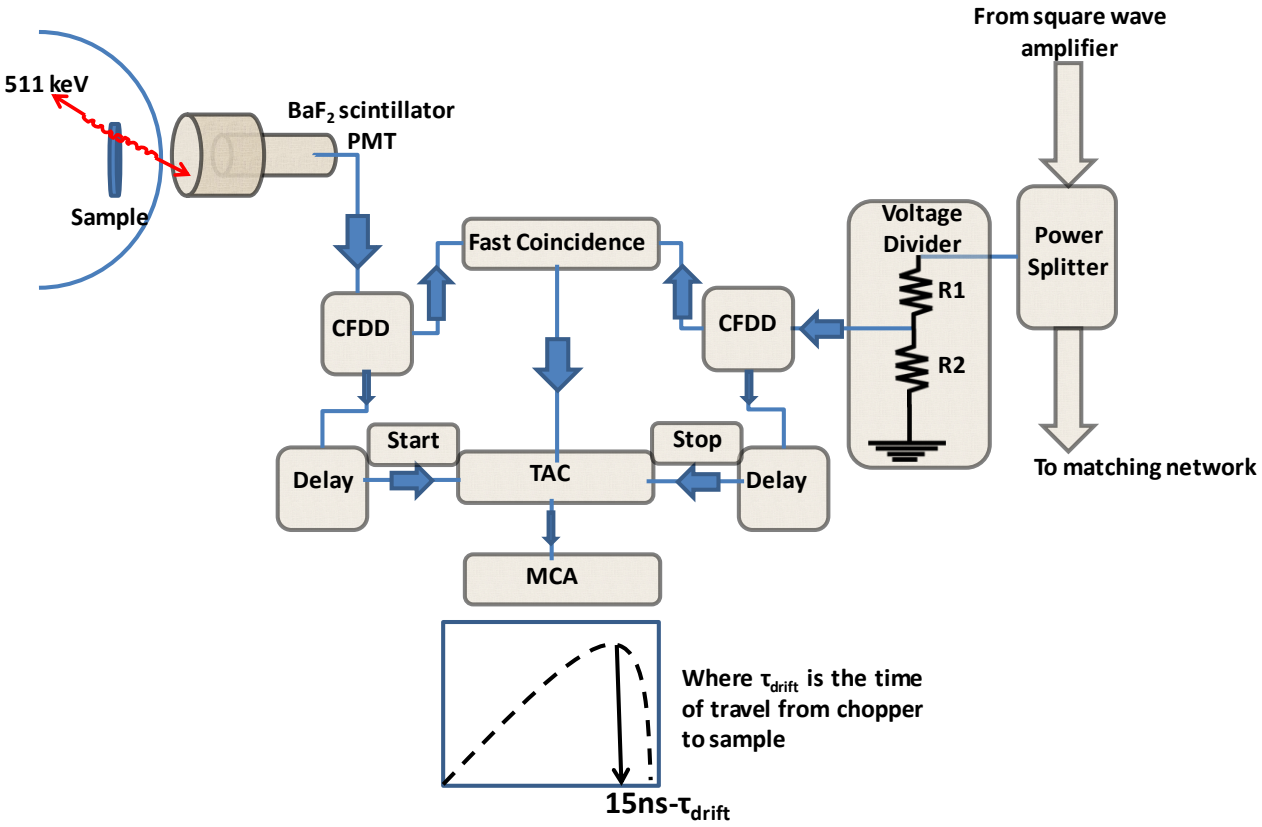

Fig. 28: Timing circuit to generate the inverted lifetime spectrum with 511 keV as start signal and square pulse from AWG as stop. The inverted pulse is centred on 15 -τ_{drift} ns if no extra delay is provided.

4.12 Summary

- A design for a pulsed positron beam using β^+ emitting ^{22}Na source was finalised with one chopper and two bunchers. The length of the bunching electrodes were finalised based on the bunching frequency at the pre-buncher and at the main-buncher.
- All the parameters critical for getting uniform time focussing at all accelerating voltages were optimized using positron trajectory calculations using SIMION [48,49].
- A UHV system to attain a vacuum of the order of 10^{-8} mbar and to contain the pulsing system has been designed, fabricated and tested. Magnetic field for the

transport of positrons are obtained through a combination of solenoid and Helmholtz coils which were wound and tested for field uniformity and stability.

- The mechanical assembly of pulsing system was designed and fabricated.
- The AWG and amplifiers for the required sine waves and square waves were procured and tested. The conceptual design for RF power coupling, impedance matching and positron lifetime generation were presented.
- The conceptual designs of the drift tube biasing and graded acceleration were finalised.

References:

1. Shultz P J and Lynn K G 1988 "*Interaction of positron beams with surfaces, thin films, and interface" Rev. Mod. Phys.* **60** 701.
2. Coleman P G, Griffith T C and Heyland G R 1973 *"A time of flight method of investigating the emission of low energy positrons from metal surfaces" Proc. R. Soc. A* **331** 561.
3. Costello D G, Groce D E, Herring D F and McGowan J Wm 1972 *"(e^+, He) Total Scattering" Can. J. Phys.* **50** 23.
4. Howell R H, Tuomissari M and Jean Y C 1990 *"Chemical modification of positronium formation at metal surfaces" Phys. Rev. B* **42** 6291.
5. Szpala S, Petkov M P and Lynn K G 2002 *"A simple positron lifetime spectrometer for a magnetically guided low-energy beam" Rev. Sci. Intrum.* **73** 147.
6. Chen H et.al. 2004 *"Durability and free volumes in polymer coatings studied by positron annihilation spectroscopy"* Mater. *Sci. Forum* **445-446** 274.
7. Moxom J and Xu J 2003 *"A positron lifetime spectrometer for a DC positron beam"* **68** 651.
8. Gidley D W, Frieze W E, Dull T L, Sun J N and Yee A F 2000 "*Probing Pore Characteristics in Low-K Thin Films Using Positronium Annihilation Lifetime spectroscopy" Mat. Res. Soc. Symp. Proc.* **612** D4.3.1.

9. Mills Jr. A P 1980 *"Time bunching of slow positrons for annihilation lifetime and pulsed laser photon absorption experiments"Appl. Phys.* **22** 273.
10. Schödlbauer D, Sperr P, Kögel G and Triftshäuser W 1988 *"A pulsing system for low energy positrons" Nucl. Instm. Meth. Phys. Res. B* **34** 258.
11. Suzuki R, Kobayashi Y, Mikado T, Ohgaki H, Chikawi M, Yamazaki T and Tomimasu T 1991 *"Slow Positron Pulsing System for Variable Energy Positron Lifetime Spectroscopy" Jap. J. Appl. Phys.* **30** L532.
12. Willutzki P, Stormer J, Kogel G, Sperr P, Britton D T, Steindl R and Triftshauser W 1994 *"An improved pulsed low-energy positron system" Meas. Sci. Technol.* **5** 548
13. Zecca A et.al. 1995 *"A pulsed positron microbeam" Europhys. Lett.* **29** 617.
14. Hirose M, Nakajyo T and Washio M 1997 *"A compact cyclotron based slow positron beam and a new positron pulsing system" App. Surf. Sci.* **116** 63.
15. Howell R H, Cowan T E, Hartley J H and Sterne P A 1997 *"Positron beam lifetime spectroscopy at Lawrence Livermore National Laboratory" AIP Conf. Proc.* **392** 451**.**
16. Fallström K and Laine T 1999 *"Construction of the Helsinki University of Technology (HUT) pulsed positron beam" Appl. Surf. Sci.* **149** 44.; Laakso A, Saarinen K and Hautojärvi P 2001 *"Positron lifetime beam for defect studies in thin epitaxial semiconductor structures" Physica B* **308-310** 1157; Reuring F 2010 *"Slow positrons in materials science: pulsed positron beam and defect studies in indium nitride" Doctoral Dissertation Department of Applied Physics Aalto University.*
17. Hamada E, Oshima N, Suzuki T, Kobayashi H, Kondo K, Kanazawa I and Ito Y 2000 *"New system for a pulsed slow-positron beam using a radioisotope" Rad. Phys. Chem.* **58** 771.
18. De Baerdemaeker J and Dauwe C 2002 *"Development and application of the Ghent pulsed positron beam" Appl. Surf. Sci.* **194** 52.
19. Iijima H, Asonuma T, Hirose T, Irako M, Kadoya K, Kumita T, Matsumoto B, Wada K and Washio M 2002 *"Time bunching of slow positrons for lifetime and time-of-flight measurements of ortho-positronium" Nucl. Inst. Meth. Phys. Res. A* **483** 641.
20. Gninenko S N 2004 *"Design of a high-efficiency pulsed positron beam for experiments with orthopositronium in vacuum" Int. J. Mod. Phys. A* **19** 3939.

21. Krause-Rehberg R, Sachert S, Brauer G, Rogov A and Noack K 2006 *"EPOS—An intense positron beam project at the ELBE radiation source in Rossendorf" Appl. Surf. Sci.* **252** 3106.
22. Alberola N et.al. 2006 *"Development of a high-efficiency pulsed slow positron beam for measurements with orthopositronium in vacuum" Nucl. Inst. Meth. Phys. Res. A* **560** 224.
23. Ohdaira T, Muramatsu M, Suzuki R, Kobayashi Y, Takanawa M, Hashimoto N, Takao K and Kobayashi Y 2007 *"Development of a Na-22 based pulsed positron beam for depth selective PALS" phys.stat.solid.(c)* **4** 4020; Suzuki R, Ohdaira T and Mikado T 2000 *"A positron lifetime spectroscopy apparatus for surface and near-surface positronium experiments" Rad. Phys. Chem.* **58** 603.
24. Hathaway A G, Moxom J, Hawari A I and Xu J 2007 *"Design of a slow pulsed positron beam for positron annihilation lifetime spectroscopy" Nuclear Science Symposium Conference Record, 2007. NSS '07. IEEE* **2** 1695; Hathaway A.G. 2012 *"High Intensity Pulsed Picosecond Positron Beam for Nanophase Examination" Doctoral Dissertation Department of Nuclear Engineering North Carolina State University.*
25. Wang B Y, Ma Y Y, Zhang Z, Yu R S and Wang P 2008 *"Performance of the Beijing pulsed variable-energy positron beam" Appl. Surf. Sci.* **255** 119.
26. Chuan-Bo G, Tao X, Chuan-Ying X, Hui-Min W, Bang-Jiao Y, Rong-Dian H and Xian-Yi Z 2008 *"Simulation of time bunching for a pulsed positron beam" Chinese Physics B* **17** 4149.
27. Sperr P, Egger W, Kögel G, Dollinger G, Hugenschmidt C, Repper R, Piochacz C 2008 *"Status of the pulsed low energy positron beam system (PLEPS) at the Munich Research Reactor FRM-II" Appl. Surf. Sci.* **255** 35.
28. Mileshina L and Nordlund A 2009 *"Design and performance of the pulsed positron beam at Chalmers University of Technology" Nucl. Inst. Meth. Phys. Res. B* **267** 2934.
29. Maekawa M and Kawasuso A 2012 *"Development of pulsed positron beam line with compact pulsing system" Nucl. Inst. Meth. Phys. Res. B* **270** 23.
30. Xu Hong-Xia, Liu Jian-Dang, Gao Chuan-Bo, Weng Hui-Min and Ye Bang-Jiao 2012 *"SIMION simulation of a slow pulsed positron beam" Chinese Physics C* **36** 251.

31. Gilbert S J, Kurz C, Greaves R G and Surko C M 1997 *"Creation of a monoenergetic pulsed positron beam" Appl. Phys. Lett.* **70** 1944.
32. Sullivan J P, Roberts J, Weed R W, Went M R, Newman D S and Buckman S J 2010 *"A trap based positron beamline for the study of materials" Meas. Sci. Technol.* **21** 085702.
33. Milner W T 1979 *"Double drift beam bunching systems" IEEE Transactions on Nuclear Science* **26** 1445.
34. Amarendra G, Viswanathan B, Venugopal Rao G, Parimala J and Purniah B 1997 *"Variable low energy positron beams for depth resolved defect spectroscopy in thin film structures" Current Science* **73** 409.
35. Coleman P G 2000 *"The generation and transport of positrons" Positron Beams And Their Applications* ed. Coleman P G (Singapore: World Scientific) p 11-40.
36. Amarendra G, Canter K F and Schoepf D C 1996 *"Study of positron yield of W(100) single crystalline foil with in situ surface characterisation" J. App. Phys.* **80** 4660.
37. Suzuki R, Amarendra G, Ohdaira T and Mikado T 1999 *"Positron re-emission from tungsten surfaces" App. Surf. Sci.* **149** 66.
38. Fischer D A, Lynn K G and Gidley D W 1986 *"High-resolution angle-resolved positron reemission spectra from metal surfaces" Phys. Rev. B* **33** 4479.
39. Canter K F and Mills Jr. A P 1981 *"Slow positron beam design notes" Can. J. Phys.* **60** 551.
40. Dahl D A 2000 *"SIMION for the personal computer in reflection," Int. J. Mass Spectrom.* **200** 3. (source: Scientific Instrument Services, Inc., Ringoes, NJ, www.simion.com).
41. Pandit V S and Sarma P R 2001 *"Generating the effect of six harmonics in beam bunchers using only two harmonics" Nucl. Inst. Meth. Phys. Res. A* **462** 349.
42. Ierusalimschy R, Henrique de Figueiredo L and Filho W C 1996 *"LUA – An extensible extension language" Software: Practice and Experience* **26** 635**.**
43. Reurings F, Laakso A, Rytsölä K, Pelli A and Saarinen K 2006 *"Compact positron beam for measurement of transmission moderator efficiencies and positron yields of encapsulated sources" Appl. Surf. Sci* **252** 3154.
44. Krause-Rehberg R, van der Walt N, Büttner L and Börner F 2004 *"A ^{22}Na positron source for use in UHV" Appl. Surf. Sci.* **221** 165.

45. Anwand W, Brauer G, Butterling M, Kissener H R and Wagner A 2012 *"Design and Construction of a Slow Positron Beam for Solid and Surface Investigations" Defect and Diffusion Forum* **331** 25.
46. http://www.netdenizen.org/emagnettest/solenoids/?thinsolenoid
47. Knoll G F 2000 *"Radiation detection and measurement"3rd edition (New York : John Wiley and Sons).*
48. Anto C V, Rajaraman R, Abhaya S, Parimala J and Amarendra G 2011 *"Design optimization of a pulsed positron beam system at IGCAR, Kalpakkam" J. Phys.: Conf. Ser.* **262** 012062.
49. Anto C V, Rajaraman R, Venugopal Rao G, Abhaya S, Parimala J and Amarendra G 2012 *"Optimization of Drift Bias in an UHV Based Pulsed Positron Beam System" AIP Conf. Proc.* **1447** 493.

The defect of equality is that we only desire it with our superiors – Henry Becque

Chapter 5

Beam extraction, diagnostics and testing

This chapter discusses the activation of the positron beam by placing ^{22}Na source and W (100) moderator into the assembly. The velocity selection of slow positrons is implemented using a combination of aperture and magnetic bend. The slow positrons have been successfully extracted and transported to the target chamber without the pulsing electrodes. The transported positrons are used to carry out demonstrative S-parameter measurements on Cu and Silicon (100) and thus the depth selectivity is demonstrated. The internal wiring of the pulsing electrodes is completed and they have been inserted into the beam line for vacuum testing, beam steering and finally for pulsing.

5.1 Introduction

The primary components for the assembly of the pulsed positron beam have been designed, procured or fabricated. The integration of these parts and their testing in two steps will be discussed in this chapter. The first step involves the extraction of the slow positrons through the magnetic bend up to the target without the pulsing electrodes inside and the demonstration of its use as a conventional slow positron beam. The second step involves the insertion of the pulsing electrodes and steering the slow positrons through the pulsing electrodes. After these objectives have been achieved the pulsing electrodes would be fired up according to the design described in the previous chapter and the final testing of the pulsed positron beam will be done. At the time of this thesis, the first stage has been completed and the required cable connections to the pulsing electrodes inside the UHV are done. The vacuum testing and beam steering through the electrodes is going through presently. Hence these will be presented here and the future work involved will be highlighted.

5.2 Moderator Annealing

Tungsten (W) single crystal in (100) orientation is used as the moderator in the transmission geometry. The thickness of the crystal is ~1µm. For handling and mounting the moderator easily, the foil is sandwiched between two Tantalum (Ta) sheets (99.999 % polycrystalline sheets) of 100 µm thickness. These Ta sheets have a central hole of 8 mm, which helps in exposing the W to the source side and towards the extraction optics. After placing the W (100) crystals between Ta sheets, they are spot welded at four corners.

The moderation efficiency of the W(100) depends on the defect content and the surface condition. The W (100) mount in Ta sheets may have some positron-trapping

open volume defects created during handling and processing. The surface may also have a thin layer of native oxide as well as adsorbed contaminants like carbon which increases the surface trapping of positrons and thus decreases the moderation efficiency. These can be removed by controlled high temperature annealing of the moderator set-up in a vacuum of the order of 10^{-6} mbar. A high vacuum, diffusion pump operated physical vapour deposition (PVD) unit has been earmarked for the moderator annealing. A 99.999% pure W polycrystalline sheet cut in the required dimension acts as the boat of the PVD set up. The W (100) crystal inside Ta sheets is annealed after placing them on the customized boat. Before the start of the annealing process the chamber as well as the copper electrodes is cleaned to remove all possible contaminants using organic solvents. First the W-boat is fixed between the copper electrodes, and a vacuum of 2×10^{-6} mbar is obtained. Then the secondary current through the boat is gradually increased at the rate 0.5A/s. Temperature is measured using the disappearing filament optical pyrometer. Temperatures were measured at 1373 K, 1873 K and 2273 K, to calibrate the secondary current and the temperature. Proper cooling to the glass chamber and to the nearby neoprene o-rings are provided using fans. The annealing is not carried out in a single step, but given in pulses to avoid excessive bending of the W boat, increase in chamber and o-ring temperatures and to avoid large increase in pressure inside the chamber. A two minute pulse at 2273 K is followed by 2-5 minute pulse at 1373 K. The vacuum degrades to 5×10^{-6} mbar during the higher temperature pulse. The time kept for low temperature pulse is adjusted to get back the starting vacuum of 2-3 $\times 10^{-6}$ mbar and to avoid excessive heating near the o-ring. Ten such high pulses are applied after which the secondary-current is brought down at 0.5A/s. After proper cooling of the W-boat the vacuum is released and the W (100) crystal inside the Ta sheets is placed on the boat. The procedure is repeated as shown in Fig. 1(a) and (b) where we could see the low

pulse and the high pulse regime. After annealing and proper cooling, the vacuum is released at the time of mounting the moderator on to the beam line. The process need not be hurried through, as good moderation efficiency was obtained even after a one hour exposure in air. The efficacy of the above process was tested by mounting a similarly annealed moderator on the slow positron beam facility in the lab where a tenfold increase in counts was observed after annealing.

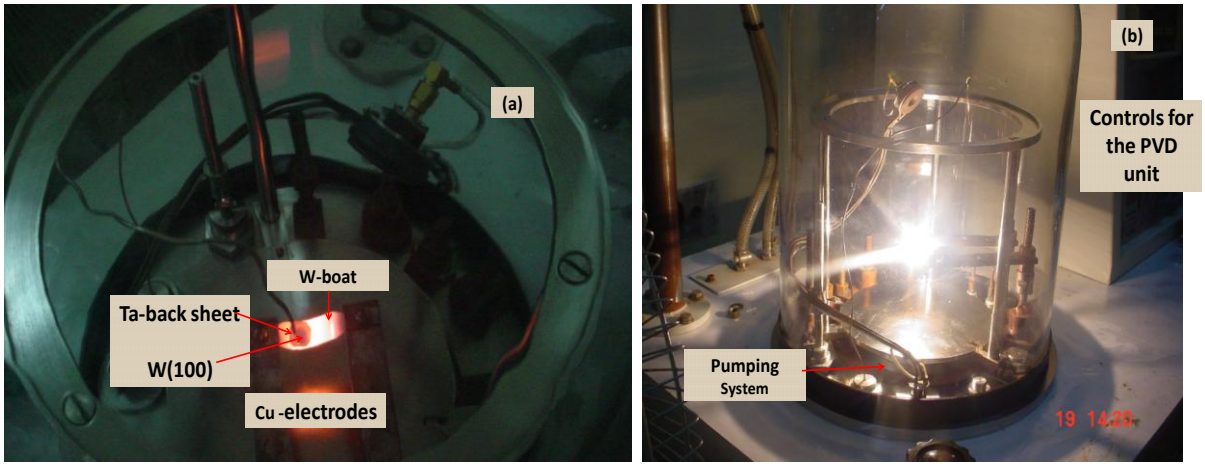

Fig. 1: (a) Moderator annealing during the low temperature pulse (~1373K). Cu electrodes, W boat, Ta back foil and W (100) are marked. (b) Flash during the high temperature pulse (~2273K).

5.3 Source Mounting and Radiation Shielding

A 50 mCi source of ^{22}Na is envisaged to be used in the positron beam line. The source comes inside a Titanium capsule sealed on the front with a Titanium window [1]. ^{22}Na source of activity greater than 10 mCi is considered to be posing an A-level hazard as given by the radio nuclide safety data sheet. Hence, a lead shielding is required to reduce the exposure rate to less than 2mR/hr at a distance of 1 foot from the source [2]. Hence, a lead shielding is built around the source chamber with enough thickness such that the standards are met. The half value layer for the 1280 keV γ field of the source is 0.67 cm of lead and a reduction in intensity by a factor of 1000 is obtained for 13 cm of

lead. Thus an interpenetrated lead stacking of 15 cm is built around the source. The lead shielding starts at ~ 17 cm from the source position (5 cm – CF 35 flange radius & 12 cm for tightening the bolts). The calculated dose rate using the RadPro [3] calculator at 30 cm for a 50 mCi source with 15 cm lead shielding is 0.08 mR/ hr or 0.7 µSv/hr. For a 3.5 mCi source this is 0.05 µSv/hr. Shielding is also provided at the bend where there will be 511 keV γ field due to fast positron collision with the tube. Apart from this, additional shielding is provided near the straight section to reduce the background for the gamma detector. Thickness of the shielding was higher very near to the source position and at the aperture which is in between the CF 63 I tube and magnetic bend and was 20 cm. A table to hold approximately 3 ton of lead was made for the Pb stacking.

Majority of the shielding was completed before source mounting and only a window was left open for the source mounting such that after the source was inserted, rest of the lead stacking could be completed from the shielded side with minimum exposure time. Enough space is put between the lead shield and the UHV system just to tighten the nuts using custom wrench. The bolts are welded on to the CF 35 flange so that minimum handling is involved while tightening the nuts. Teflon gasket is used at this flange so that better sealing is obtained with minimum effort. Since the intensity of the gamma field reduces according to the square law, remote handling is preferred. Hence, while mounting the source, a 1m long custom tweezers were used for screwing the source on to the source-moderator mounting arrangement. The Teflon cylinder holding the moderator is pressed on to the source after this. Manual handling is only required at the step where the CF 35 zero length adaptor with source-moderator assembly and all biasing wires are inserted into the UHV tube and nuts are hand tightened. Further tightening is done with custom wrench. For testing the slow positron beam and transport of positrons through the magnetic field a 3.5 mCi source is inserted in the beam line. The

measured dose rate on the lead shield which is approximately 30 cm away from the source was < 0.1 µSv/hr which matches with the calculations above. Fig. 2 shows the lead shielding provided at the source side, near bend and at the start of the straight section.

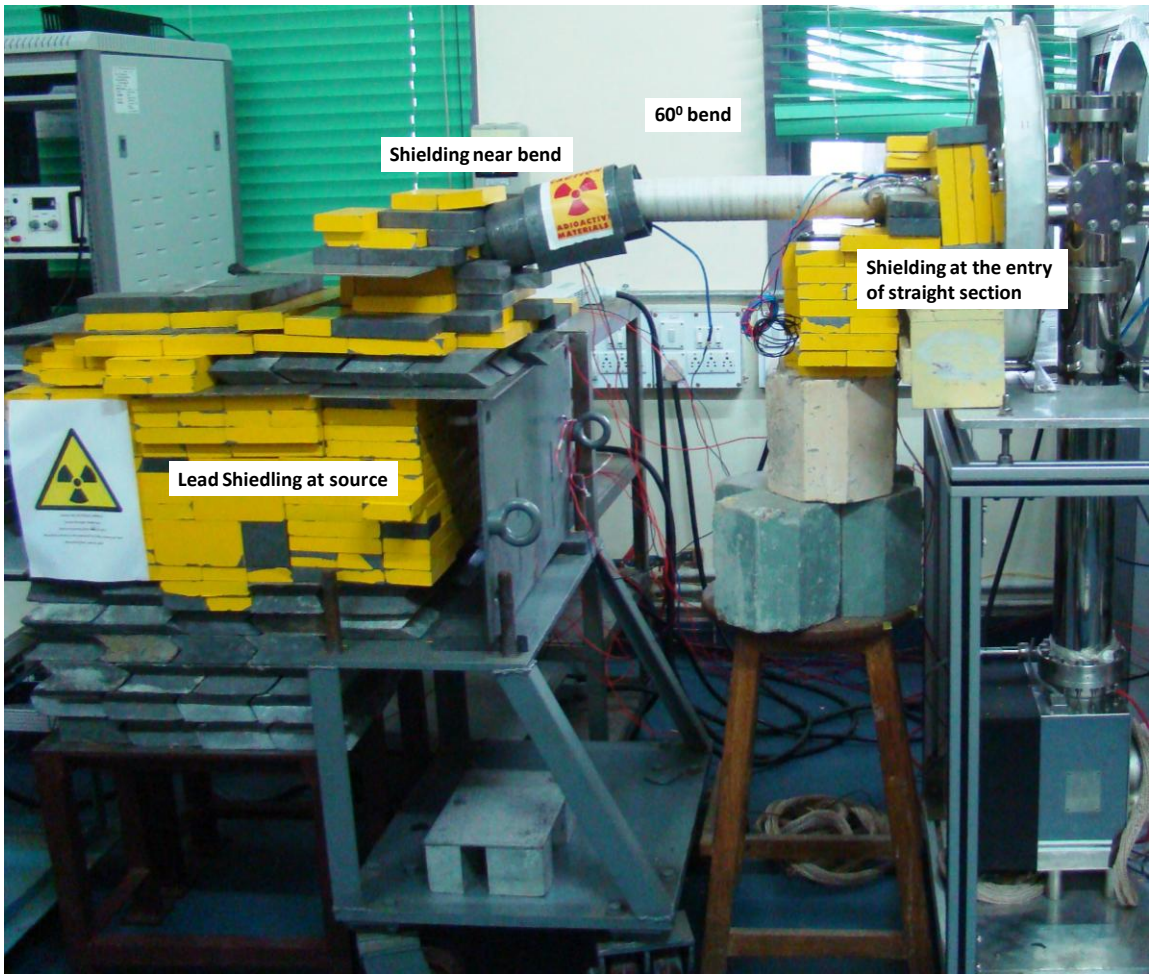

Fig. 2: Lead shielding provided near the source side, at the bend and near the straight section.

5.4 Slow positron extraction and measurements

The system after full assembly is as shown in Fig. 3. The extraction of the slow positron beam was done in two stages. First extraction was at the end of the magnetic bend and the second one at the target. The beam was deviated from its path, and was forced to hit the wall of the UHV tube by keeping a 300 Gauss horse shoe magnet at one

side of the CF 63 magnetic bend perpendicular to the beam path. Annihilation 511 keV γ was detected by NaI (Tl) based detector which was kept at the opposite side. Once the beam was obtained at the straight section, the slow positron beam was transported to the target chamber by activating the Helmholtz coils. The Doppler broadening S-parameter measurements were carried out at three representative points on two standard samples to confirm the depth selectivity. The low activity of the source was responsible for the measurements being done only at three points.

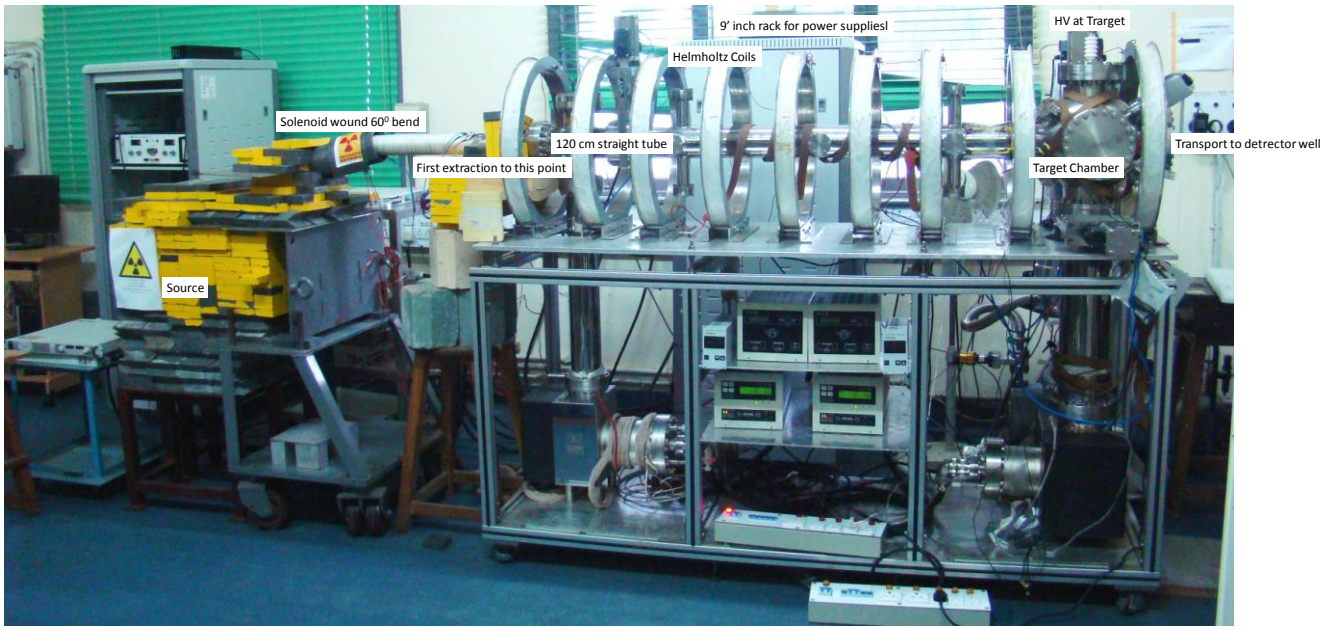

Fig. 3: Positron beam line assembly without the pulsing electrodes inside. The set up was tested for its ability to extract and transport slow positrons from the source to the target.

5.4.1 Magnetic Shielding

One of the major problems of using a photo multiplier based scintillation detector in a magnetic field is its effect on the accelerating electrons inside the photo multiplier tube resulting in a reduction in the amplitude of the output pulse. This is seen as a shift in the peak towards lower channels as well as a reduction in intensity as shown in Fig .4

where the detector is placed anti-parallel to the field and the field intensity at the detector is ~20 Gauss. Hence appropriate magnetic-shielding from the field is required to have faithful reproduction of the gamma signal. High permeability Mu-metal sheets with high saturation field were wound around the detector. A reduction in magnetic field intensity is seen inside the handmade shield. However the field was still high enough to affect the output. It was observed that when the detector was kept perpendicular to the guiding field near the solenoid winding at the magnetic bend, the attenuation in the amplitude was less and the provided shield was enough to have negligible amplitude reduction. This is because, the magnetic shield works best when the shield is perpendicular to the field and the transverse field has less effect on the photo multiplier tube. When the beam was transported to the target chamber where it was necessary to put the detector along the axial field, high purity germanium (HpGe) detector was used instead of scintillation detectors as the initial tests were to reproduce S-parameter curves. The HpGe detector showed negligible effect with axial magnetic field. However similar shield was put around the detector as well. For future use the strategy used in the NCSU pulsed beam [4] will be followed with solenoid winding on the shielded detector to nullify the magnetic field at the PMT.

5.4.2 Magnetic Field for slow positron extraction

The schematic of the geometry used till the magnetic bend is as shown in Fig. 5. As described in Chapter 4, an aperture of 16 mm diameter is put at 26 cm from the source between the CF 63 I tube and the magnetic bend. This helps in avoiding the fast positrons from entering the magnetic velocity selector as well as ensuring that the beam is centred. Two coils attached to the flanges correct for the dip in the field due to the absence of solenoid winding right on top of the flange. Hence the parameters to be

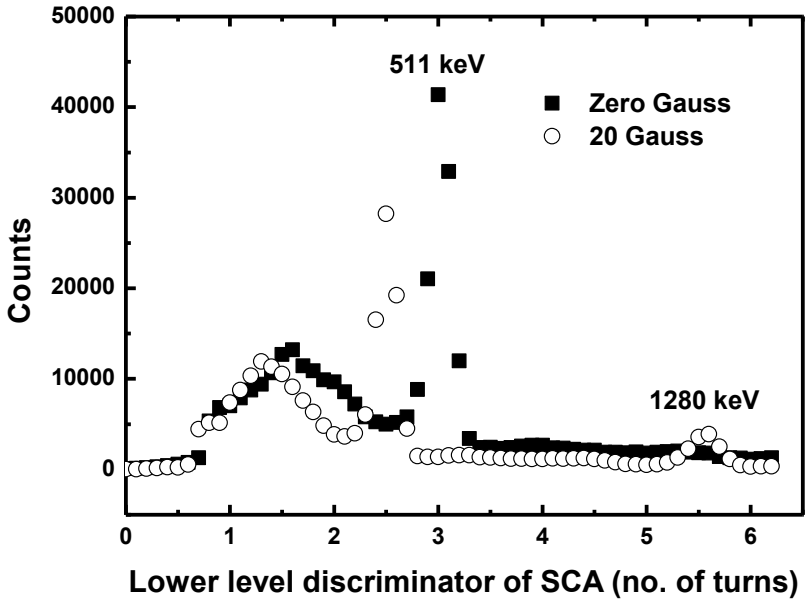

Fig. 4: Effect of magnetic field on the output of the NaI (Tl) + PMT based scintillation detector. A reduction in intensity as well as shift to lower voltages is seen for field as low as 20 Gauss

adjusted to extract positrons were the magnetic field up to the bend and drift correction coils on the bend. A positive bias is given to the moderator with respect to the extracting electrode. Hence the positron which is emitted with work function energy of 3 eV gets repelled by the moderator and hence acquires an additional energy equal to the repulsive potential. Thus a positive bias of 75V leads to an overall energy of 78 eV for the positron.

Majority of the fast positrons do not undergo moderation and just pass through it. The separation between these fast positrons and slow moderated one's are achieved using the magnetic bend. Fast positrons escaping the moderator along the magnetic axis pass straight through the aperture and hit the upper wall of the bend due to the large Larmor radius of its helical path. Whereas the fast positrons which are emitted at an angle with field follows the magnetic field in a helical path and depending on the value

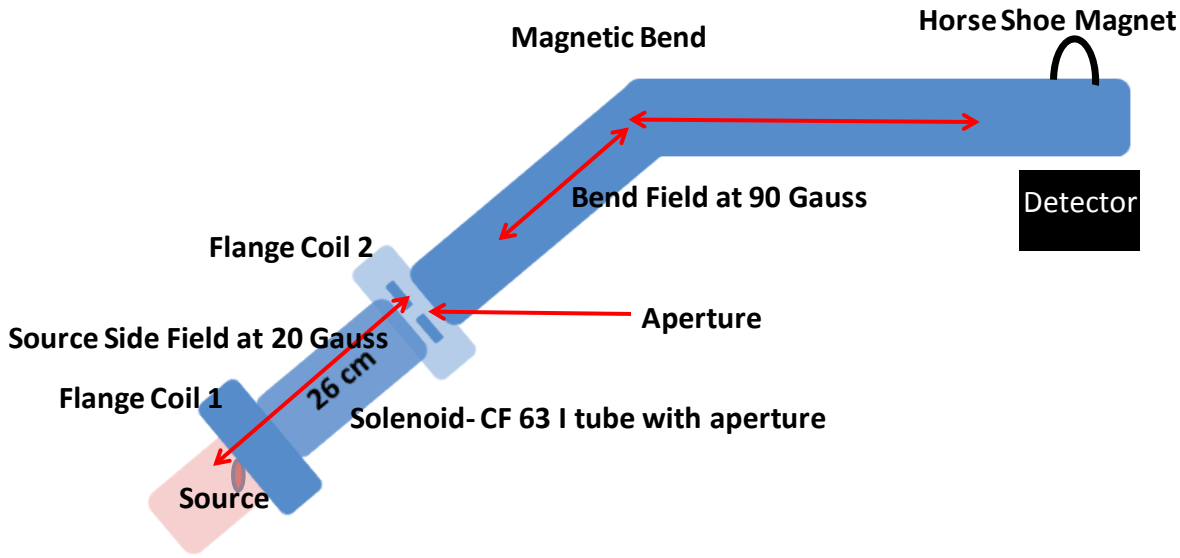

Fig. 5: Transport magnetic field setup from source to the bend. Source is mount on a 10.5 cm long CF 63 I tube on which solenoid winding is absent. The field producing components start from the Flange coil 1. Aperture is a mechanical disc with 16 mm opening.

of the field intensity, velocity and emission angle it could be filtered out at the aperture. Hence, the first parameter which needs optimization is the axial field. A uniform field of 90 Gauss was initially maintained in the region denoted in schematic in Fig. 5 and this is given in Fig. 6(a) where the source, aperture and magnetic bend positions are marked. The variation in the counts (under the region of interest -511 peak) as a function of the moderator bias voltage for this field arrangement is shown in Fig. 6(b). An increase in counts is seen with the bias voltage, however the background i.e. counts at zero moderator bias is high and a clear 511 keV peak could be seen even at an opposite bias i.e. the extraction electrode at a small positive bias with respect to the moderator, making it difficult to identify the origin of the 511 keV from slow positrons alone. This shows that some of the fast positrons are able to cross the aperture and get transported across the bend due to its shallowness as well as due to the high field intensity. Hence it was decided to reduce the field very near the source side such that the radius of the helical path of high velocity positrons is such that it would not cross the aperture. Thus the

aperture acts as a first level screening for slow positrons and the bend acts like a second velocity selection. The variation in zero bias counts with different source side magnetic field values are shown in Fig. 6(c). From this it was decided to have ~ 20 Gauss near the source side with counts just above the background. The variation in counts with bias voltage is shown for ~ 20 Gauss in source side and ~ 90 Gauss at the magnetic bend is by red circles in Fig. 6 (b). From this it was seen that at a bias of +75 V i.e. at 78 eV maximum number of positron are transported till the straight section of the bend to be detected by the detector. Keeping a +75 V bias on the moderator, the output of the detector is shown in solid green line, whereas with a +75 V bias on the extraction electrode, the output of the detector is shown in dashed red lines in Fig. 7. This shows clearly the extraction and separation of slow positrons across the bend. The extracted slow positrons are transported till the target chamber by activating the Helmholtz coils and detecting 511 keV counts using the NaI (Tl) based detector kept perpendicular to the beam path and using horse shoe magnet as before on the walls of the UHV tube. The net field from the magnetic bend to the target chamber is shown in Fig. 8.

As the bend was shallow and since the aperture made sure of the beam centring, drift correction or steering was not required for the extracted beam. However both drift and steering coils need to be activated when the beam is steered through the pulsing tubes of 15 mm internal diameter and when the target position is centred with respect to this pulsing arrangement with 15 mm exposure area. For Doppler broadening measurements 25 mm diameter sample mounting was used. For S-parameter measurements an HpGe detector having an energy resolution of 1.45 keV at ^{137}Cs 662 kev γ line with a shaping time of 6 μs is placed inside the detector well.

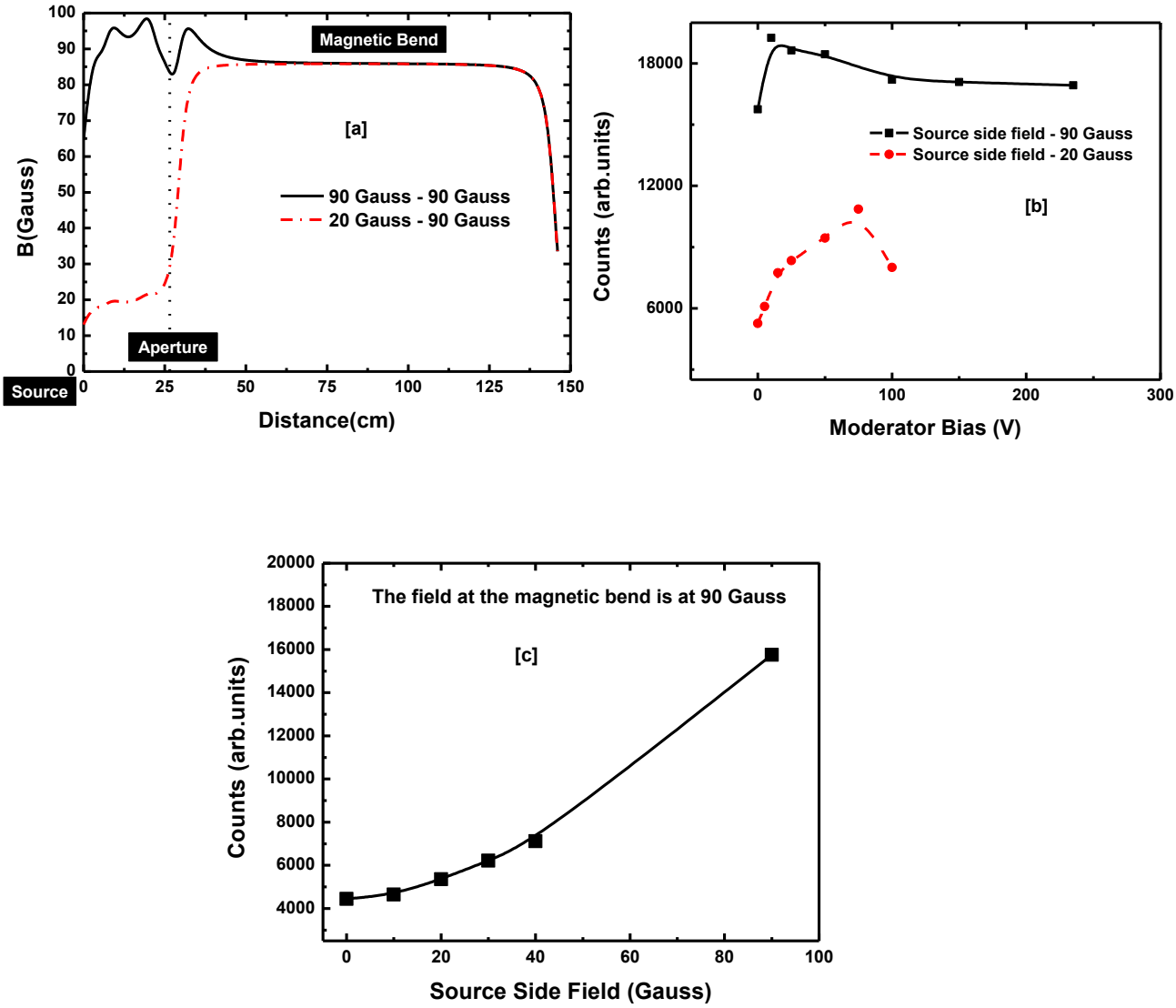

Fig. 6: (a) Transport magnetic field from source up to the magnetic bend. Black solid line indicates 90 gauss from the source side to the magnetic bend whereas red dashed line indicates 20 Gauss near the source side and 90 Gauss at the magnetic bend. (b) Variation of counts with different moderator bias with two source side field values – one at 90 Gauss (solid lines) and another at 20 Gauss (dashed lines). (c) Keeping the bend at 90 Gauss, the zero bias counts are noted for different source side field.

.

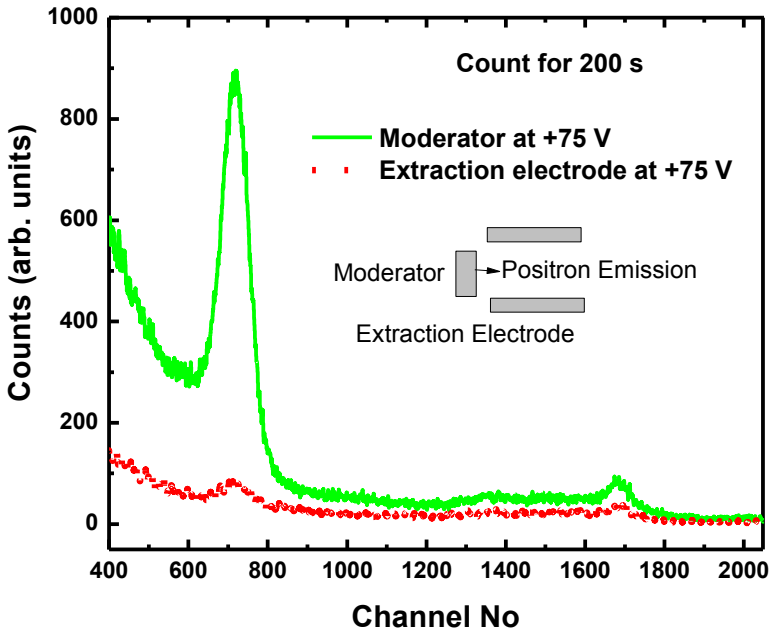

Fig.7 : Beam count at the bend with different moderator bias. Beam on (green) when moderator is at +75 V and beam off (red) when the extraction electrode is at + 75 V. This is achieved after fixing the axial field at 20 Gauss – 90 Gauss combination.

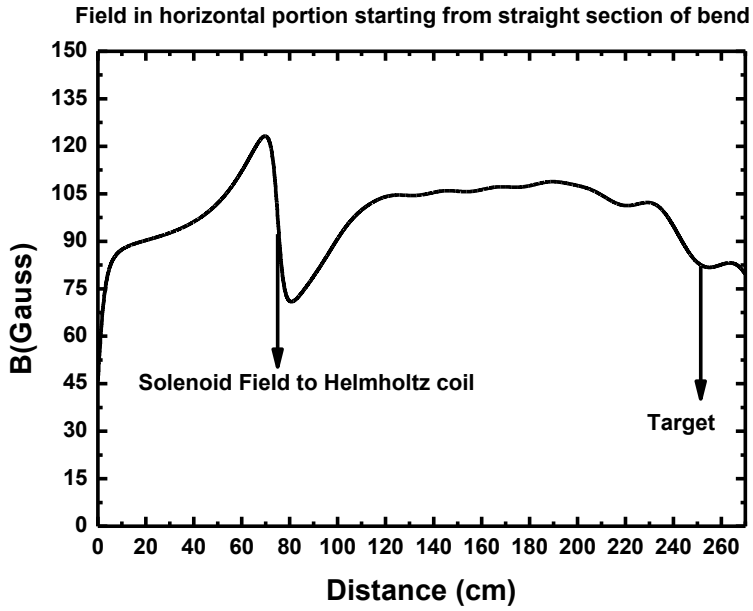

Fig. 8 : Magnetic field intensity from the bend region to the target chamber. The target position and solenoid to Helmholtz field transition region are shown using arrow marks.

5.4.3 Doppler Broadening Measurements

The extraction of the slow positrons up to the target position was further confirmed by carrying out Doppler broadening S-parameter measurements on Copper plate used as a temporary sample mounting arrangement as well as on Silicon (100) single crystal. For Doppler broadening measurements, the moderator was biased to +250 V and hence the mean energy of the positrons reaching the target chamber will be 253 eV. Measurements were carried out at three representative target high voltages. The measurement was limited to three points due to low count rate with 3mCi source. The results are shown in Fig. 9 where an increasing trend is seen for Silicon and a decreasing trend is seen for the Copper plate. This is consistent with the reported S-parameter trends for Cu and Si.

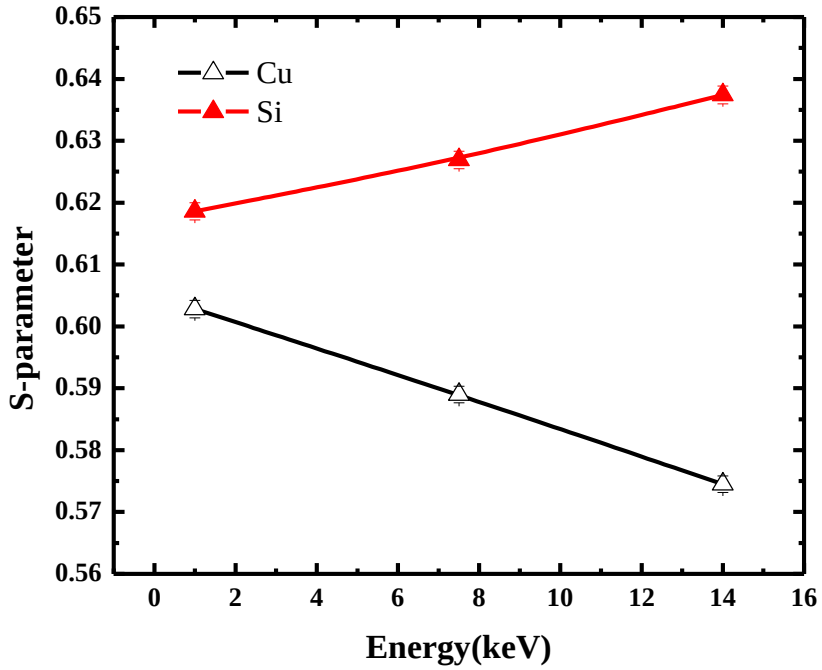

Fig. 9: S-parameter versus accelerating voltage for Copper and Si (100) crystal.

5.5 Electrical connections in the vacuum side

The electrical connection to the pulsing electrodes which has to be inserted into the beam line is completed at the time of thesis. The RF power is coupled to the chopper ring by connecting the 50 Ω matched RG-58U high voltage, UHV compatible Kapton insulated cable (M/S Kurt J Lesker) to the ring using a through hole provided for electrical connection. The outer braid of the cable is connected to the front ring with respect to which the 50 MHz square wave and +15V DC bias is given. The other end of the cable is connected to the instrumentation feed through with grounded SMA type connectors. The central copper conductor of a similar cable is used to power the buncher electrodes; the outer braid providing insulation from cross talk or signal pick up as it goes to the beam ground. The electrodes which serve as ground for the RF power, is also DC offset to -250 V. These three tubes which are at -250 V are short using the RG58 U cable through the central conductor. Here again the outer braids are given to the ground preventing them from picking up any RF signals. A common output is taken from one of the three electrodes and taken to a CF 16 feed through. The connection to the feedthrough is through push fit connectors. The bias to the last drift tube is taken from a similar CF 16 electrical feedthrough. The cabling wires are again with protective ground outer braids. The graded accelerators are planned to be connected with 100 MΩ epoxy coated high voltage resistors with voltage tolerance of > 3.5 kV. However in the phase one testing of pulsing electrode the graded accelerators is biased to the final drift tube voltage. Fig. 10 (a-c) shows the connections given to each of the units described. After connection the part till the drift tube is inserted into the 120 cm long tube and is connected to the beam line. The graded accelerators are later connected through the CF 150 port of the target chamber. At the time of submission of thesis, vacuum testing and steering of positrons through the electrodes has been taken up.

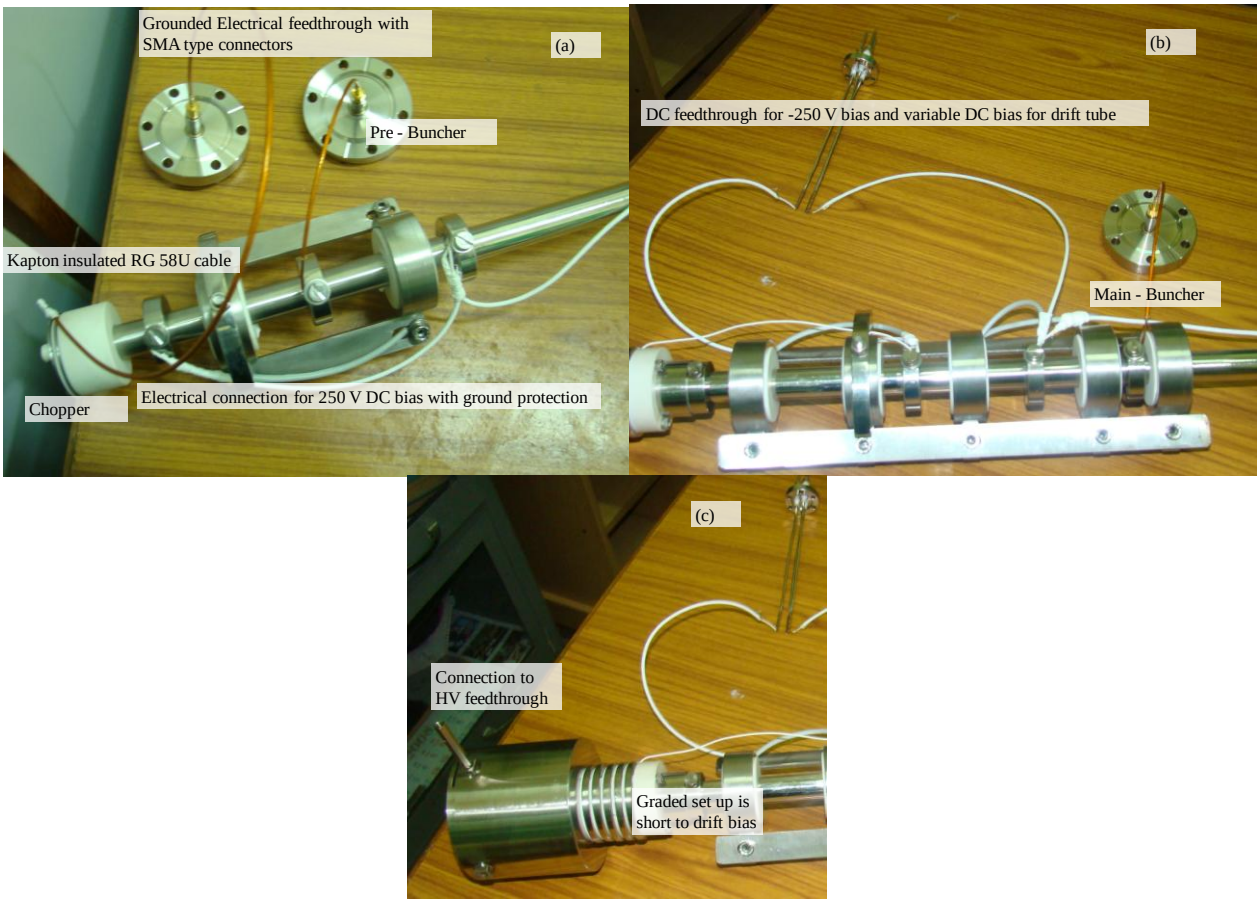

Fig. 10: (a) Chopper and pre-buncher connected to the grounded feedthorugh using RG58 U cable's central conductor. (b) Drift tube and 250 V bias is through braided wires which minimizes RF signal pickup. (c) Graded accelerator and drift short for the first phase of testing. The HV connection is given to the Faraday cage.

5.6 Summary

- The UHV beam line to hold the pulsing system has been fabricated and assembled. The Na-22 source of activity 3.5 mCi has been mounted and lead shielding has been arranged for safe working environment around the beam line.
- Annealed W (100) moderator was placed in front of the source for the production of slow positrons with proper extraction bias.

- The slow positrons were extracted across the magnetic bend by optimizing the axial field at the source and the bend region.
- The extracted positrons were transported up to the target chamber by activating the Helmholtz coils.
- The depth selectivity was confirmed by carrying out Doppler broadening S-parameter measurements on Cu and Si (100) samples.
- Electrical connections inside the UHV chamber are made taking care of signal pick up by stray Cu wires.

5.7 Future Steps

- The capacitance values of the chopper and bunching electrodes at 50 MHz and 200 MHz has to be measured at the atmosphere side of the feedthroughs in the operating vacuum condition. This helps in determining the values of other components in the coupling network.
- The slow positron beam has to be steered through the pulsing electrodes up to the target chamber by adjusting the drift correction as well as the steering coils near the target chamber.
- The RF power and DC bias will be given to all the electrodes after the completion of above steps. The impedances are to be matched for maximum power transfer. The entire system is integrated along with the timing circuit consisting of two CFDD, Fast coincidence system and an MCA for lifetime measurements. The faithful generation of stop signal using square wave input to the CFDD has to be tested before the integration. The timing circuit integration also involves putting proper delay cables for getting TAC output.

- A beam automation system has to be designed to have a complete control of the beam system. Hardware control to switch off the high voltage acceleration system as well as the RF power circuitry in case of vacuum failure has to be incorporated. Initial design of Labview control has been done where setting the HV is achieved using a programmable system on chip (PSoC) and MCA control is achieved.
- A data analysis routine in line of VEPFIT [5] has to be designed for getting depth resolved lifetime components.

References

1. Krause-Rehberg R, van der Walt N, Büttner L and Börner F 2004 *"A ^{22}Na positron source for use in UHV" Appl. Surf. Sci.* **221** 165.
2. http://www.stanford.edu/dept/EHS/prod/researchlab/radlaser/RSDS_sheets/Na-22.pdf
3. http://www.radprocalculator.com/
4. Hathaway A.G. 2012 *"High Intensity Pulsed Picosecond Positron Beam for Nanophase Examination" Doctoral Dissertation Department of Nuclear Engineering North Carolina State University.*
5. van Veen A, Schut H, de Vries J, Hakvoort R A and Ijpma M R 1990 *"Analysis of positron profiling data by means of VEPFIT" Positron Beam for Solids and Surfaces AIP Conf. Proc. No.* **218** ed Schultz P J, Massoumi G R and Simpson P J (New York:AIP) 171.

Chapter 6

Summary and Future Outlook

6.1 Introduction

The thesis presented the results primarily generated using beam based positron spectroscopy on the analysis of impurity - vacancy interaction in Nitrogen implanted Phosphorous doped n type Cz-Si (100) as well as on the isochronal thermal evolution of defects in self-ion implanted HOPG. The studies could throw light into many known and unknown phenomenon as well as showed the existence of certain defect structures. The design and development of a pulsed positron beam system for the proper identification of defect species is described in the later part of the thesis. The progress of this development has been highlighted in the thesis. The major findings and important future work required has been put up in the subsequent sections corresponding to each work.

6.2 Nitrogen implanted n type Cz-Si (100)

Nitrogen is an important constituent in Silicon during device fabrication and so its interaction with vacancies in silicon has been investigated after nitrogen implantation at two doses. Important findings of the study are

- Trans projected range deep level defects were seen in Silicon implanted to a dose of $1x10^{15}$ ions/cm^2 which were found to be annealed out by 473 K. Such defects were not seen at a lower dose of $1x10^{14}$ ions/cm^2.
- Clear evidence for Nitrogen – Vacancy complexing were seen for lower dose sample. However, for the higher dose sample coexistence of large vacancy clusters masked their existence.

- Nitrogen has an anomalous diffusion pattern and oxygen in-diffusion starts after the removal of Nitrogen from the system.

It was difficult to pin point the nature of trans-projected range defects as well as the nature of defects at 873 K in the higher dose sample. Hence, a positron lifetime investigation on similarly prepared samples could clarify their nature. Isothermal investigations at identified temperature ranges could shed some light into the activation mechanism of N-V complex formation. The study could also be extended to higher doses in small steps to identify the nature of such complexes when silicon is amorphized as well as during the early stages of nitridation. Slow positron studies have to be complemented by techniques like XPS to look at the evolution of N-core shell peaks with dose and thermal treatment and thus get an idea about their structure. FTIR studies could also be used to track the divacancy peak during isochronal and isothermal studies all of which would help to formulate a complete physical principle of Nitrogen-vacancy interaction.

Currently for 22 nm and 14 nm MOSFET fabrication, complex metal oxide is used as the gate and its nitridation is done for vacancy removal. The efficacy of nitrogen implantation to trap vacancies can be probed in such metal oxide/SOI heterostructures and thus, understand the nitrogen vacancy interaction across the interface. This would be a valuable information for device engineers to control their fabrication inventories. The understanding of Nitrogen-vacancy interaction in such complex systems has to start from what was observed in simple systems like nitrogen in silicon.

6.3 Self ion implanted HOPG

Even after six decades of study, defect structure and its thermal evolution in graphite is not understood completely. This knowledge has become particularly important in this age of nano-engineering of graphite like structure and use of graphite tiles in plasma facing walls of fusion reactors. In the present thesis the dependence of defect density and defect type on the thermal evolution has been investigated using slow positron beam spectroscopy in $^{12}C^{+}$ ion implanted HOPG at two doses - $1x10^{15}$ ions/cm^2 and $1x10^{14}$ ions/cm^2. Important findings are

- Ridged network structure was seen on the implanted surface in high dose sample which showed small changes in network density after complete annealing cycle. Low dose sample showed small protrusions on the surface in the as implanted sample and curling was seen to be remaining after the complete annealing cycle.
- The disorder peak intensity ratio with the graphitic peak in Raman spectrum showed two recovery regimes, a fast one till 473 K and slow recovery beyond that. The fast recovery was assigned to I-V recombination, whereas the slow one was due to the defect migration to surface.
- For low dose sample, I-V recombination assisted recovery was seen from 373 K and defect migration to surface from 623-773 K. However for high dose sample, I-V recombination assisted recovery was seen only from 423 K, with a major drop near surface at 523 K. Defect migration to surface was noticed from 723 K after the release of open volume defects from interplanar divacancy like defects at the end of range which was stable till 673 K.
- For high dose sample the S-parameter at implanted zone went lower than the un implanted graphite after complete annealing cycle pointing to cross linking interstitials in the interlayer region.

Here again a qualitative picture has been drawn based on the observed defect kinetics which could only be confirmed by doing a depth resolved positron lifetime spectroscopy and thus identify the various defect structures. The study has to be done in isothermal mode at specific temperatures to calculate the activation energies involved in fast and slow recovery process. Topography evolution has to be followed diligently at every annealing step using STM with superior atom level resolution to comment on vacancy or adatom migration on surface. Implantation has to be carried at shallower depths to have better correlation with Raman data. Ab-initio simulations have to be carried out to calculate positron annihilation characteristics for different defect structures proposed to be existing in the present system which can be compared with the obtained results. The study has to be extended to higher doses to understand open-volume defect structure evolution during the amorphization process.

6.4 Development of Pulsed Positron Beam

The development of a pulsed positron beam has been taken up in the lab to improve the investigation of defect structures in a depth resolved manner. The major steps in this direction which have been completed are given below.

- The design of pulsed positron beam has been finalised with one chopper and two bunchers. The chopper and the pre-buncher works at 50 MHz and the main buncher works at 200 MHz. Based on this, the length of the bunching electrode tubes were finalised to be equivalent to a phase difference of π for the reference positron.
- The UHV system has been designed and fabricated to house the pulsing electrodes and tested to obtain a vacuum of ~10^{-9} mbar.

- Magnetic transport of the positron beam from the source to the target is obtained by solenoid and Helmholtz fields and these were designed, wound and tested.
- The Arbitrary wave form generators and the required amplifiers were procured and tested. The impedance matching network for the sine wave and coupling network of the square wave has been conceptualised based on serial LC resonance circuit. The timing circuit for the generation of lifetime spectrum is also decided.
- The initial testing of the magnetic bend for slow positron velocity selection has been done with 3.5 mCi source and S-parameter Doppler broadening measurements were carried out on Cu and Si (100) sample.
- Electrical connection to the pulsing electrodes which goes inside the UHV chamber has been completed and its integration with primary beam line is over.

Further work that needs to be done is highlighted here. The beam will be steered through the pulsing electrodes and after proper impedance matching the RF power will be given. This is followed by the integration of the timing circuit and testing of stop signal generation from CFDD. Once these are completed the first experiments to generate lifetime spectrum would be done. The future effort will be aimed at getting a proper lifetime spectrum and a better time resolution. There is also an effort to measure and reduce the beam diameter through magnetic lensing at the sample position. An automation system with complete control of the experiment needs to be developed the first steps of which have already been completed.

The use of fast digital oscilloscope for the generation of lifetime spectrum by collecting signals directly from PMT anode has already been demonstrated in the lab. The immediate modification is to replace the analogue timing circuit with the digital

timing assembly with a faster acquisition card such that there is greater control on the data analysis and thus avoid to a great extent accidental event counting by introducing stringent coincidence conditions. This step would help in improving the resolution of the system. Once time resolution of the order of ~ 300 ps is obtained, two problems discussed earlier in the thesis needs to be pursued for confirmation of the nature of defects in the irradiated Si and Graphite.

In next phase of development, modifications like in situ annealing of the moderator, multiple sample mounting and load lock arrangement for sample mounting to maintain the beam line at a vacuum of 10^{-8} mbar even during sample mounting are planned and the design has started. Efforts to have a variable time gap between positron pulses from 20 ns to higher values are planned by replacing the grid type chopper to deflection type. The data analysis part is yet another area which requires effort to combine the bulk lifetime analysis routine to solving the diffusion equation of positron inside the sample and hence chalk out a strategy to avoid contribution from lifetimes from different depth scales thus improving the depth resolution.

Planning has already started for the extension of the present pulsed positron beam design to a high intensity positron beam. Three possible routes are explored. The KAMINI reactor inside IGCAR, Kalpakkam with a neutron flux of 8.0×10^{12} $cm^{-2}s^{-1}$ at the core centre can be utilized for the production of positrons through (n,γ) reaction and pair production. Other two scenarios explored are LINAC and higher energy Laser pulses to produce high intensity positrons. Radiation damage studies in structural materials, porosity evolution in separation membranes and defects in thin film heterostructures for solar cell applications are some problems explored for future application of the laboratory based pulsed positron facility.

List of Publications

1. **Anto C V**, Abhaya S, Magudapathy P, Amarendra G and Nair K G M 2010 *"Depth profiling of vacancy defects and their thermal stability in N-implanted Si: A Positron Annihilation study" J. Phys. D: Appl. Phys.* **43** 325401.

2. **Anto C V**, Arunkumar J, Rajaraman R, Nair K G M and Amarendra G 2011 *"Characterization of Vacancy Defects in Carbon Ion Irradiated Graphite Using Positrons" AIP Conf. Proc.* **1349**, 1281.

3. **Anto C V**, Balamurughan A K, Magudapathy P, Dash S, Nair K G M and Amarendra G 2013 *"Thermally initiated nitrogen – vacancy interaction in nitrogen implanted silicon"* Accepted to DAE SSPS - 2013

4. **Anto C V**, Rajaraman R, Abhaya S, Parimala J and Amarendra G 2011 *"Design optimization of a pulsed positron beam system at IGCAR, Kalpakkam" J. Phys.: Conf. Ser.* **262** 012062.

5. **Anto C V**, Rajaraman R, Venugopal Rao G, Abhaya S, Parimala J and Amarendra G 2012 *"Optimization of Drift Bias in an UHV Based Pulsed Positron Beam System" AIP Conf. Proc.* **1447** 493.

6. **Chirayath V A**, Viswanath R N, Rajaraman R, Amarendra G and Sundar C S 2013 "*Ligament coarsening in Nanoporous Gold : A positron annihilation Study" MRSI AGM-2013 February 11-13 IGCAR Kalpakkam.* *

7. Viswanath R N, **Chirayath V A**, Rajaraman R, Amarendra G, and Sundar C S 2013 *"Ligament coarsening in nanoporous gold: Insights from positron annihilation study" App. Phys. Lett.* **102** 253101. *

8. Arunkumar J, David C, **Anto C V**, Nair K G M, Kalavathi S, Rajaraman R, Amarendra G, Panigrahi B K, Magudapathy P and Kennedy J 2011 *"A study on*

the redistribution of ion-implanted nitrogen in Ti-modified austenitic steel" Journal of Nuclear Materials, **414** 382.*

9. Annalakshmi O, **Anto C V**, Hari Babu S, Jose M T and Amarendra G 2009 *"Positron Annihilation studies on CaSO4:Dy theromluminescence phospors" Physica Status Solidi (c)* **6** 2516. *

10. Ragunanthan V, Hari Babu S, **Anto C V**, Rajaraman R, Amarendra G, Saroja S, Sundar C S, Ana Alamo and Baldev Raj 2009 "Positron annihilation studies on 9Cr Reduced Activation Ferritic/Martensitic steels" *Physica Status Solidi (c)* **6** 2307. *

To be submitted/under preparation

1. Anto C V et. al. 2013 *"Defect evolution in Carbon ion implanted Highly Oriented Pyrolytic Graphite: Positron and Raman Spectroscopic studies"*

2. Anto C V et.al. 2013 *"Slow Positron beam extraction and design of a pulsed positron beam"*

3. Anto C V et.al. 2013 *"Development of a beam based lifetime system"*

---

* Not included in thesis